



Académie universitaire Wallonie-Europe
Université de Liège
Faculté des Sciences Appliquées
Département d'Electricité, Electronique
et Informatique (Institut Montefiore)

Reduced-order modelling of active distribution networks for large-disturbance simulations

Gilles Chaspierre

Liège, Belgium, October 2020

Submitted in partial fulfilment of the requirements for the degree of
Doctor of Philosophy (Ph.D.) in Engineering Sciences

Examining Committee

Professor (President of Jury), Cristophe Geuzaine, Université de Liège, Belgium

Professor Jovica V. Milanovic, The University of Manchester, UK

Professor Marc Petit, CentraleSupélec Paris, France

Patrick Panciatici, Scientific Advisor, R&D department, RTE, France

Professor Bertrand Cornélusse, Université de Liège, Belgium

Professor Thierry Van Cutsem (Ph.D. advisor), FNRS and Université de Liège, Belgium

Abstract

Distribution systems are getting more and more complex owing to the increasing number of Inverter-Based Generators (IBGs) connected at Medium-Voltage (MV) level. This makes distribution networks more and more responsive and their influence on the whole power system dynamics increases. Therefore, it becomes important for Transmission System Operators (TSOs) to model those Active Distribution Networks (ADNs) in their dynamic studies.

First, this thesis deals with the derivation of reduced-order, “grey-box” models of ADNs, intended for dynamic simulations of the transmission system. The ADNs are assumed to host IBGs as well as static and motor loads, whose dynamic parameters are affected by uncertainty. This latter issue is addressed using Monte-Carlo simulations. The parameters of the equivalents are adjusted to match as closely as possible the average of the randomized responses, while their dispersion is accounted for through the weights of the weighted least-square minimization. A procedure is used to remove from the identification the parameters with negligible impact. To avoid over-fitting, the equivalents are tuned for multiple large-disturbance simulations. A recursive procedure is used to select the smallest possible subset of disturbances involved in the least-square minimization.

Next, the methodology is extended to account for changing operating conditions. This consists of testing the accuracy of a set of previously derived equivalents, and updating the best of them if its accuracy is not satisfactory. In order to update the equivalent with minimal effort, an approach minimizes the number of parameters to update. In most cases, the results coincide with expectations coming from “engineering judgment”, involving the adjustment of a (very) small subset of parameters.

Finally, a new application for a Battery Energy Storage System (BESS), connected at distribution level, is proposed. Its active and reactive powers are controlled such that the net power entering the distribution network matches the response of the available equivalent to large disturbances in the transmission system. The response of the equivalent is simulated in real time. This would allow using with a higher guarantee of accuracy the equivalent model in dynamic simulations of the transmission system. The BESS is supposed to be connected at the main substation of the distribution grid and its control does not use any model of that grid.

All simulations reported in the thesis have been carried out on three ADN test systems with different characteristics, one of them being derived from an existing distribution grid. The tests involve large disturbance scenarios that trigger nonlinear, discontinuous responses of IBGs and loads.

Acknowledgements

I am filled with joy and excitement. I do not realize that I am actually writing the acknowledgments of my thesis. I still remember my first day as a PhD student. I was reading the acknowledgments of a thesis related to my work. Back then, the moment when I would have to write my own acknowledgments seemed like a distant dream, and yet, here we are. And nothing would have been possible without all the people that helped and supported me during the past four years.

First and foremost, I wish to express my deepest gratitude to my supervisor, Prof. Thierry Van Cutsem, for everything he has done for me during my PhD studies. I am so grateful he has devoted such a considerable amount of his time to guide me through my research. It was my greatest honor to work with a man like him, whose experience, knowledge and thoroughness inspired me and pushed me to my very best. What I learned from him will remain a source of inspiration for the rest of my professional life.

I would also like to thank each one of the members of the committee for devoting their time to assess this thesis.

During these years, I had the fortune to collaborate and benefit from the interactions with many researchers from other institutions. This project was funded by RTE, the French Transmission System Operator. I would especially like to thank the people from the R&D department of RTE, Dr. Patrick Panciatici who makes this project possible and whose excellent suggestions significantly contribute to the accomplishment of this thesis; and Dr. Guillaume Denis for the valuable feedbacks and comments during our meetings. I would like to extend my thanks to Thibault Prevost for his interest and relevant remarks when he attended some of the meetings at RTE. I also had the pleasure of enjoying a very fruitful collaboration with the research group of Prof. Pierluigi Mancarella during an internship at the University of Melbourne in Australia. I would like to thank him for offering me the opportunity of such a great abroad experience in a highly ranked institution. Among his team, my special thanks go to my friend Mehdi Ghazavi Dozein who welcomed me the first day of my internship and with whom I had the pleasure to work on a very interesting project. I wish him the best towards the accomplishment of his PhD studies. I also would like to extend my sincere thanks to Prof. Gustavo Valverde, from the University of Costa Rica, and his

PhD student for sharing valuable information that helped me to improve my thesis.

It would be impossible to forget my former colleagues and friends from University of Liège. While I am today the only PhD student of Prof. Van Cutsem's team, when I started my PhD studies, I had the pleasure to meet Dr. Tilman Weckesser, Dr. Hamid Soleimani and Dr. Lampros Papangelis. We had some great times together sharing lunches, coffee breaks or even birthday cakes. I would like to thank them all for integrating me so nicely in the team and to have always been available when I needed support in my work. I wish them the best. I also want to thank Prof. Petros Aristidou, from Cyprus University of Technology (and former PhD student of the University of Liège), who shared his expertise and offered me his assistance whenever I encountered software issues. Last but not least, a special thank to Dr. Mevludin Glavic whose broad view on the literature considerably helped me to start my thesis and who was always happy to guide and help me when I needed it.

I would like to extend my appreciation to all researchers who briefly joined our group and with whom I shared insightful discussions about work and life : Dr. Gustav Lammert, Luis David Pabon Ospina, Miguel Angel Gonzales, Stefan Stankovic and Georgios Misyris.

Outside the work environment, this thesis would not have been possible without the support of my friends. I wish to particularly thank Simon Bernard, in whom I can always find support and who has always been like a brother to me. I also want to thank my engineers friends and particularly Alexandre Danthine, Kevin Hedia and Bertrand Bourseau, who, at some point, have shown some interest in my work.

I cannot find the words to express my gratitude to my family: my parents, Véronique and Alain, for always being there for me and supporting my decisions; my little sister, Pauline, who has always been proud of her big brother and who makes me feel like I am able to achieve anything; my grandfather, Hubert, who always wanted me to become an engineer and whose stories learned me a lot about life. My last thanks and all my love go to my girlfriend Léa, for standing by my side in this adventure and being such a source of happiness in my life.

To my late grandmothers, Janine and Angèle, who I know would have been proud.

‘Never confuse education with intelligence,
you can have a PhD and still be an idiot.’

Richard P. Feynman

Contents

Abstract	i
Acknowledgements	v
1 Introduction	1
1.1 Background and motivations	1
1.2 Illustrative example	3
1.3 Overview of dynamic equivalencing approaches	5
1.4 Requested features and first choice of the equivalent model	11
1.5 Challenges, objectives and contributions of this thesis	12
1.6 Test systems used in this thesis	14
1.7 Outline of this report	17
1.8 Mathematical notations	18
1.9 Publication list	18
2 Modelling of active distribution network components	21
2.1 Models under the phasor approximation	21
2.2 Generic load model	24
2.3 Generic IBG model	27
2.4 Synchronous generator model	34
2.5 Equivalent representation of the transmission system	35
2.6 Illustration of model responses to large disturbances	40
2.7 Summary	51

3	Dealing with model uncertainty	53
3.1	Introduction	53
3.2	Model randomization in MC simulations	54
3.3	Extracting statistics	57
3.4	Extracting a representative parameters set	63
3.5	Choosing the number of MC simulations	68
3.6	Summary	70
4	ADN equivalent: structure, modelling and parameter identification	71
4.1	Approach and overview	71
4.2	Models in the dynamic equivalent	72
4.3	Weighted least-square identification	77
4.4	Solving the optimization problem	77
4.5	Recursive training	78
4.6	Discarding non significant parameters	79
4.7	Initialization of equivalent	80
4.8	Overview of simulation results	81
4.9	Simulation results with ADN No 1	81
4.10	Simulation results with ADN No 2	97
4.11	Simulation results with ADN No 3	107
4.12	Reduction of model complexity	115
4.13	Summary	115
5	Update of the equivalent with operating conditions	117
5.1	Multiple equivalents for multiple operating conditions	117
5.2	On the TSO-DSO share of work	118
5.3	Handling of new operating conditions : overview of procedure	119
5.4	Building a new equivalent with minimal update effort	122
5.5	Summary and conclusions	135

6	Control of a battery energy storage system to compensate for the equivalent inaccuracies	137
6.1	Introduction	138
6.2	Overview of the proposed BESS control	138
6.3	Modelling the BESS, its converter and its controller	139
6.4	Voltage phasor measurement process	144
6.5	Simulation results	145
6.6	Summary and conclusions	164
7	General conclusion	167
7.1	Summary of work and main contributions	167
7.2	Directions for future work	169
	Appendices	171
A	Comparison of ULiège IBG and WECC type 4 models	173
A.1	Overview of the WECC type 4 model	173
A.2	Assumptions and selected configuration	174
A.3	Optimal adjustment of the ULiège IBG model parameters	177
A.4	Simulation results	178
B	Alternative objective functions for the identification of the equivalent	183
B.1	Non-weighted least-square objective	183
B.2	Alternative weighted least-square objective	183
B.3	Barrier functions	184
C	Measurement-based identification of aggregate PV models	187
C.1	Overview of the event	187
C.2	Measurement-based identification	188
C.3	Modelling of network components	191
C.4	Test system for the parameter identification	193
C.5	Simulation results	194
C.6	Scalability of the method	196

D PMU measurements processing	197
D.1 Overview of the model	197
D.2 Analytical expression of the weights	198
D.3 On the size of the time window	200
D.4 Fine tuning of the weights	201
 Bibliography	 203

Chapter 1

Introduction

This chapter presents the background and main motivations for the research presented in this thesis. It describes various approaches to power system dynamic equivalencing and then discusses in some more details the equivalencing of active distribution networks. The desirable features of the equivalent model for the application targeted in this thesis are presented, the challenges and contributions of this research work are listed and the test systems used are described. The chapter ends with an outline of this report and the list of resulting publications.

1.1 Background and motivations

Environmental concerns drive the sustained replacement of conventional generation units, such as Synchronous Generators (SGs), by Inverter-Based Generators (IBGs) such as PhotoVoltaic (PV) units or Wind Turbines (WTs). Many of these IBGs are connected to lower voltage levels, which increases the complexity of distribution systems. The resulting Active Distribution Networks (ADNs) will have a growing influence on the whole power system dynamics. The dynamics of the future power systems will indeed arise from an increased number of distributed components. For instance, solar PV has become the worlds fastest-growing energy technology, with gigawatt-scale markets in an increasing number of countries. By the end of 2018, the leading countries for cumulative PV capacity were China, the United States, Japan, Germany and India [Ren20]. As an illustration, the evolution of PV capacity by country and region from 2008 to 2018 is shown in Fig. 1.1, mainly for residential and commercial rooftop installations, connected to the distribution system.

This replacement of conventional transmission-connected generators by small, dispersed IBGs induces a reduction of the short-circuit level in the transmission grid, which can result in higher voltage sensitivity, and exacerbates the influence of ADNs on power system dynamics triggered

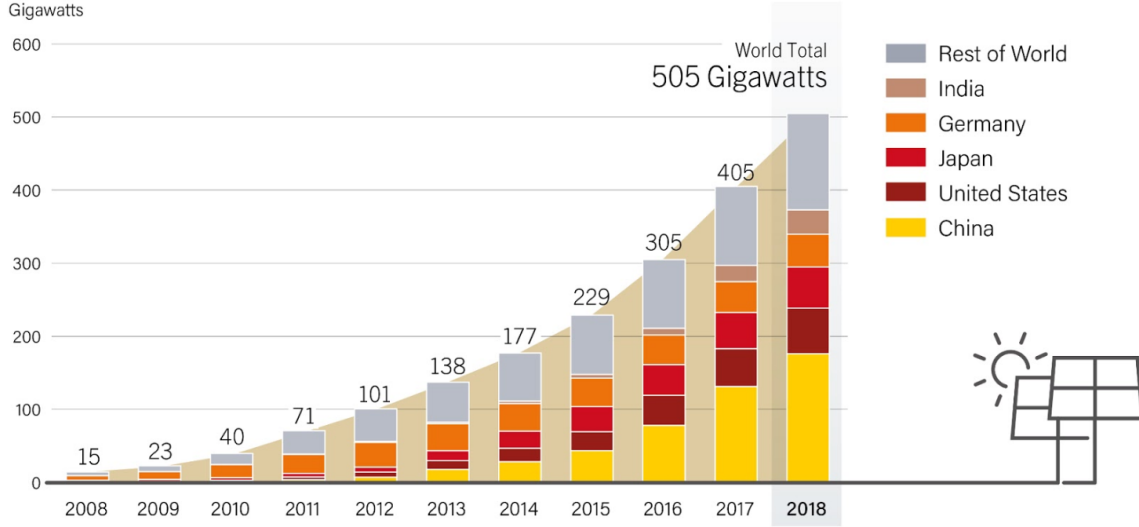


Figure 1.1: Evolution of PV capacity by country and region from 2008 to 2018 [Ren20]

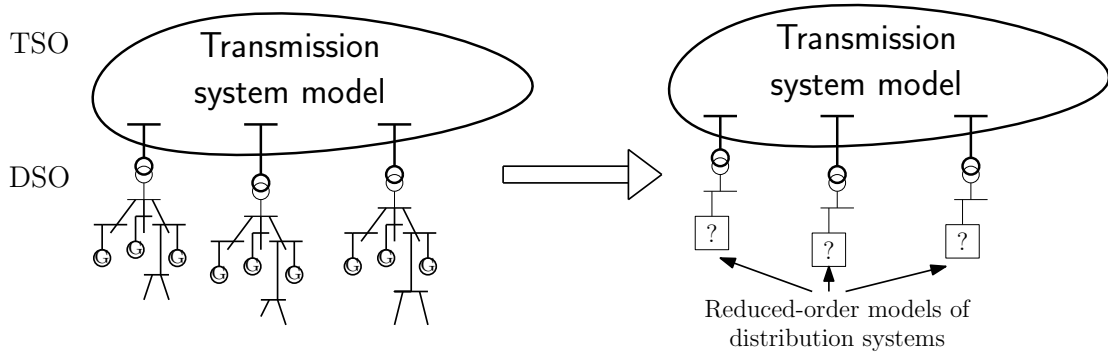


Figure 1.2: From detailed T&D model to dynamic equivalents of distribution systems

by disturbances [DMSY18, JPK⁺18]. Hence, it becomes more and more important for Transmission System Operators (TSOs) to account for the contributions of such ADNs in power system dynamic studies. Furthermore, the post mortem analysis of several major blackouts have unveiled the inaccurate modelling of distribution grids [ZM17].

One approach of this modelling issue could be the simulation of the Combined Transmission and Distribution Systems (CoTDS). This particular application of co-simulation techniques has been the subject of recent publications such as [P. 15, VKA18, BA19], for instance.

However, in spite of the progress made in co-simulation of CoTDS, collecting all the parameters and matching the operating point of concern may represent a prohibitive data processing tasks for the TSO.

Another obstacle could be the confidentiality of data. While the Distribution System Operator (DSO) of a Medium-Voltage (MV) and Low-Voltage (LV) grid is usually entitled to collect data about the connected equipment, sharing this information with the TSO may raise legal issues in some countries.

Clearly, to tackle all these issues, it makes more sense for the DSOs to process the data of their own systems and derive a reduced, “anonymized” models of significantly lower complexity than the original, unreduced models that they have assembled.

Those equivalents are intended to be “attached” to the model of the transmission system for use by the TSO in its power system dynamic studies, and more particularly for the simulation of large disturbances taking place in the transmission system. The passing from a detailed T&D model to dynamic equivalents attached to the transmission system model is sketched in Fig. 1.2.

This approach requires the equivalent to show a good compromise between accuracy and simplicity. It remains to figure out which type of reduced-order model is the most suited for the targeted applications.

Note that, in the remaining of the report, the terms “equivalent” and “reduced-order model” are used interchangeably.

1.2 Illustrative example

To further illustrate the need for proper (unreduced and reduced) ADN models, a simple academic example is presented next.

Consider the small system shown in Fig. 1.3 in which the load obeys the well-known “exponential model” :

$$P(V) = P_o \left(\frac{V}{V_o} \right)^\alpha \quad (1.1)$$

$$Q(V) = Q_o \left(\frac{V}{V_o} \right)^\beta, \quad (1.2)$$

where P_o (resp. Q_o) is the initial active (resp. reactive) power consumed and V_o is the initial voltage. The exponents α and β are parameters usually adjusted based on the knowledge of the underlying distribution system, or based on measurements gathered after an incident. We assume $\alpha = \beta = 2$, i.e. the load behaves as a constant admittance.

The IBG obeys a model which will be detailed in Chapter 2.

Due to its simplicity (only two parameters to adjust), the exponential model is still widely used by TSOs to represent distribution systems in their dynamic simulations. Therefore, the detailed

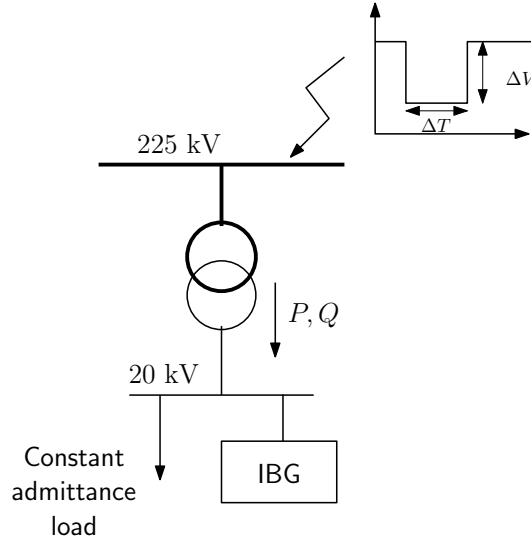


Figure 1.3: Small system illustrating the difference between the active (P) and reactive (Q) powers of a constant admittance load and an IBG model vs. a constant admittance load only in response to voltage dips applied on the high voltage bus

model of the system in Fig. 1.3 is going to be compared with a simplified model in which the net load seen by the transmission system is represented by the exponential model with $\alpha = \beta = 2$ ¹.

Initially the load consumes 15 MW and 2 Mvar, while the IBG produces 10 MW and no reactive power. Thus we have :

- in the detailed model : $P_o = 15$ MW, $Q_o = 2$ Mvar, $\alpha = \beta = 2$ for the load in parallel with the IBG;
- in the simplified model : $P_o = 15 - 10 = 5$ MW and $Q_o = 2 - 0 = 2$ Mvar, $\alpha = \beta = 2$ for the aggregate model of the load and the IBG.

The disturbance considered is a voltage dip as shown in Fig. 1.3 with $\Delta V = 0.5$ pu and $\Delta T = 0.25$ s. This variation is applied on the high voltage (225 kV) side of the transformer.

Figure 1.4 shows the dynamic evolution of the active and reactive powers entering the distribution system with the detailed and the simplified model, respectively. It is clear that the responses are in complete disagreement.

The situation is even worse for a more severe disturbance such as the one considered in Fig. 1.5, corresponding to $\Delta V = 0.7$ pu and $\Delta T = 0.25$ s. This voltage drop leads to the disconnection

¹The values of α and β could be adjusted to partly take into account the presence of the IBG. This improvement has not been considered in this simple illustrative example

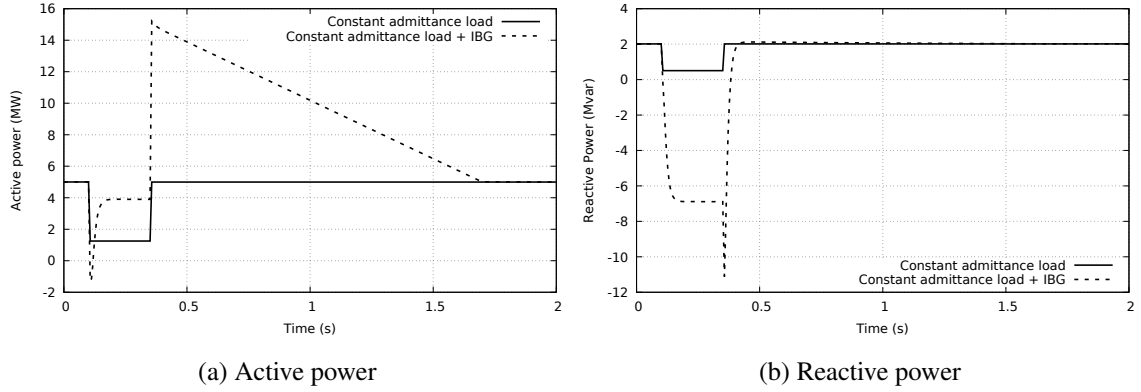


Figure 1.4: Comparison of active and reactive power responses to a voltage dip $\Delta V = 0.5$ pu and $\Delta T = 0.25$ s in the system of Fig. 1.3

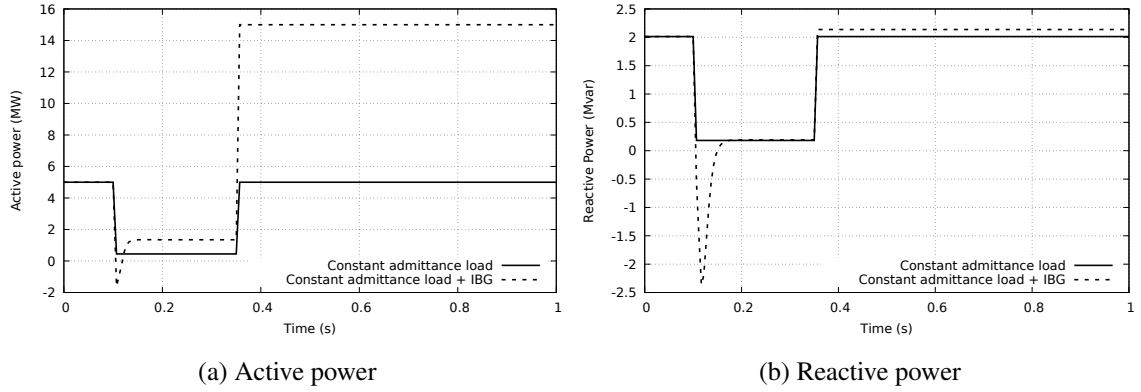


Figure 1.5: Comparison of active and reactive power responses to a voltage dip $\Delta V = 0.7$ pu and $\Delta T = 0.25$ s in the system of Fig. 1.3

of the IBG and, hence to a final increase of the power flow in the transformer, which is totally overlooked by the aggregate exponential model.

This example emphasizes the importance to build more elaborate models of (active) distribution networks, able to account for IBGs, for use by the TSOs in their dynamic simulations and stability studies.

1.3 Overview of dynamic equivalencing approaches

In forming a power system dynamic equivalent the whole system is usually divided into three sub-systems: the *study sub-system*, i.e., the part of interest to be modeled in detail, a *boundary sub-system* retained in the system model and the *external sub-system* replaced by an equivalent [SS04, ANL⁺12]. In the case of concern here, the study system is the transmission system and

the external system is the distribution system which has to be replaced by a lower-order model without overlooking its dynamic impact on the transmission system. Distribution systems are usually connected to one single bus of the transmission system, through one transformer (or several transformer in parallel). It is then reasonable to take this transformer as the boundary sub-system and keep it explicitly in the equivalent model.

The main approaches to power system dynamic equivalencing can be categorized into:

- the dynamic model reduction approaches;
- the coherency approaches;
- the parameter identification approaches.

Dynamic model reduction approaches apply mathematically sound techniques for model order reduction. These approaches include, among others, the Hankel-norm approximation [Glo89], the Singular Value Decomposition (SVD) [GR71] and the Krylov methods [BHP94]. In the modal approach, which is prevailing among model reduction techniques in the field of power systems, the set of differential-algebraic equations describing the entire unreduced system is linearized. Then, the eigenvalues and eigenvectors of the linearized system are computed and used to identify the modes which have negligible effect on the study system. The latter are eliminated when forming the equivalent.

Coherency approaches are intimately linked to SGs. The major steps are [ANL⁺12, ODD03, AP12]:

- identification of coherent generator groups: typically all generators which swing together at the same frequency and with small angle differences are identified as one group;
- connection of all generator buses within a coherent group to a single equivalent bus, through ideal transformers with complex ratios;
- replacement of all the so connected generators by one equivalent generator, attached to the equivalent bus; the model and parameters of that generator are obtained by a dedicated dynamic aggregation method.

In parameter identification approaches, the original system response is either measured or simulated and fitting techniques (e.g. Euclidian norm minimization) are used to determine the unknown model parameters. The former case refers to measurement-based approaches, preferred when no model of the original system is available, and the latter case refers to simulation-based approaches, requiring a detailed model of the system to reduce.

Parameter identification approaches generally involve three steps [L. 99]:

- representation of the external system by an equivalent with hypothesized structure, much simpler than the original system it replaces;
- formulation of an error function to compare the equivalent system response with the original system response;
- estimation of the parameters of the hypothesized model so that the error function is minimized.

Parameter identification approaches can be further divided into white-box, black-box and grey-box approaches, respectively [Lju01, Boh06].

A white-box model is a model in which the structure is perfectly known and has been constructed entirely from prior knowledge and physical insight [Lju01]. Therefore, in white-box approaches, the equivalent hypothesized structure actually involves an exact mathematical model of all physical components of the system by writing down all known relationships between relevant variables. Then, the parameters of this known structure based on first principles are identified.

A Black-box model is a model for which no physical insight is used or available, but the chosen model structure is selected from a known model family [Lju01]. The structure of the model is thus not known a priori. The objective is to map the input data set to the output data set in such a way that the outputs of respectively the modelled system and its equivalent are close. There are several linear and nonlinear black-box model structures available to choose from. For instance, autoregressive exogenous [BCR⁺18], autoregressive moving average exogenous [RTS07] and output error [Lju01] methods have been found useful for representing dynamic systems. The model structures vary in complexity depending on the flexibility needed to accommodate the dynamics and noise in the system. In the literature, black-box models are preferred when no data on the replaced system is available. In that case, measurement-based approaches are required, since simulations of the system model are impossible.

The grey-box model is typically developed using a known structure for the equivalent (instead of the exact composition of physical components) with unknown parameters. The parameters are then estimated in a way similar to those in the black-box model. The grey-box model is, thus, a combination of white-box and black-box models, allowing more flexibility in parameter estimation than with the white-box model and better understanding of the behaviour than in the black-box model [Boh06]. In the literature, grey-box models are often preferred when a sufficient amount of data is available, since the structure of the grey-box model embeds the physical knowledge of

the system. In that case, both measurement or simulation-based approach can be used, as a system model can be built based on available data and simulation can be performed.

In the area of dynamic equivalencing of distribution networks, as long as the latter were passive (i.e. with very few Distributed Generators (DGs) connected to the distribution grids), the focus was on aggregating load dynamics. This also included representing the effect of load tap changers, mainly in the context of voltage stability studies [IEE95, R. 96, T. 06].

The need for more appropriate equivalent models appears with the increased amount of distributed components, connected to distribution grids whose impact on the transmission system dynamics can no longer be neglected, especially at heavy penetration levels [DDTR96]. Moreover, those distributed units will be more and more requested to support the transmission system in the event of a disturbance [N. 17], which makes appear new types of controls whose influence on ADN's dynamic response and thus on bulk power systems dynamics can be strong [JPK⁺18].

Probably the first work related to ADN dynamic equivalents, although not explicitly, is the one reported in [M. 96]. It focuses on the impact of DGs on transmission system stability. It was suggested that a simplified model of ADN should represent the aggregate load of the distribution feeder next to the aggregate generation on that feeder. A simple approach was proposed to extend the previously used models in order to include the effects of the distribution transformer and introduce an equivalent load and an equivalent generator. However, the details on how the equivalent model was formed were not provided.

Similarly, the works presented in [A. 07, Ish08] also focus on the impact of DGs on bulk transmission system stability. A dynamic equivalent of ADN is proposed based on Hankel-norm approximation. The model is fitted to a particular operating point obtained from a power flow calculation. A linearized model is first produced by combining the state space model of the generator and the model of the network into a single linear model. Model reduction is then performed using Hankel-norm approximation with a specified error bound. Clearly, the so proposed dynamic equivalents are valid only for a given operating point, and the procedure needs to be repeated for different operating conditions.

A parameter identification approach was used to obtain the dynamic equivalent of an ADN in [Fen12]. This approach treats the ADN as a black-box model, considering a lack of detailed information on the network structure and parameters. Voltage and frequency are used as inputs, and active and reactive powers as outputs. The result is a state space auto-regressive exogenous model. This method offers simplicity of implementation as there is no need for detailed information about the network. However, the equivalent model produced is highly dependent on the type and location of the disturbance in the transmission system.

A coherency approach for ADN dynamic equivalencing was considered in [Pre16] for transient

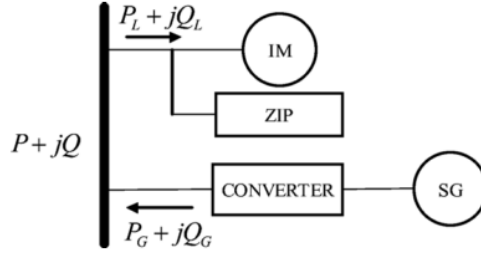


Figure 1.6: Example of a dynamic equivalent of ADN [Zal12, S. 13, J. 13]

and small-signal stability analysis. It improves existing coherency approaches by using a time-domain decomposition of state variables to determine coherent groups and obtain the parameters of equivalent generators. A coherency approach was also considered in [H. 15] where Prony analysis was used together with a support vector classifier to determine coherent groups of generators. The equivalent was built for a specific type of dynamic studies, namely frequency stability.

A related research on dynamic equivalencing of microgrids is reported in [A. 15, Jay15]. The proposed method builds upon previous investigations on dynamic equivalencing of bulk transmission systems. A modal approach is also used.

A non-linear dynamic model reduction technique for distribution system model reduction was proposed in [G. 16]. System reduction is based on the covariance matrix (as an extension of empirical Grammians) obtained from simulation or experimental data, combined with artificial neural networks to yield a black-box equivalent. Although quite recent, this interesting work does not consider DGs connected to the distribution network but takes only load dynamics into account.

The works pointed out hereafter appear promising as they rely on appealing engineering approaches and also in terms of application to real systems.

In the approach presented in [Zal12, S. 13, J. 13], a grey-box model structure is considered to represent the dominant behaviour of the ADN system only, and leaves the mismatch part of the system response to be approximated using an optimization method adjusting some of the parameters of the grey-box model. The assumed model structure of the ADN equivalent comprises a converter-connected SG in parallel with a composite load model, as shown in Fig. 1.6. Active and reactive powers are the outputs, voltage and frequency are the inputs of the equivalent model. All input and output data are “measured” at the point of connection of the ADN to the transmission system. The parameter estimation procedure is shown in Fig. 1.7. For parameter estimation, the Levenberg-Marquardt algorithm is used to minimize the sum of squared differences between the data points and the fitted curve, as it is both fast and effective.

Reference [Gut02] describes a practical solution, in use by utilities across the Western Electricity

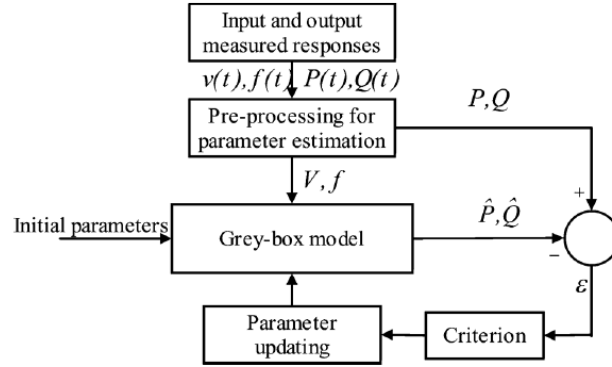


Figure 1.7: Parameter estimation procedure [Zal12, S. 13, J. 13]

Coordinating Council (WECC) (formerly WSCC) in North America. The procedure involves the following steps:

- replace the transmission system at the connection point with a large machine (or an infinite bus);
- make step changes in voltage and frequency at the connection point and record the active and reactive powers;
- use Prony analysis to identify the involved transfer functions (between voltage/frequency variations and active/reactive power) and obtain the equivalent model. The transfer functions (reduced-order models) exhibit the same dynamic response as the original distribution system and represent the dynamics of DG-load combinations and do not change the steady state power flow conditions of the grid.

Finally, the work presented in [Boe16] proposed an iterative procedure to derive the equivalent, whose structure is shown in Fig. 1.8. Each type of DG unit (e.g. PV, WT or Combined Heat and Power (CHP)) is represented by a distinct equivalent generator while the loads are also aggregated. Those generators and the aggregated load are connected to the distribution transformer through an equivalent network impedance Z_{eq} .

A detailed classification of methods can also be found in [ANL⁺12] and [F. 13]. A recent and extended review of load modelling, including ADNs, is available in [AWW⁺17].

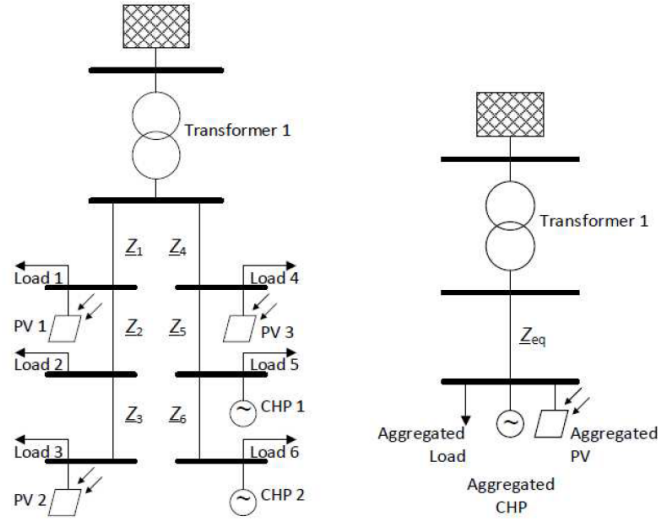


Figure 1.8: Detailed (left) and equivalent (right) ADN [Boe16]

1.4 Requested features and first choice of the equivalent model

The merits of the existing approaches should be assessed in terms of their ability to meet a number of specific requirements. In this respect, the following are desirable features of an ADN dynamic equivalent:

- be as simple as possible;
- be of significantly lower size than the original system model;
- be able to reproduce the dynamic response of the active and reactive powers at the point of interconnection with the transmission system;
- be suited for simulations involving large disturbances in the transmission system;
- be physically interpretable, e.g. in terms of role played by its various components;
- be able to encompass typical controls or protections of DG units such as Low Voltage Ride-Through (LVRT), dynamic voltage support, under/over voltage tripping, contribution to frequency support, etc.;
- be valid for a wide range of operating conditions, or be easily updated for varying network operating conditions.

Regarding modal analysis approaches, they are based on state space models linearized around an equilibrium point. While this can significantly reduce the model complexity, it is well known

to be valid for small deviations around a given operating point. Their use in response to large disturbances is questionable.

By definition, coherency approaches focus on SGs. Hence, they can hardly be applied to components interfaced to the grid with power electronics, such as PV units or WTs.

Parameter identification approaches appear attractive since they apply to a wide range of components and are compatible with large disturbances taking place in the transmission system.

The focus in this thesis is on large disturbances, such as faults taking place in the transmission system. The fact remains that measurements of the ADN response to such events are little available and, if they are, the number of events is too limited for identifying an equivalent valid for other disturbances. This is why a simulation-based approach has been considered in this research. Simulations are thus performed on detailed models of ADNs and their active and reactive power responses are used to identify the unknown parameters of their corresponding equivalent model. Note that the measurement-based approach is not completely left aside. Indeed, we also present equivalent aggregated models of PV units whose parameters have been adjusted based on measurements collected during the August 2018 separation event in Australia [Aus19a]. More details can be found in Appendix C.

Black-box approaches have been recently proposed, e.g. in [C. 19, E. 19]. They appear to be suitable when no model of the ADN is available. In this case parameters are mostly identified from measurements with the already mentioned limitation in terms of events covered.

Instead, this thesis deals with a reduced-model of the grey-box type, as recommended in [J. 14] and [N. 17] for instance. It is clear that a major advantage of grey-box models is their ability to embed physical knowledge about the system in the structure of the equivalent, which is appealing from an engineering point of view as well as for the end users of the model.

Additional examples of grey-box models identification of ADNs can be found in [F. 17, G. 18, X. 18, F. 19, X. 19, N. 19]. These works present some limitations which are worth being addressed. For instance, it appears that very little attention has been paid to the uncertainty affecting the dynamic models of the original, unreduced ADN from which the equivalent is derived. Furthermore, the proposed models do not reproduce the discontinuous response of IBGs, in particular the tripping of some of them, which may have serious impacts on the power system response.

1.5 Challenges, objectives and contributions of this thesis

There is quite a number of challenges associated with the setting up of a general methodology to derive an ADN dynamic equivalent. Table 1.1 offers a non-exhaustive list of these challenges with objectives addressing them.

Table 1.1: Challenges and objectives of thesis

Challenges	Objectives of thesis
Dispersed units in distribution systems exhibit discontinuous controls leading to nonlinear behaviour	The equivalent model must be able to account for the nonlinear behaviour of dispersed IBGs, such as tripping of some of them
Distribution systems are large and hosts various components	The methodology must be applicable to large realistic distribution systems and not be bound to particular components
ADN models are affected by uncertainty	Uncertainty must be accounted for in the identification of the equivalent
The equivalent model is intended to be used for the simulation of various types of disturbances	The equivalent must be suitable for multiple disturbances, but with a limited number of them involved in its identification
The complexity of the identification process can be large and the model interpretation difficult	The number of parameters to identify must remain “as small as possible” to reduce the problem complexity and improve its interpretation
Variations of load, generation and topology impact the ADN response to disturbances	The ADN equivalent must be easily updated to accommodate various operating conditions
There will be unavoidable discrepancies between the response of the equivalent and that of the real ADN	Suggest a practical way to compensate for the reduced-order model inaccuracies

This thesis offers a number of contributions fulfilling the objectives listed in Table 1.1.

1. The first contribution deals with the modelling of IBGs. Rather than a detailed representation of all components and controls, such as in [MG14b] for instance, a generic model is used, which aims at capturing the variation of the injected current with the terminal voltage and grid frequency. Nevertheless, the embedded controls obey recent grid-code requirements (e.g. [IEE19]) and the model is easily updated in response to evolutions of those grid requirements.
2. A procedure is proposed in order to discard from the identification the parameters with a

negligible impact. The objective is to decrease the complexity of the model identification, but also to make the parameter values more consistent from one case to another and, hence, easier to interpret [L. 99].

3. In order to avoid over-fitting one particular scenario which, at the same time, preserving the computational burden of handling numerous disturbances, a procedure has been set up to select the smallest possible subset of disturbances, from which the parameters are identified. The procedure guarantees the accuracy of the equivalent with respect to disturbances not involved in the identification of the parameters.
4. The methodology is validated for various ADNs hosting dispersed generators as well as motor loads. While it can be generally assumed that the network model itself is accurate, dynamic models of connected components are affected by uncertainty. This uncertainty has been taken into account in the identification of the equivalent model parameters.
5. Furthermore, an approach is proposed to assess the accuracy of the equivalent with respect to changing ADN operation conditions. The parameters of the equivalent are updated when it is found not accurate enough. The objective is to have a limited number of parameter sets covering a wide range of operating conditions.
6. Finally, a new application is proposed for a battery energy storage system connected at distribution level. It consists of controlling its active and reactive power in order for the net power entering the distribution network to match a dynamic equivalent model in response to a large disturbance in the transmission system.

1.6 Test systems used in this thesis

Mainly two different ADNs, hosting dispersed IBGs, are considered in this thesis. They are supposed to host both Type-4 Wind Turbines (WTs) and PV units, which can be represented in dynamic studies by the same, so-called full-converter model. Indeed, the converter of Type-4 WTs decouples the dynamics of the generator from the rest of the device, as pointed out for instance by the WECC Renewable Energy Modeling Task Force reports [MG14a, MG14b].

1.6.1 ADN No 1

The first test system is a variant of the CIGRE² MV Distribution Network Benchmark [B⁺14]. Its one-line diagram is shown in Fig. 1.9. The grid feeds residential as well as industrial loads. It hosts both dispersed large capacity (e.g. large PV installations or WTs) and small residential IBGs (e.g. rooftop PVs). Large capacity IBGs have fault-ride through and reactive current injection

²Conseil International des Grands Réseaux Électriques

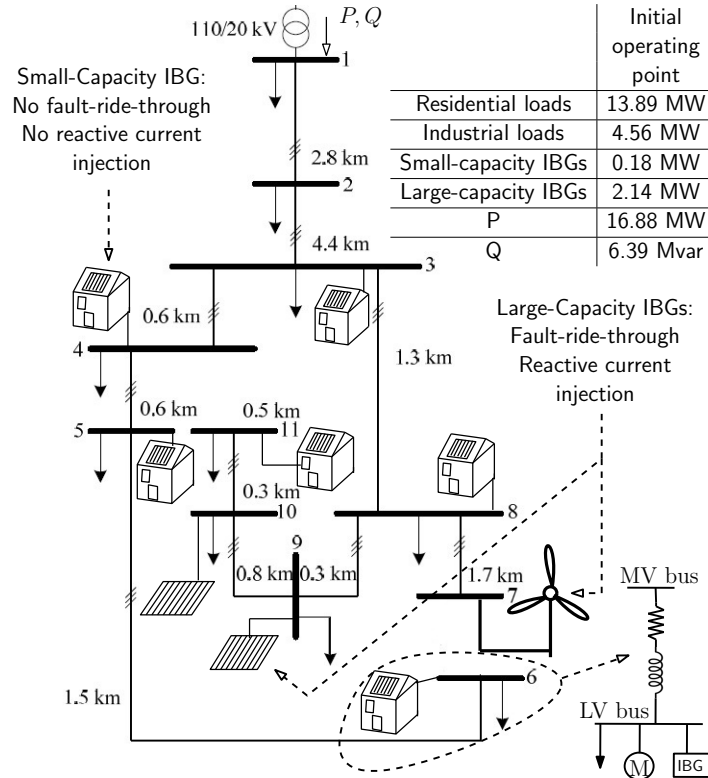


Figure 1.9: ADN No 1: One-line diagram of CIGRE Medium-Voltage Distribution Network

capabilities, while small residential IBGs have not. The residential IBGs and loads are in fact aggregated models connected behind an equivalent LV impedance as shown in the lower right corner of Fig.1.9. Initially, the residential loads consume 13.89 MW, while the industrial loads consume 4.56 MW. Large capacity IBGs account for a production of 2.14 MW, with an installed capacity of 3.08 MW. Residential IBGs initially produces 0.18 MW, half of the total residential capacity. Before any disturbance, the net power entering the system is 16.88 MW/6.39 Mvar.

1.6.2 ADN No 2

The second test system is a modified version of the 75-bus 11-kV distribution system previously used in [SBGVC16, G. 18, CPVCss]. Its one-line diagram is given in Fig. 1.10. In total, the system hosts 22 dispersed IBGs, belonging to two categories : large-capacity PV systems and WTs. WTs are located closer to the main substation. All IBGs have fault-ride through and reactive current injection capabilities. Their total capacity is 14.8 MW. The initial IBG production is 9.8 MW. The WTs operate at 80 % of their capacity, and the PV units at 50 % of their capacity. The loads are connected to the $(75-22=)$ 53 buses with no IBG. The total initial consumption is 19.8 MW / 3.40 Mvar. The net power entering the system is 10.33 MW / 3.63 Mvar.

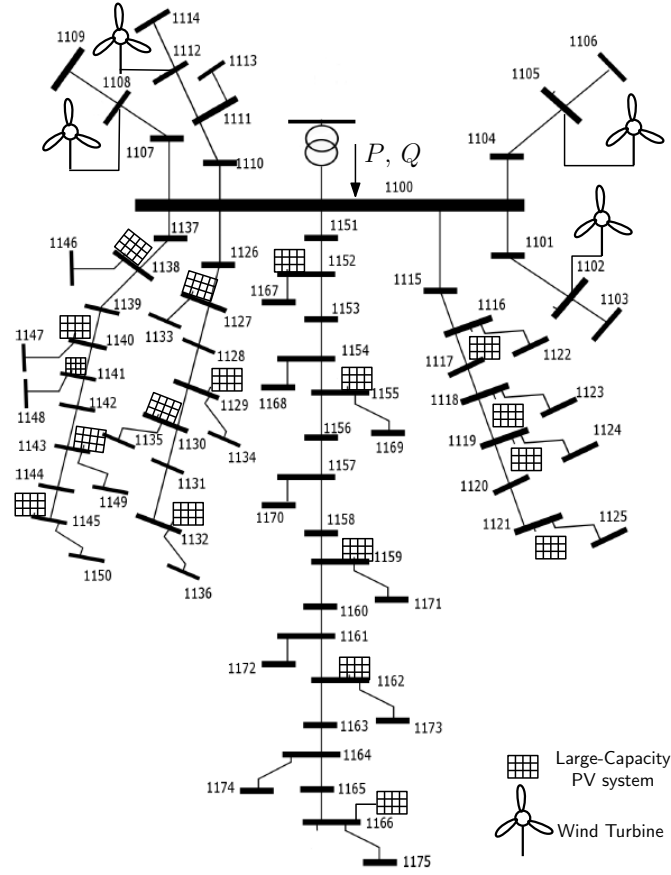


Figure 1.10: ADN No 2: One-line diagram of 75-bus 11-kV distribution grid

1.6.3 ADN No 3

Additionally, a real Australian distribution system is also considered in some part of this thesis.

The model of this 22-kV distribution grid includes 92 buses. It is connected to the 63-kV sub-transmission network through a single transformer. Its one-line diagram is given in Fig. 1.11. The grid hosts numerous small-scale dispersed PV units for a total capacity of 5.3 MW as well as eight SGs all connected to bus 48 and accounting for a CHP unit. All SGs have the same technical characteristics, in particular a nominal apparent power of 1.5 MVA. Therefore, a single SG is considered in the model, whose capacity is scaled to the number of individual SGs in operation.

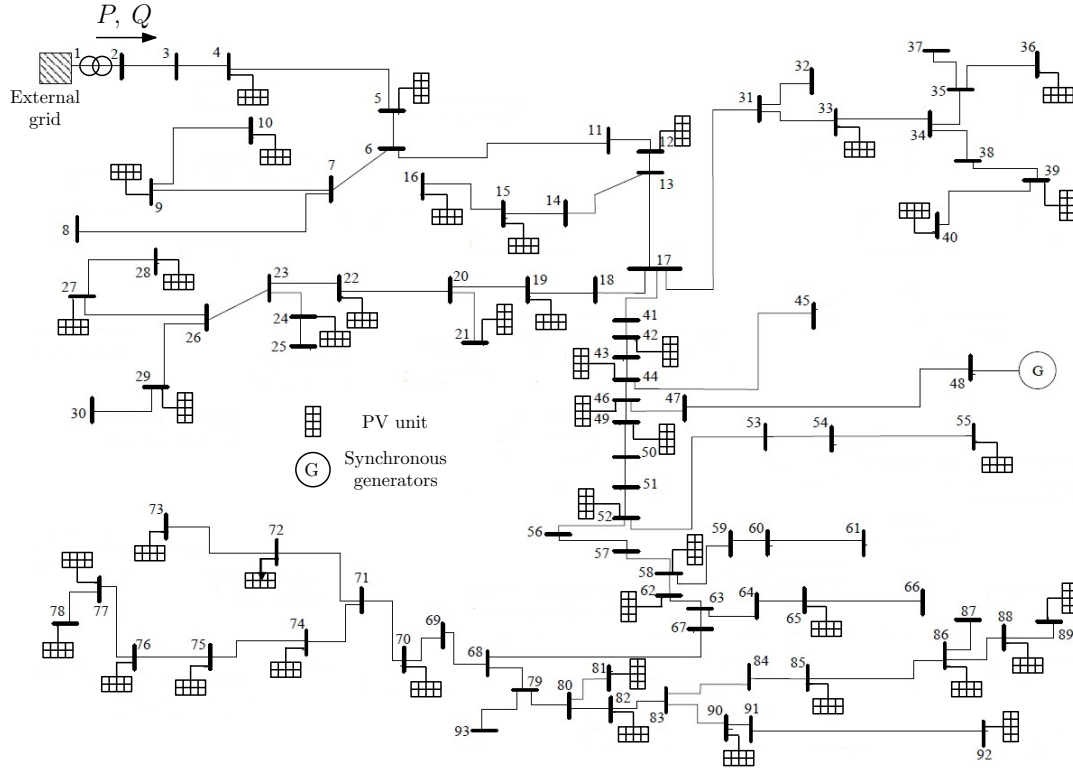


Figure 1.11: ADN No 3: One-line diagram of a real Australian ADN

1.7 Outline of this report

This report is organized as follows.

Chapter 2. The phasor approximation has been adopted in this work and the models aims at rendering the impact of ADNs on transmission system dynamics. After a brief recall of the phasor approximation, the model of loads and IBGs used in this thesis are presented in detail. The load is divided into a static and a dynamic part. As regards IBGs, the chapter focuses on the controls responding to large voltage or frequency variations. The second part of the chapter aims at illustrating and describing the individual responses of the above components connected to a distribution network, in response to large disturbances taking place in the transmission system.

Chapter 3. This chapter addresses the issue of the uncertainty affecting the parameters of the ADN models. Monte-Carlo simulations are used to assess the impact of parameter uncertainty on dynamic power responses. Among a set of randomized system evolutions, time-varying averages and standard deviations are extracted. These statistics are used latter for the derivation of the equivalent models. Uniform as well as Gaussian distributions of the uncertain parameters are considered. The chapter also proposes a method to estimate the number of randomized system evolutions needed. Simulation results are reported on each of the ADNs presented in Section 1.6.

Chapter 4. This chapter details the proposed methodology for the identification of ADN equivalents. First, the least-square minimization and optimization algorithm are detailed. Next, a procedure is used to remove from the identification the parameters with negligible impact. To avoid over-fitting, the equivalent is tuned for multiple large-disturbance simulations. Then, a recursive procedure is used to select the smallest possible subset of disturbances involved in the least-square minimization. Finally simulation results on the test are reported and the accuracy of the equivalent models is checked for various types of disturbances.

Chapter 5. Changing operating conditions require changing the equivalent model. Therefore, this chapter presents an approach to update the latter in response to varying operating conditions. An approach is proposed to minimize the number of parameters to update. This is illustrated through simulation results on ADN No 2. The TSO-DSO share of work is also discussed.

Chapter 6. This chapter proposes a new application for a Battery Energy Storage System (BESS) connected to a distribution grid. It consists of controlling its active and reactive powers so that the net power entering the distribution grid evolves with the distribution voltage as closely as possible to the response provided by an equivalent model, in the event of a large disturbance taking place in the transmission system. First the overall configuration as well as the BESS model are presented. Then simulation results, illustrating the performance of the BESS, are provided on ADN No 1.

Chapter 7. The last chapter summarizes the main achievements and outlines possible extensions for future work.

1.8 Mathematical notations

In this thesis the following notation is being used :

- vectors are denoted by lowercase bold letters;
- matrices are denoted by uppercase bold letters;
- all vectors are column vectors.

1.9 Publication list

This thesis expands material that has been published in various journals and presented at various conferences:

- [1] **G. Chaspierre**, P. Panciatici and T. Van Cutsem. Dynamic Equivalent of a Distribution Grid Hosting Dispersed Photovoltaic Units. IREP 2017 Symposium, Espinho (Portugal), 2017.
Also available at <http://hdl.handle.net/2268/212146>.

- [2] **G. Chaspierre**, P. Panciatici and T. Van Cutsem. Modelling Active Distribution Networks under Uncertainty: Extracting Parameter Sets from Randomized Dynamic Responses. Proceedings of the 20th Power Systems Computation Conference (PSCC), Dublin, 2018.
Also available at <http://hdl.handle.net/2268/221475>
- [3] **G. Chaspierre**, P. Panciatici and T. Van Cutsem. Aggregated Dynamic Equivalent of a Distribution System hosting Inverter-based Generators. Proceedings of the 20th Power Systems Computation Conference (PSCC), Dublin, 2018.
Also available at <http://hdl.handle.net/2268/221474>
- [4] **G. Chaspierre** and T. Van Cutsem. Identification of a Reduced-Order Model of an Active Distribution Grid Using Recursive Training. Proceedings of the IEEE Benelux Young Researchers Symposium, Brussels, 2018.
Also available at <http://hdl.handle.net/2268/223756>
- [5] **G. Chaspierre**, G. Denis, P. Panciatici and T. Van Cutsem. Identification of a Dynamic Equivalent of an Active Distribution Network from Monte-Carlo Simulations. Proceedings of the 8th Solar Integration Workshop, Stockholm (Sweden), 2018.
Also available at <http://hdl.handle.net/2268/227450>
- [6] **G. Chaspierre**, G. Denis, P. Panciatici and T. Van Cutsem. Dynamic equivalent of an active distribution network taking into account model uncertainties. Proceedings of the IEEE PES PowerTech conference, Milan (Italy), 2019.
Also available at <http://hdl.handle.net/2268/234316>
- [7] **G. Chaspierre**, G. Denis, P. Panciatici and T. Van Cutsem. An active Distribution Network Equivalent derived from large-disturbance Simulations with Uncertainty. IEEE Transactions on Smart Grid, 2020.
Also available at <http://hdl.handle.net/2268/247832>

The following articles have been accepted for publication or are still under preparation :

- [8] **G. Chaspierre**, M. Ghazavi Dozein, G. Denis, P. Panciatici and T. Van Cutsem. Dynamic equivalent of a real distribution grid hosting photovoltaic and synchronous generators. Accepted for publication in the CIGRE Science and Engineering Journal, 2021.
Also available at <http://hdl.handle.net/2268/251188>
- [9] M. Ghazavi Dozein, **G. Chaspierre**, P. Mancarella, P. Panciatici and T. Van Cutsem. Frequency Response from Solar PV: A Dynamic Equivalence Closed Loop System Identification Approach. To be submitted in IEEE Systems Journal.

The following work has been published by the author, albeit not in direct link to the subject of this thesis :

- [10] M. Ghazavi Dozein, **G. Chaspierre** and P. Mancarella. Contribution to System Frequency Stability and Resilience from PV Plants: A Closed-loop System Identification Approach. 55th International Universities Power Engineering Conference, 2020.

Also available at <http://hdl.handle.net/2268/248970>

Chapter 2

Modelling of active distribution network components

This chapter details the model of loads and IBGs used in this thesis. The ADN model aims at rendering the impact on transmission system dynamics of numerous loads and IBGs dispersed in a distribution grid. Rotor angle, frequency and voltage stability studies are targeted [Kun94, HMR⁺20]. The focus is on transients lasting up to 10 to 20 seconds after a large disturbance, but features relevant to long-term dynamics can be easily added [HMR⁺20]. The unreduced and the equivalent ADN models assume a balanced three-phase distribution grid and are used in dynamic simulations in phasor mode (also known as RMS simulations or quasi-sinusoidal approximation) [Kun94] typical of large-scale dynamic studies.

This chapter is organized as follows. Section 2.1 briefly recalls basics of the phasor-mode approximation. Section 2.2 presents the generic load model and Section 2.3 the generic IBG model and its various controls. Section 2.4 deals with the representation of the transmission system subject to disturbances and the power responses of individual components connected to a distribution network are illustrated in Section 2.5. Finally, Section 2.6 summarizes the chapter.

2.1 Models under the phasor approximation

With the continuous development of IBGs, there is a growing need for Electro-Magnetic Transient (EMT) simulations where power system components are adequately modeled to simulate high-frequency transients in power systems. This makes EMT programs valuable in studies of the effects of power-electronic devices on system behaviour [K. 18]. However, as the equivalent model of concern in this work is intended to be attached to the transmission system model to conduct large-scale dynamic studies, EMT models are not suited, mainly due to the small time step

involved (in the order of fifty microseconds or even less) and the size of the transmission system. Instead, models under the phasor approximation are preferred. The phasor approximation consists of approximating network voltages and currents by sinusoidal functions of time at the fundamental frequency (50 or 60 Hz) but with varying amplitudes and phase angles [Kun94, VCct]. The fast dynamics of the network are then neglected which allows using time steps larger than-say-five milliseconds, making the simulation more suitable for large-scale studies.

2.1.1 Network model

The network is modeled by the following algebraic equations :

$$\bar{I} = \mathbf{Y} \bar{V} \quad (2.1)$$

where \bar{I} is the vector of complex currents injected in the network at various buses, \bar{V} is the vector of complex voltages at the various buses, and \mathbf{Y} is the network admittance matrix. Matrix \mathbf{Y} involves network impedances determined at fundamental frequency (or possibly updated with frequency when the latter significantly deviates from its nominal value) [VCct].

Thus the voltage and current evolutions take on the form:

$$v(t) = \sqrt{2}V(t)(\cos \omega_N t + \phi(t)) \quad (2.2)$$

$$i(t) = \sqrt{2}I(t)(\cos \omega_N t + \psi(t)) \quad (2.3)$$

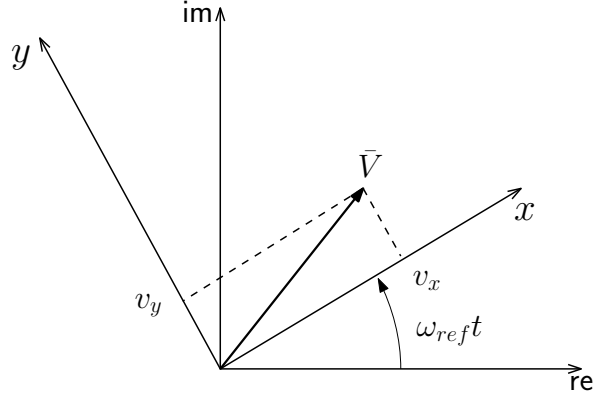
where the effective values ($V(t)$, $I(t)$) and the phase angles ($\phi(t)$, $\psi(t)$) vary with time. ω_N is the nominal angular frequency of the system, i.e. $\omega_N = 2\pi f_N$, where f_N is the nominal frequency.

Equations (2.2) and (2.3) can be rewritten as :

$$v(t) = \sqrt{2} \operatorname{re} \left[V(t) e^{j(\omega_N t - \omega_{ref} t + \phi(t))} e^{j\omega_{ref} t} \right] = \sqrt{2} \operatorname{re} \left[(v_x(t) + jv_y(t)) e^{j\omega_{ref} t} \right] \quad (2.4)$$

$$i(t) = \sqrt{2} \operatorname{re} \left[I(t) e^{j(\omega_N t - \omega_{ref} t + \psi(t))} e^{j\omega_{ref} t} \right] = \sqrt{2} \operatorname{re} \left[(i_x(t) + ji_y(t)) e^{j\omega_{ref} t} \right] \quad (2.5)$$

where re denotes the real part and $v_x + jv_y$ (resp. $i_x + ji_y$) is the voltage phasor \bar{V} (resp. the current phasor \bar{I}) in rectangular coordinates, expressed with respect to (x, y) axes rotating at the reference angular speed ω_{ref} , as shown in Fig. 2.1 for the voltage. The reference speed can be either the nominal angular frequency ω_N or the angular speed of the center of inertia, obtained from the individual rotor speeds of the synchronous machines [Kun94, VCct]. Since the latter, connected to the transmission system, are not considered in most of this work, ω_{ref} has been taken as ω_N .

Figure 2.1: (x, y) reference frame for phasor mode simulation

2.1.2 Load and IBG injectors

The loads and IBGs are modeled as current injectors. Each injector obeys a set of nonlinear Differential-Algebraic Equations (DAEs) assuming three-phase balanced operation.

In compact form, the j -th injector, attached to the k -th bus, can be written as :

$$\mathbf{\Gamma}_j \dot{\mathbf{x}}_j = \mathbf{\Phi}_j(\mathbf{x}_j, v_{xk}, v_{yk}) \quad (2.6)$$

where \mathbf{x}_j is the injector state vector including both differential and algebraic variables, while v_{xk} and v_{yk} are the previously defined rectangular components of the bus voltage. $\mathbf{\Gamma}_j$ is a matrix whose l -th row contains either all zeros or all zeros but a single one. In the former case, the l -th equation is algebraic while in the latter case, the l -th equation is differential.

Note that \mathbf{x}_j includes in particular the rectangular components (i_{xj}, i_{yj}) of the current injected in the connection bus, i.e. $\mathbf{x}_j = [i_{xj} \ i_{yj} \ \dots]^T$.

2.1.3 DAE solver used

All simulations have been performed with the RAMSES (Rapid Multi-threaded Simulation of Electric power Systems) software developed at the University of Liège. RAMSES solves the network equations (2.1) and the injector DAEs (2.6) together, using a Schur-complement formulation allowing decomposition and parallel processing. The differential equations are algebraized using second-order Backward Differentiation Formula (BDF2). Further details regarding this solver can be found in [Ari15, P. 14] and various examples in [VCct].

The typical time step used is 0.005 s.

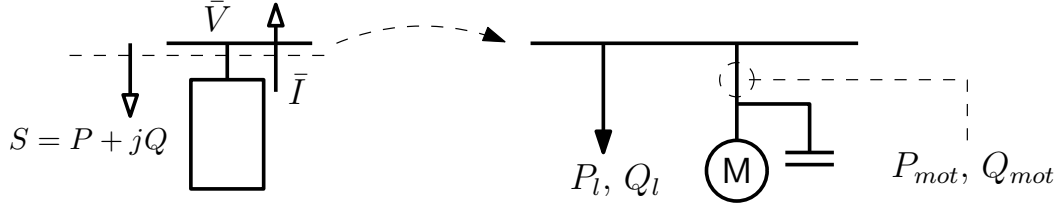


Figure 2.2: Overview of the load model

2.2 Generic load model

The load model is depicted in Fig. 2.2. It is decomposed into a static part and a dynamic part. The total complex power consumed by the load is given by :

$$S = P + jQ = (P_l + P_{mot}) + j(Q_l + Q_{mot}) \quad (2.7)$$

where P_{mot} and Q_{mot} are the active and reactive power consumed by the dynamic part representing an Induction Motor (IM), while P_l and Q_l are the active and reactive power consumed by the static part.

The injected current being oriented towards the network, the power is given by :

$$P + jQ = -\bar{V}\bar{I}^* = -(v_x + jv_y)(i_x - ji_y). \quad (2.8)$$

Decomposing into real and imaginary parts leads to :

$$P = -v_x i_x - v_y i_y \quad (2.9)$$

$$Q = v_x i_y - v_y i_x. \quad (2.10)$$

In accordance with (2.6), the bus voltage components v_x and v_y (see Fig. 2.1) can be considered as inputs, while the current components i_x and i_y can be treated as outputs.

2.2.1 Dynamic load model

The dynamic part of the load consists of a single-cage IM with a third-order model [Kun94]. A schematic representation of the IM is shown in Fig. 2.3, obtained after replacing the three-phase stator and rotor windings by (ds, qs, dr, qr) windings attached to (d, q) axes rotating at angular speed $\omega_{ref} = \omega_N$ [VCct].

Initially, the active and reactive powers consumed by the IM are given by :

$$P_{mot0} = f_{Pm} P_0 \quad (2.11)$$

$$Q_{mot0} = P_{mot0} \tan(\phi_m) \quad (2.12)$$

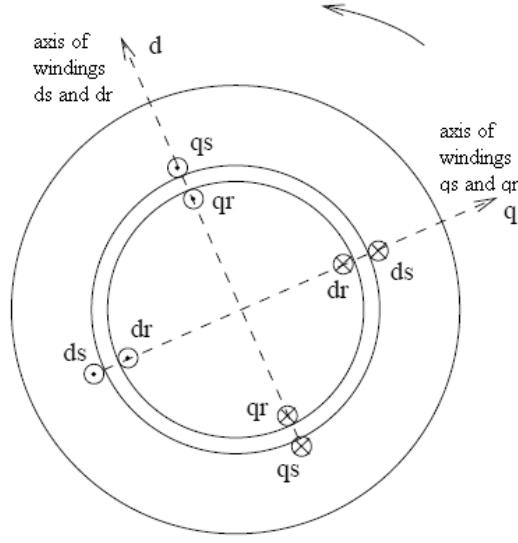


Figure 2.3: Simplified induction motor representation [VCct]

where f_{P_m} is the fraction of total active power initially consumed by the motor and $\phi_m = \cos^{-1}(\cos(\phi_m))$ with $\cos(\phi_m)$ the power factor of the motor. Additionally, the nominal power of the motor is given by :

$$S_{nom} = \frac{P_{mot0}}{LF} \quad (2.13)$$

where LF is the load factor of the motor.

Neglecting transformer voltages, the stator equations can be written as :

$$v_{ds} = R_s i_{ds} + \omega_{ref} \psi_{qs} \quad (2.14)$$

$$v_{qs} = R_s i_{qs} - \omega_{ref} \psi_{ds} \quad (2.15)$$

while the rotor equations take on the form :

$$\frac{d\psi_{dr}}{dt} = -R_r i_{dr} - (\omega_{ref} - \omega_r) \psi_{qr} \quad (2.16)$$

$$\frac{d\psi_{qr}}{dt} = -R_r i_{qr} + (\omega_{ref} - \omega_r) \psi_{dr} \quad (2.17)$$

with the flux-current relations :

$$\psi_{ds} = L_{ss} i_{ds} + L_{sr} i_{dr} \quad (2.18)$$

$$\psi_{qs} = L_{ss} i_{qs} + L_{sr} i_{qr} \quad (2.19)$$

$$\psi_{dr} = L_{sr} i_{ds} + L_{rr} i_{dr} \quad (2.20)$$

$$\psi_{qr} = L_{sr} i_{qs} + L_{rr} i_{qr}. \quad (2.21)$$

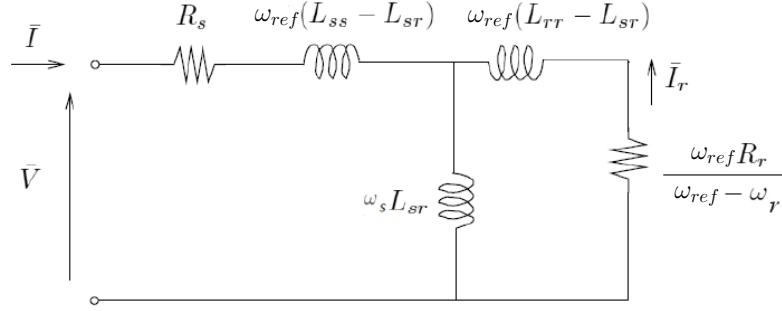


Figure 2.4: Equivalent circuit of the IM [VCct]

The well-known equivalent circuit of the IM with its parameters is given in Fig. 2.4 in which the electrical part is “static” and the rotor angular speed ω_r varies according to the rotor motion equation :

$$2H \frac{d}{dt} \omega_r = \psi_{dr} i_{qr} - \psi_{qr} i_{dr} - T_{mo} (A \omega_r^2 + B \omega_r + C) \quad (2.22)$$

where H is the inertia constant, ω_r is the speed of the rotor (in per unit). The last term in (2.22) is the mechanical torque, decomposed into three parts with $A + B + C = 1$. T_{mo} is thus the value of that torque at the synchronous speed $\omega_r = 1$ pu. Compensation shunt capacitor shown in Fig. 2.2 is determined to meet the specified initial net reactive power consumption Q_{mot0} (see (2.12)).

2.2.2 Static load model

The active and reactive powers consumed by the static part of the load are given by :

$$P_l = (1 - f_{Pm}) P_0 \left[a_1 \left(\frac{V}{V_0} \right)^{\alpha_1} + a_2 \left(\frac{V}{V_0} \right)^{\alpha_2} + (1 - a_1 - a_2) \left(\frac{V}{V_0} \right)^{\alpha_3} \right] \quad (2.23)$$

$$Q = (Q_0 - Q_{mot0}) \left[b_1 \left(\frac{V}{V_0} \right)^{\beta_1} + b_2 \left(\frac{V}{V_0} \right)^{\beta_2} + (1 - b_1 - b_2) \left(\frac{V}{V_0} \right)^{\beta_3} \right] \quad (2.24)$$

where

- P_0 is the initial active power consumption of the load
- f_{Pm} is the fraction of the total active power initially consumed by the motor
- Q_0 is the initial reactive power consumption of the load
- Q_{mot0} is the initial reactive power consumption of the motor (with its compensation)
- V is the bus voltage magnitude

- V_0 is the reference bus voltage, taken as the initial voltage of the dynamic simulation

In (2.25), a_1 , a_2 and $(1 - a_1 - a_2)$ represent the fractions of the load characterized by the exponents α_1 , α_2 and α_3 , respectively, with usually $0 \leq a_1 \leq 1$ and $0 \leq a_2 \leq 1$. The same applies to (2.26) and the coefficients b_1 and b_2 . In the remaining of this thesis, it has been chosen to set $a_1 = b_1 = 1$ (i.e. $a_2 = b_2 = 0$). Therefore, Eqs. (2.23) and (2.24) are reduced to :

$$P_l = (1 - f_{Pm})P_0 \left(\frac{V}{V_0} \right)^\alpha \quad (2.25)$$

$$Q = (Q_0 - Q_{mot0}) \left(\frac{V}{V_0} \right)^\beta. \quad (2.26)$$

2.3 Generic IBG model

The generic IBG model captures the main behaviour of the inverter while ignoring fast switching transients [AMM19]. More precisely, it aims at capturing the variations of the injected current with the terminal voltage and frequency, instead of focusing on a detailed modelling of internal components. The model parameters can be tuned to accommodate recent grid-code requirements such as those specified in [Tro09], [KV11], [KHL13] and [BVK13] and more recently in [IEE19] and [EUG19]. With respect to more elaborated models, this model thus offers a significant advantage as it can be easily updated in response to grid codes evolution. Indeed, facing continuous system strength and inertia reduction in power systems [DMSY18, MDH⁺18], the DG units connected at distribution level are more and more requested to support the grid in the event of disturbances, which leads to regularly adapting the grid codes [VFGL⁺18].

The model is shown in block-diagram form in Fig. 2.5. As already mentioned, the IBG is modelled as a current injector. The terminal voltage components v_x and v_y (see Fig. 2.5) can be considered as inputs, and the current components i_x and i_y as outputs. The model includes controls responding to large voltage and frequency variations as well as a Phase-Locked Loop (PLL). Most of the controls rely on the measured voltage magnitude at the terminal bus V_m which differs from the terminal voltage :

$$V = \sqrt{v_x^2 + v_y^2} \quad (2.27)$$

by a simple lag block with time constant T_m . T_g is the equivalent time constant of the converter current controller. Other blocks in the model rely on the “local” frequency computed by the PLL and denoted by ω_{pll} .

2.3.1 Phase Locked Loop

The Phase Locked Loop (PLL) sets the reference frame for the IBG. More precisely, it provides an estimate θ of the “true” phase angle θ_r of the voltage phasor \bar{V}_m (see Fig. 2.6). With θ known,

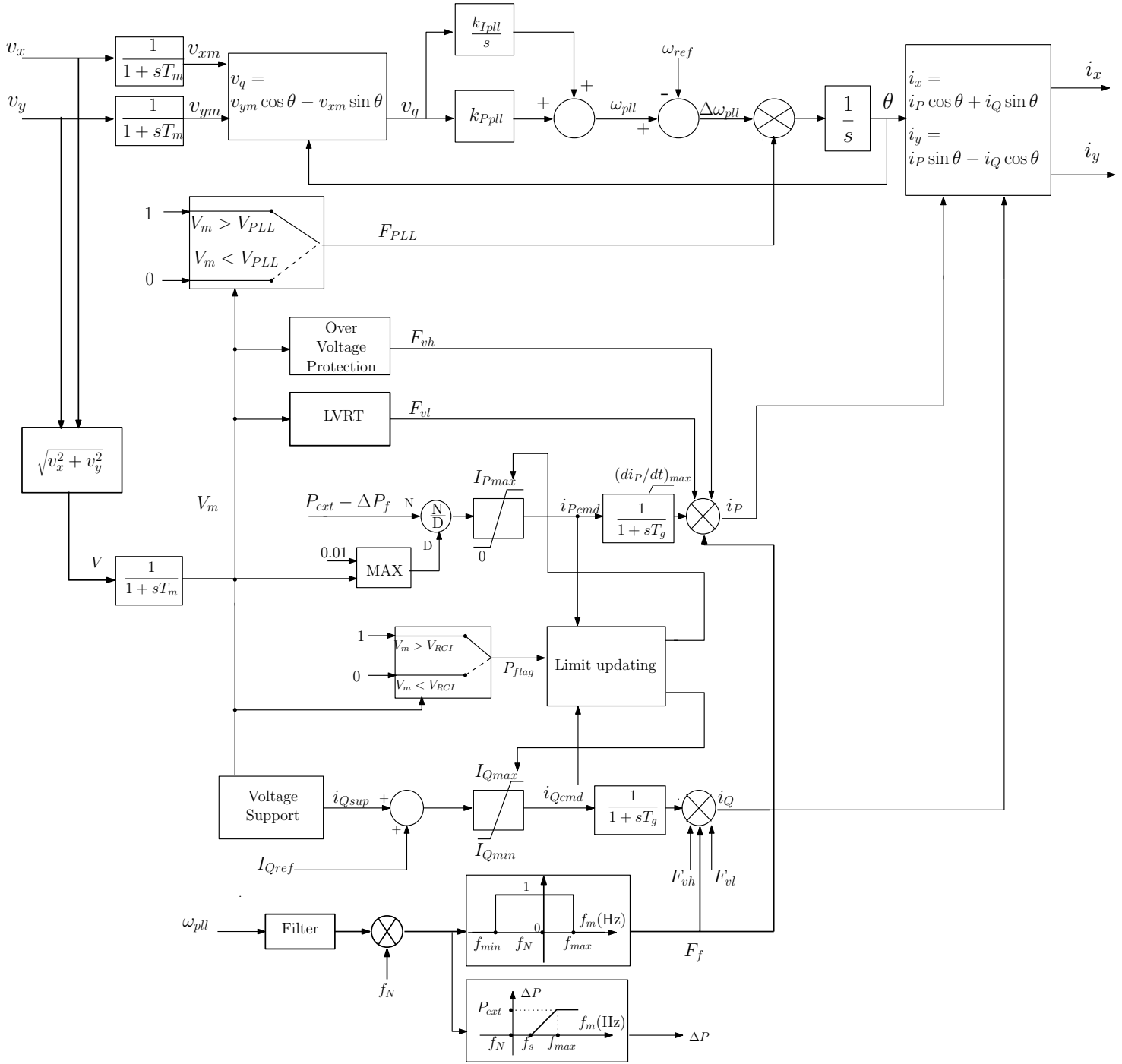


Figure 2.5: Block-diagram of the generic model of an IBG

the controllers can adjust the current phasor with respect to the voltage phasor, in order to obtain the desired active and reactive powers. The PLL aligns the direct d axis with the voltage phasor

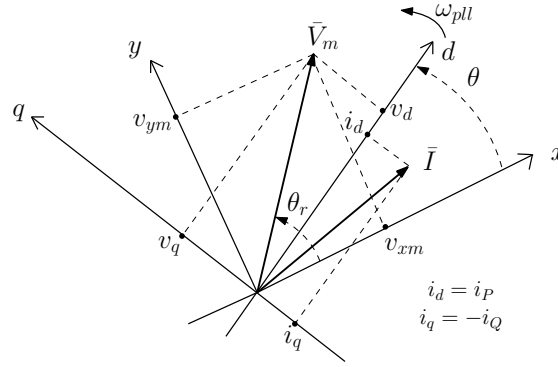
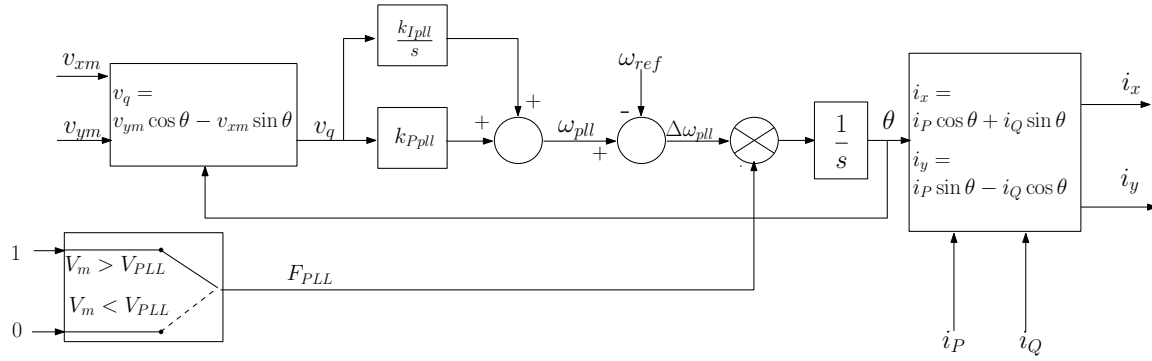
Figure 2.6: Representation of the (x, y) and (d, q) reference frames for the PLL

Figure 2.7: PLL block diagram

\bar{V}_m . As shown in Fig. 2.6, the quadrature q axis is orthogonal and ahead of the d axis.

In steady state, $\theta = \theta_r$, the phasor \bar{V}_m is aligned with the d axis, its v_d component is equal to V_m and its v_q component to zero. Furthermore, the component i_d of the current is the active current i_P , while the component i_q is the reactive current with opposite sign, i.e. $i_q = -i_Q$. The latter are obtained from the controls as detailed later on in this section.

The (d, q) reference axes rotate at the angular speed ω_{pll} , which is also the network angular frequency estimated by the PLL. Following a transient, the PLL adjusts that speed until the d axis again coincides with the voltage phasor. A simple, generic model of this adjustment has been considered and is shown in Fig. 2.7.

The transformation from the (x, y) to the (d, q) reference frame for the voltage can be obtained

from Fig. 2.7 as :

$$v_d = v_{xm} \cos \theta + v_{ym} \sin \theta \quad (2.28)$$

$$v_q = -v_{xm} \sin \theta + v_{ym} \cos \theta \quad (2.29)$$

where v_{xm} and v_{ym} are the measured voltage components in the (x, y) reference frame. As shown in the figure, (2.29) is used to obtain v_q , which is brought to zero by a PI controller, whose parameters k_{Ipl} and k_{Ppl} can be adjusted to change the response time of the PLL.

The same transformation is used for the currents with :

$$i_d = i_x \cos \theta + i_y \sin \theta \quad (2.30)$$

$$i_q = -i_x \sin \theta + i_y \cos \theta. \quad (2.31)$$

An additional feature of the model is the PLL “freezing” in low voltage conditions. If the terminal voltage is severely depressed, i.e. V_m drops below the threshold V_{PLL} , the PLL is temporarily “frozen” to avoid instability [B. df]. This is obtained by switching F_{PLL} from one to zero (see Fig. 2.7).

2.3.2 Controls responding to large voltage deviations

Low Voltage Ride-Through (LVRT)

An important feature of IBGs is their LVRT capability, requiring them to remain connected to the grid during a fault as long as the voltage is above a reference curve, as shown in Fig. 2.8. On the other hand, they are allowed (but not requested) to disconnect if the voltage is found below the curve [Tro09, DAB⁺09, BVK13, IEE19, EUg19]. This curve can be adjusted by modifying the six parameters T_1 , T_{int} , T_2 , V_{min} , V_{int} and V_r . The unit disconnection is modeled by the variable F_{vl} switching from one to zero (see Fig. 2.5).

Overvoltage protection

When V_m exceeds a high voltage threshold, the unit is assumed to trip without delay to avoid damaging insulation materials and electronic components.

The unit disconnection is modeled by the variable F_{vh} (see Fig. 2.5) switching from one to zero.

Reactive current injection

Units may be requested to inject an additional reactive current i_{Qsup} into the grid in order to support the terminal voltage [Tro09, BVK13, IEE19, EUg19]. As shown in Fig. 2.9, the injected

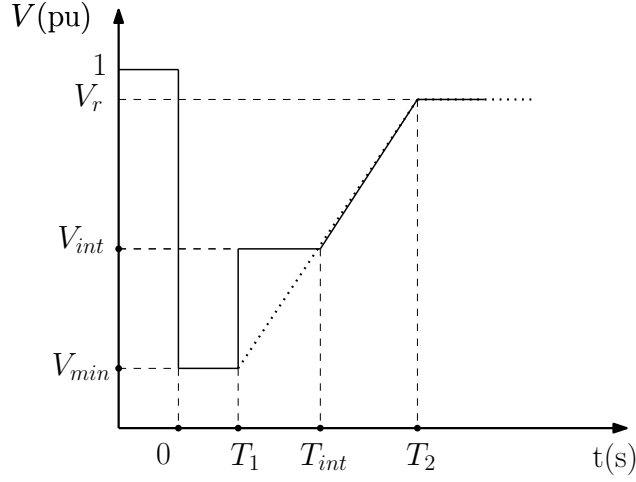
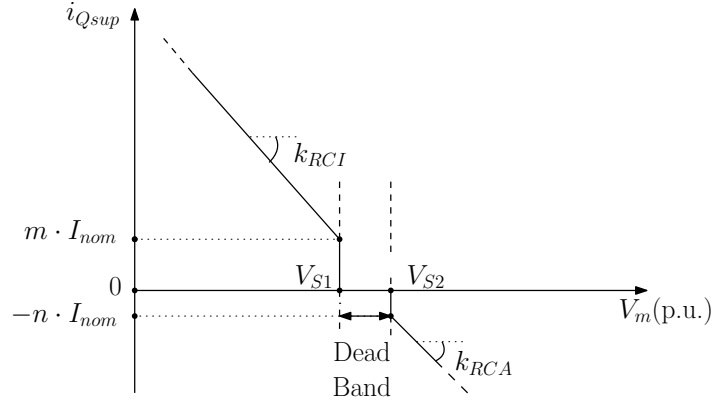
Figure 2.8: Parametrized LVRT curve (fault occurring at $t = 0$)

Figure 2.9: Parametrized reactive current injection

reactive current varies with the measured voltage according to :

$$\text{if } V_m \leq V_{S1} : i_{Qsup} = k_{RCI}(V_{S1} - V_m) + m I_{nom} \quad (2.32)$$

$$\text{if } V_m > V_{S2} : i_{Qsup} = k_{RCA}(V_{S2} - V_m) - n I_{nom} \quad (2.33)$$

$$\text{else : } i_{Qsup} = 0. \quad (2.34)$$

I_{nom} is the inverter nominal current. The parameters m , k_{RCI} , V_{S1} , n , k_{RCA} and V_{S2} allow changing the characteristics of voltage support, or even disabling this service (for instance, for small residential units connected to a Low Voltage (LV) grid).

Note that, according to Eq. (2.33), in case of overvoltage, a reactive current is drawn from the grid (i.e. the unit absorbs reactive power) to alleviate the terminal voltage rise.

The component I_{Qref} (see Fig.2.5) is added to the reactive current setting to comply with some

grid codes requiring a nonzero reactive power in steady state [Tro09, BVK13] or for some slow control of the distribution grid [SB17].

Active current injection

The solar irradiation or wind speed is assumed constant over a simulation interval of a few seconds as considered in this thesis. This leads to a constant power P_{ext} (see Fig. 2.5). For longer simulation intervals, P_{ext} may be varied during the simulation to model the changing weather conditions.

Dividing P_{ext} by the voltage V_m and limiting the result to I_{Pmax} as discussed in the sequel yields the active current command i_{Pcmd} .

Active - reactive priority

For efficient voltage support, units are assumed to give priority to reactive current injection during a fault [MG14b]. This may require reducing the active current in order to avoid exceeding the inverter current limit I_{nom} . The maximum active and reactive currents are thus given by :

$$I_{Pmax} = P_{flag}I_{nom} + (1 - P_{flag})\sqrt{I_{nom}^2 - i_{Qcmd}^2} \quad (2.35)$$

$$I_{Qmax} = P_{flag}\sqrt{I_{nom}^2 - i_{Pcmd}^2} + (1 - P_{flag})I_{nom}. \quad (2.36)$$

In normal operating conditions, i.e. when $V_{S1} < V_m < V_{S2}$ (see Fig. 2.9), priority is given to active current and the variable P_{flag} is at one. In that case, the maximum value of the active current (I_{Pmax}) is set to I_{nom} and the maximum value of the reactive current (I_{Qmax}) depends on the active current command i_{Pcmd} . When the voltage falls below V_{S1} , priority is given to reactive current, P_{flag} switches to zero, I_{Qmax} is set to I_{nom} and I_{Pmax} depends on i_{Qcmd} .

2.3.3 Active current recovery

In the event of severe fault, the active current is reduced to leave room for reactive current injection. After fault clearing, once the voltage has recovered to normal values, the IBG active current is allowed to recover [Wei15]. The recovery cannot be too fast to prevent fast dynamics that can destabilize the system, but not too slow either to avoid long lasting power imbalances. To model this, the lag block with time constant T_g in Fig. 2.5 includes an internal rate limiter. Figure 2.10 shows in some more details, how the rate of increase of i_P is limited. The input is i_{Pcmd} (see Fig. 2.5).

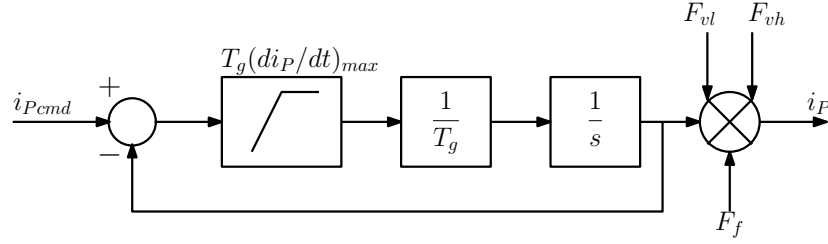


Figure 2.10: Detailed representation of the lag block including lag time constant T_g and rate limiter $(di_P/dt)_{max}$

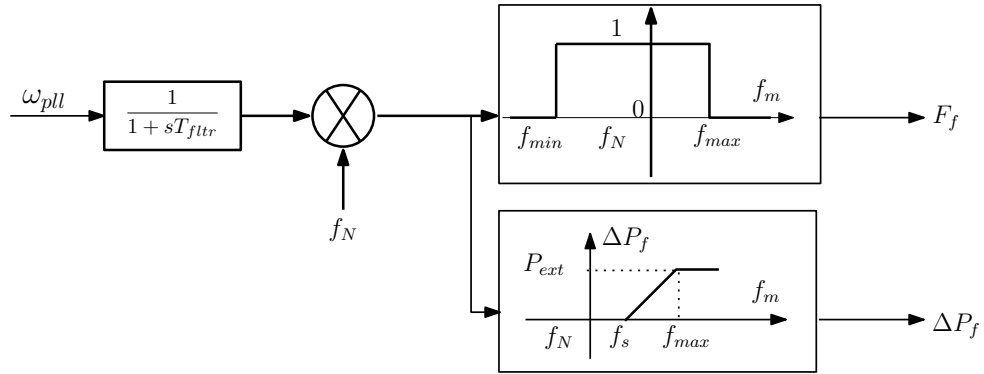


Figure 2.11: Part of the model for controls responding to a frequency deviation

2.3.4 Controls responding to frequency deviations

The block-diagram rendering the response of the IBG to a large enough frequency deviation is shown in Fig. 2.11 [Tro09, BVK13]. In this figure, ω_{pll} is the angular grid frequency (in pu) estimated by the PLL. The latter is filtered (through a first-order transfer function with a time constant T_{fltr}) to avoid abnormal frequency measurements during a short-circuit that might lead to an unwanted disconnection of the IBG, as it was observed during the event described in [Cor17b]. The output of the filter is multiplied by the nominal frequency f_N in Hz.

Under and over-frequency protection

Typically, the unit is allowed to disconnect if the frequency is outside the bounds $[f_{min} \ f_{max}]$. In Fig. 2.5, this is modelled by the variable F_f , which switches from one to zero if the filtered measured frequency is outside the acceptable range of values, as shown in Fig. 2.11.

Over-frequency control

Some IBGs may be requested to decrease their active power output in the event of an over-frequency. Most grid codes require the unit to start reducing its active power output by a quantity

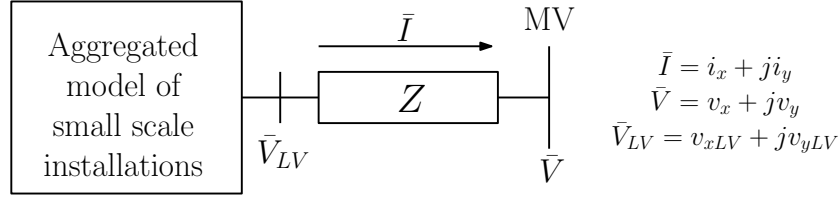


Figure 2.12: Aggregated model of small scale units connected to a MV bus

ΔP_f when the frequency is greater than f_s . The unit then participates into over-frequency control with full capacity if the frequency reaches the cut-off value f_{max} (see Fig. 2.11) [Tro09, BVK13]. Moreover, the unit is requested to sustain its minimum active power level until the frequency is back to normal values [BVK13].

The correction ΔP_f is applied to the initial active power P_{ext} generated by the IBG (see Fig. 2.5).

Under-frequency control

This model assumes that the IBG is operated for maximum power tracking, thus leaving no head-room for power increases. Therefore an increase of the active power output in response to under-frequency is not considered.

2.3.5 Aggregated model of small scale units connected to a MV bus

As LV networks are generally not modeled in detail, the IBG model is also used to represent a cluster of small residential installations (e.g. rooftop PVs) generally connected at LV level. The model of this cluster is connected to a MV bus through an equivalent impedance accounting for the LV distribution feeder and the MV-LV transformer. This is shown in Fig. 2.12 and leads to the equation :

$$\bar{V}_{LV} = \bar{V} + Z\bar{I}. \quad (2.37)$$

Decomposing this equation in the (x, y) reference frame leads to :

$$v_{xLV} + v_{yLV} = v_x + jv_y + (R + jX)(i_x + ji_y). \quad (2.38)$$

2.4 Synchronous generator model

As some parts of this thesis will deal with a real Australian distribution system hosting SGs (see Section 1.6.3), a SG model has been used.

The SGs connected at distribution level are represented with a fifth-order model of the synchronous machine [Kun94], a constant mechanical power and a generic model of the excitation system

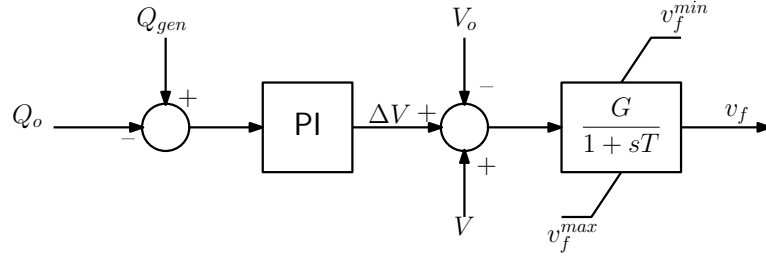


Figure 2.13: SG excitation system : Q_{gen} is the reactive power produced, V the terminal voltage and v_f the field voltage [IEE05]

including a reactive power control loop and a simple exciter, as shown in Fig. 2.13. The model is inspired from Var controller Type II model in [IEE05], p.38, which is representative of excitation systems for small synchronous machines connected at distribution level that are not supposed to regulate the system voltage.

2.5 Equivalent representation of the transmission system

Instead of being modeled in detail, the transmission system is replaced by a voltage source able to impose large variations of its amplitude, phase or frequency to mimic typical voltage evolutions in response to disturbances in the transmission system. The voltage source is depicted in Fig. 2.14 and its associated phasor is noted \bar{V}_{tr} . The pre-disturbance value of \bar{V}_{tr} is denoted \bar{V}_{tr}^0 and is shown in the (x, y) reference frame in Fig. 2.15, where ϕ_0 is the pre-disturbance voltage phase angle and ω_N is the nominal angular frequency (see Section 2.1.1). $v_{tr,x}^0$ and $v_{tr,y}^0$ are the projections of \bar{V}_{tr}^0 on the x and y axes, i.e. :

$$v_{tr,x}^0 = V_{tr}^0 \cos \phi_0 \quad (2.39)$$

$$v_{tr,y}^0 = V_{tr}^0 \sin \phi_0. \quad (2.40)$$

2.5.1 Variation of voltage magnitude

The variation of the voltage magnitude implies an increase or a decrease of V_{tr} from V_{tr}^0 to V_{tr}^m such as represented in Fig. 2.16 in the (x, y) reference frame. The new projections of the voltage phasor are given by :

$$v_{tr,x}^m = V_{tr}^m \cos \phi_0$$

$$v_{tr,y}^m = V_{tr}^m \sin \phi_0.$$

An example of voltage magnitude variation is the voltage dip, depicted in Fig. 2.17, corresponding to 40 % voltage magnitude reduction during 100 ms. The latter allows to mimic the effect of a

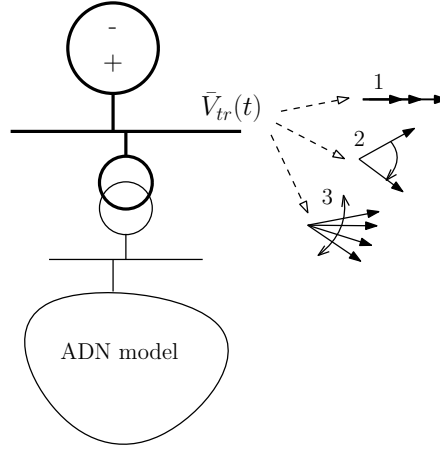


Figure 2.14: Representation of the transmission system model by a voltage source able to vary 1: its amplitude, 2: its phase, 3: its frequency

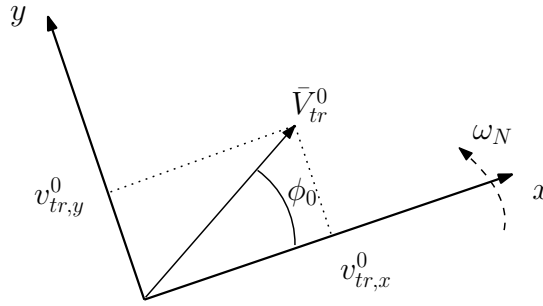


Figure 2.15: Representation of the pre-disturbance voltage \bar{V}_{tr}^0 in the (x, y) reference frame

balanced three-phase short circuit on the transmission grid. Voltage dips are characterized by their depth ΔV_{tr} , which depends on the fault location in the transmission network, and their duration ΔT , which relates to protection performances.

2.5.2 Variation of voltage phase angle

A variation of the voltage phase angle is represented in Fig. 2.18 in the (x, y) reference frame, where \bar{V}_{tr} changes from \bar{V}_{tr}^0 to \bar{V}_{tr}^p . The new projections of the voltage phasor are given by :

$$v_{tr,x}^p = V_{tr}^0 \cos(\phi_0 + \Delta\phi) \quad (2.41)$$

$$v_{tr,y}^p = V_{tr}^0 \sin(\phi_0 + \Delta\phi). \quad (2.42)$$

An example of voltage phase angle variation is the phase jump, depicted in Fig. 2.19, corresponding to a phase jump of 10 degrees. The latter typically mimics the effect of circuit breaker opening in a transmission line to clear a fault.

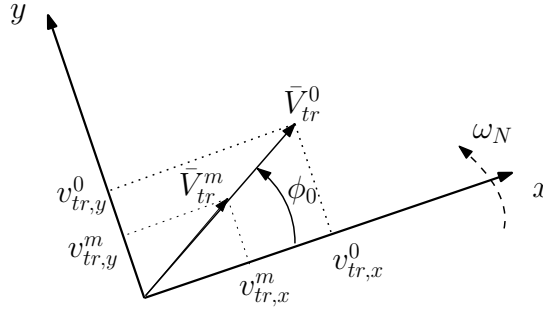
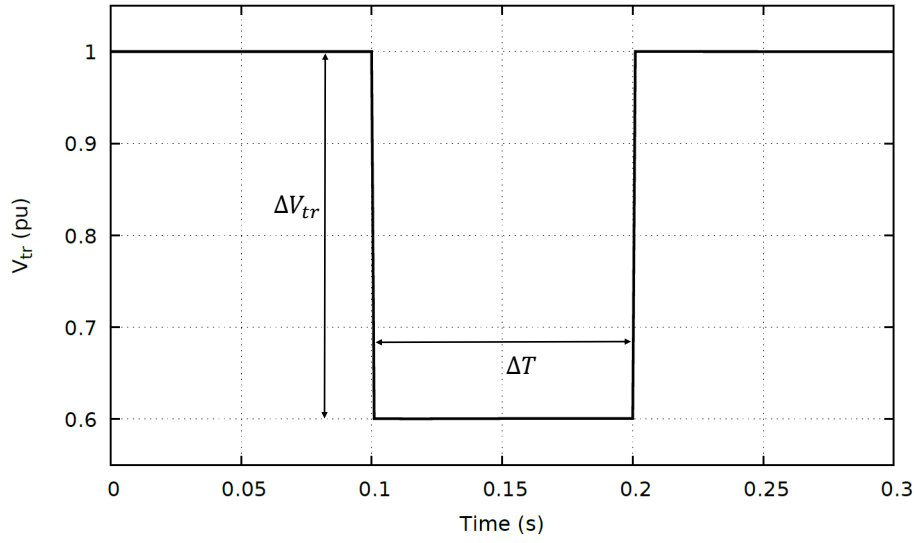
Figure 2.16: Representation of the voltage magnitude variation in the (x, y) reference frame

Figure 2.17: Example of voltage magnitude variation: voltage dip

2.5.3 Variation of voltage frequency

In this work, the frequency deviations are obtained by simulating the response of a generic turbine-speed governor system to an active power imbalance. The model is inspired from [PV14, WFGVC17] and is shown in Fig. 2.20. It renders the contribution of a large number of power plants. ΔP_m is the change of mechanical power, ΔP_e the total change of active power and $\Delta \omega$ the variation of system angular frequency. The inertia constant H , the droop R and the time constants T_1 and T_2 are tuned to match a typical frequency response.

A variation of the voltage frequency is sketched in Fig. 2.21 in the (x, y) reference frame. The projections of the voltage phasor are given by :

$$v_{tr,x}(\phi(t)) = V_{tr}^0 \cos \phi(t) \quad (2.43)$$

$$v_{tr,y}(\phi(t)) = V_{tr}^0 \sin \phi(t) \quad (2.44)$$

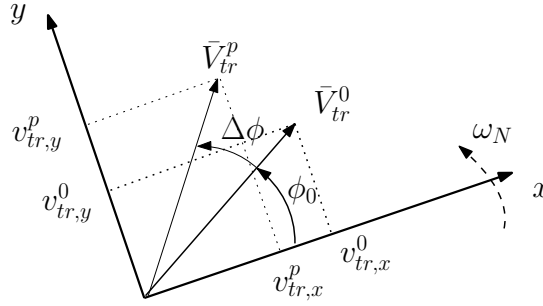
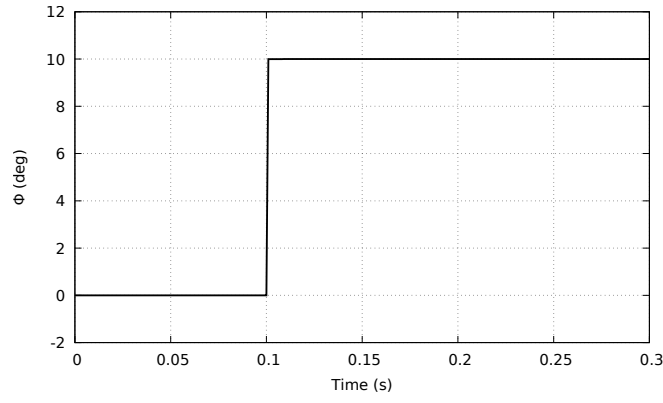
Figure 2.18: Representation of the voltage phase angle variation in the (x, y) reference frame

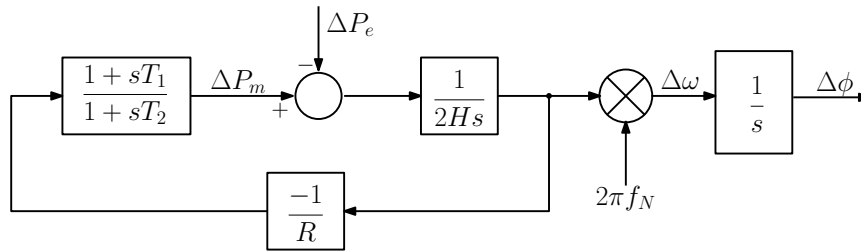
Figure 2.19: Example of voltage phase angle variation: phase jump

where the evolution of the phase angle is given by :

$$\phi(t) = \phi_0 + \Delta\phi(t) \quad (2.45)$$

with the variation $\Delta\phi(t)$ obtained by integration of $\Delta\omega$, as shown in Fig. 2.21.

An example of frequency response is shown in Fig. 2.22. The latter would correspond to the outage of a generator in the transmission system with inertial and primary frequency control.

Figure 2.20: Generic frequency control loop ($\Delta\phi$ is in rad)

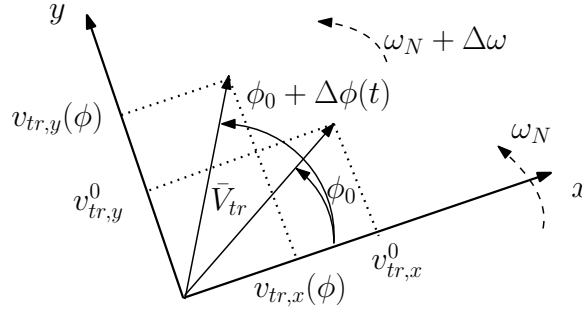
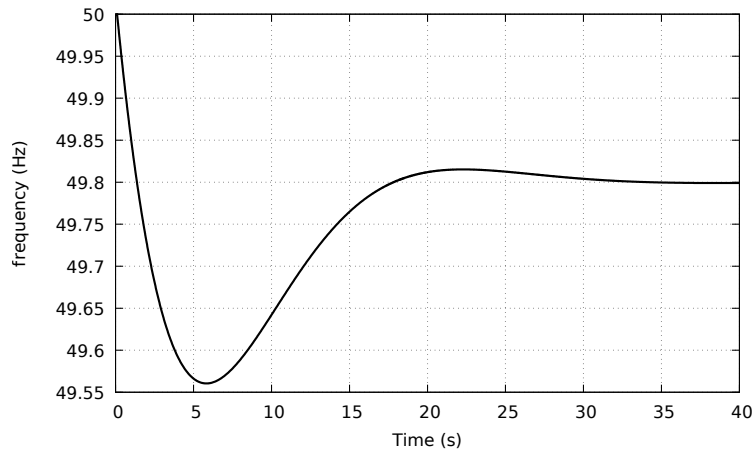
Figure 2.21: Representation of the voltage frequency variation in the (x, y) reference frame

Figure 2.22: Example of primary frequency response

2.5.4 Combined voltage variations

Clearly, it is possible to combine the variations of magnitude, phase and frequency to obtain a more elaborate voltage signal. For instance, the oscillations of voltage magnitude and phase angle can be combined to mimic the effect of an interarea electromechanical oscillation in the transmission system. In that case, the evolutions of the voltage magnitude and phase angle take on the form :

$$V_{tr}(t) = A_v e^{at} \sin(2\pi bt) \quad (2.46)$$

$$\phi(t) = A_\phi e^{at} \sin(2\pi bt) \quad (2.47)$$

where A_v and A_ϕ impose the amplitude of the oscillations, b is their frequency and a their damping. The damping ratio of the oscillations is defined by :

$$DR = \frac{-a}{\sqrt{a^2 + b^2}} \quad (2.48)$$

and it relates to a and b through :

$$a = \frac{-DR \ b}{\sqrt{1 - DR^2}}. \quad (2.49)$$

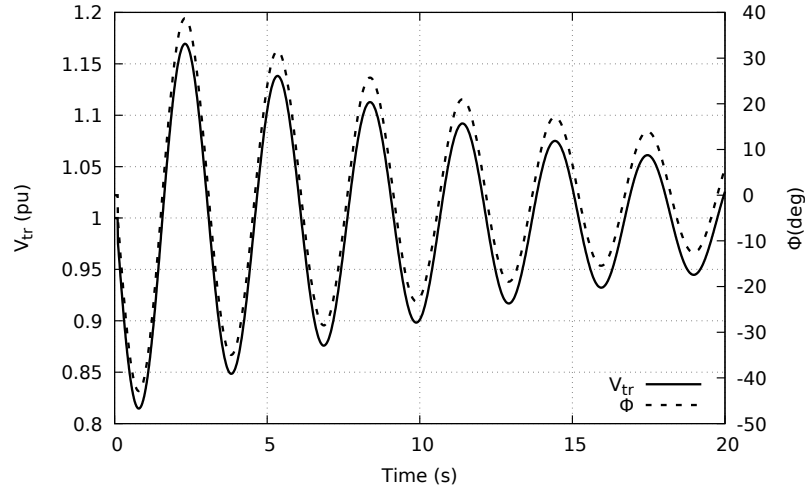


Figure 2.23: Example of voltage magnitude and phase oscillations; $DR = 0.2$ and $b = 0.33$ Hz

An example of voltage magnitude and phase oscillations with $DR = 0.2$ and $b = 0.33$ Hz, typical of an inteara electromechanical oscillation, is given in Fig. 2.23.

2.6 Illustration of model responses to large disturbances

To illustrate the models presented so far, justify the choice of some of their parameters and introduce the larger-scale simulations of the next chapter, this section presents a few examples of power responses of individual components connected to a distribution network, to large disturbances taking place in the transmission system.

2.6.1 Individual load responses

We first focus on the behaviour of the composite load model presented in Section 2.2, in response to the various disturbances presented in Section 2.5. The load is located at some distance of the entry point of the 75-bus distribution grid, presented in Section 1.6. The load is split into a constant admittance part and an Induction Motor (IM) with a load fraction $f_{Pm} = 0.2$, an initial power factor $\cos \phi_m = 0.85$ (with the compensation shunt capacitor) and a load factor of 0.6 (see Section 2.2.1). The other parameters of the IM (see Fig. 2.4 and Eq. (2.22)) are chosen in realistic ranges of values [C. 94].

Voltage dip

A reduction of 50 % of the transmission voltage magnitude V_{tr} during 250 ms is considered. The resulting voltage evolution at the load bus is shown in Fig. 2.24a, while the active and reactive

powers consumed by the load are shown in Figs. 2.24b and 2.24c, respectively. Finally, the motor speed evolution in response to the considered voltage dip is shown in Fig. 2.24d.

Under the effect of the reduced voltage, the active and reactive powers of the constant admittance load decrease. Regarding the motor, its internal electromagnetic force (emf) remains unchanged during the first moment of the voltage dip, and the active and reactive powers consumed by the motor suddenly decrease under the effect of the voltage reduction. At the first moment of the voltage dip, it can be seen that the motor produces reactive power, which takes negative values. Then, the motor windings start to demagnetize, which reduces the electromagnetic torque T_e . The reduction of T_e leads to the deceleration of the rotor (see Eq. (2.22)), as seen in Fig. 2.24d. The decrease of the motor speed decreases the equivalent motor impedance (in particular the resistance $\frac{\omega_{ref} R_r}{\omega_{ref} - \omega_r}$ (see Fig. 2.4)), which makes the motor drawing more current, re-increasing the active and reactive powers consumption.

When the voltage recovers, so do the active and reactive powers consumed by the constant admittance load. Regarding the motor, the emf remains constant during a short period of time after voltage recovery, while the equivalent impedance of the motor is still reduced. The power consumed by the motor thus suddenly increases, leading to active and reactive power spikes. Then the windings of the motor start to re-magnetize, increasing T_e , which makes the rotor accelerate. The equivalent motor impedance re-increases under the effect of motor acceleration, which brings the active and reactive powers progressively back to their pre-event values. The reactive power of the motor includes the effect of the compensation shunt capacitor.

Note that the disturbances considered in this thesis do not lead to motor stalling. The stalling is typical from air conditioning systems whose compressors are driven by classical motors. This type of load, widespread in the USA for instance [IRL⁺12], is not considered in the thesis.

Phase jump

The active and reactive power responses to a voltage phase jump of 10 degrees are shown in Figs. 2.25a and 2.25b, respectively. Both the active and the reactive powers have the same behaviour. The motor internal electromotive force remaining unchanged when the phase jump occurs results in a variation of the motor current, which in turn increases the powers consumed by the motor, leading to power spikes. Soon after, the electromotive force of the IM adjusts its value and the additional current component vanishes reducing the powers to the pre-event value as well.

Frequency deviation

Figure 2.26 shows the active and reactive power responses of the composite load under the effect of respectively an under- and an over-frequency transient, which could result from the outage of

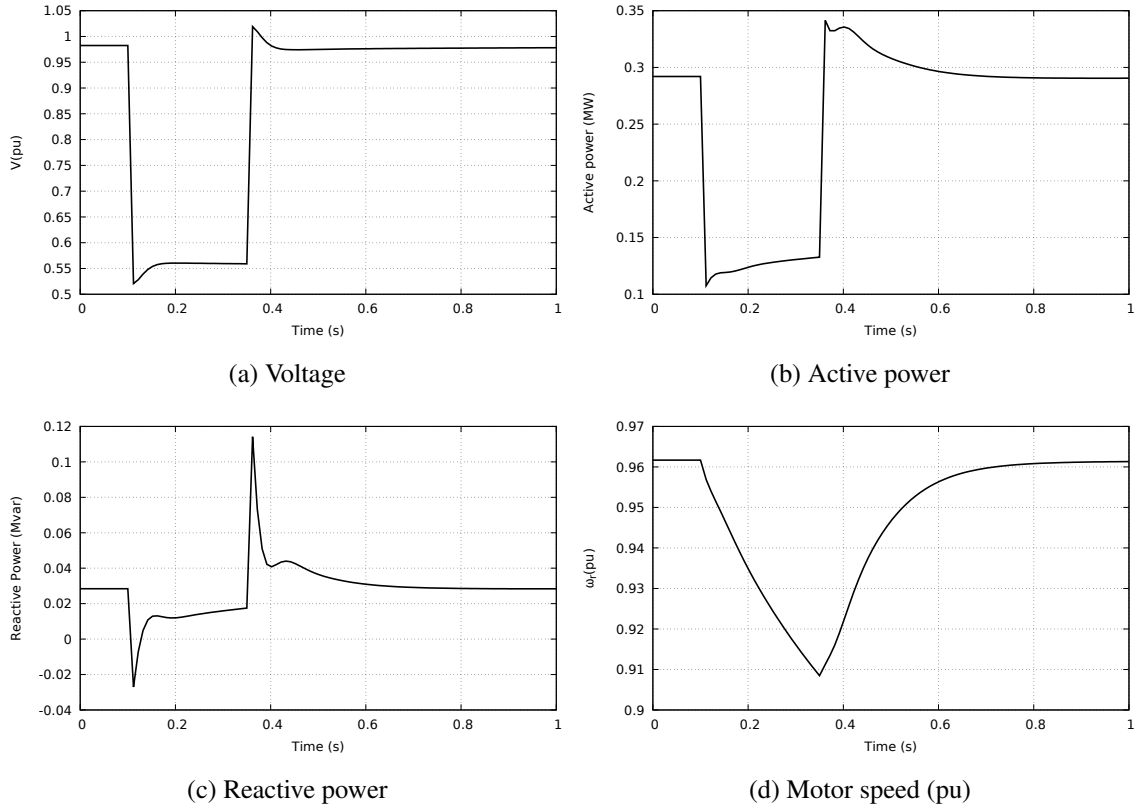


Figure 2.24: Voltage, active and reactive powers and motor rotor speed of the composite load in response to a voltage dip of 50 % lasting 250 ms taking place at $t = 0.1$ s

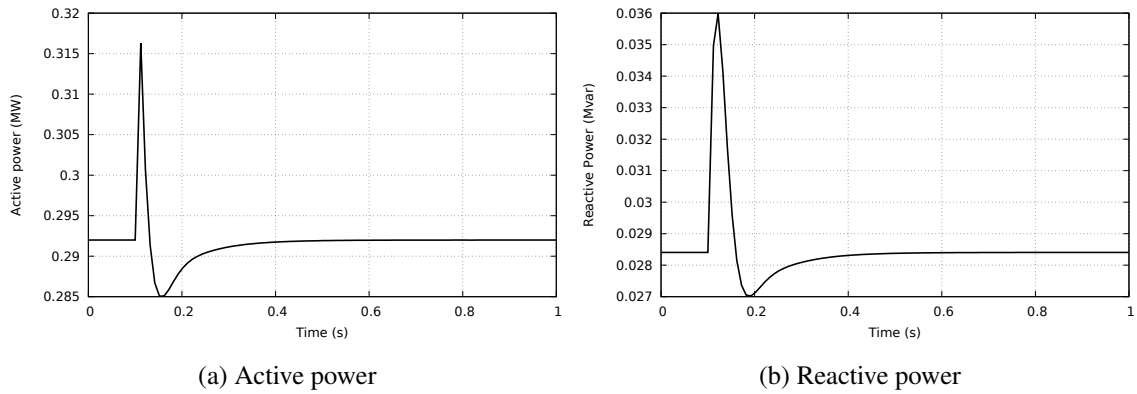


Figure 2.25: Active and reactive powers of the composite load in response to a voltage phase jump of 10 degrees taking place at $t = 0.1$ s

a generator in the former case and the tripping of a large load in the latter case. The motor speed evolution is shown in Fig. 2.26b.

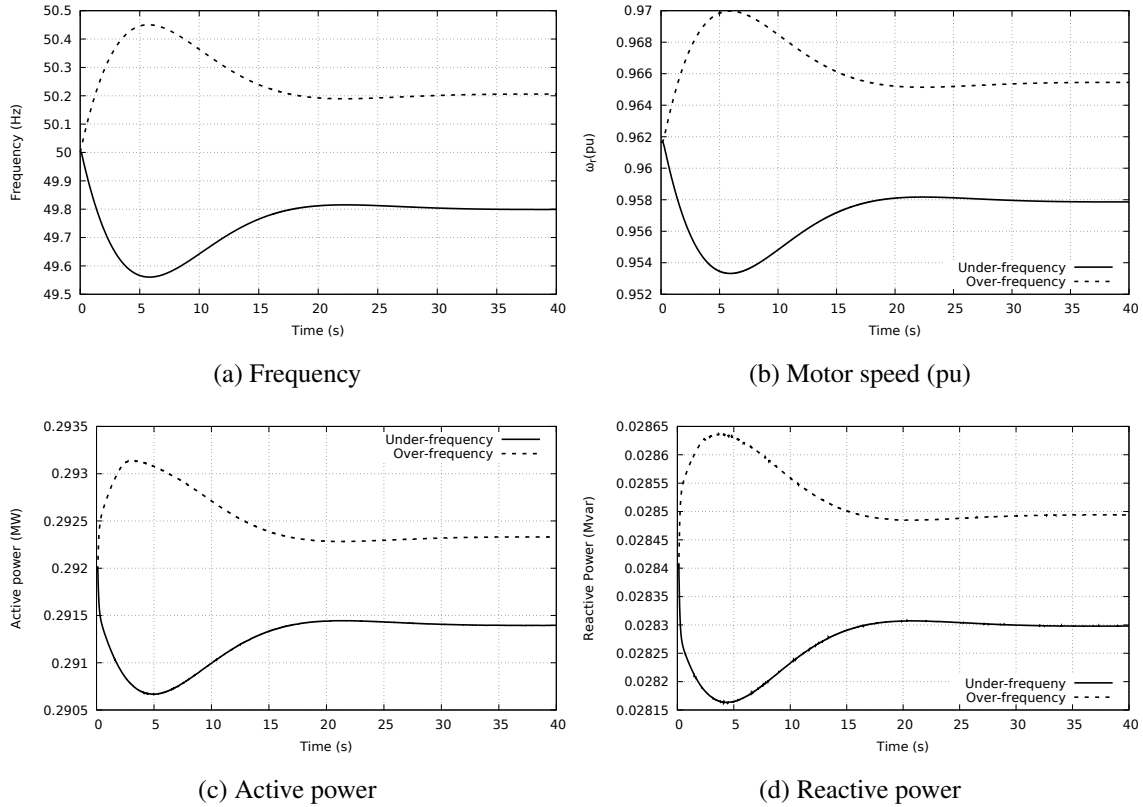


Figure 2.26: Active and reactive powers and motor rotor speed of the composite load to under- and over-frequency transients

The IM adjusts its rotor speed with the network frequency. In the event of an over-frequency, the rotor speed increases, which increases the power consumed by the load. Indeed, the mechanical torque remaining almost unchanged for the speed variations of concern here, the variations of the active power follow those of the frequency. The same applies in case of an under-frequency, where the rotor speed decreases.

Note that the static part of the load is not sensitive to frequency in the model considered in this thesis.

Electromechanical oscillations

Finally, the active and reactive power responses of the load to electromechanical oscillations are given in Fig. 2.27. The voltage oscillations are those shown in Fig. 2.23.

After some transients, the active and reactive powers of the load simply oscillates with the voltage magnitude. The impact of the voltage angle oscillations is less visible.

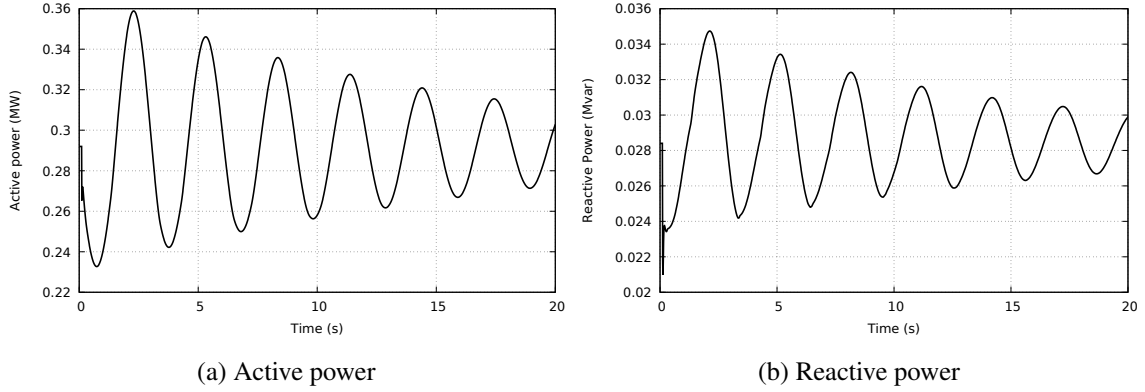


Figure 2.27: Active and reactive power responses of the load to electromechanical oscillations

2.6.2 Individual IBG responses

This section illustrates the dynamic behaviour of the IBG modeled as presented in Section 2.3 for the various disturbances presented in Section 2.5.

The IBG is also located at some distance of the entry point of the 75-bus distribution grid presented in Section 1.6. The IBG operates initially at unity power factor and produces 50 % of its nominal capacity. P_{ext} (see Fig. 2.5) is assumed constant for the duration of the simulations. The values of the model parameters were chosen in accordance with specific grid codes [KHBL13, BVK13, Wei15, rV15].

Voltage dip

To illustrate the various features of the model, three scenarios are considered:

1. short-circuit in the transmission system with "reasonable" voltage dip ($\Delta V_{tr} = 0.3$ pu) cleared normally in 100 ms;
2. short-circuit in the transmission system with a pronounced voltage dip ($\Delta V_{tr} = 0.7$ pu) cleared normally in 100 ms;
3. short-circuit in the transmission system with the same pronounced voltage dip ($\Delta V_{tr} = 0.7$ pu) cleared by back-up protections in 350 ms;

Scenario 1 Figure 2.28a shows the time evolution of the IBG terminal voltage (V) as well as the corresponding measured value (V_m) (see Section 2.3). The LVRT characteristic (see Section 2.3.2) is superimposed for easy reference. It is seen that the voltage remains largely above the LVRT

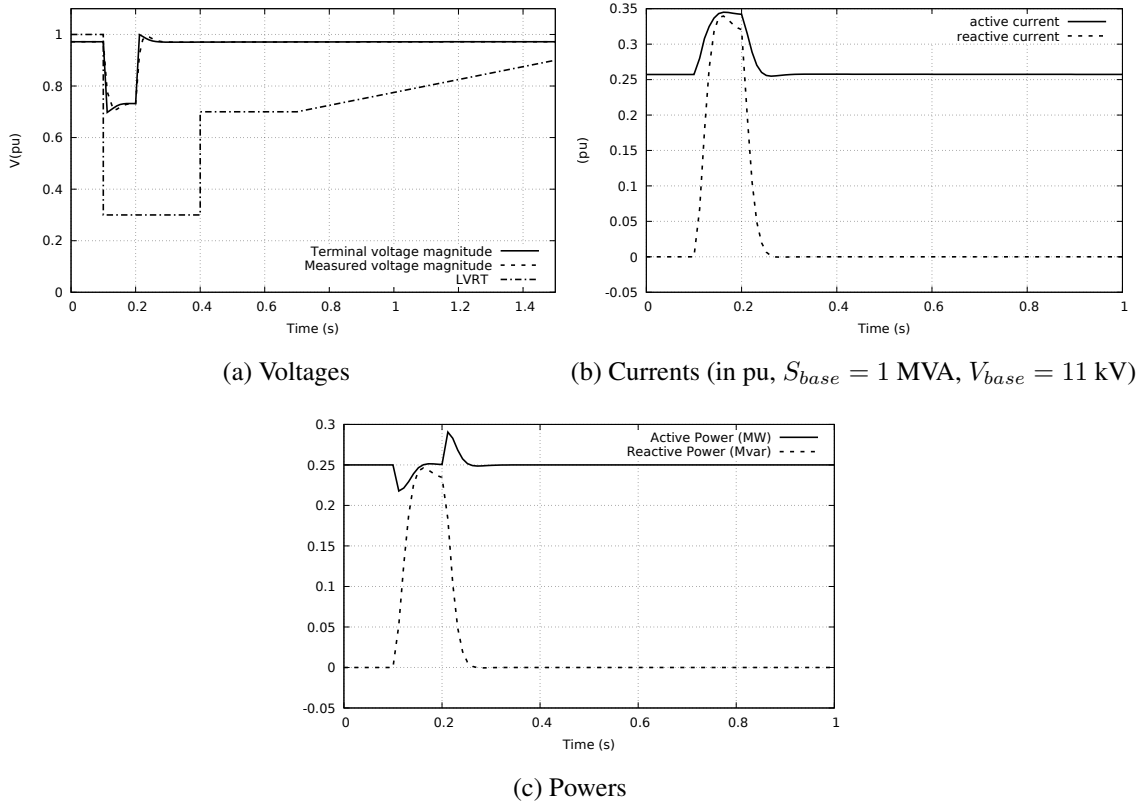


Figure 2.28: Voltage, currents and powers of the IBG: Scenario 1

curve. Figure 2.28b shows the active and reactive currents injected by the IBG in response to the voltage dip. As explained in Section 2.3.2, the unit injects reactive current to support its terminal voltage during the fault. The rather small decrease of the voltage is such that the IBG current remains well below its upper limit and, hence, no active current is sacrificed. Instead, the latter increases under the effect of the low voltage, in order to meet the active power set point P_{ext} .

The active and reactive powers generated by the IBG in response to the disturbance can be seen in Fig. 2.28c. Apart from some transients at the fault occurrence and clearing, the active power remains close to its pre-fault value. The reactive power is zero before the fault, as the unit initially operates at unity power factor, while it increases significantly during the voltage dip due to reactive current injection before returning to zero when the fault is cleared.

Scenario 2 The time evolution of the terminal and measured voltages for Scenario 2 are shown in Fig. 2.29a, again with the LVRT characteristic. It is seen that, while the voltage drops more than in Scenario 1, it still remains above the LVRT curve. Therefore, no disconnection takes place.

The active and reactive currents injected by the IBG into the grid are shown in Fig. 2.29b. The

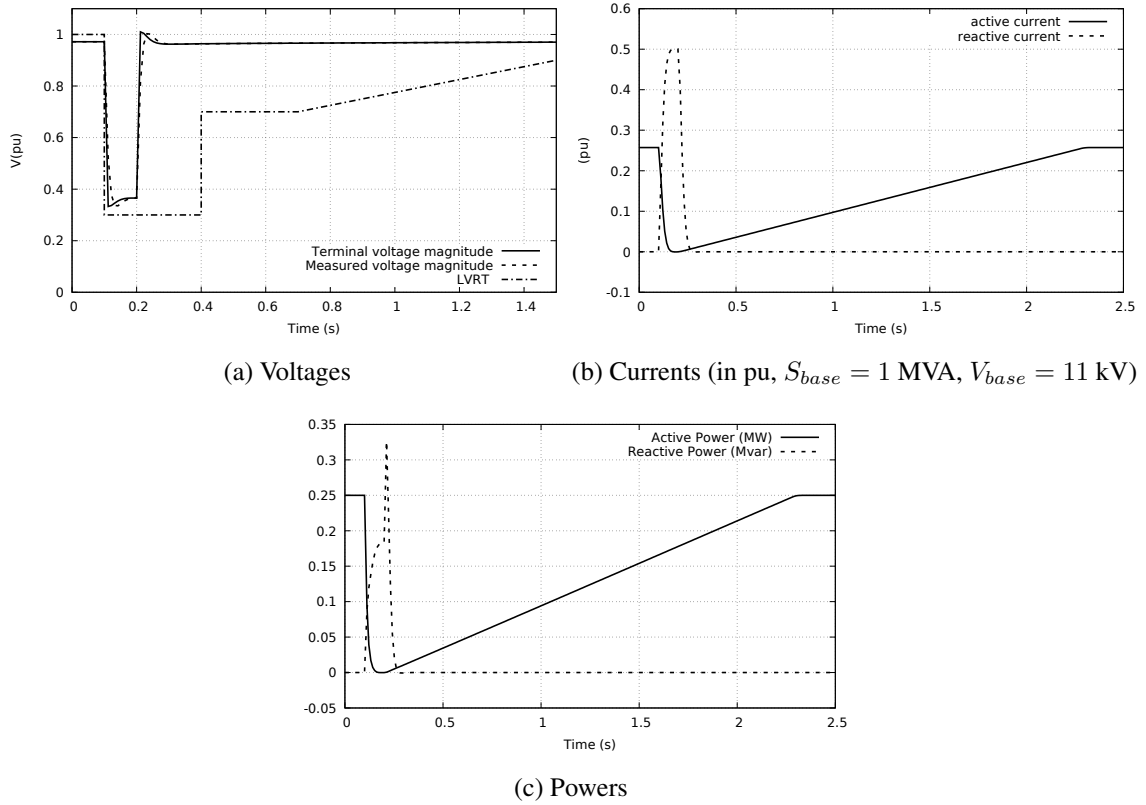


Figure 2.29: Voltage, currents and powers of the IBG: Scenario 2

amount of reactive current requested for voltage support is such that the active current must be decreased in order to not exceed the inverter current limit. When the fault is cleared, the reactive current returns to zero, as the voltage support is no longer requested, while the active current is ramped up at a rate of 0.125 pu/s imposed by the limiter shown in Fig. 2.10.

Figure 2.29c shows the active and reactive powers generated by the IBG. The active power evolution is similar to the active current one. Regarding the reactive power, the latter increases as expected during the fault, because of the additional reactive current injection, but additionally, a spike is observed when the fault is cleared. Indeed, due to the voltage measurement time constant, the unit keeps injecting reactive current for a short period of time, although the true voltage has already recovered.

Scenario 3 The simulation results for the third scenario are given in Fig. 2.30. The duration of the fault has been taken large on purpose, in order to illustrate the disconnection of the IBG before fault clearing.

The terminal as well as the measured voltage magnitudes are shown in Fig. 2.30a. The voltage

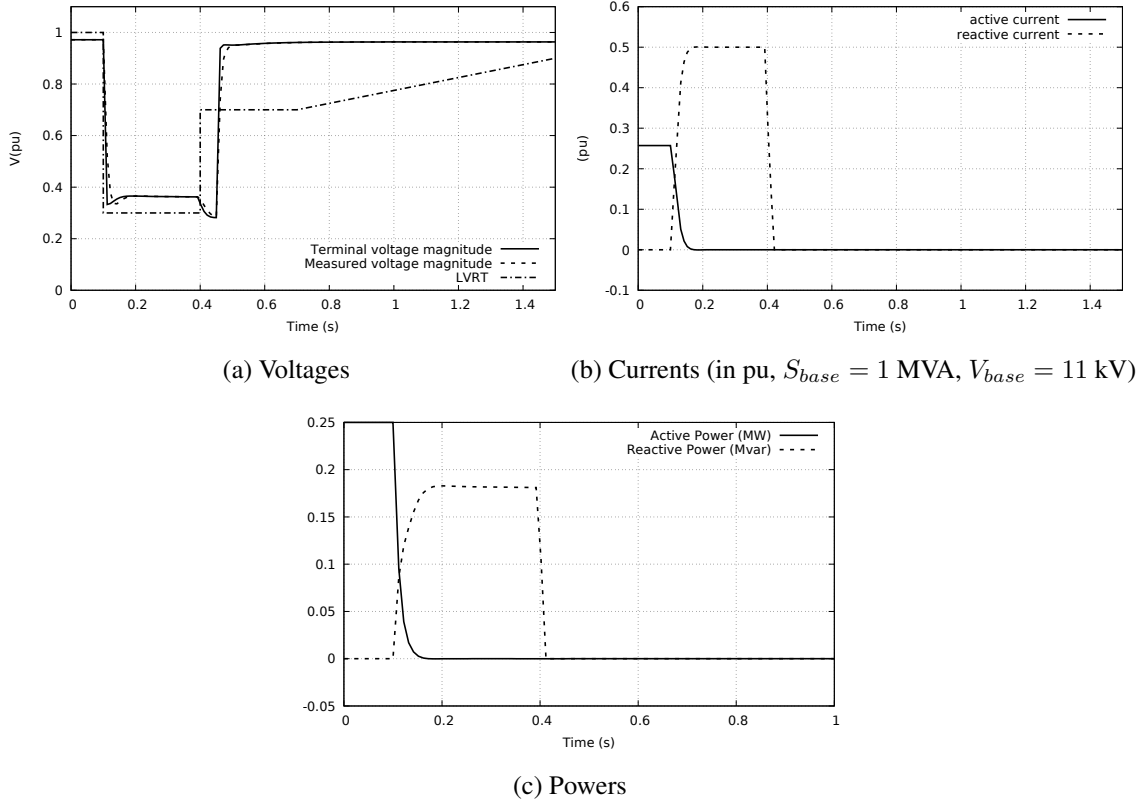


Figure 2.30: Voltage, currents and powers of the IBG: Scenario 3

support provided by the IBG is visible : the residual voltage slightly increases in the first instants following the voltage drop. At $t = 0.4$ s, however, the measured voltage crosses the LVRT characteristic, which causes the unit disconnection. Since the IBG is not supporting the voltage any longer, the latter is further decreased before the fault is cleared.

Figure 2.30b shows the active and reactive currents injected by the unit. As seen in the previous scenario, during the voltage dip, the unit is requested to inject reactive current. The active current is reduced to zero in order to not exceed the inverter maximum current and leave room for full reactive current injection. At $t = 0.4$ s, when the unit disconnects from the grid, the reactive current falls to zero as expected and the active current remains at zero. The same holds true for the active and reactive powers (see Fig. 2.30c).

As mentioned in Section 2.5, the frequency estimate provided by the PLL is filtered to avoid abnormal measurements during a short-circuit, which would lead to unwanted disconnection of the IBG. Such a malfunction was observed in Southern California on August 16, 2016. Due to a severe forest fire, which had rapidly moved toward an important transmission corridor, the 500-kV grid experienced multiple faults. Some of these faults resulted in the loss of a significant

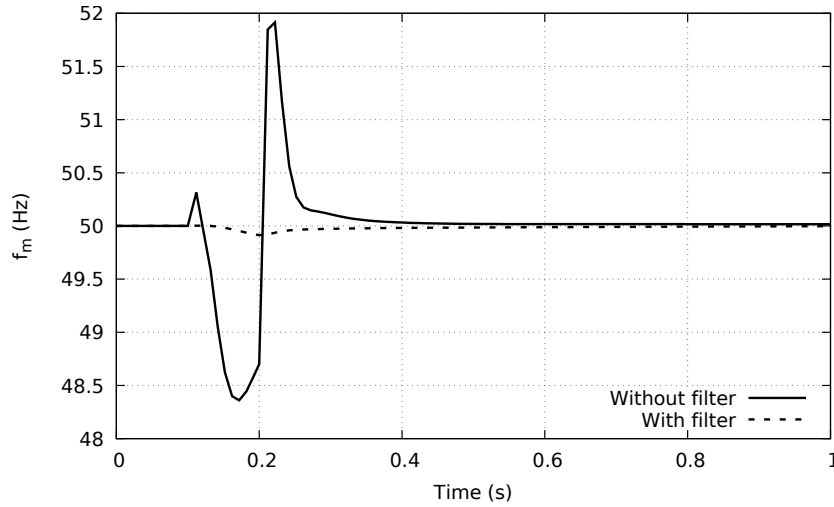


Figure 2.31: Illustration of the frequency measured by the PLL (f_m) with and without filter: Scenario 2

amount of solar PV generation. The study published in [Cor17b] has pointed out that inverters that respond to near instantaneous frequency measurements are exposed to false tripping during transients generated by faults on the power system. One of the recommendation was to impose a minimum delay for frequency detection and/or implement a proper filtering.

Within the limit of validity of the phasor approximation, the above behaviour is illustrated here in Scenario 2. The frequency “measured” by the PLL in this scenario is shown in Fig. 2.31, with and without filter. The latter has been simply modeled by a first-order transfer function with a time constant of one second. It clearly shows that, without filter, the frequency deviation measured by the PLL is so large that the unit will trip, while the filter smoothens significantly the input signal, thus avoiding such unwanted disconnection. Clearly, the IBGs are expected to support the grid during and after a short circuit, not aggravate the severity of the initiating event.

Note that time constant value of the first-order filter has been arbitrary chosen to illustrate the above mentioned malfunction, while a delay of a few seconds is suggested in [Cor17b].

Phase jump

The IBG is little responsive to any voltage phase jump. This is explained by the grid-following control [PGG⁺20] which adjusts the current phasor to the voltage phasor. Following a pure phase jump, the active and reactive currents are expected to change only due to the transient behavior of the PLL.

As an illustration, the PLL response to a voltage phase jump of 10 degrees at the transmission

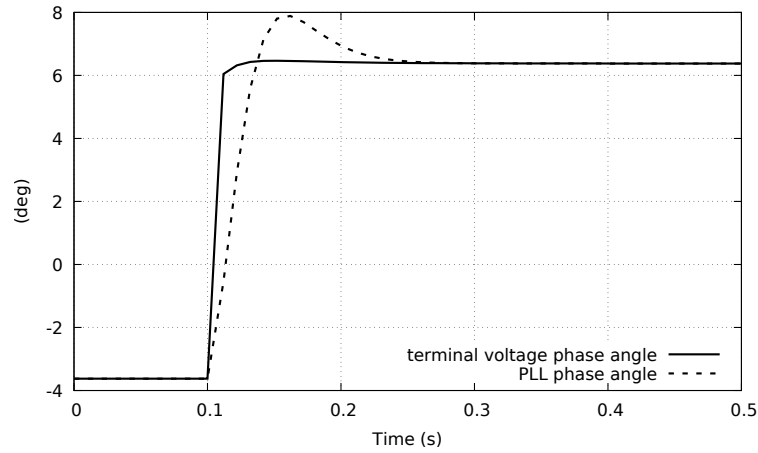


Figure 2.32: Response of the PLL to a phase jump of 10 degrees at the transmission level

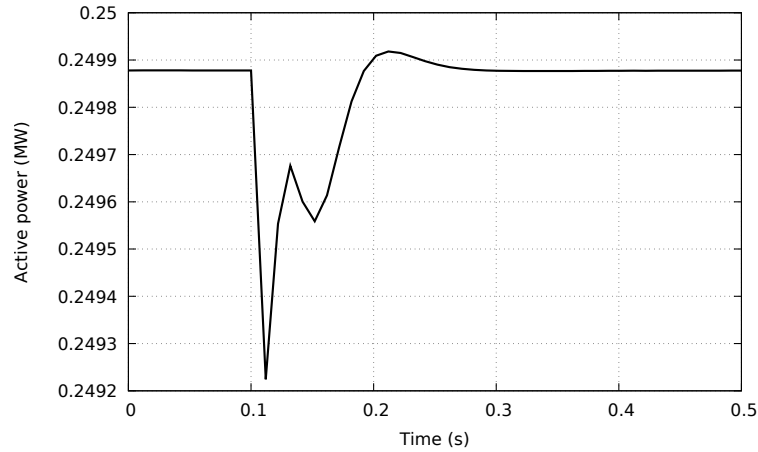


Figure 2.33: IBG active power response to a phase jump of 10 degrees at the transmission level

level is shown in Fig. 2.32. The PLL phase angle is plotted together with the real voltage phase angle. The PLL has been tuned to have a response time of 100 ms. The pre-disturbance reactive power generated by the IBG being zero, the effect of the phase jump on the latter is not visible, while the effect on the active power is marginal, as can be seen in Fig. 2.33.

Frequency deviation

As already mentioned, the IBG does not react to a decrease in frequency, as no active power headroom is available. On the other hand, it is expected to provide a droop response to an over-frequency by decreasing its active power output (see Fig. 2.11). Moreover, the unit is requested to sustain its minimum active power level until the frequency has returned to normal values.

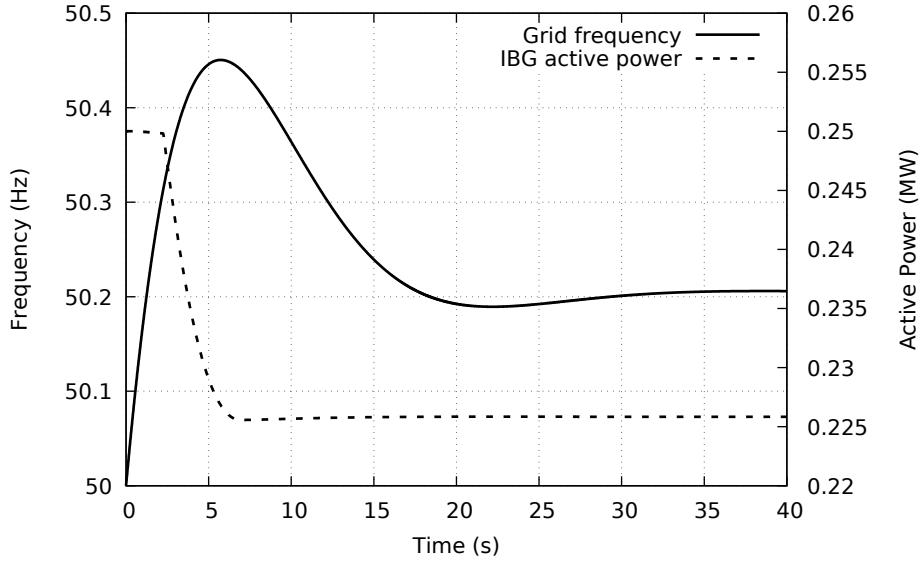


Figure 2.34: IBG active power response to an over-frequency transient

An example of over-frequency transient is shown in Fig. 2.34, which could result from the loss of a large load. The active power generated by the IBG is also depicted. As required, the unit starts to decrease its active power output when the frequency reaches some threshold and stops when frequency has reached its maximum. Then the unit sustains its output, as frequency has not returned yet to normal operating values.

Note that the part of the IBG model including controls responding to frequency deviations (see Fig. 2.11) has been extensively used in the frame of an internship at the University of Melbourne (Australia), where we deviate from the initial philosophy of the thesis. Indeed, instead of simulation-based identification, parameters of the IBG model have been adjusted based on measurements collected during the August 2018 separation event in Australia, which has led to large frequency deviations [Aus19a]. More details and simulation results are offered in Appendix C.

Electromechanical oscillations

The active and reactive power responses of the IBG to electromechanical oscillations are shown in Fig. 2.35. The transmission voltage oscillations are those shown in Fig. 2.23.

The voltage magnitude deviations are sufficiently small so that the IBG is not required to decrease its active power, which remains almost constant. On the other hand, the IBG, requested to inject reactive current when the voltage magnitude V_m falls below the threshold $V_{S1} = 0.9$ pu (see Fig. 2.9), produces reactive power “pulses” whose amplitude is proportional to the decaying deviation $V_{S1} - V_m$.

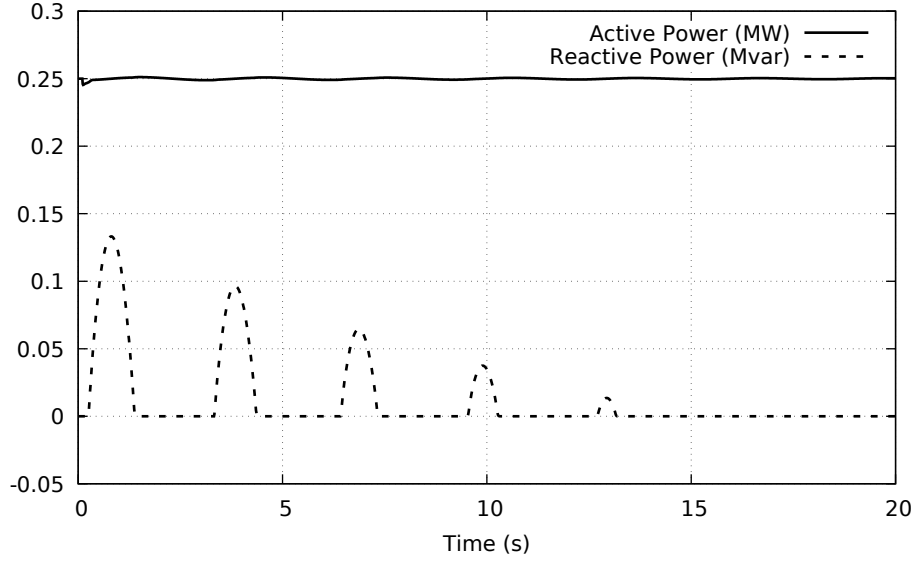


Figure 2.35: Active and reactive power responses of the IBG to electromechanical oscillations

2.6.3 Comparison of IBG and WECC type 4 models

Finally, the IBG model developed for this thesis has been compared with the Type 4, full-converter model recommended by WECC [MG14a] for power systems dynamics and stability studies. While our IBG model is basically a first-order model in which the active and reactive currents follow their reference with the converter time constant T_g , the WECC model is a higher order model including, in addition to T_g , some PI controllers and involving a larger number of parameters.

Simulation results are presented in Appendix A. The active and reactive currents and powers of both models are compared in response to voltage dips of various severities. They show that a real good match can be achieved between both models. This further confirms that the model used in this thesis is representative

2.7 Summary

Generic load and IBG models have been detailed in this chapter. The load model is divided into a static and a dynamic part while the IBG model renders the controls of the converter in response to voltage and frequency deviations, in adequacy with current grid code requirements. These models are used under the phasor-mode approximation, typical of large-scale dynamic studies. Rotor angle, frequency and voltage stability studies are targeted. The transmission system is modeled by a voltage source able to vary its magnitude and phase angle. The latter is used to generate various voltage signals to account for typical events taking place in the transmission system. Furthermore, examples have been given of model responses to various large disturbances. Finally, the attention

was drawn on the good agreement between the relatively simple model of this thesis and the Type 4 WECC model [MG14a].

The proposed models are deemed representative of what could be used in practice, considering the available information and grid codes. Moreover, the methodology exposed in the next chapters is not limited to particular models but, instead, holds for a wide variety of them. More importantly, it has been ensured that the model accounts for representative nonlinearities encountered in practice.

Chapter 3

Dealing with model uncertainty

This chapter addresses the issue of the uncertainty affecting the ADN models. It proposes a simple methodology to take into account that uncertainty and assess its impact on dynamic power responses. Among a set of randomized system evolutions, either statistics or a representative dynamic response can be extracted. The latter can be used for the identification of ADN equivalents.

This chapter is organized as follows. Section 3.1 presents the motivation and objectives of this work. The model randomization to assess the uncertainty is described in Section 3.2. Then the methods to extract statistics and a representative dynamic response from randomized system evolutions are presented in Section 3.3 and 3.4, respectively, together with simulation results. Section 3.5 proposes an approach to estimate the number of randomized system evolutions needed. Finally, Section 3.6 summarizes the material of this chapter.

3.1 Introduction

As the goal of this thesis is to derive reduced-order models of ADNs using a simulation-based approach, the first step consists of setting up detailed, i.e. unreduced models of ADNs. One major issue when setting up such a model lies in the uncertainty affecting the behaviour of its components. Their dynamic models involve parameters which are not known accurately. This is a well-known fact for loads in general. For instance, it is customary to include an equivalent motor representing the cumulated effects of a population of smaller motors (as detailed in Section 2.2.1), but its parameters are usually set to “typical” values (e.g. [C. 94]). This is also true for IBGs in so far as grid codes specify a range of admissible behaviours [IEE19, EUg19], but leave the manufacturers with some freedom in the setting of the equipment parameters.

In this work, it is assumed that the individual dynamic behaviour of IBGs, loads, etc. can be reasonably well captured by a parameterized model, but the values of its parameters are uncertain.

A well-known approach to deal with such uncertainty consists of performing Monte-Carlo (MC) simulations [Moo97, RC13], involving in this case random variations of the parameters. Thus, for given disturbances and operating points, a set of randomized time responses is generated [HPN00, CPVCss]. Statistics such as the average (or the median) and the standard deviations provide useful information on the time-varying impact of parameter uncertainty. Moreover, the randomized time responses can be processed to derive a reference response, from which a representative ADN instance can be identified.

This approach bears similarity with the one of [ZWM11], where a number of scenarios (obtained by varying load, IBG composition, fault location, etc.) were considered and the ADN active and reactive power responses grouped into a small number of clusters to reduce the computational effort for the derivation of an ADN equivalent. In this work, uncertainty affects the parameters of the ADN model rather than the scenarios, and it turns out that a much larger set of randomized responses is considered.

In this chapter, for sake of clarity and simplicity, only voltage dips are considered. The latter are obtained by varying the \bar{V}_{tr} voltage shown in Fig. 2.14. Indeed, compared with frequency variations or phase jumps, severe voltage dips will exacerbate the discontinuous behaviour of IBGs and the nonlinearities of load dynamics. Therefore the effect of parameters uncertainty on the dynamic behaviour of the ADN model will be more visible.

3.2 Model randomization in MC simulations

Consider a distribution network feeding n_L loads and hosting n_G IBGs. For simplicity, and without loss of generality, the same “generic” model is used - though with different parameter values - for each IBG, and similarly for the loads. Let π_G (resp. π_L) be the number of parameters of the IBG (resp. load) model. Thus, the vector \mathbf{p} of parameters of the whole ADN model involves $n_G \pi_G + n_L \pi_L$ components.

Monte-Carlo simulations involve random variations of \mathbf{p} with $\mathbf{p}^{min} \leq \mathbf{p} \leq \mathbf{p}^{max}$. The components of \mathbf{p} are treated as independent random variables. If no other information is available, it makes sense to make \mathbf{p} obey a uniform distribution between the specified bounds \mathbf{p}^{min} and \mathbf{p}^{max} [HPN00]. Alternatively, the distribution can be centered around the middle of the interval by assuming a truncated Gaussian distribution with averages $\boldsymbol{\mu} = (\mathbf{p}^{min} + \mathbf{p}^{max})/2$ and $(\mathbf{p}^{max} - \mathbf{p}^{min})/6$ as vector of standard deviations.

It must be emphasized that the parameters are randomized from one MC simulation to another, but also from one bus to another inside the same MC simulation.

Starting from the same initial operating point, a set of d disturbances is simulated with s instances

of the same model corresponding to the randomly drawn parameter vectors $\mathbf{p}^{(1)}, \dots, \mathbf{p}^{(s)}$.

The parameters randomized in our MC simulations and their corresponding range of values are shown in Table 3.1. The range of values for residential motors, connected to LV network, differs from industrial motors, connected to MV network. The former are denoted with a “r” in Table 3.1 and the latter with a “i”. The nominal currents of the IBGs are assumed to be known; hence, they are not randomized.

Another source of uncertainty stems from the LVRT capability of individual IBGs. Grid codes state that they *are allowed* to disconnect if their voltages fall below the LVRT curve, but *do not request* their disconnection, on the contrary. This has been taken into account by also randomizing the disconnection of IBGs in the MC simulations: the parameters V_{min} of the LVRT characteristic (see Fig. 2.8) is treated as a random discrete variable that can either take the value of 0.3 or 0 pu. In the former case, disconnections occur for severe voltage dips. In the latter case, the IBG never disconnects from the grid. This uncertainty on V_{min} has not been considered for ADN No 1, as it hosts a limited number of large-capacity IBGs.

The variables of interest are the active (P) and reactive power (Q) entering the ADN (see Figs. 1.9 and 1.10).

Table 3.1: List of randomized parameters and associated range of values

Parameter	Mathematical expression	Related figure or equation	Range of values
Motor stator resistance	R_s	Fig. 2.4	[0.03 0.13] pu (r) [0.01 0.05] pu (i)
Motor rotor resistance	R_r	Fig. 2.4	[0.03 0.13] pu (r) [0.008 0.05] pu (i)
Motor magnetizing reactance	L_{sr}	Fig. 2.4	[1.8 3] pu (r) [2.5 4] pu (i)
Motor stator leakage reactance	$L_{ss} - L_{sr}$	Fig. 2.4	[0.07 0.15] pu (r) [0.06 0.1] pu (i)
Motor rotor leakage reactance	$L_{rr} - L_{sr}$	Fig. 2.4	[0.06 0.15] pu (r) [0.06 0.2] pu (i)
Inertia constant of the motor	H	Eq. (2.22)	[0.26 1] s (r) [0.28 1.5] s (i)
Motor fraction of quadratic mechanical torque	A	Eq. (2.22)	[0.2 1]
Motor load factor	LF	Eq. (2.13)	[0.4 0.6] (r) [0.6 0.8] (i)
Fraction of initial motor active power consumption	f_{Pm}	Eq. (2.11)	[0 0.2] (r) [0.2 0.4] (i)
Initial motor power factor	$\cos\phi_m$	Eq. (2.12)	[0.85 0.95] (r) [0.95 1] (i)
Load static part exponent	α	Eq. (2.25)	[1 2]
Load static part exponent	β	Eq. (2.26)	[1.5 3]
IBG maximum rate of active current recovery	$(\frac{di_P}{dt})_{max}$	Fig. (2.10)	[0.2 0.5] pu/s
IBG PLL response time	τ_{PLL}	Fig. 2.7	[0.05 0.15] s
IBG current controller time constant	T_g	Fig. 2.5	[0.01 0.03] s
IBG slope of reactive current vs. voltage	k_{RCI}	Fig. 2.9	[2 6] pu/pu
IBG voltage threshold of reactive injection	V_{S1}	Fig. 2.9	[0.85 0.95] pu
IBG minimum voltage of LVRT	V_{min}	Fig. 2.8	{0, 0.3} pu

3.3 Extracting statistics

For the j -th disturbance ($j = 1, \dots, d$), the i -th instance $\mathbf{p}^{(i)}$ of \mathbf{p} ($i = 1, \dots, s$) and a discrete time instant k , the following values are extracted from the MC simulations :

- $P(j, k, \mathbf{p}^{(i)})$ the active power at time k obtained with $\mathbf{p}^{(i)}$
- $Q(j, k, \mathbf{p}^{(i)})$ the corresponding reactive power
- $\mu_P(j, k)$ the average of the s values $P(j, k, \mathbf{p}^{(i)})$
- $\mu_Q(j, k)$ the average of the s values $Q(j, k, \mathbf{p}^{(i)})$
- $\sigma_P(j, k)$ the standard deviation of the s values $P(j, k, \mathbf{p}^{(i)})$
- $\sigma_Q(j, k)$ the standard deviation of the s values $Q(j, k, \mathbf{p}^{(i)})$.

These statistics will be used when deriving the ADN equivalent. In particular, its parameters will be adjusted to approach as closely as possible the average power evolutions μ_P and μ_Q , while the reciprocal of $\sigma_P^2(j, k)$ and $\sigma_Q^2(j, k)$ will be used as weighting factors. This will be covered in more detail in the next chapter.

The rest of this section presents MC simulation results for the test systems presented in Section 1.6. Uniform distributions of the parameters are considered first, followed by the results obtained with Gaussian distributions.

3.3.1 Simulation results for ADN No 1 - uniform distributions of the parameters

Figure 3.1 shows the randomized time evolutions of respectively P and Q entering the ADN No 1, in response to a voltage dip of depth $\Delta V_{tr} = 0.3$ pu and duration $\Delta T = 100$ ms, in the upper part of the figure and for $\Delta V_{tr} = 0.6$ pu and $\Delta T = 250$ ms in the lower part. Uniform distributions of the parameters have been considered. All curves start from the same value since a single operating point is considered here.

The overall evolution is explained as follows. During the voltage dip the load with exponential model decreases, while the large-capacity IBGs sacrifice active power to inject reactive power. The load with exponential model recovers together with V_{tr} . Some additional power is drawn transiently by the re-accelerating motors (see Section 2.6.1 for a more detail explanation on motors behaviour in response to voltage dips). The large-capacity IBGs return to unity power factor while ramping up their active power (this is mostly visible in Fig. 3.1c for the more severe voltage dip). P settles slightly above its value before disturbance, due to the undervoltage tripping of the small-capacity IBGs.

The figures also show the distributions of the randomized power values at one time instant after

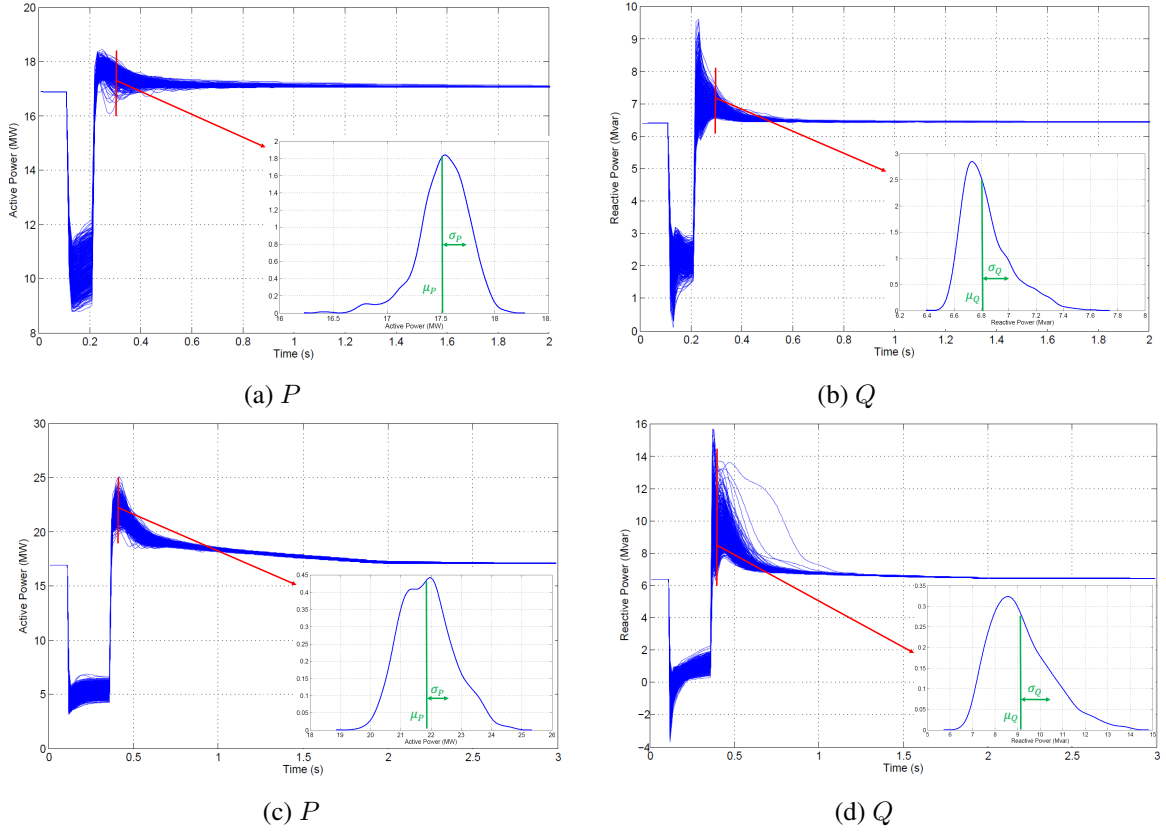


Figure 3.1: Randomized evolutions of P and Q in response to the voltage dip $\Delta V_{tr} = 0.3$ pu, $\Delta T = 100$ ms (upper part) and $\Delta V_{tr} = 0.6$ pu, $\Delta T = 250$ ms (lower part) (ADN No 1)

the voltage recovery. They are not far from Gaussian distributions. The averages $\mu_P(j, k)$ and $\mu_Q(j, k)$, and the standard deviations $\sigma_P(j, k)$ and $\sigma_Q(j, k)$ are extracted at all times k .

3.3.2 Simulation results for ADN No 2 - uniform distributions of the parameters

The sub-figures of Fig. 3.2 show the randomized time evolution of P and Q entering the ADN No 2 in response to a voltage dip of depth $\Delta V_{tr} = 0.5$ pu and duration $\Delta T = 100$ ms. The explanation of the overall evolution is the same as for ADN No 1, since both system host components with the same model. However, the transient behaviour of P that follows the voltage recovery is different from that observed in ADN No 1. Indeed, the decrease in P appears to be slower. This can be explained by the larger amount of active power sacrificed during the voltage dip, since the initial IBG active power production is more important. The IBGs then ramp up their active power. This takes between 1.8 and 3.8 s to the various IBGs. Moreover, the effect of reactive current injection by IBGs during the fault is also more pronounced, as the reactive power flow Q reverses during the voltage dip (see Fig. 3.2b, where Q takes negative value).

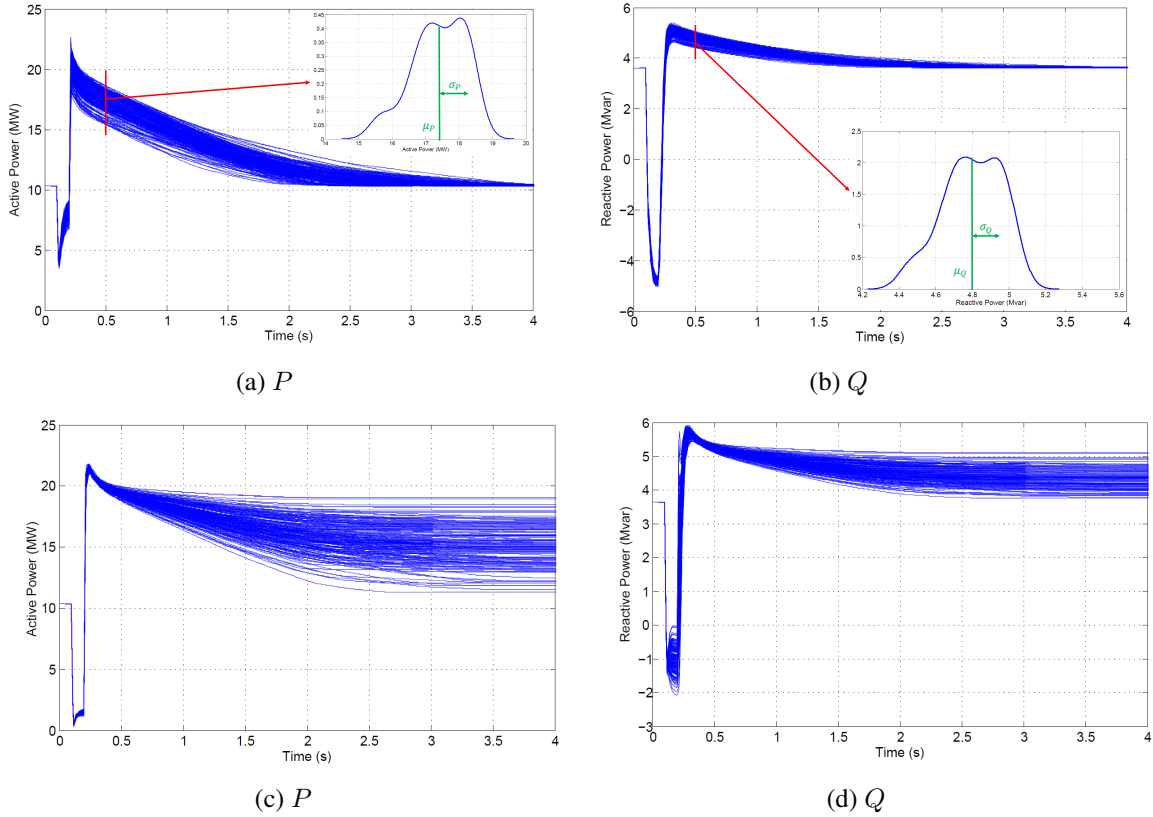


Figure 3.2: Randomized evolutions of P and Q in response to the voltage dip $\Delta V_{tr} = 0.5$ pu, $\Delta T = 100$ ms (upper part) and $\Delta V_{tr} = 0.8$ pu, $\Delta T = 100$ ms (lower part) (ADN No 2)

Figure 3.2 also shows the distribution of power values at $t = 0.5$ s with the corresponding values of μ_P , σ_P , μ_Q and σ_Q . Note that there are no “outliers” in the set of system responses. This justifies using the averages μ_P and μ_Q . If outliers were present, the median would provide a more robust representative evolution.

The lower part of Fig. 3.2 shows the evolutions of P and Q in response to the more severe disturbance. The large dispersion of final values results from the random disconnection of IBGs.

3.3.3 Simulation results for ADN No 3 - uniform distribution of the parameters

To show that the methodology easily accommodates other types of load components and other types of dispersed generators, we report in this section on simulation results with the Australian distribution system presented in Section 1.6.3. The latter hosts PV units and Synchronous Generators (SGs). Sample of simulation results are offered in the sequence.

Due to their size, location and monitoring, the SGs are considered to have accurately known

models and parameters. Therefore, their parameters are not randomized.

It is first assumed that the system has the following initial operating point. A single SG in operation produces 1 MW / 0.15 Mvar. The PV units operate at 50 % of their capacity, with unity power factor. The distribution grid feeds a total load of 18.2 MW. It receives a net power of 14.8 MW / 3.2 Mvar from the upper voltage level.

It is noteworthy that the simulations have considered a plausible future scenario with Australian distributed PV units obeying an updated grid code similar to IEEE std 1547-2018, as suggested in [Aus19b], with retro-fitting of existing units.

The upper sub-figures of Fig. 3.3 show the randomized time evolutions of respectively P and Q entering the distribution system, in response to a voltage dip of depth $\Delta V_{tr} = 0.3$ pu and duration $\Delta T = 250$ ms.

The overall evolution is explained as follows. During the voltage dip, the load with exponential model decreases while the PV units curtail their active current to leave room for reactive current injection. This, together with the additional reactive current injection from the SG, causes a reactive power flow reversal, as confirmed by Fig. 3.3b. The small active and reactive power oscillations after voltage recovery originate from the SG. When the voltage recovers its initial value, so do the powers of loads with exponential model, while the re-accelerating motors draw additional power. Furthermore, after voltage recovery, the PV units ramp up their active power, which has been partially sacrificed to leave room for reactive current injection. This takes between one and two seconds; the effect can be seen in Fig. 3.3a.

The plots also show the distributions of power values at $t = 0.5$ s, as well as the corresponding μ_P , σ_P , μ_Q and σ_Q values. The small dispersion of reactive power evolutions is explained by the fact that they are mainly influenced by the SG response, whose parameters have not been randomized.

Next, it is assumed that all eight SGs are in operation and produce all together 8 MW/1.5 Mvar. The initial load and PV production is the same as previously.

The lower sub-figures of Fig. 3.3 show the randomized time evolutions of respectively P and Q entering the distribution system, in response to a voltage dip of depth $\Delta V_{tr} = 0.3$ pu and duration $\Delta T = 250$ ms.

The most striking fact with respect to the case with one SG in operation is the oscillation of the active power after voltage recovery, originating from SGs rotor motion. Moreover, the additional reactive current injection by the SGs is more visible, causing an 8 Mvar reverse reactive power flow during the voltage dip (see Fig. 3.3d). The distribution of power values at $t = 0.5$ s and the corresponding μ_P , σ_P , μ_Q and σ_Q are also shown. With eight SGs in operation, the dispersion of

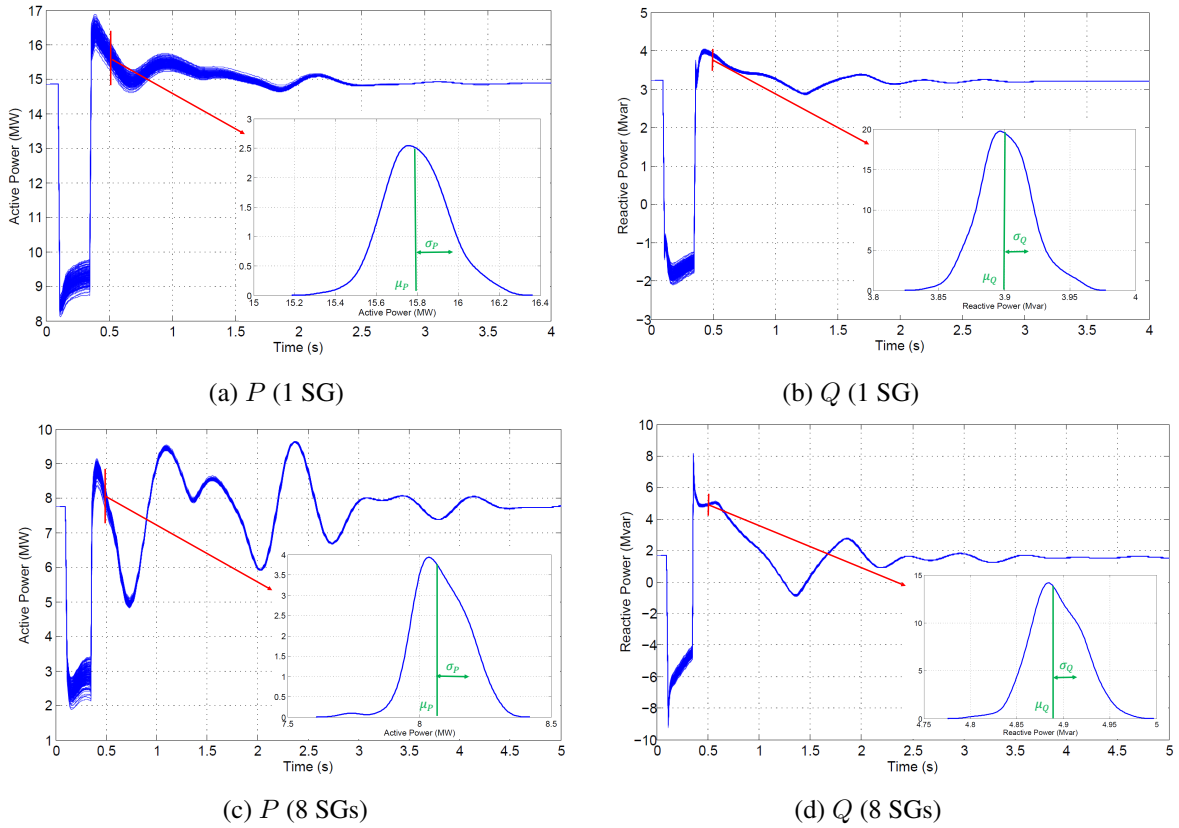


Figure 3.3: Randomized evolutions of P and Q with 1 SG connected (upper part) and 8 SGs connected (lower part); voltage dip $\Delta V_{tr} = 0.3$ pu, $\Delta T = 250$

active and reactive power values is significantly reduced, as the dynamic behaviour of the distribution system is now almost only governed by the SGs response, whose parameters have not been randomized.

The remaining of this section presents results obtained with Gaussian distributions of the parameters for ADN No 2.

3.3.4 Simulation results for ADN No 2 - Gaussian distributions of the parameters

MC simulations with randomized parameters obeying a Gaussian, instead of a uniform distribution are reported here. For coherency between the two cases, the Gaussian distribution of parameter p_i has its average set to $(p_i^{min} + p_i^{max})/2$ and its standard deviation to $(p_i^{max} - p_i^{min})/6$, where p_i^{min} (resp. p_i^{max}) is the lower (resp. upper) bound of the uniform distribution.

Figure 3.4 shows the randomized evolutions of the active power P and reactive power Q in response to a voltage dip of depth $\Delta V_{tr} = 0.5$ pu and duration $\Delta T = 100$ ms. The curves can

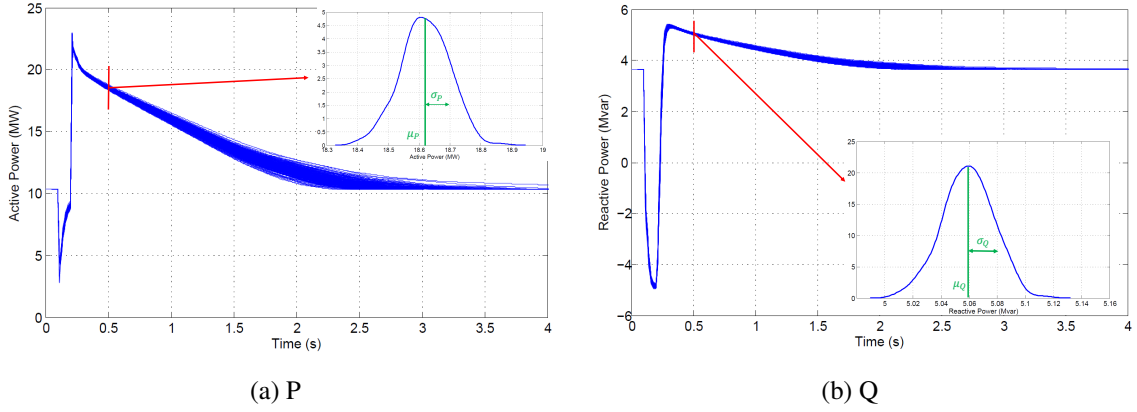


Figure 3.4: Gaussian randomized parameters: P and Q responses to the voltage dip $\Delta V_{tr} = 0.5$ pu, $\Delta T = 100$ ms (ADN No 2)

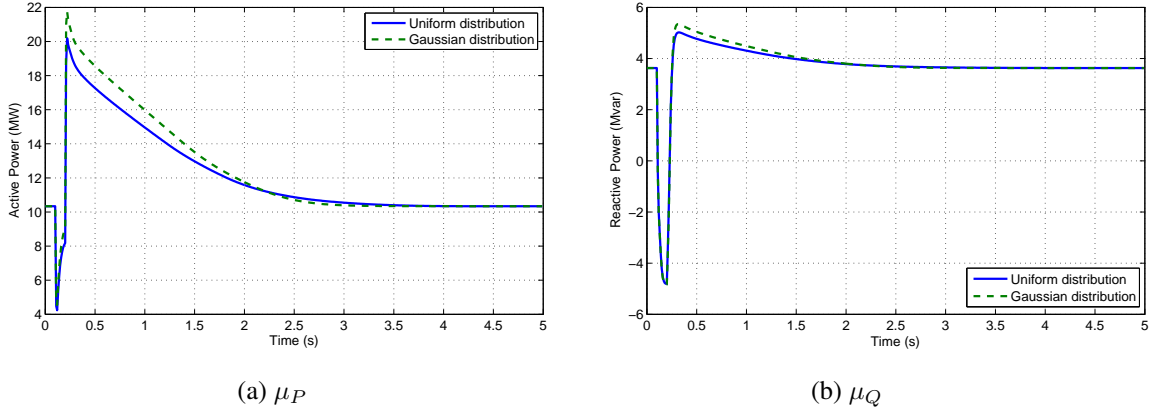


Figure 3.5: Evolutions of μ_P and μ_Q for uniform and Gaussian distributions of the parameters; voltage dip $\Delta V_{tr} = 0.5$ pu, $\Delta T = 100$ ms (ADN No 2)

be compared with those in Fig. 3.2. As expected, the responses are significantly less dispersed. Furthermore, the distributions of P and Q values at $t = 0.5$ s are closer to Gaussian ones.

Figure 3.5 shows, for the same disturbance, the evolution of μ_P and μ_Q for a uniform and a Gaussian distribution of parameters, respectively. The difference is marginal. Figure 3.6 shows the corresponding evolutions of σ_P and σ_Q . The difference between both distributions is pronounced over a 2-second time interval after the recovery of voltage. The Gaussian distribution yields smaller σ_P and σ_Q values, which confirms the smaller dispersion of the power responses.

All in all, whether the parameter distribution is Gaussian or uniform influences only marginally the average evolution. The difference lies more in the values of the evolutions σ_P and σ_Q . Due to the reduced uncertainty with respect to uniform distributions, standard deviations tend to have

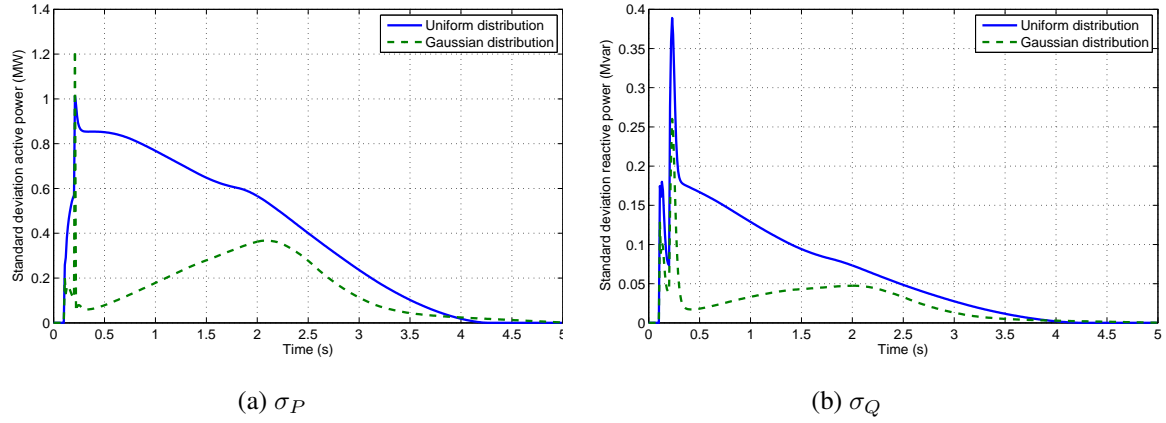


Figure 3.6: Evolutions of σ_P and σ_Q for uniform and Gaussian distributions of the parameters; voltage dip $\Delta V_{tr} = 0.5$ pu, $\Delta T = 100$ ms (ADN No 2)

much smaller values, especially following the voltage recovery. Similar conclusions can be drawn for ADN No 1 and 3.

Only uniform distributions of the randomized parameters will be considered in the rest of the thesis.

3.4 Extracting a representative parameters set

Instead of using μ_P and μ_Q to extract a representative response of the ADN (to be used later on to derive its equivalent), an alternative is to identify a representative instance of the ADN model. There is more than one interpretation of the term “representative”. It may depend on the type of study, it may not be the same for the distribution system operator as for the transmission one, or it may even be of interest to keep several representative simulations. In this work it has been chosen to : (i) select one dynamic response corresponding to one of the s parameter vectors $\mathbf{p}^{(i)}$, (ii) select the one closest to the average of the s responses.

Furthermore, the representative response should not be selected on the basis of a single disturbance, with the risk of over-fitting that particular scenario. Instead, d different disturbances are considered, and a single parameter vector \mathbf{p}^* is going to be extracted for all of them together.

Two methods were investigated to identify \mathbf{p}^* , the instance of \mathbf{p} which fulfills the above requirements.

3.4.1 First method

The average power responses are computed as ($j = 1, \dots, d; k = 1, \dots, n$) :

$$\mu_P^{(s)}(j, k) = \frac{1}{s} \sum_{i=1}^s P(\mathbf{p}^{(i)}, j, k) \quad (3.1)$$

$$\mu_Q^{(s)}(j, k) = \frac{1}{s} \sum_{i=1}^s Q(\mathbf{p}^{(i)}, j, k) \quad (3.2)$$

where n is the number of time steps in the simulation. \mathbf{p}^* is the parameter instance which yields the active and reactive power responses closest to the averages, over all disturbances. It is the solution of the discrete optimization :

$$\min_{\mathbf{p}^{(i)} \in \{\mathbf{p}^{(1)}, \dots, \mathbf{p}^{(s)}\}} \left\{ \sum_{j=1}^d \sum_{k=1}^n \left[P(\mathbf{p}^{(i)}, j, k) - \mu_P^{(s)}(j, k) \right]^2 + \sum_{j=1}^d \sum_{k=1}^n \left[Q(\mathbf{p}^{(i)}, j, k) - \mu_Q^{(s)}(j, k) \right]^2 \right\}. \quad (3.3)$$

3.4.2 Second method

Alternatively, \mathbf{p}^* can be directly identified as the parameter instance that yields the response to which the other responses have minimal dispersion. This amounts to solving :

$$\min_{\mathbf{p}^{(i)} \in \{\mathbf{p}^{(1)}, \dots, \mathbf{p}^{(s)}\}} \left\{ \sum_{\substack{\ell=1 \\ \ell \neq i}}^s \sum_{j=1}^d \sum_{k=1}^n \left[P(\mathbf{p}^{(i)}, j, k) - P(\mathbf{p}^{(\ell)}, j, k) \right]^2 + \sum_{\substack{\ell=1 \\ \ell \neq i}}^s \sum_{j=1}^d \sum_{k=1}^n \left[Q(\mathbf{p}^{(i)}, j, k) - Q(\mathbf{p}^{(\ell)}, j, k) \right]^2 \right\}. \quad (3.4)$$

3.4.3 Simulation results

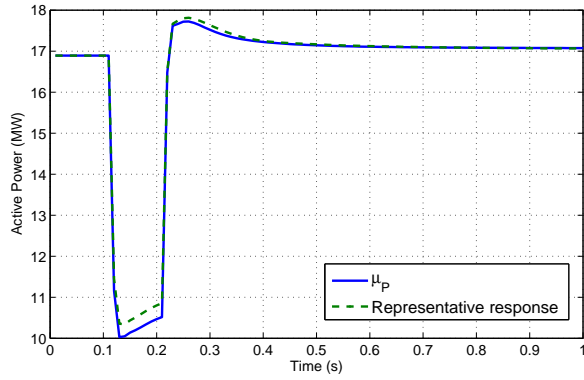
Both methods were applied to extract the \mathbf{p}^* parameter vector for ADN No 1 and ADN No 2. The $d = 14$ disturbances considered are listed in Table 3.2. Both methods turned out to identify the same parameter vector \mathbf{p}^* .

For ADN No 1, the corresponding active and reactive power evolutions are shown in Figs. 3.7 and 3.8 together with the averages μ_P and μ_Q for disturbances No 3 and 10, respectively. It can be seen that the curves coincide very well.

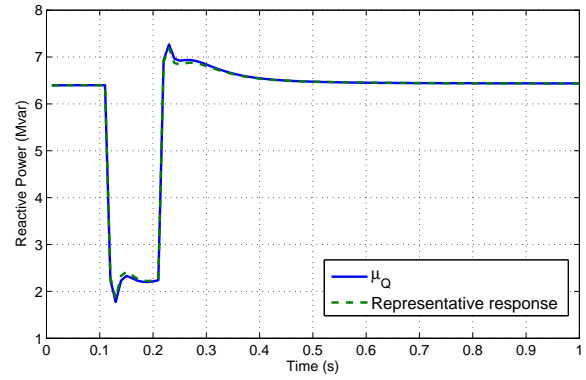
Table 3.2: Disturbances considered to extract p^*

disturb. No	ΔV_{tr} (pu)	ΔT (s)
1	0.2	0.10
2	0.2	0.25
3	0.3	0.10
4	0.3	0.25
5	0.4	0.10
6	0.4	0.25
7	0.5	0.10
8	0.5	0.25
9	0.6	0.10
10	0.6	0.25
11	0.7	0.10
12	0.7	0.25
13	0.8	0.1
14	0.8	0.25

Similarly, for ADN No 2, the active and reactive power evolutions together with the averages μ_P and μ_Q are shown in Figs. 3.9 and 3.10 in response to disturbances No 7 and 13, respectively. Again, the curves coincide well, despite a small difference for the active power response to disturbance No 7 (see Fig. 3.9a). The reason lies in the choice of multiple disturbances to extract the representative set of parameters p^* . The latter satisfies in the best possible way all d time responses, but no one in particular.

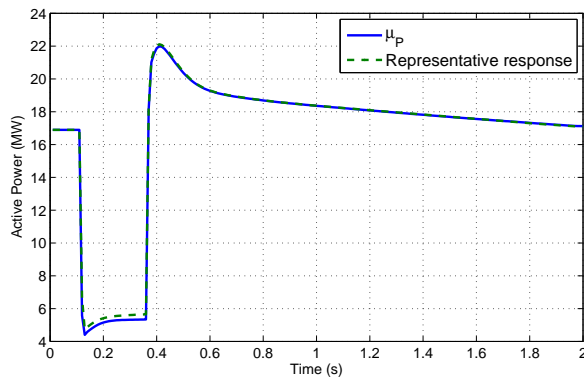


(a) Active Power

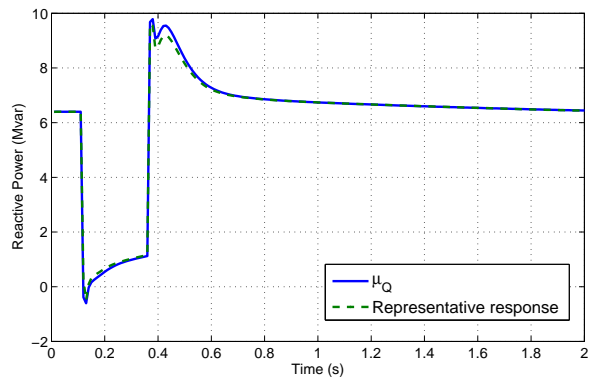


(b) Reactive power

Figure 3.7: Average powers μ_P and μ_Q and response given by the methods of Section 3.4.1 and 3.4.2 ; disturbance No 3 (ADN No 1)

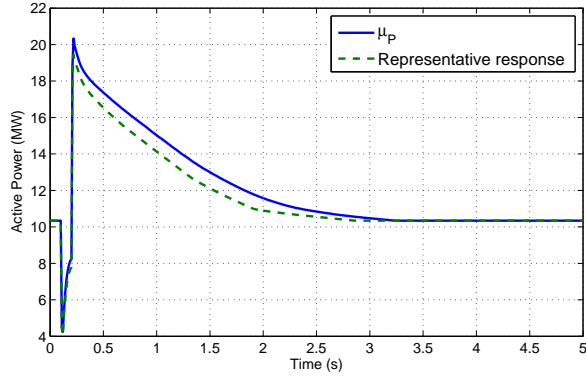


(a) Active Power

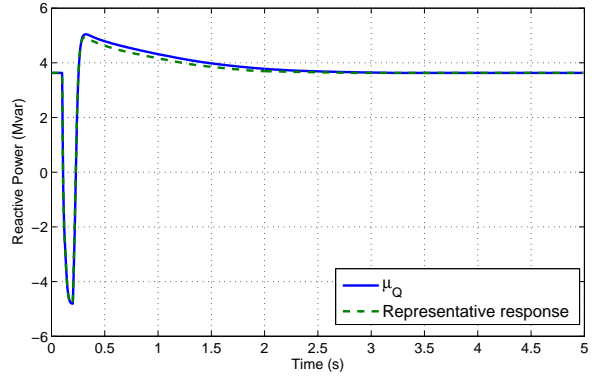


(b) Reactive power

Figure 3.8: Average powers μ_P and μ_Q and response given by the methods of Section 3.4.1 and 3.4.2 ; disturbance No 10 (ADN No 1)

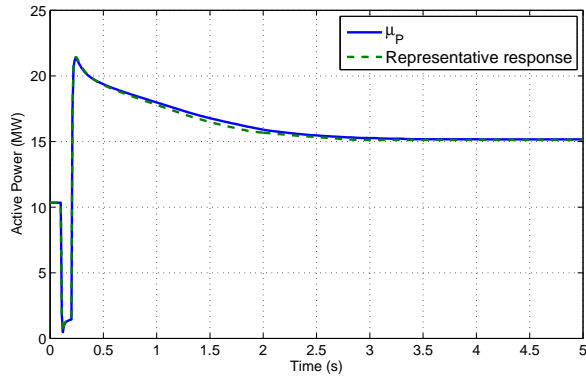


(a) Active Power

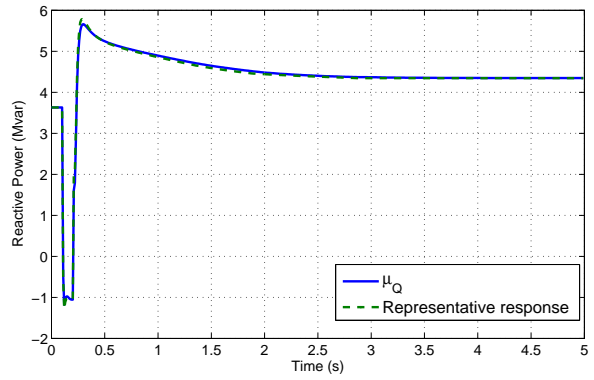


(b) Reactive power

Figure 3.9: Average powers μ_P and μ_Q and response given by the methods of Section 3.4.1 and 3.4.2 ; disturbance No 7 (ADN No 2)



(a) Active Power



(b) Reactive power

Figure 3.10: Average powers and the responses closest to these averages ; disturbance No 13 (ADN No 2)

3.5 Choosing the number of MC simulations

One of the issues often quoted with MC simulations is the proper choice of their number. This is a compromise between representativity of the sample and computational burden. Keeping in mind that the purpose is to extract the reference values μ_P and μ_Q , MC simulations can be stopped when those values stop varying significantly with the growing value of s [CPVCss]. The detailed procedure is as follows.

1. Initialize: $s = s_o, g = 0$
2. draw at random an initial set of s_o parameter vectors $(\mathbf{p}^{(1)}, \dots, \mathbf{p}^{(s_o)})$
3. for each parameter vector, simulate the ADN response to each of the d disturbances
4. compute the average power responses $\mu_P^{(s)}(j, k)$ and $\mu_Q^{(s)}(j, k)$
5. generate a new random parameter vector $\mathbf{p}^{(s+1)}$
6. for this parameter vector, simulate the ADN response to the d disturbances
7. compute the new average power responses $\mu_P^{(s+1)}(j, k)$ and $\mu_Q^{(s+1)}(j, k)$
8. compare them with the previous averages by computing the Euclidean distance over all the disturbances :

$$\varepsilon = \sqrt{\varepsilon_P^2 + \varepsilon_Q^2} \quad (3.5)$$

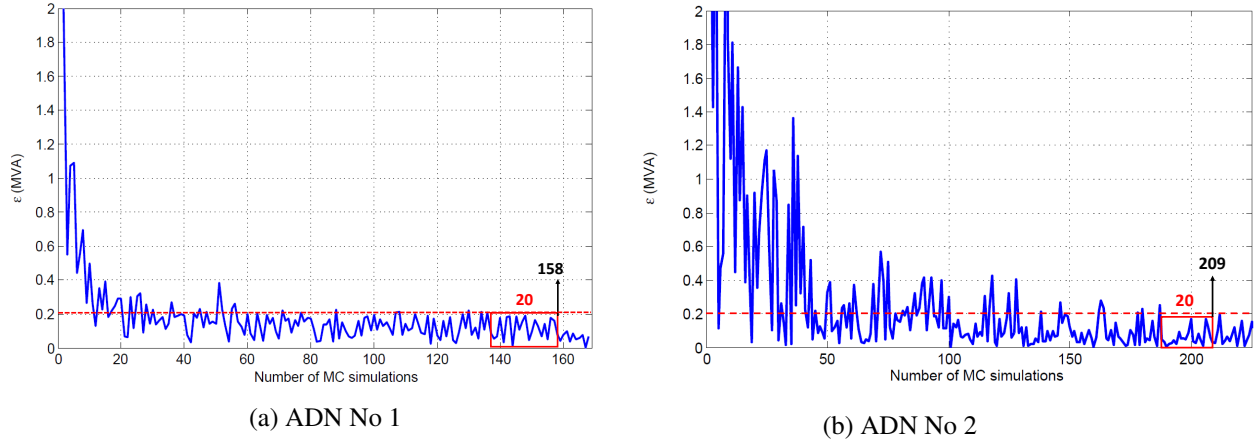
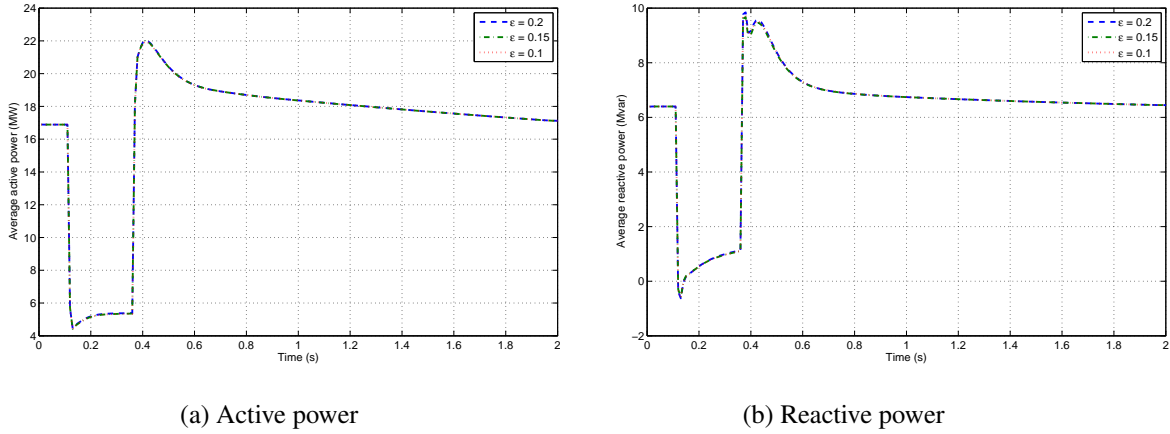
$$\text{with } \varepsilon_P^2 = \frac{1}{dn} \sum_{j=1}^d \sum_{k=1}^n \left[\mu_P^{(s+1)}(j, k) - \mu_P^{(s)}(j, k) \right]^2 \quad (3.6)$$

$$\varepsilon_Q^2 = \frac{1}{dn} \sum_{j=1}^d \sum_{k=1}^n \left[\mu_Q^{(s+1)}(j, k) - \mu_Q^{(s)}(j, k) \right]^2 \quad (3.7)$$

9. if $\varepsilon \leq \delta$ then $g \rightarrow g + 1$; else $g = 0$
10. If $g = g_{max}$ then stop; else increment $s \rightarrow s + 1$ and go to Step 5.

In this algorithm, $\mu_P^{(s)}(j, k)$ is the value of $\mu_P(j, k)$ computed over the first s MC simulations, and similarly for reactive power.

An example of variation of ε with s is given in Fig. 3.11, for $s_o = 1$. It was chosen to stop MC simulations when ε remains smaller than 0.2 MVA for 20 successive values of s (i.e. $\delta = 0.2$ and $g_{max} = 20$). Results are given in Fig. 3.11a for ADN No 1 and Fig 3.11b for ADN No 2. Comparing both figures, the more striking fact is the faster decrease of ε for ADN No 1. It appears

Figure 3.11: Evolution of ε with s (14 disturbances of Table 3.2)Figure 3.12: Evolution of μ_P and μ_Q for different values of ε ; disturbance No 10 (ADN No 1)

that 158 instances are sufficient for ADN No 1, while 209 instances are required for ADN No 2. This results from the fact that ADN No 2 hosts significantly more large IBGs than ADN No 1 and the random variation of IBG parameters have a strong impact on the dynamic responses and, hence, on their average.

The value of ε is a compromise between representativity of the sample and computational burden. For instance, when decreasing ε to 0.15 MVA (resp. 0.1 MVA) s increases to 219 (resp. 304) for ADN No 1 and 260 (resp. 320) for ADN No 2. The corresponding time evolutions of μ_P and μ_Q are shown in Fig. 3.12 (resp. Fig. 3.13), relative to disturbance No 10 and ADN No 1 (resp. disturbance No 7 and ADN No 2). For both ADNs, there is clearly no gain of accuracy in setting ε lower than 0.2 MVA.

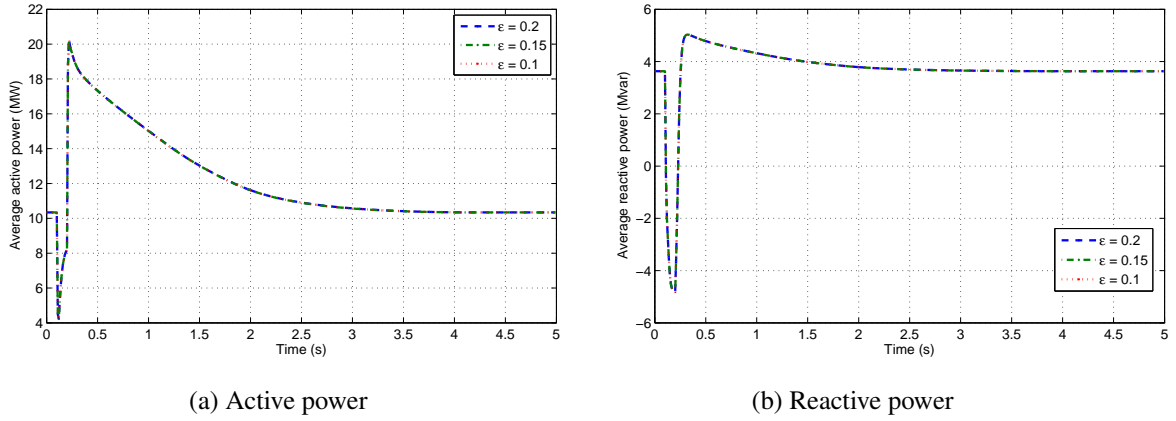


Figure 3.13: Evolution of μ_P and μ_Q for different values of ε ; disturbance No 7 (ADN No 2)

3.6 Summary

This chapter has proposed a methodology to take into account the uncertainty affecting dynamic behaviours of ADN components. The latter involves MC simulations. From randomized time evolutions, statistics such as the average and the standard deviation are extracted. The latter will be used to account for the impact of uncertain parameters when deriving the ADN equivalent. The difference between uniform and Gaussian distributions of the uncertain parameters has been analyzed. As an alternative to those statistics, a method to extract a representative parameter set has also been outlined. It yields representative dynamic responses very close to those given by μ_P and μ_Q . Finally, the simple procedure adopted to select the number of MC simulations has been presented.

Note that, in the remaining of the report, the average power responses μ_P and μ_Q are preferred as reference for the derivation of the equivalent rather than the response of a single representative instance of the ADN model.

Chapter 4

ADN equivalent: structure, modelling and parameter identification

This chapter is the core of the thesis. It deals with a methodology for the identification of reduced-order ADN models, for a single operating point. The approach involves several steps detailed in this chapter.

The material is organized as follows. Section 4.1 offers an overview of the approach. Additional features included in ADN equivalent models as well as typical topologies are presented in Section 4.2. Section 4.3 details the least-square identification of the reduced model parameters while Section 4.4 describes the optimization algorithm that has been used to solve the minimization problem. Sections 4.5 and 4.6 respectively, present procedures to select disturbances and to discard “non-significant” parameters. The initialization of the equivalent is briefly explained in Section 4.7. Section 4.8 gives an overview of the simulation results and in the next three sections, the methodology is applied to the test systems presented in Chapter 1 and already considered in Chapter 3. Section 4.12 gives an overview of the achieved model complexity reduction for each ADN. Finally, Section 4.13 summarizes the chapter material.

4.1 Approach and overview

After extracting statistics from MC simulations of detailed ADN models, the next step consists of deriving reduced-order models of these ADNs.

A well-known identification procedure consists of adjusting the parameters of the reduced model to approach in the least-square sense the response of the unreduced, detailed system. In order to account for uncertainty, the approach considered in this thesis consists of: (i) using the average of

the randomized MC simulations as reference, and (ii) weighting the deviations with respect to the latter to account for the dispersion observed in MC simulations.

The number of parameters to adjust should be kept “as small as possible”, to make the least-square minimization less demanding, but also the parameter values more consistent from one case to another and, hence, easier to interpret [L. 99]. To that purpose, a method inspired of the Least Absolute Shrinkage and Selection Operator (LASSO) has been adopted to discard from the identification the parameters with a negligible impact. The original LASSO method was proposed for linear regression and presented in [Tib96]. In the power systems field, a nonlinear variant has been used in [RWR12] to reduce the number of parameters of an induction motor and in [RL17] for improving parameter estimation of a synchronous machine.

Another distinctive feature of the procedure proposed in this thesis is the training of the equivalent from multiple disturbances (in the transmission system). The main objective is to avoid over-fitting one particular scenario. This is one advantage of the simulation-based approach. Indeed, the risk of over-fitting is important when the parameters of an equivalent are adjusted based on measurements collected after a single event.

Since handling numerous disturbances can be demanding, a recursive procedure is proposed to select the smallest possible subset of disturbances, from which the parameters are identified. The procedure guarantees the accuracy of the equivalent with respect to disturbances not involved in the training.

4.2 Models in the dynamic equivalent

4.2.1 Network

The following assumptions are made regarding the distribution grid :

- it is three-phase;
- its operation is balanced;
- it is connected to the transmission system through a single bus.

As previously mentioned, the equivalent model adopted is of the grey-box type. It involves aggregated models of system components such as loads and IBGs. The originally distributed IBGs (resp. loads) are aggregated into equivalent IBGs (resp. loads). They can be differentiated according to their location in the grid, technical characteristics and/or voltage level. The aggregated components are placed behind equivalent impedances accounting for the network effects.

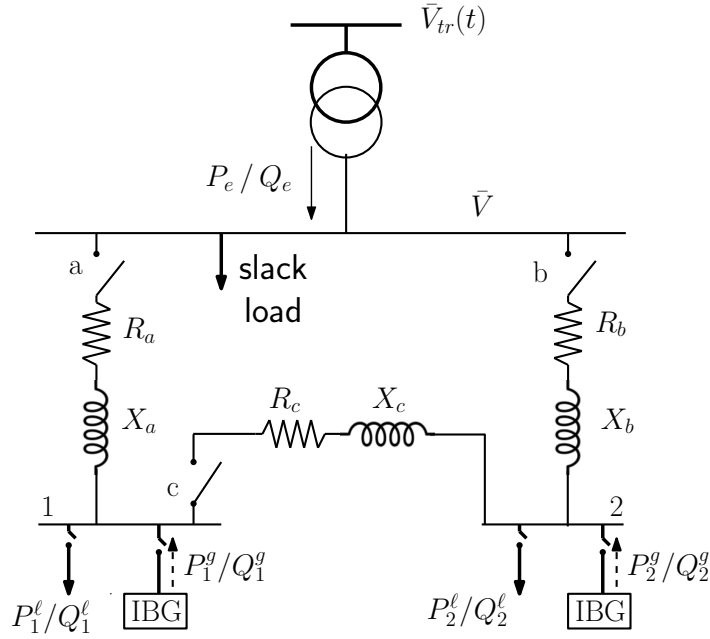


Figure 4.1: Possible topologies of the “grey-box” ADN equivalent

Figure 4.1 shows a structure of ADN equivalent that can accommodate various configurations. Three variants are considered, as summarized in Table 4.1.

In Variant 1, all loads are aggregated into one equivalent load and all IBGs in one equivalent IBG, both connected to bus 1 behind the equivalent impedance $R_a + jX_a$. Bus 2 and the other two impedances are not used.

Variant 2 is preferred if the loads and IBGs are located at very distinct places in the distribution grid. Bus 1, connected through the impedance $R_a + jX_a$, gathers the aggregated loads while bus 2, connected through $R_b + jX_b$, gathers the lumped IBGs. The third impedance is not used.

Variant 3 distinguishes between loads and IBGs connected at Medium Voltage (MV) and Low Voltage (LV) buses, respectively. The former are aggregated at bus 2, behind the impedance $R_b + jX_b$ accounting for the MV grid effects, while the latter are lumped at bus 1, connected to bus 2 through the impedance $R_c + jX_c$ accounting for the LV network effects.

4.2.2 Aggregated load

The model used for the aggregated load in the equivalent is the one used for individual loads in the original, unreduced ADN. It has been detailed in Section 2.2.

Table 4.1: Example of topologies for the equivalent (see Fig. 4.1)

	VARIANT 1	VARIANT 2	VARIANT 3
switch a	closed	closed	open
switch b	open	closed	closed
switch c	open	open	closed
P_1^ℓ/Q_1^ℓ	lumped load	lumped load	load at LV level
P_1^g/Q_1^g	lumped IBG	-	IBG at LV level
P_2^ℓ/Q_2^ℓ	-	-	load at MV level
P_2^g/Q_2^g	-	lumped IBG	IBG at MV level

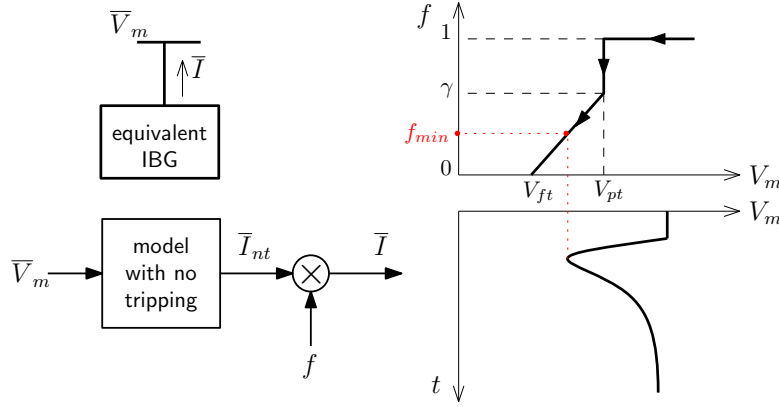


Figure 4.2: Simple under-voltage partial tripping feature of the aggregated IBG

4.2.3 Aggregated IBG

Similarly, the model used for the aggregated IBG retains the features of the model detailed in Section 2.3. However, the aggregated model must account for the possible tripping of *some* IBGs in the original distribution system.

The voltages being different from one IBG bus to another, during a fault, some units may trip while the others remain connected. Since we consider a single aggregated IBG, the aforementioned situation is accounted by providing the aggregated IBG with a “partial tripping” feature, instead of the LVRT characteristic, detailed in Fig. 2.8. As sketched in Fig. 4.2, it consists of multiplying the output current \bar{I}_{nt} given by the model without tripping by a factor f ($0 < f < 1$) evolving as depicted in the right part of Fig. 4.2. When the measured voltage V_m of the equivalent IBG falls below the V_{pt} threshold, f drops to γ , which corresponds to losing a fraction $1 - \gamma$ of the IBGs. For further voltage drops, f decreases linearly with V_m . Full disconnection ($f = 0$) takes place for $V_m = V_{ft}$. If V_m recovers before reaching V_{ft} (as shown in Fig. 4.2) f remains at the f_{min}

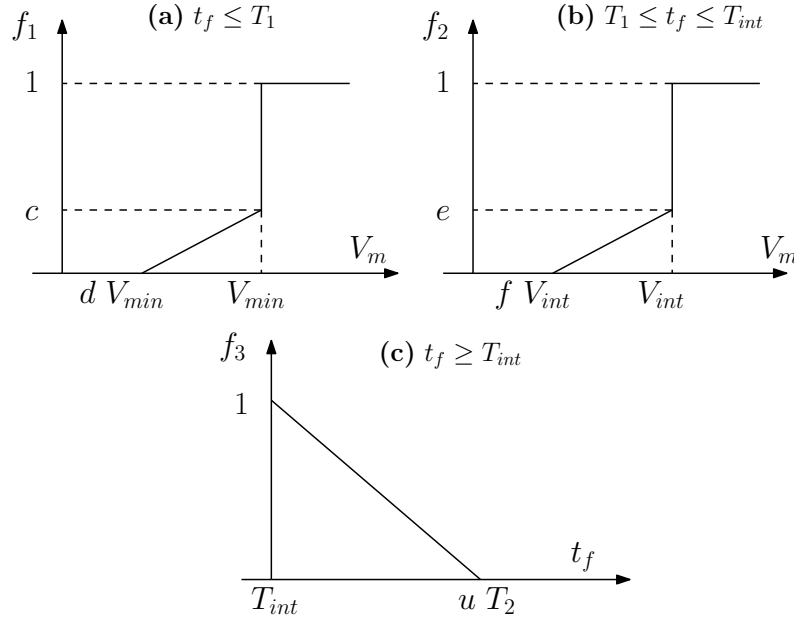


Figure 4.3: More elaborated partial tripping feature of the aggregated IBG

value corresponding to the voltage nadir. The parameters γ , V_{pt} and V_{ft} have to be identified. This technique bears some similarity with the one used in [PWR⁺].

While only the tripping of IBGs during voltage dips is considered in this thesis, the tripping of units taking place after fault clearing could be taken into account using the following, more elaborate partial tripping model [CPVC].

Let us define t_f as the time during which the terminal voltage V_m stays below the V_r threshold defined in Fig. 2.8. Partial tripping is reflected by multiplying the unit output current by :

$$F = f_1 f_2 f_3 \quad \text{with} \quad 0 \leq f_1, f_2, f_3 \leq 1$$

where f_1 , f_2 and f_3 relate to the three time intervals considered hereafter (the symbols are defined in Fig. 2.8).

1st case: $t_f \leq T_1$

f_1 varies with V_m as shown in Fig. 4.3a, where $0 \leq c, d \leq 1$. It is assumed that a fraction $1 - c$ of the units trips as soon as V_m drops below V_{min} , while the remaining units are progressively disconnected as V_m further drops, as shown by the inclined part of the curve. f_1 remains at its minimal value.

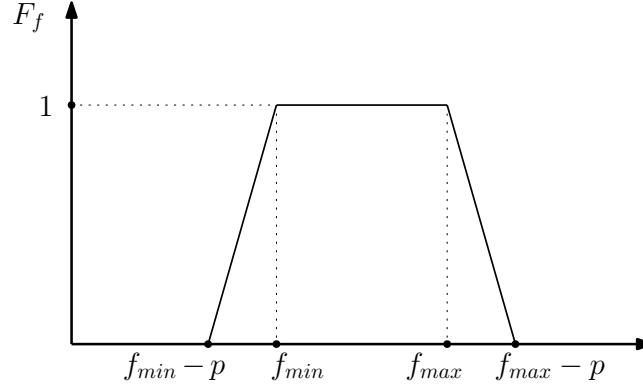


Figure 4.4: Partial tripping feature of the aggregated IBG in response to frequency deviations

2nd case: $T_1 < t_f \leq T_{int}$

In this case, tripping will take place if $V_m < V_{int}$. The factor f_2 varies with V_m as shown in Fig. 4.3b, similar to Fig. 4.3a, but with V_{int} substituted to V_{min} and (e, f) to (c, d) . f_2 remains at its minimal value.

3rd case: $T_{int} < t_f$

In post-fault conditions, tripping may take place due to slow voltage recovery. This is reflected by f_3 which decreases linearly with $t_f - T_{int}$ as shown in Fig. 4.3c, involving the additional parameter u , with $T_{int}/T_2 < u \leq 1$. f_3 remains at its minimal value.

Note that f_1 , f_2 and f_3 stop varying after the voltage V_m has recovered above V_r , considering that the IBGs are not reconnected.

The above model involves five parameters (namely c, d, e, f and u) to be identified, i.e. two additional parameters with respect to the simple model described in Fig. 4.2. For instance, it could be used for distribution grids hosting large industrial motors causing delayed voltage recovery [LPPO⁺18], due to their re-acceleration after fault clearing.

The model can also be extended in order to account for the tripping of IBGs in response to a large frequency deviation. A multiplier is also used, as in Fig. 4.2, but with the frequency dependency explained hereafter.

The current multiplier based on frequency deviation is computed according to the characteristic shown in Fig. 4.4 and inspired from [MG14b]. Once the frequency f computed by the PLL of the equivalent IBG is out of a specified range $[f_{min} \ f_{max}]$, the IBG current is reduced according to a ramp characterized by the parameter p . The latter accounts for the variability in frequency measurements of individual PLLs.

4.3 Weighted least-square identification

The equivalent is tuned so that its responses to disturbances match the average response of the randomized unreduced system considered in Chapter 3.

The parameters to identify are grouped in a vector θ . The latter is adjusted so that, for each discrete time k and for all disturbances j , the active power $P_e(\theta, j, k)$ (resp. the reactive power $Q_e(\theta, j, k)$) entering the equivalent (see Fig. 4.1) approaches in the least square sense the average $\mu_P(j, k)$ (resp. $\mu_Q(j, k)$) obtained from MC simulations.

Thus the following constrained optimization is considered :

$$\min_{\theta} F(\theta) = \frac{1}{d} \sum_{j=1}^d [F_P(\theta, j) + F_Q(\theta, j)] \quad (4.1)$$

$$\text{where } F_P(\theta, j) = \frac{1}{N} \sum_{k=1}^N \left[\frac{P_e(\theta, j, k) - \mu_P(j, k)}{\sigma_P(j, k)} \right]^2 \quad (4.2)$$

$$F_Q(\theta, j) = \frac{1}{N} \sum_{k=1}^N \left[\frac{Q_e(\theta, j, k) - \mu_Q(j, k)}{\sigma_Q(j, k)} \right]^2 \quad (4.3)$$

$$\text{and with } \theta^L \leq \theta \leq \theta^U \quad (4.4)$$

where N is the number of discrete times of the simulation. The bounds θ^L and θ^U keep θ in realistic ranges of values.

Note that each term in (4.2) (resp. (4.3)) is weighted by the inverse of the variance $\sigma_P^2(j, k)$ (resp. $\sigma_Q^2(j, k)$) to reflect the dispersion of the MC responses. By so doing, at a given time k , the deviation from $\mu_P(j, k)$ (resp. $\mu_Q(j, k)$) is more penalized if the dispersion of the power response in the MC simulations is small. Conversely, at a time k when a large dispersion is observed, denoting a large impact of parameter uncertainty, the deviation of the equivalent from $\mu_P(j, k)$ (resp. $\mu_Q(j, k)$) is less penalized. Note that if $\sigma_P(j, k)$ or $\sigma_Q(j, k)$ becomes too small (when the system reaches a steady state), the subsequent times k are not included in (4.2, 4.3) to avoid distorting the minimization.

Alternatives to the objective function (4.1) are proposed and discussed in Appendix B.

4.4 Solving the optimization problem

An analytical expression of even the gradient of the objective function (4.1) being impossible to derive, standard mathematical programming methods cannot be envisaged to solve the least-square minimization problem (4.1)-(4.4). Instead, a metaheuristic, derivative-free optimization method has been preferred. Among the wide variety of metaheuristic methods, an evolutionary

algorithm, namely Differential Evolution (DE) [PSL05] has been preferred. The choice of DE was motivated by the comparison reported in [VT04], where it outperformed other algorithms on various benchmark problems. A systematic comparison with other methods - such as those used in [MF02], [MA13], [YZP07], [GRBP16] - was outside the scope of this research. While other algorithms could offer a most welcome speed-up, DE has been found to be a reliable solver for the optimization problem (4.1)-(4.4) in a very large number of cases.

The solver has been derived from the open source Python code available in [P. 18]. The version of the algorithm is denoted *rand/1/bin* because θ is randomly chosen and only one vector difference is added to it. The binomial crossover strategy was used to mix the information of the trial and the target vectors. The crossover factor (also called *mutation rate*), i.e. the probability that a parameter will be inherited from a mutant, has been chosen in the range $[0.9 \ 1]$ as it has shown to give better results. Moreover, at each new generation, the mutation factor is randomly selected in the range $[0.5 \ 1]$ as it has been found that this technique may improve convergence significantly [PSL05]. More information is available in [P. 18] as well.

Since the DE algorithm is iterative, a proper stopping criterion is important. It was found appropriate to stop iterating when, for all disturbances ($j = 1, \dots, d$) :

$$F_P(\theta, j) \leq 1 \text{ and } F_Q(\theta, j) \leq 1 \quad (4.5)$$

i.e. when the deviation of $P_e(\theta, j, k)$ from $\mu_P(j, k)$ (resp. $Q_e(\theta, j, k)$ from $\mu_Q(j, k)$) is smaller than $\sigma_P(j, k)$ (resp. $\sigma_Q(j, k)$) on average over discrete times k . Assuming that the distribution of power values is close to Gaussian (see Fig. 3.2 for instance), (4.5) guarantees that the response of the equivalent falls within the 70 % of power evolutions located around the average.

Yet a maximum number of DE iterations is enforced in case (4.5) is not satisfied.

4.5 Recursive training

The larger the number d of disturbances, the lower the risk to over-fitting but the larger the computational burden to solve the minimization problem (4.1)-(4.4). To tackle this problem, a recursive procedure has been devised, which consists of focusing on a subset of disturbances from which the parameters are identified. More precisely, “training” disturbances are progressively added, until the equivalent is found sufficiently accurate with respect to all other, non-trained disturbances. The detailed procedure is as follows :

1. A set of c candidate disturbances is initially defined. For each disturbance, MC simulations are performed and the time-varying averages $\mu_P(j, k)$, $\mu_Q(j, k)$ and standard deviations $\sigma_P(j, k)$, $\sigma_Q(j, k)$ are collected (see Chapter 3).

2. A small subset of disturbances is selected for the initial training : $d := d_0 << c$.
3. The minimization problem (4.1)-(4.4) is solved, with the stopping criterion (4.5), yielding the solution $\hat{\theta}$. The following worst scores are determined :

$$F_P^{max}(\hat{\theta}) = \max_{j=1,\dots,d} F_P(\hat{\theta}, j) \quad (4.6)$$

$$F_Q^{max}(\hat{\theta}) = \max_{j=1,\dots,d} F_Q(\hat{\theta}, j) \quad (4.7)$$

4. With that value $\hat{\theta}$, the scores $F_P(\hat{\theta}, i)$ and $F_Q(\hat{\theta}, i)$ are computed for each non-trained disturbance i .
5. If, for all of them :

$$F_P(\hat{\theta}, i) \leq \max(1, F_P^{max}(\hat{\theta})) \quad (4.8)$$

$$F_Q(\hat{\theta}, i) \leq \max(1, F_Q^{max}(\hat{\theta})), \quad (4.9)$$

then, the procedure stops; else, the disturbance with the largest value of $F_P(\hat{\theta}, i)$ is added to the training set and similarly for the one with the largest value of $F_Q(\hat{\theta}, i)$, unless it is the same disturbance. d is increased by 1 or 2, accordingly.

6. Steps 3 to 5 are repeated using the last value $\hat{\theta}$ as initial guess in the minimization.

The right-hand side in (4.8) and (4.9) is justified as follows. If the worst scores of the trained disturbances do not satisfy the tolerance of 1 specified in (4.5), that tolerance is also relaxed for the non-trained disturbances.

4.6 Discarding non significant parameters

As mentioned at the beginning of the chapter, a procedure that bears the spirit of the LASSO method is used to discard the less significant parameters of the least-square minimization, for higher computational efficiency, better consistency and easier interpretation of the results.

The method consists of adding a penalty term to (4.1) as follows :

$$\min_{\theta} F(\theta) + \lambda \sum_{l=1}^n |\theta_l^{ref} - \theta_l| \quad (4.10)$$

where λ is a scaling factor, n is the size of θ and θ^{ref} is a reference value for the parameters. The penalty term tends to make θ_l depart from its θ_l^{ref} reference only if this yields a significant decrease of $F(\theta)$, i.e. if θ_l has a significant influence on $F(\theta)$, thereby making the dynamic response of the equivalent more accurate.

The procedure starts with λ set to a large value λ_0 , which yields $\hat{\theta} \simeq \theta^{ref}$. Then, λ is decreased steps by steps (namely divided by an integer a larger than one at each step). For each value, the minimization problem (4.1)-(4.4) is solved with the penalty term added as in (4.10). This procedure is repeated until the accuracy condition (4.5) is satisfied.

At this point, the components of $\hat{\theta}$ and θ^{ref} are compared. For the l -th component ($l = 1, \dots, n$), if :

$$\frac{|\hat{\theta}_l - \theta_l^{ref}|}{\theta_l^{ref}} \leq \delta \quad (4.11)$$

where δ is a small tolerance, the parameter of concern is considered to have little impact, since constraining θ_l to remain close to its reference θ_l^{ref} has little impact on the final scores $F_P(\hat{\theta}, j)$ and $F_Q(\hat{\theta}, j)$.

A non significant parameter is given the estimated value (i.e. $\theta_l = \hat{\theta}_l$), and is removed from θ .

By default, θ^{ref} is set to the middle of the interval in which the parameters of the equivalent vary (see (4.4)), i.e. :

$$\theta^{ref} = \frac{\theta^L + \theta^U}{2}. \quad (4.12)$$

For the significant parameters, the estimated value $\hat{\theta}_l$ is used to update the limits in (4.4) :

$$\theta_l^L = \hat{\theta}_l - \alpha \hat{\theta}_l \quad (4.13)$$

$$\theta_l^U = \hat{\theta}_l + \alpha \hat{\theta}_l \quad (4.14)$$

where $0 \leq \alpha \leq 1$. The recursive procedure of Section 4.5 is then applied with the original objective function (4.1).

Remark. It may happen that a parameter θ_l impacts the dynamic response of the equivalent, but remains close to its reference value θ_l^{ref} , because the latter happens to be near optimal. Therefore, it would be more accurate to state that the method identifies parameters whose variations from their reference values improve the dynamic response of the equivalent. Note, however, that if a parameter θ_l is unduly labeled as non significant, this has limited consequence on accuracy since it is set to its near optimal value θ_l^{ref} .

4.7 Initialization of equivalent

With reference to Fig. 4.1, the initial load active and reactive powers $P_1^\ell, Q_1^\ell, P_2^\ell$ and Q_2^ℓ are obtained by summing the corresponding dispersed load powers in the unreduced ADN. Similarly, P_1^g, Q_1^g, P_2^g and Q_2^g are obtained by summing the corresponding dispersed IBG powers.

Let us remind that the equivalent resistances R_a, R_b, R_c and reactances X_a, X_b, X_c are themselves components of the θ vector. Hence, the losses in those impedances change from one value of θ to another during the optimization. On the other hand, the values of the initial active (resp. reactive) power P_e (resp. Q_e) entering the ADN equivalent should not change with θ . Those values are typically forecasted or measured by the TSO and should be matched by the equivalent. Hence, to satisfy the power balance, a “slack” load is added, as shown in Fig. 4.1. This load, usually small [G. 18], is treated as a constant admittance for simplicity.

4.8 Overview of simulation results

The next sections present the simulation results for the three ADNs presented in Chapter 1.

Extensive tests have shown that the equivalent trained from voltage dips properly covers other types of disturbances, such as voltage oscillations or frequency variations. This will be illustrated in the sequel. The reverse is not true. The candidate training disturbances are thus voltage dips. They are listed in Table. 4.2. They are applied to all three systems.

For ADN No 1, all scenarios involve total disconnection of residential IBGs, since they have no LVRT capability, while large-capacity IBGs never disconnect from the grid. On the other hand, ADN No 2 hosts large (non-residential) IBGs and some of them trip under the effect of voltage drops. For ADN No 3, the partial tripping of IBGs is also taken into account.

4.9 Simulation results with ADN No 1

The ADN No 1 system has been introduced in Chapter 1 and its one-line diagram is shown in Fig. 1.9. As mentioned above, scenarios with partial tripping of large-capacity IBGs are not considered while the disconnection of residential IBGs is taken into account.

4.9.1 Topology and parameters of the equivalent

The topology of the equivalent of ADN No 1 is shown in Fig. 4.5. It corresponds to Variant 3 in Table 4.1, with $R_b + jX_b$ accounting for the MV grid, and $R_c + jX_c$ for the LV networks. The aggregated load and IBG attached to bus 1 account for residential loads and small-capacity IBGs while those attached to bus 2 relate to industrial loads and large-capacity IBGs.

The full set of parameters to identify is as follows (see Table 3.1 for their counterparts in the unreduced models) :

Table 4.2: Candidate disturbances for the identification of ADN equivalents

disturb. No	ΔV_{tr} (pu)	ΔT (s)
1	0.2	0.10
2	0.2	0.25
3	0.3	0.10
4	0.3	0.25
5	0.4	0.10
6	0.4	0.25
7	0.5	0.10
8	0.5	0.25
9	0.6	0.10
10	0.6	0.25
11	0.7	0.10
12	0.7	0.25
13	0.8	0.1
14	0.8	0.25

- for the LV and MV aggregated load : α and β of the exponential model and, for the motor, the stator and rotor resistances R_s and R_r , the magnetizing inductance L_{sr} , the two leakage reactances $(L_{ss} - L_{sr})$ and $(L_{rr} - L_{sr})$, the inertia constant H and the load factor LF ;
- for the aggregated IBG at bus 2 : the nominal current I_{nom} , the maximum rate of recovery of the active current $(\frac{dip}{dt})_{max}$, the slope k_{RCI} and V_{S1} threshold (see Fig. 2.9);
- for the network equivalent impedances : R_b, R_c, X_b and X_c .

This leads to a total of 26 parameters in θ .

Note that the parameters of the aggregated IBG attached to bus 1 accounting for small, residential LV installations are not included in θ since it immediately trips for all considered disturbances; hence, its parameters have no influence on the dynamic response of the system.

Moreover, while the IBG nominal current I_{nom} parameter was not randomized in the MC simulations of the unreduced system (see Section 3.2), when dealing with the equivalent, it is included in θ . Indeed, further simulations (not reported here) have shown that slightly adjusting this parameter can significantly improve the accuracy of the equivalent.

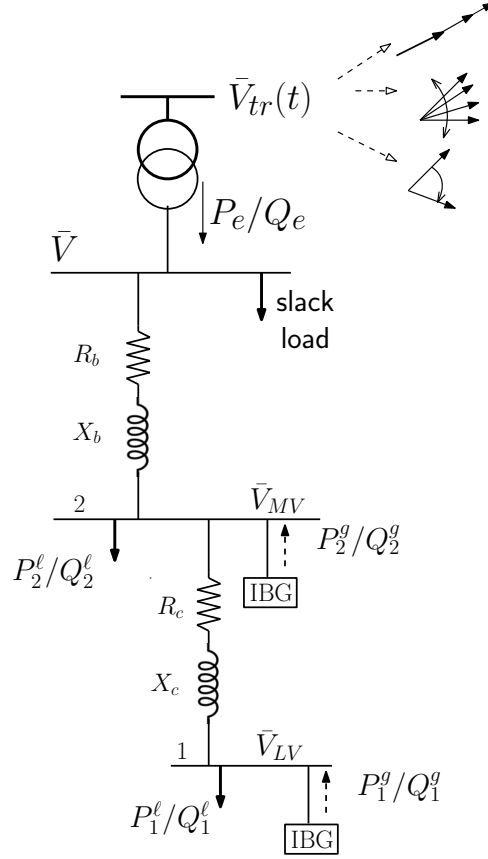


Figure 4.5: Topology of the equivalent (ADN No 1)

4.9.2 Steps of the reduced model identification

The bounds θ^L and θ^U of the search interval in (4.4) have been set to plausible values of the corresponding parameters, similar to the range of variations in Table 3.1, inspired of the literature (e.g. [C. 94]) or grid codes.

The equivalent is identified in three steps :

1. the equivalent impedances $R_b + jX_b$ and $R_c + jX_c$ have been first estimated using a network reduction technique. Then, the DE algorithm is let to adjust R_b , X_b , R_c and X_c in intervals centered on those initial estimates.
2. parameters with low or little influence on the accuracy of the equivalent have been discarded by the method of Section 4.6. Among the 26 parameters, 16 have been discarded;
3. the 10 remaining parameters have been optimized by the recursive training algorithm of Section 4.5.

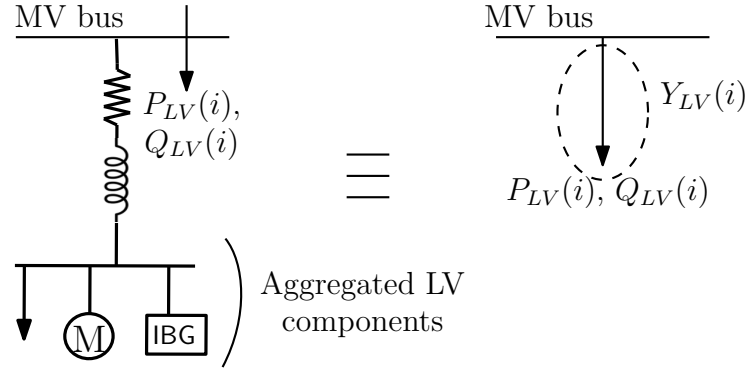


Figure 4.6: Network reduction technique : Equivalent admittance of an MV bus to which aggregated LV components are connected behind an equivalent LV impedance

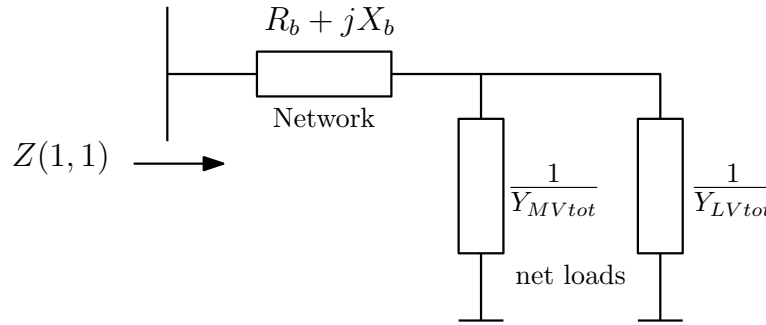


Figure 4.7: Network reduction technique : Estimation of the reference value of the equivalent impedance $R_b + jX_b$ (ADN No 1)

4.9.3 Step 1: Estimation of the network equivalent impedances

The LV impedances of the unreduced ADN are equivalent impedances accounting for LV feeders and transformers (see Fig. 1.9). Their values have been randomized in the MC simulations in realistic ranges of values. Therefore the equivalent LV impedance is initially set to the middle of this interval of variation.

While it is rather easy to choose the intervals $[\theta^L \ \theta^U]$ for the dynamic model parameters (of the load and IBG), it is less the case for the equivalent impedance $R_b + jX_b$ (see Fig.4.5). Instead, a network reduction technique has been used to obtain the θ^{ref} value, as detailed hereafter.

Let us denote by \mathbf{Y}_{net} the nodal admittance matrix of the unreduced network, as shown in Fig. 1.9, but *without the main transformer*.

First, for each MV bus i , the net load (i.e. the consumption minus the generation) $P_{MV}(i) +$

$jQ_{MV}(i)$ is replaced by an admittance consuming the same power under the voltage $\bar{V}_{MV}(i)$:

$$Y_{MV}(i) = \frac{P_{MV}(i) - jQ_{MV}(i)}{|\bar{V}_{MV}(i)|^2}. \quad (4.15)$$

The same applies to the MV buses to which aggregated LV components are connected behind an equivalent LV impedance as shown in Fig. 4.6. In this case, we have :

$$Y_{LV}(i) = \frac{P_{LV}(i) - jQ_{LV}(i)}{|\bar{V}_{LV}(i)|^2}. \quad (4.16)$$

The nodal admittance matrix \mathbf{Y} of the combined network and net loads is obtained by adding the Y_{MV} and Y_{LV} values to the corresponding diagonal term, i.e. :

$$\mathbf{Y}(i, j) = \mathbf{Y}_{net}(i, j) \text{ for } i \neq j \quad (4.17)$$

$$\mathbf{Y}(i, i) = \mathbf{Y}_{net}(i, i) + Y_{MV}(i) + Y_{LV}(i). \quad (4.18)$$

The equivalent impedance seen from the entry point of the network, namely bus 1 in Fig. 1.9, is given by the corresponding diagonal term $\mathbf{Z}(1, 1)$ of the impedance matrix :

$$\mathbf{Z} = \mathbf{Y}^{-1}. \quad (4.19)$$

As shown in Fig. 4.7, $\mathbf{Z}(1, 1)$ is also the sought impedance $R_b + jX_b$ in series with two lumped impedances in parallel. $\frac{1}{Y_{MVtot}}$ and $\frac{1}{Y_{LVtot}}$ account for the total net MV and LV loads in parallel, respectively :

$$\frac{1}{Y_{MVtot}} = \frac{1}{\sum_i Y_{MV}(i)} \quad (4.20)$$

$$\frac{1}{Y_{LVtot}} = \frac{1}{\sum_i Y_{LV}(i)}. \quad (4.21)$$

The $R_b + jX_b$ impedance is thus obtained as :

$$R_b + jX_b = \mathbf{Z}(1, 1) - \frac{1}{Y_{MVtot} + Y_{LVtot}}. \quad (4.22)$$

4.9.4 Step 2: Identifying the significant parameters

The LASSO method has been used on disturbances No 8 and 11 (see Table. 4.2) as they yield the worst scores $F_P^{max}(\hat{\theta}^{ref})$ and $F_Q^{max}(\hat{\theta}^{ref})$ given by (4.6) and (4.7).

Figure 4.8 shows a plot of the objective function $F(\hat{\theta})$ vs. the penalty term $\sum_{l=1}^n |\theta_l^{ref} - \theta_l|$, for decreasing values of λ . As expected, while λ is decreased, the deviation of $\hat{\theta}$ with respect to θ^{ref} increases, and $F(\hat{\theta})$ decreases. At the point marked with a circle, corresponding to $\lambda = 0.25$, the accuracy criterion (4.5) is satisfied. The corresponding scores are $F_P^{max}(\hat{\theta}) = 0.58$ and $F_Q^{max}(\hat{\theta}) = 0.57$.

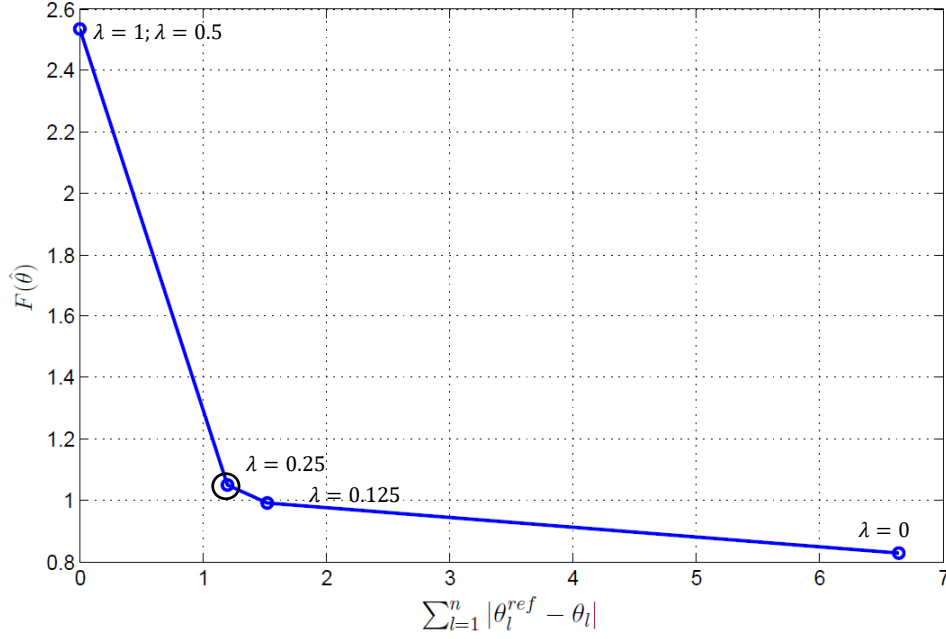


Figure 4.8: $F(\hat{\theta})$ vs. $\sum_{l=1}^n |\theta_l^{ref} - \theta_l|$ for decreasing values of λ (ADN No 1)

Figure 4.9 shows the relative differences defined in (4.11), for each of the 26 parameters. With a threshold $\delta = 5\%$, represented by the dashed red line, 10 parameters are identified as significant. These are :

- for the aggregated LV load: the exponents α, β of the exponential model;
- for the aggregated MV load: the rotor and stator resistances R_r and R_s , the leakage reactance ($L_{rr} - L_{sr}$) and the load factor LF ;
- for the aggregated IBG: the nominal current I_{nom} , the maximum rate of recovery of the active current $(\frac{di_p}{dt})_{max}$ and the slope k_{RCI} (see Fig. 2.9);
- for the equivalent network impedances: X_c . Note that the absence of R_c , R_b and X_b tends to confirm that the impedances estimated by network reduction were appropriate.

It can be seen that I_{nom} is retained as significant, which confirms that this parameter plays a significant role in the accuracy of the equivalent.

The validity of this approach has been verified as follows. The DE algorithm involving random changes of the variables, two separate executions may yield different values of $\hat{\theta}$. To assess this, the results of a set of separate executions of the DE algorithm have been compared, for the 26- and the 10-dimensional vectors θ , respectively. In the former case, some components $\hat{\theta}_l$ exhibit

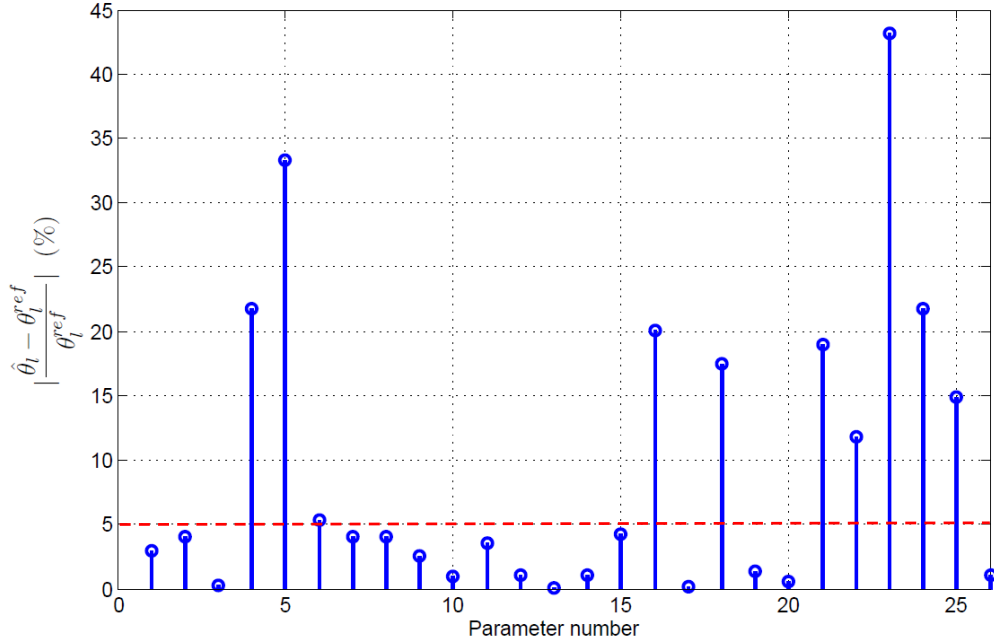
Figure 4.9: LASSO method: final values of $|\hat{\theta}_l - \theta_l^{ref}| / \theta_l^{ref}$ (in %) (ADN No 1)

Table 4.3: Results of recursive training algorithm (ADN No 1)

Iteration	Trained disturbances	trained disturbances		non trained disturbances	
		F_P^{max}	F_Q^{max}	F_P^{max}	F_Q^{max}
1	11, 8	0.58	0.57	24.37	0.57
2	11, 8, 2	0.88	0.92	4.32	0.93
3	11, 8, 13, 5	0.75	0.65	0.48	0.63

significant variations, making comparisons difficult. With the 10-dimensional vector, on the other hand, a much lower variability has been observed, i.e. the variations from one DE execution to another are insignificant. An illustration is provided in Fig. 4.10, showing 20 separate estimates of the exponent β of the aggregated LV load, labeled β_{LV} in the figure, when 26 and 10 components are included in θ , respectively. It is clear that the variability of the estimate from one run of DE to another is much smaller in the 10 components case. This yields a better model interpretation and consistency, which are expected advantages of a grey-box model.

4.9.5 Step 3: Optimizing the significant parameters

The recursive training iterations are shown in Table 4.3. The $c = 14$ candidate disturbances have been listed in Table 4.2. Columns 3 and 4 in Table 4.3 give the worst scores defined by (4.6,

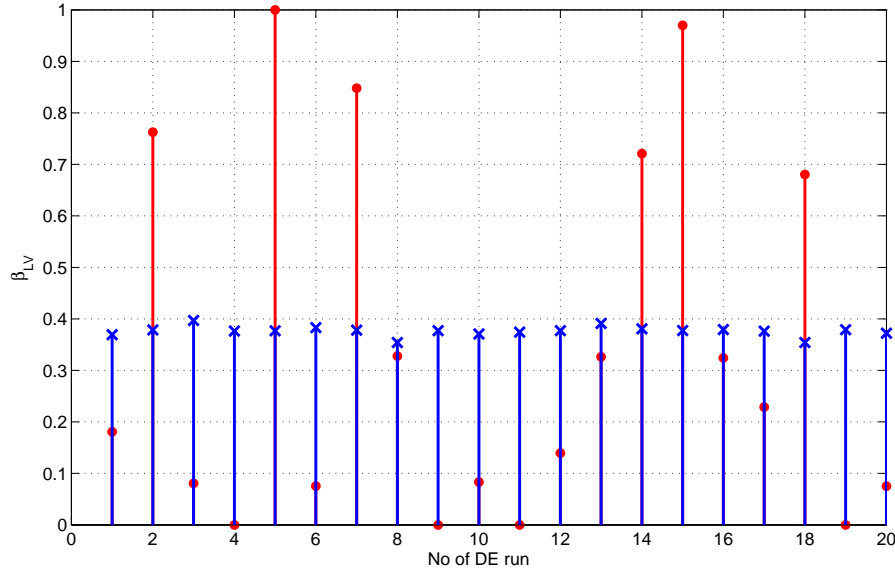


Figure 4.10: Variability of β_{LV} estimates over 20 runs of the DE solver. Red disks refer to the case with 26 components in θ ; blue crosses refer to 10 components. The range of values has been normalized so that the minimum bound is equal to 0 and the maximum to 1

4.7), while columns 5 and 6 give the corresponding worst scores of the non-trained disturbances. After three iterations all non-trained disturbances show scores lower than the worst score of the trained ones, i.e. the stopping criterion (4.8, 4.9) is satisfied. Note that the first line in Table 4.3 corresponds to the scores obtained at Step 2 of the procedure.

Figure 4.11 shows the active and reactive power evolutions of the equivalent for disturbance No 10 (see Table. 4.2) *not used for its training*. It matches accurately the average responses given by μ_P and μ_Q . Figure 4.11 also shows the 5th and 95th percentiles, which reflect the dispersion of the randomized responses of the unreduced system.

The same observations are made in Fig. 4.12 for disturbance No 3, also *not used for its training*.

As expected, it can be seen in Figs. 4.11b and 4.12b, for instance, that the discrepancies between the equivalent response and μ_Q are more pronounced when the dispersion of power values are large (reflected by the 5th and 95th percentile) i.e. when the corresponding weights in the least-square minimization are smaller (see Section. 4.3).

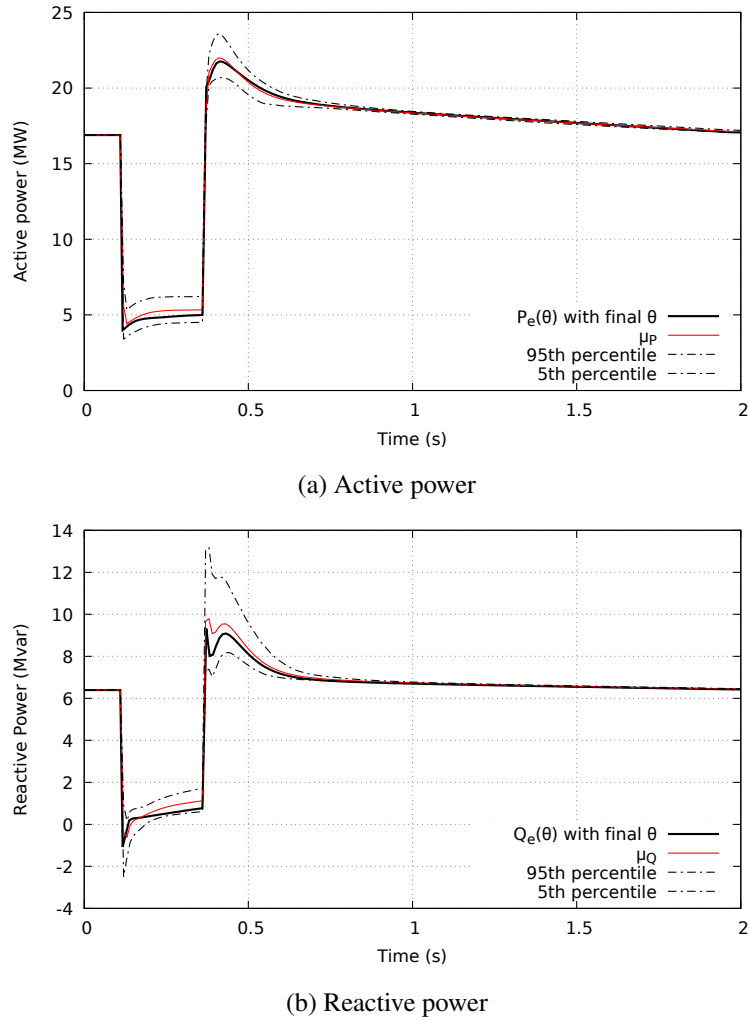
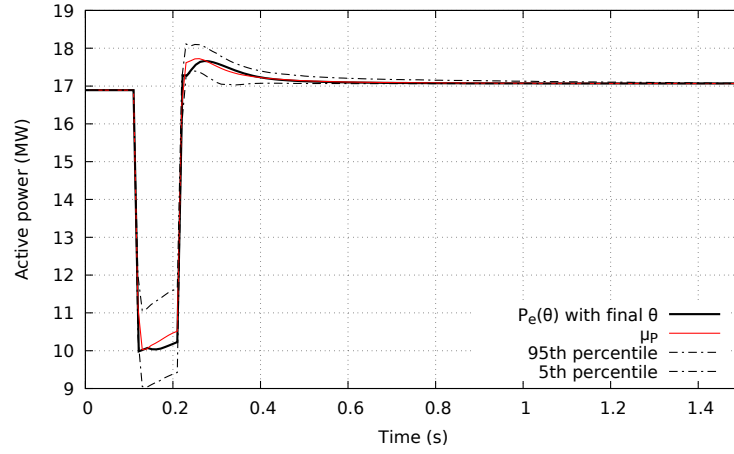


Figure 4.11: Active and reactive power responses to the non-trained disturbance No 10 (ADN No 1)

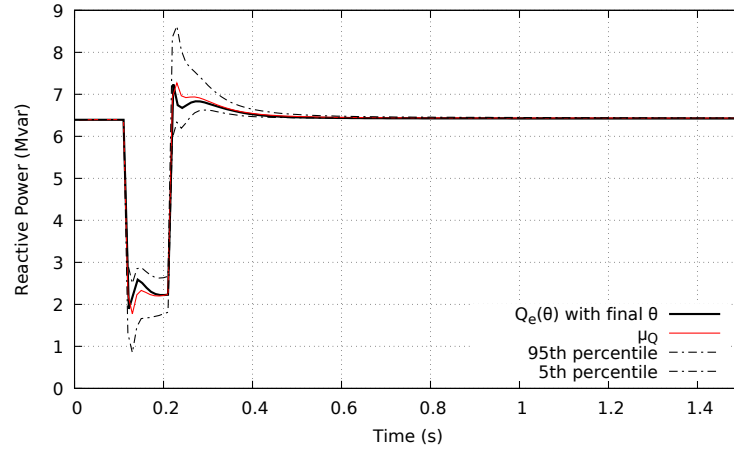
4.9.6 Accuracy of the equivalent for other disturbances

Figure 4.13 shows the active and reactive power responses of the equivalent to a very different (and also non-trained) disturbance, namely an oscillation of the magnitude and phase angle of \bar{V}_{tr} (see Fig. 4.5). The time evolution of the voltage magnitude and phase angle were shown in Fig. 2.23; they could reproduce the effect of an interarea electromechanical oscillation in the transmission system. It can be seen in Figs. 4.13a and 4.13b that the active and reactive power responses of the equivalent matches almost perfectly μ_P and μ_Q . The latter have been obtained from randomized responses of the unreduced system to that disturbance.

Finally, the accuracy of the equivalent is assessed for the frequency transient shown in Fig. 2.22,



(a) Active power



(b) Reactive power

Figure 4.12: Active and reactive power responses to the non-trained disturbance No 3 (ADN No 1)

imposed by varying the phase angle of \bar{V}_{tr} . Figure 4.14 shows the evolutions of P_e (resp. Q_e) and μ_P (resp. μ_Q), respectively. (Again, the latter has been obtained from randomized responses of the unreduced system to that disturbance).

It can be seen in Fig. 4.14b that the reactive power response of the equivalent matches almost perfectly μ_Q while, in Fig. 4.14a, larger discrepancies are observed. However, the power deviation being very small, the accuracy of the equivalent remains acceptable.

This confirms the good accuracy of the equivalent for other type of disturbances not considered for the identification of its parameters.

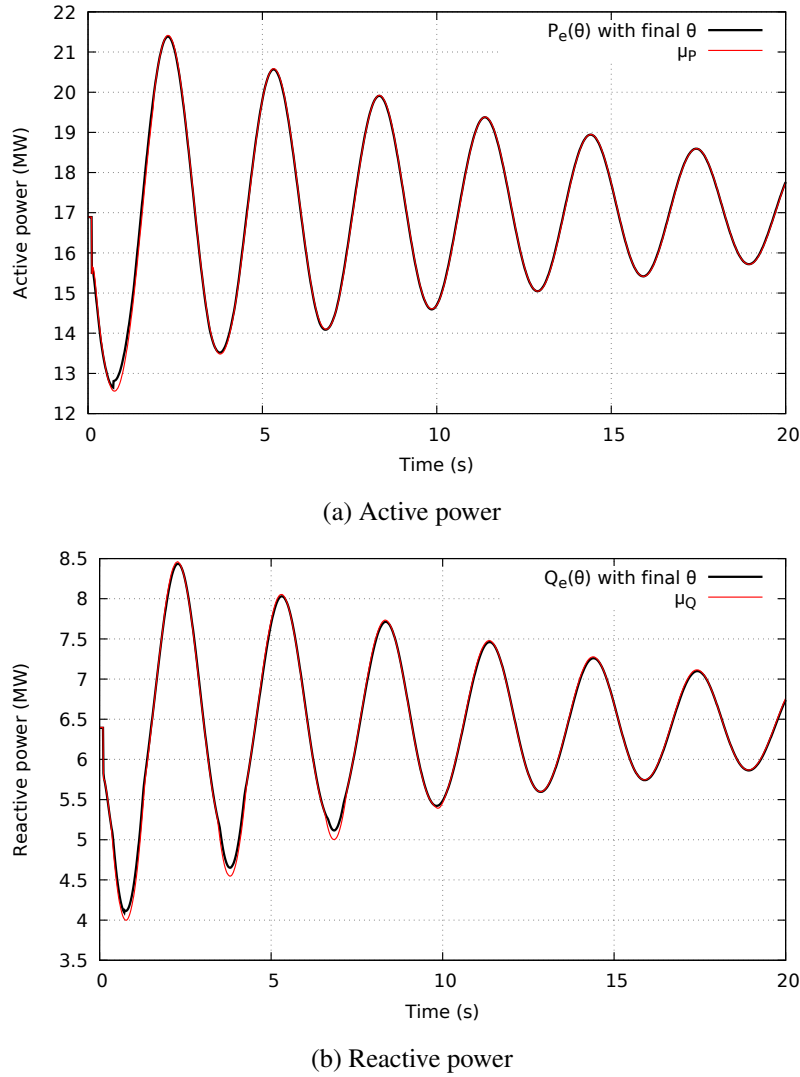


Figure 4.13: Active and reactive power responses to an electromechanical oscillation (ADN No 1)

4.9.7 Accuracy of the ADN equivalent in a long-term voltage instability scenario

This section aims at checking the accuracy of the equivalent in a long-term voltage instability scenario affecting the transmission system. Its response is compared to the response of the unreduced ADN, subject to the same transmission system weakening. Instead of a sharp voltage drop and recovery considered in the training disturbances, the equivalent is now tested against a slowly developing but pronounced voltage decay, typically caused by Load Tap Changers (LTCs) attempting to restore distribution voltages and overexcitation limiters protecting the synchronous machines [VCV98]. To this purpose, the V_{tr} voltage (see Fig. 4.5) is progressively varied to reproduce realistic voltage evolution stemming from the long-term voltage unstable evolution of a

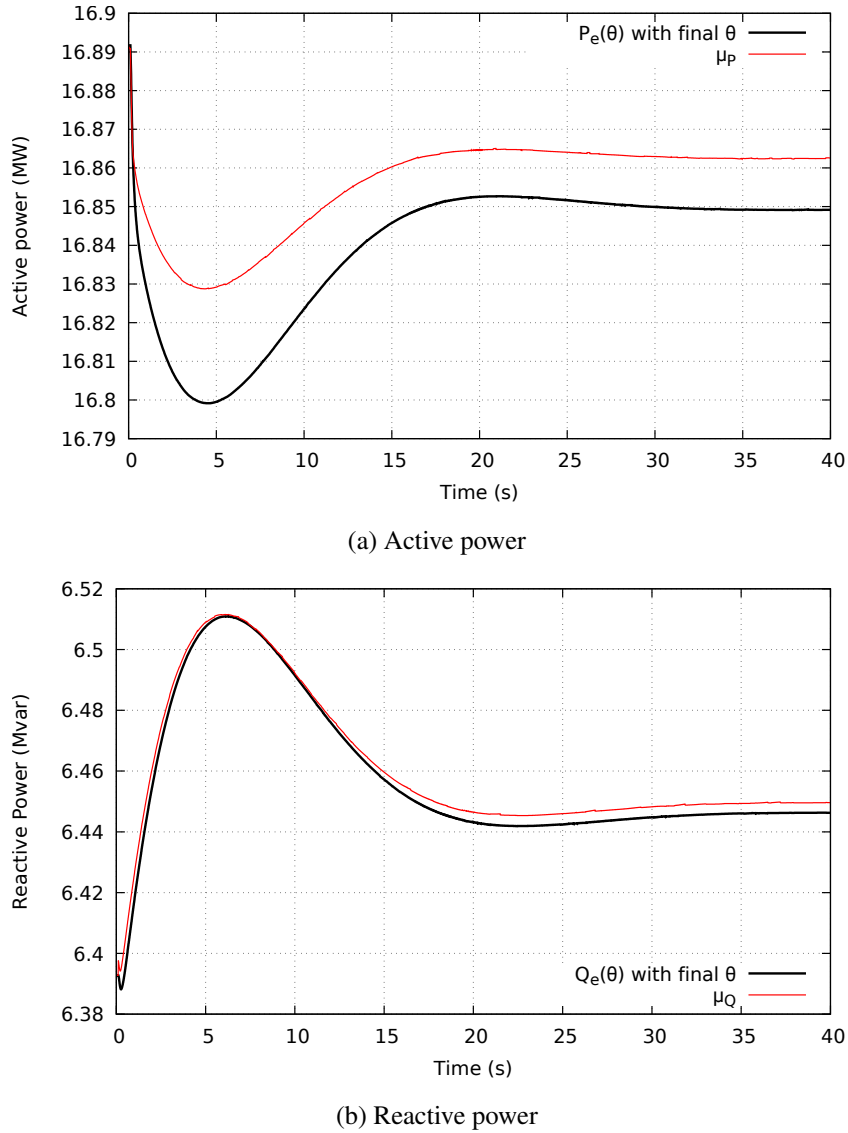


Figure 4.14: Active and reactive power responses to frequency transient (ADN No 1)

transmission system.

The IEEE Nordic test system for voltage stability analysis and security assessment [VCGR⁺15] is used to this purpose. More particularly, its operating point A is considered. The initiating disturbance is a three-phase solid fault on line 4032-4044. The fault lasts 0.1 s and is cleared by opening the line, which remains opened. Long-term voltage instability results. The evolution of a few transmission voltages is shown in Fig. 4.15.

The voltage evolution at bus 1041, the most severely impacted by the disturbance, is applied to

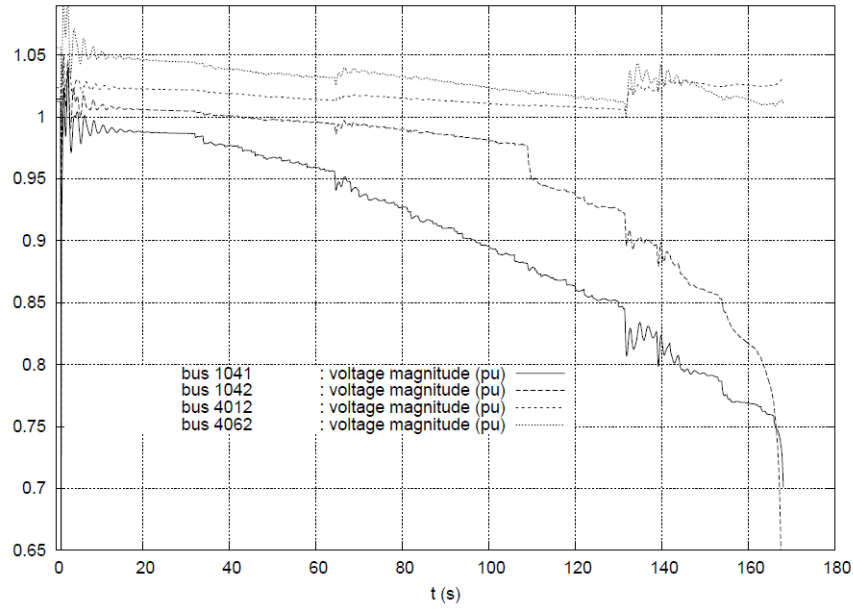


Figure 4.15: IEEE Nordic test system, operating point A : evolution of transmission voltages in response to a fault on line 4032-4044 cleared by opening that line; taken from [VCGR⁺15], page 37

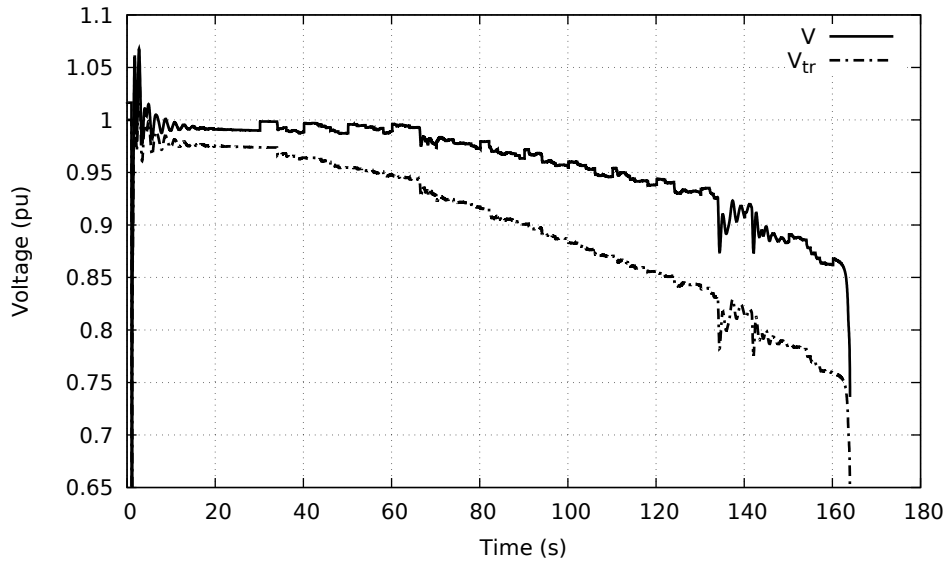


Figure 4.16: Long-term voltage instability: evolution of V_{tr} and V

the HV bus of the distribution transformer in both the unreduced and the reduced models. The LTC of the transformer is let to vary in response to the sagging transmission voltage. Figure 4.16 shows the transmission voltage V_{tr} , i.e. the voltage of bus 1041 and the distribution voltage V (see

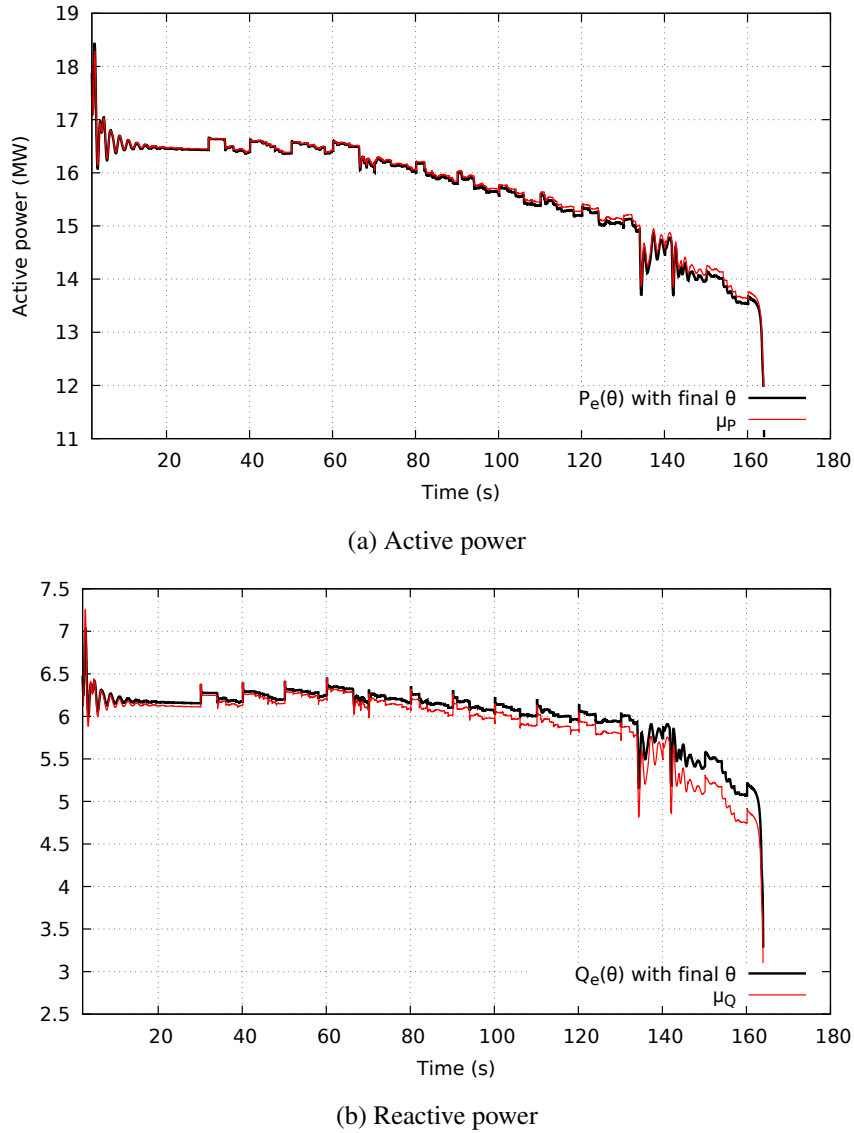
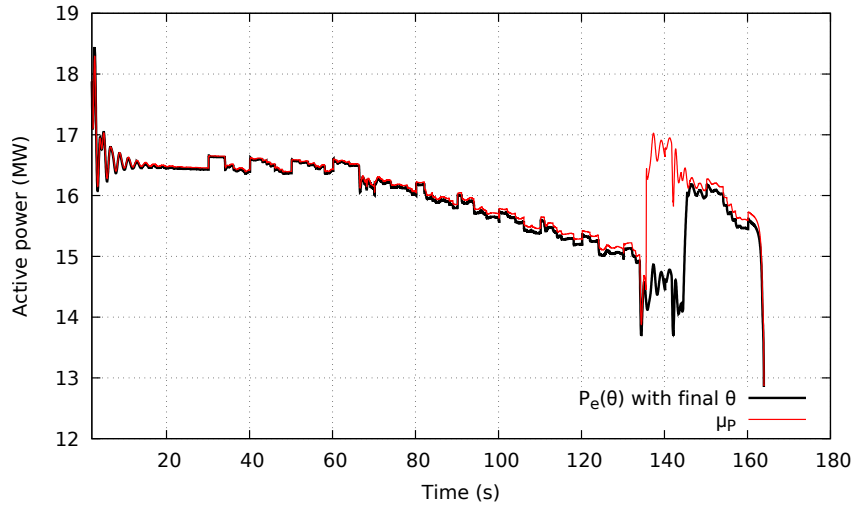


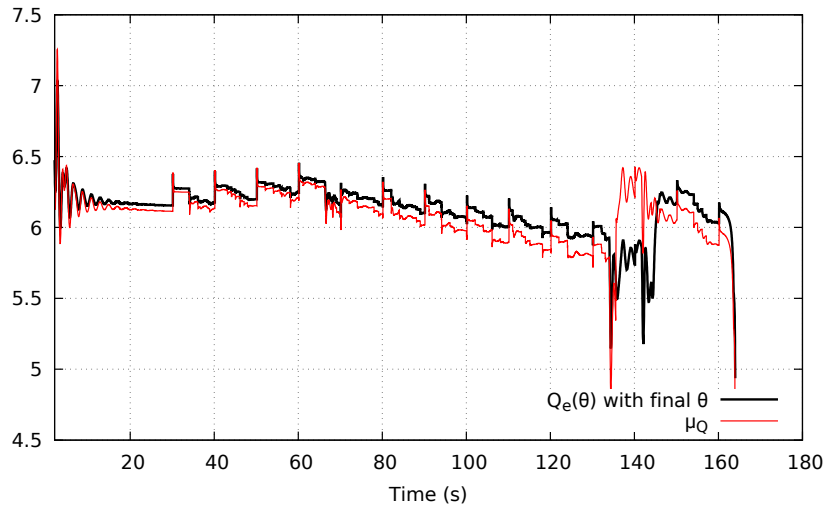
Figure 4.17: Long-term voltage instability : active and reactive power evolutions, no disconnection of IBGs

Fig. 4.5), which is controlled by the LTC. The whole distribution system responds to this voltage change. It can be seen that until 70 s, the LTC manages to keep V at an acceptable value. After 70 s, the fall of V_{tr} is such that the LTC cannot keep V in its deadband any longer, which is typical of voltage instability [VCGR⁺15, VCV98].

The evolution of the active and reactive powers given by the equivalent vs. μ_P and μ_Q respectively, is shown in Fig. 4.17. The figure focuses on the time interval that follows the line opening.



(a) Active power

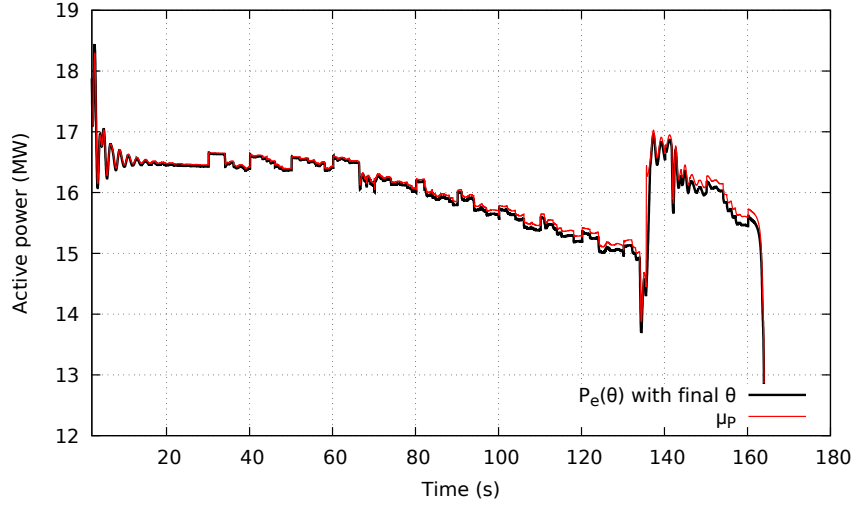


(b) Reactive power

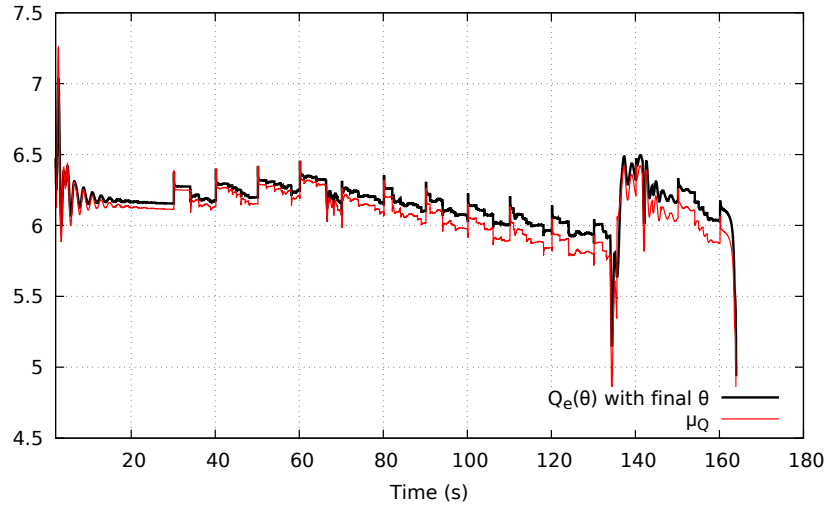
Figure 4.18: Long-term voltage instability : active and reactive power evolutions, disconnection of IBGs represented

In a first step, the undervoltage disconnection of IBGs is not taken into account; they remain connected throughout the simulation. It can be seen that, while a small shift in reactive power is observed, the equivalent reproduces accurately the response of the unreduced system. The first tap change takes place at $t = 25$ s and then every 10 s. Its effect is clearly seen in the figure, when the net power entering the ADN shows spikes. Expectedly as the transmission voltage reaches very depressed values, the inaccuracy of the equivalent is more pronounced.

In a second step, the disconnection of IBGs has been accounted for in the simulation. According



(a) Active power



(b) Reactive power

Figure 4.19: Long-term voltage instability : active and reactive power evolutions, disconnection of IBGs represented and adjustment of the parameter V_r in the equivalent

to the LVRT characteristic shown in Fig. 2.8, they are expected to disconnect when their terminal voltage falls below V_r for a duration longer than T_2 . By default, V_r is set to 0.9 pu and T_2 to 1.5 s.

Let us recall that, no partial tripping feature has been considered for the aggregate large-capacity IBG present in the equivalent, as no disturbance leading to large-capacity IBGs disconnection has been considered. Therefore, the disconnection of the aggregate IBG is merely based on the classical LVRT characteristic, whose parameters have been unchanged and applied to the aggregate equivalent IBG.

Figure 4.18 shows the corresponding active and reactive power evolutions. It can be seen that the disconnection of all the large-capacity IBGs in the unreduced system occurs around $t = 135$ s, while the aggregate IBG in the equivalent trips around $t = 145$ s, leading to a discrepancy between the equivalent and the reference responses. This is caused by the lumping approximation in the equivalent, leading to a difference between the terminal voltage of the aggregate IBG and the voltages of the individual IBGs dispersed in the network. Note, however, that both responses differ by a time delay only. The trajectories separate when the transmission voltage is already abnormally low.

In fact, a small adjustment of the V_r parameter in the equivalent is sufficient to reconcile both trajectories. This is illustrated in Fig. 4.19 where V_r has been increased from 0.9 to 0.92 pu. In this case, the disconnections of the equivalent IBG and the original IBGs take place at the same time.

It can be also concluded that, while the ADN equivalent has been trained for short-term voltage evolutions, it can be used in long-term voltage studies as well.

4.10 Simulation results with ADN No 2

The ADN No 2 system has been introduced in Chapter 1 and its one-line diagram is shown in Fig. 1.10. One significant difference with respect to the ADN No 1 system is the tripping of large-capacity IBGs. As previously mentioned, the three-parameter partial tripping model is used in this thesis (see Fig. 4.2).

4.10.1 Topology and parameters of the equivalent

The topology of the equivalent model of ADN No 2 is shown in Fig. 4.20. The distributed IBGs (resp. loads) of the original system are lumped into one aggregated IBG (resp. load). The aggregated load and the aggregated IBG are connected through distinct impedances $R_a + jX_a$ and $R_b + jX_b$ to account for their different distributions within the ADN. This corresponds to Variant 2 in Table 4.1.

The full set of parameters to identify is as follows (see Table 3.1 for their counterparts in the unreduced models) :

- for the aggregated load : α and β in the exponential model and, for the motor, the stator and rotor resistances R_s and R_r , the magnetizing inductance L_{sr} , the two leakage reactances $(L_{ss} - L_{sr})$ and $(L_{rr} - L_{sr})$, the inertia constant H and the load factor LF ;

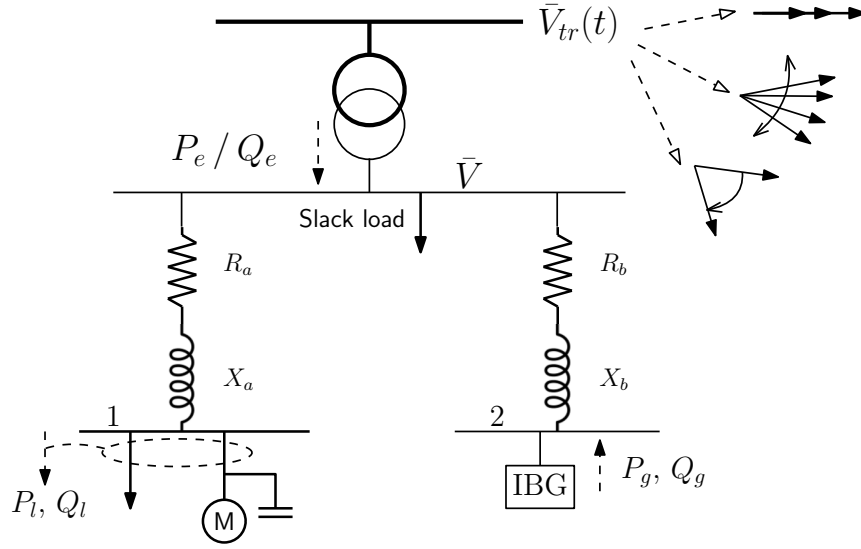


Figure 4.20: Topology of the equivalent (ADN No 2)

- for the aggregated IBG : the nominal current I_{nom} , the maximum rate of recovery of the active current $(\frac{di_p}{dt})_{max}$, the slope k_{RCI} and V_{S1} threshold, γ , V_{pt} and V_{ft} (partial tripping);
- for the equivalent network impedances : R_a , R_b , X_a and X_b .

This leads to a total of 20 components in θ .

4.10.2 Steps of the reduced model identification

As for ADN No 1, the bounds θ^L and θ^U of the search interval in (4.4) have been set to plausible values of the corresponding parameters.

For this ADN, the equivalent is identified in four steps :

1. the equivalent impedances $R_a + jX_a$ and $R_b + jX_b$ have been first estimated using the network reduction technique of Section 4.9.3. Then, the DE algorithm is let to adjust R_a , X_a , R_b and X_b in intervals centered on the so obtained estimates;
2. scenarios without IBG disconnection have been considered, leaving aside the γ , V_{pt} and V_{ft} parameters. Among the $(20-3=)$ 17 remaining parameters, 10 have been identified as significant by the method of Section 4.6;
3. those 10 parameters have been optimized by the recursive training algorithm of Section 4.5;
4. scenarios with IBG disconnection have been used to identify γ , V_{pt} and V_{ft} , with the previous 10 parameters being set to their values found at Step 2.

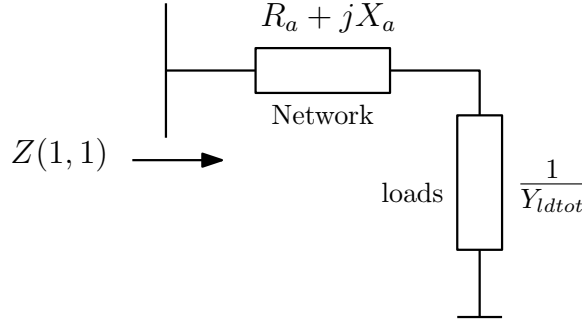


Figure 4.21: Network reduction technique : Estimation of the reference value of the equivalent impedance $R_a + jX_a$ (ADN No 2)

4.10.3 Step 1: First estimation of the network equivalent impedances

The same network reduction technique as for ADN No 1 has been used. The difference with respect to ADN No 1 is that no LV bus is considered here, which makes the reduction technique even simpler.

In this case, the $R_a + jX_a$ impedance is obtained as :

$$R_a + jX_a = Z(1,1) - \frac{1}{Y_{ldtot}} \quad (4.23)$$

where $Z(1,1)$ is the equivalent impedance seen from the entry point of the network (bus 1100 in Fig. 1.10), i.e. the sought impedance $R_a + jX_a$ in series with a lumped impedance representing all loads in parallel as shown in Fig. 4.21.

The same applies to $R_b + jX_b$ where the equivalent impedance seen from the entry point of the network is given by the sought impedance $R_b + jX_b$ in series with a negative lumped impedance representing all IBGs production in parallel.

4.10.4 Step 2: Identifying the significant parameters

The LASSO method has been used on disturbances No 7 and 8 with intermediate values of the voltage dip (see Table. 4.2) as they yield to the worst scores $F_P^{max}(\hat{\theta}^{ref})$ and $F_Q^{max}(\hat{\theta}^{ref})$.

Figure 4.22 shows plot of the objective function $F(\hat{\theta})$ vs. the penalty term $\sum_{l=1}^n |\theta_l^{ref} - \theta_l|$, for decreasing values of λ . The same trend is observed as for the ADN No 1 system. At the point marked with a circle, corresponding to $\lambda = 0.125$, the accuracy criterion (4.5) is satisfied. The corresponding scores are $F_P^{max}(\hat{\theta}) = 0.77$ and $F_Q^{max}(\hat{\theta}) = 0.97$.

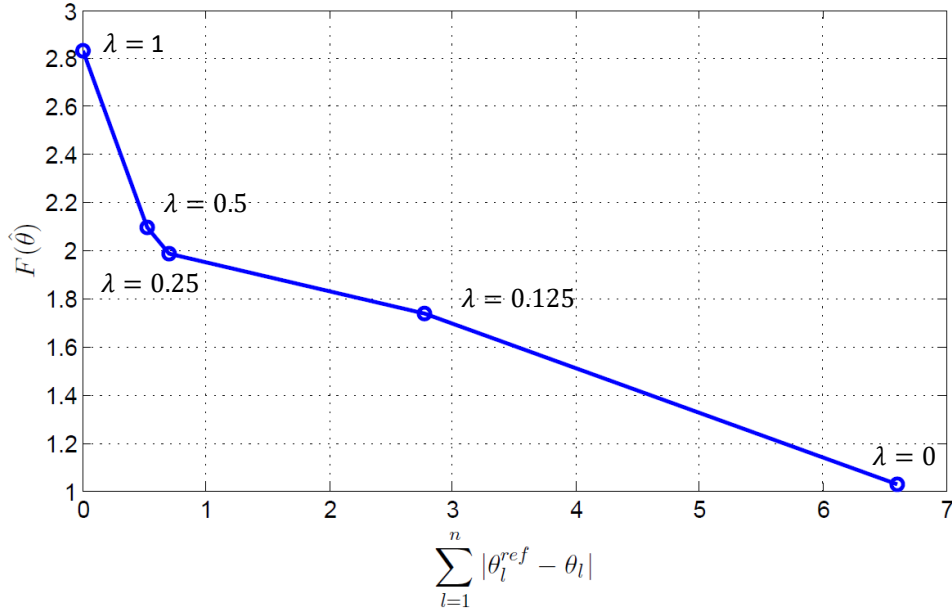


Figure 4.22: $F(\hat{\theta})$ vs. $\sum_{l=1}^n |\theta_l^{ref} - \theta_l|$ for decreasing values of λ

Figure 4.23 shows the relative differences defined in (4.11), for each of the 17 parameters. With a threshold $\delta = 5\%$, represented by the dashed red line, seven parameters are identified as non-significant. These are :

- for the aggregated load : the exponent β , the stator resistance R_s , the magnetizing reactance L_{sr} and the inertia constant H of the motor;
- for the aggregated IBG : no parameter is discarded;
- for the equivalent impedances : R_a , R_b and X_a . Again, this tends to confirm that the impedances estimated by network reduction were appropriate.

As for the ADN No 1, to validate the method and observe the variability of parameter values given by multiple DE runs, the results of 20 separate executions of the DE algorithm have been compared, for the 17- and the 10-dimensional vectors θ , respectively. In the former case, some components $\hat{\theta}_l$ exhibit significant variations. With the 10-dimensional vector, a much lower variability has been observed, i.e. the variations from one DE execution to another are insignificant. An illustration is provided in Fig. 4.24, showing 20 separate estimates of the V_{S1} component (see Fig. 2.9), when 17 and 10 components are included in θ , respectively.

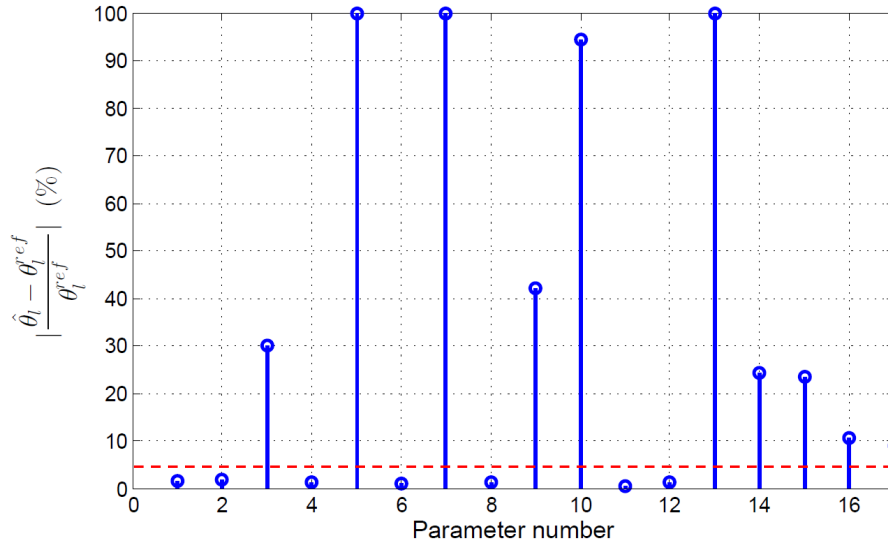


Figure 4.23: LASSO method: final values of $|\hat{\theta}_l - \theta_l^{ref}|/\theta_l^{ref}$ (in %)

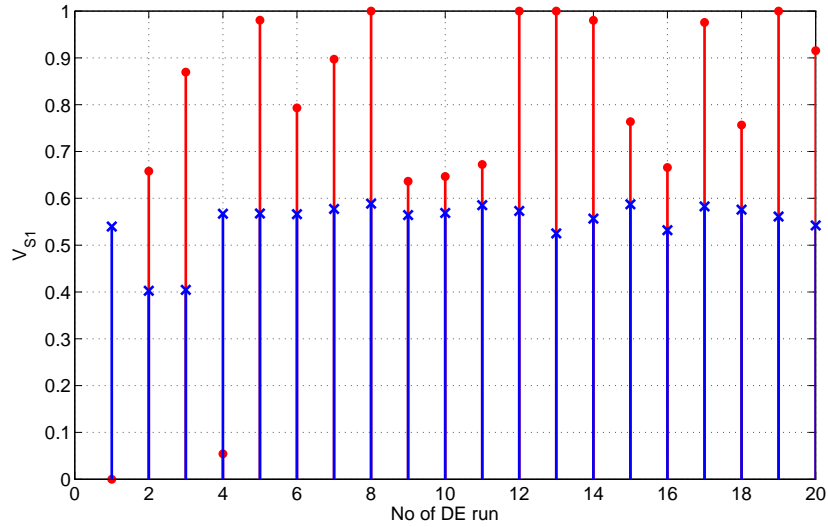


Figure 4.24: Variability of V_{S1} estimates over 20 runs of the DE solver. Red disks refer to the case with 17 components in θ ; blue crosses refer to 10 components. The range of values has been normalized so that the minimum bound is equal to 0 and the maximum to 1

4.10.5 Step 3: Optimizing the significant parameters

The recursive training iterations are shown in Table 4.4. The $c = 12$ candidate disturbances are the voltage dips No 1 to 12 (see Table. 4.2) not causing IBGs disconnection. Columns 3 and 4 in

Table 4.4: Results of recursive training algorithm (ADN No 2)

Iteration	Trained disturbances	trained disturbances		non trained disturbances	
		F_P^{max}	F_Q^{max}	F_P^{max}	F_Q^{max}
1	7, 8	0.78	0.96	1.57	2.34
2	7, 8, 11, 12	1.15	1.01	4.32	0.93
3	7, 8, 11, 12, 6	1.24	1.13	1.31	1.08
4	7, 8, 11, 12, 6, 2	1.29	1.21	0.79	0.87

Table 4.4 give the worst scores, while Columns 5 and 6 give the corresponding worst scores of the non-trained disturbances. After four iterations all non-trained disturbances show scores lower than the worst score of the trained ones, i.e. the stopping criterion (4.8, 4.9) is satisfied. Again, the first line in Table 4.3 corresponds to the scores obtained at Step 2.

Figure 4.25 shows the active and reactive power evolutions of the equivalent obtained after Step 3 for the disturbance No 10 (see Table. 4.2) *not used for its training*. It matches accurately the average responses given by μ_P and μ_Q . The same figure shows the 5th and 95th percentiles, which reflect the dispersion of the randomized responses of the unreduced system.

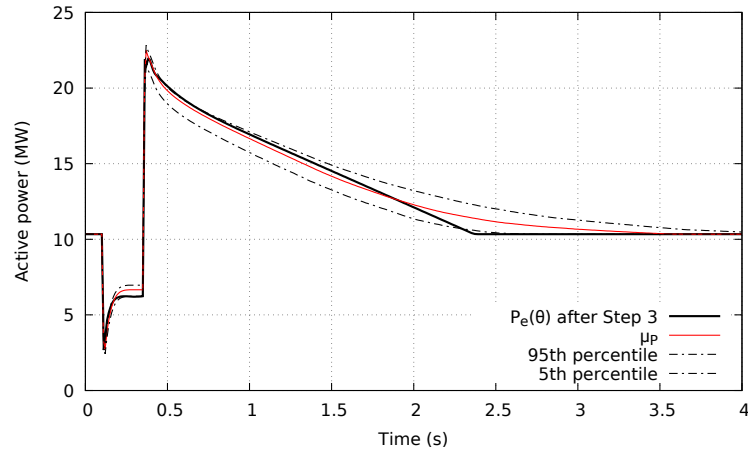
4.10.6 Step 4: Optimizing the partial tripping parameters

The algorithm is finally executed on the whole set of $c = 14$ disturbances but focusing now on the values of γ , V_{pt} and V_{ft} relative to partial tripping. This leads to adding to the training set the most severe disturbance (No 14).

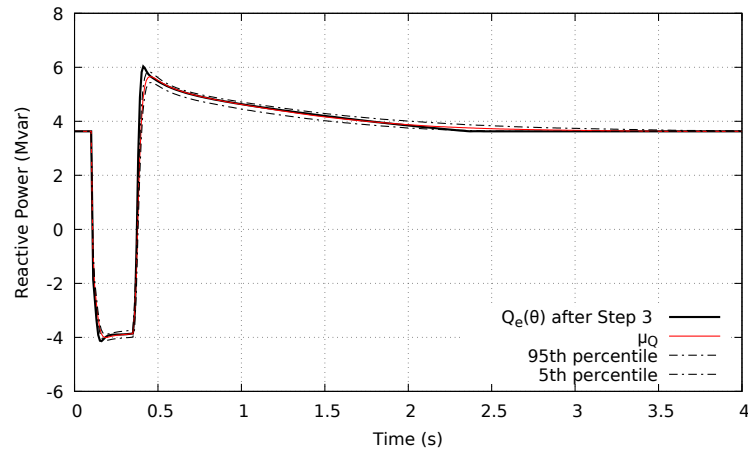
Again, the accuracy of the equivalent is illustrated in response to a disturbance not used for its training, namely No 13, for which some IBGs disconnect. Figure 4.26a shows with dotted line the evolution of P_e for the intermediate $\hat{\theta}$ obtained after Step 3. As γ , V_{pt} and V_{ft} have not yet been optimized, IBG tripping is ignored and the response is inaccurate. On the other hand, the P_e response for the final $\hat{\theta}$ obtained after Step 4 is shown with heavy solid line. It matches accurately the average response given by μ_P , in particular its final value. Similar curves relative to Q_e are given in Fig. 4.26b. They confirm the accuracy of the equivalent for the reactive power.

4.10.7 Accuracy of the equivalent for other disturbances

Figure 4.27 shows the active and reactive power responses of the equivalent to the very different (and also non-trained) oscillatory disturbance already considered in Section 4.9.6. It can be seen in



(a) Active power



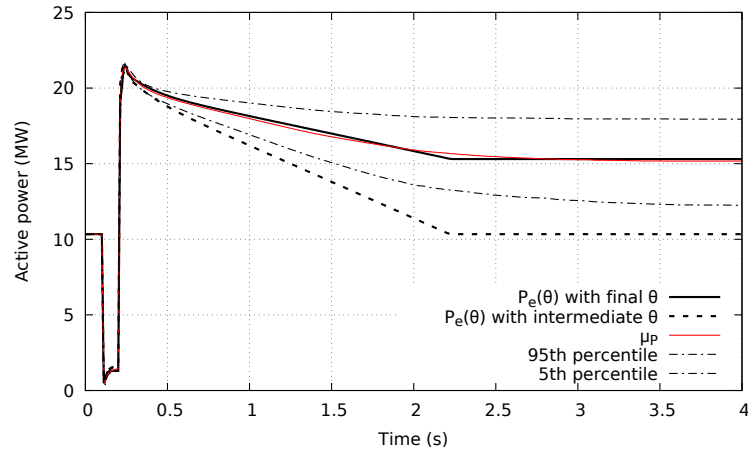
(b) Reactive power

Figure 4.25: Active and reactive power responses to the non-trained disturbance No 10 after Step 3 (ADN No 2)

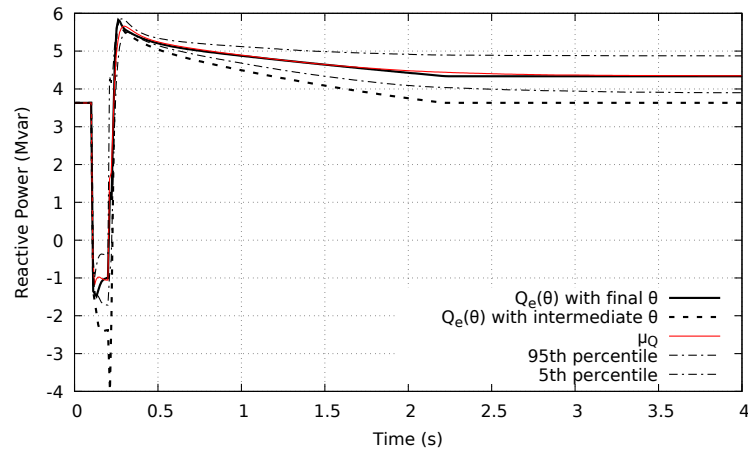
Fig. 4.27a that the active power response of the equivalent matches almost perfectly μ_P , obtained from randomized responses of the unreduced system to that disturbance.

Figure 4.27b show the evolution of respectively Q_e and μ_Q . The overall accuracy is good, in particular near the first two nadirs. The discrepancies observed in the subsequent swings are due to a little excessive reactive current injection by the IBG in the equivalent (transiently decreasing the net reactive load considered in the figure). This is confirmed by Fig. 4.28, showing the reactive power output of the equivalent IBG. The IBG produces reactive power periodically, each time the voltage falls below the voltage threshold V_{S1} (see Fig. 2.9).

Finally, the accuracy of the equivalent is assessed for the frequency transient already considered in



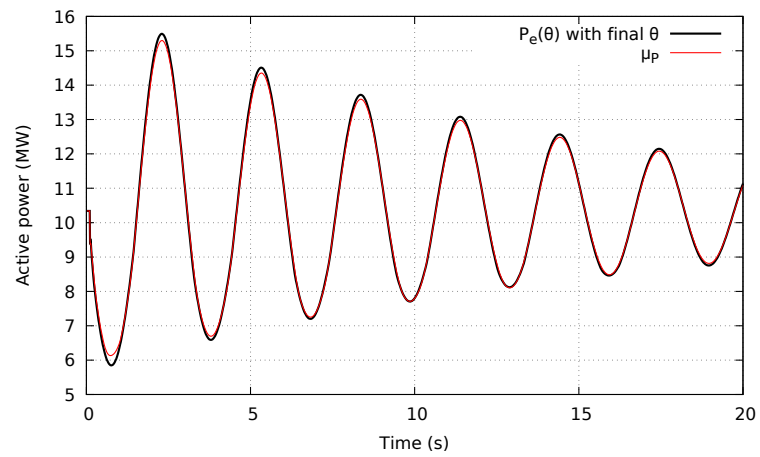
(a) Active power



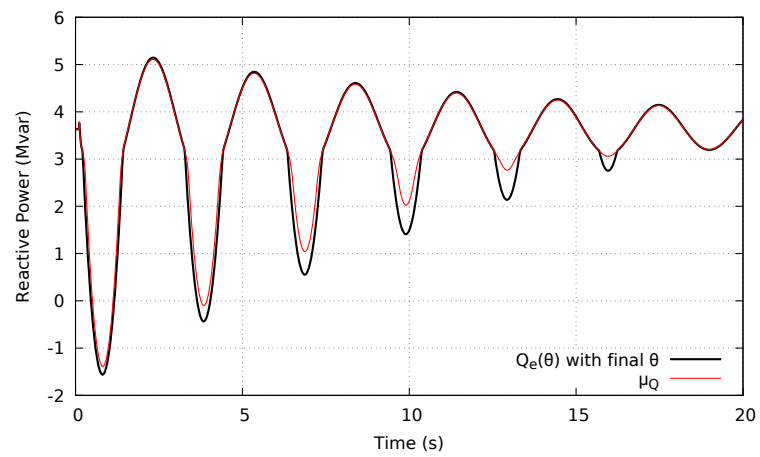
(b) Reactive power

Figure 4.26: Active and reactive power responses to the non-trained disturbance No 13 after Step 4 (ADN No 2)

Section 4.9.6. Figure 4.29 shows the evolutions of P_e (resp. Q_e) and μ_P (resp. μ_Q), respectively. The accuracy of the equivalent is further confirmed by the perfect match of these curves.



(a) Active power



(b) Reactive power

Figure 4.27: Active and reactive power responses to an electromechanical oscillation (ADN No 2)

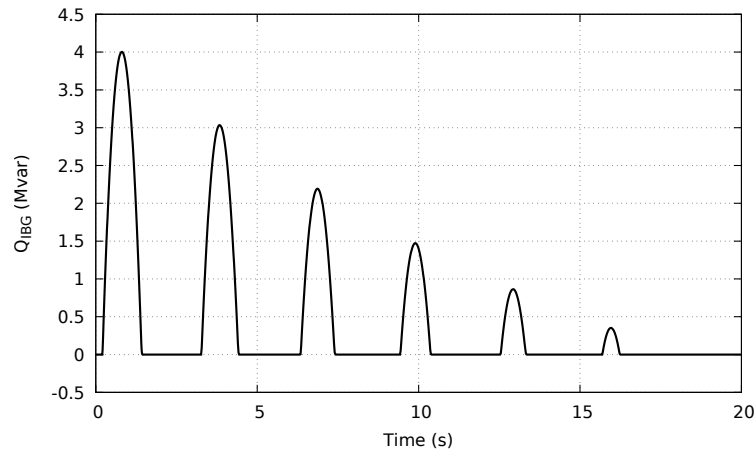
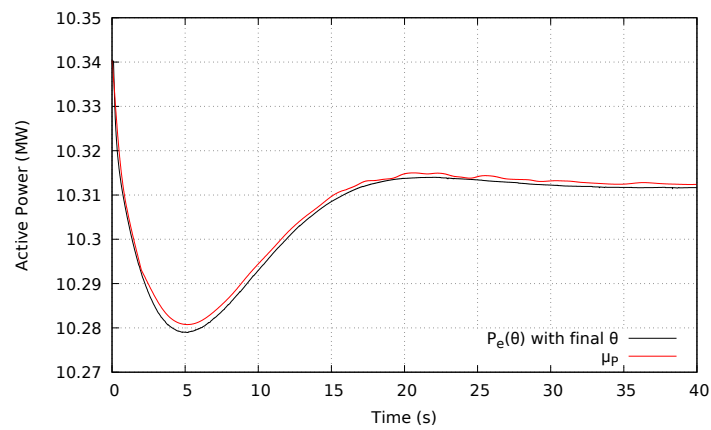
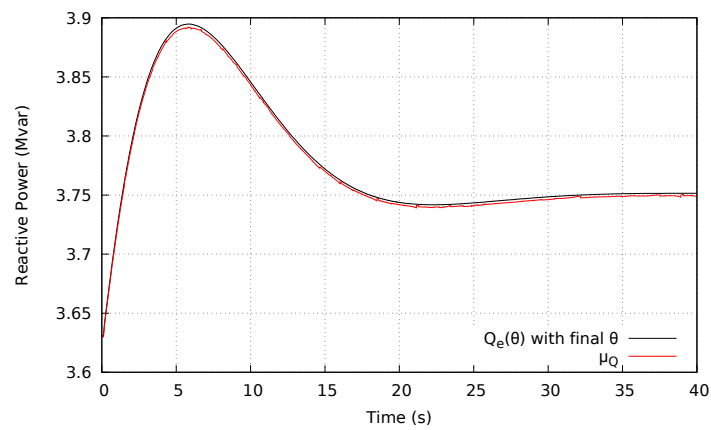


Figure 4.28: Reactive power generated by the IBG in response to an electromechanical oscillation



(a) Active power



(b) Reactive power

Figure 4.29: Active and reactive power responses to frequency transient (ADN No 2)

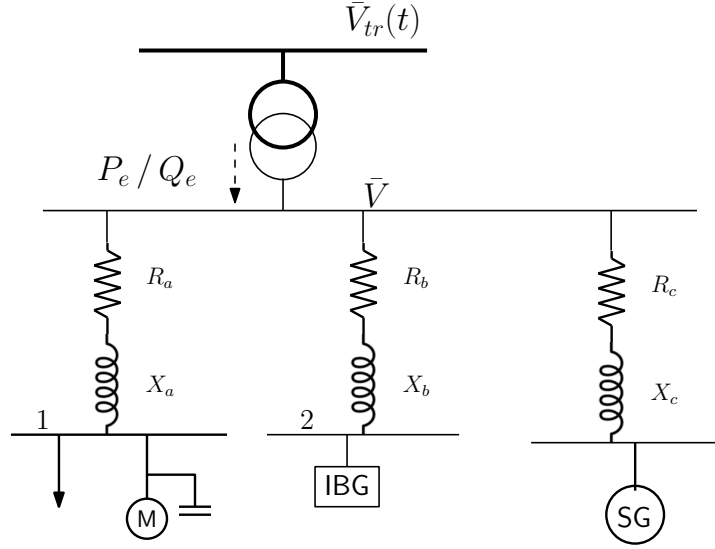


Figure 4.30: Topology of the equivalent (ADN No 3)

4.11 Simulation results with ADN No 3

This section presents the results obtained on ADN No 3, the real distribution system introduced in Chapter 1. Its one-line diagram is shown in Fig. 1.11. Let us recall the major difference with respect to the previous ADN systems is the presence of Synchronous Generators (SGs).

4.11.1 Topology and parameters of the equivalent

The topology of the equivalent is shown in Fig 4.30. It is similar to the topology of ADN No 2 (see Fig. 4.20) but with the aggregated SG connected behind an additional equivalent branch of impedance $R_c + jX_c$. Incidentally, such a configuration is recommended in [Cor17a] as it can differentiate generators by technical characteristics and/or grid requirements.

In addition to the parameters of the equivalent ADN No 2, the set of parameter includes :

- for the aggregated SG : the inertia constant, H^{SG} and the nominal apparent power, S_{nom}^{SG} . Although these parameters were not randomized in the MC simulations of the unreduced system (see Section 3.3.3), they have been included in θ since further tests have shown that by slightly adjusting them, the accuracy of the equivalent is significantly improved;
- for the equivalent network impedances : R_c and X_c .

This leads to a total of 24 components in θ .

Table 4.5: Retained parameters in the equivalent ADN No 3

Component	One SG	Eight SGs
Network	-	R_c
Load	$L_{ss} - L_{sr}, H$	α
IBG	$I_{nom}, (\frac{di_p}{dt})_{max}, k_{RCI}$	I_{nom}
SG	H^{SG}, S_{nom}^{SG}	H^{SG}, S_{nom}^{SG}

For this ADN, the tripping of IBGs is also taken into account. Therefore the steps to identify the equivalent are similar to those presented in Section 4.10.2. To avoid redundancy with previous sections, only a sample of results are shown. Two configurations are considered :

1. one SG in operation;
2. all eight SGs in operation.

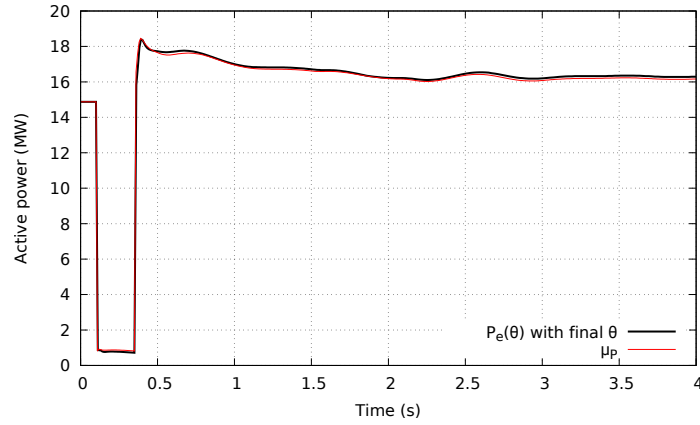
4.11.2 Simulation results for one SG in operation

First, the parameters of partial tripping γ , V_{pt} and V_{ft} are left aside. Among the 21 remaining parameters, 14 have been discarded by the method of Section 4.6. The seven significant parameters are listed in Table 4.5. It can be seen that S_{nom}^{SG} and H^{SG} are retained, which confirms that these parameters play a significant role in the accuracy of the equivalent.

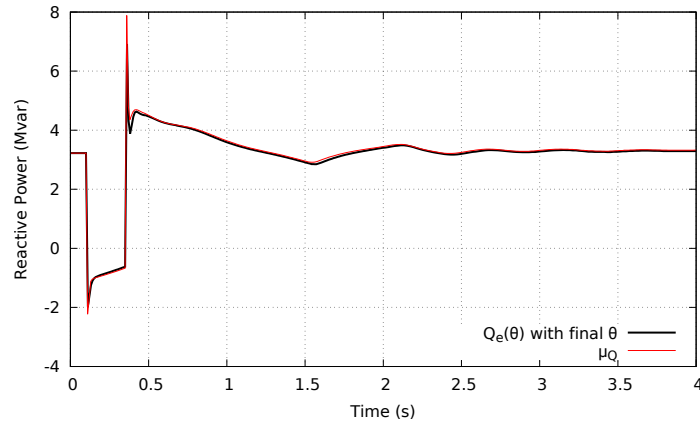
The recursive procedure of Section 4.5 is then applied on the set of remaining parameters. First, disturbances No 1 to 12 (see Table. 4.2) are considered. Five of them, namely No 4, 5, 6, 7 and 12 are selected in the training set.

Next, the identification focuses on the γ , V_{pt} and V_{ft} parameters. The seven already treated parameters are fixed to their estimated values. The whole set of 14 disturbances is now considered, thus including disturbances No 13 and 14, which trigger IBGs disconnection. The recursive procedure adds disturbance No 13 to the training set.

For illustration purposes, the accuracy of the equivalent is shown in response to disturbance No 14, for which some PV units disconnect. Note that this disturbance was not selected to enter the training set. Figure 4.31a shows that the active power of the equivalent matches perfectly the average response μ_P , shown with red line. In particular both curves end up in the same value, further demonstrating the ability of the equivalent to estimate the amount of disconnected IBGs, even for a disturbance not involved in its training.



(a) Active power



(b) Reactive power

Figure 4.31: Active and reactive powers in response to the non-trained disturbance No 14 (ADN No 3 with one SG)

Similar curves relative to the reactive power are given in Fig. 4.31b. They confirm the accuracy of the equivalent for the reactive part.

The accuracy of the equivalent has been also assessed for the very different (and also non-trained) oscillatory disturbance already considered in Sections 4.9.6 and 4.10.7.

Figure 4.32 shows the active and reactive power responses of the equivalent. P_e matches almost perfectly the reference evolution μ_P . As regards the reactive power, while the overall accuracy is also very good, some discrepancies are observed during the first four voltage nadirs. This is due to a small lack of reactive power production by the equivalent IBG, with respect to the IBGs dispersed in the original system.

Similarly, the accuracy of the equivalent has been checked for the frequency transient already con-

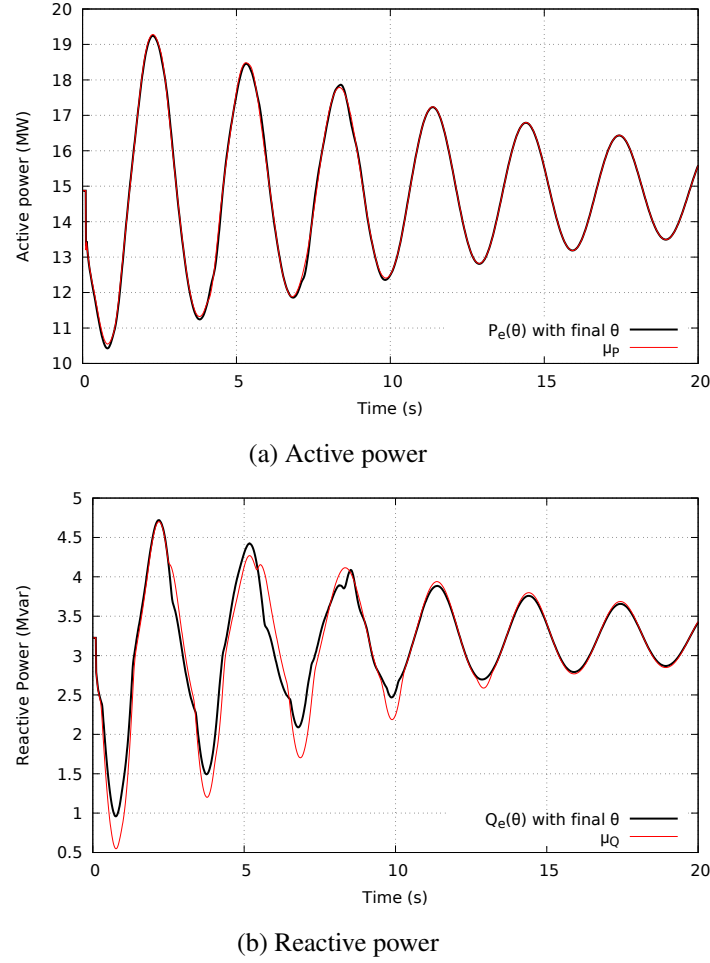


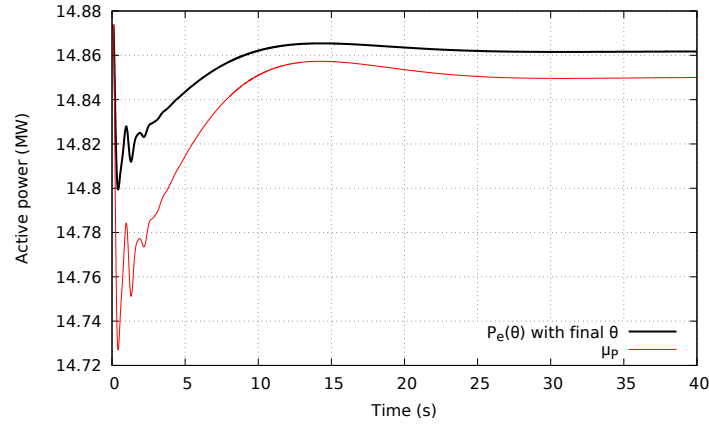
Figure 4.32: Active and reactive powers in response to an electromechanical oscillation (ADN No 3 with one SG)

sidered in previous sections. The evolutions of P_e (resp. Q_e) and μ_P (resp. μ_Q), respectively, are shown in Fig. 4.33. While some discrepancies are observed, the small power deviations confirm the accuracy of the equivalent.

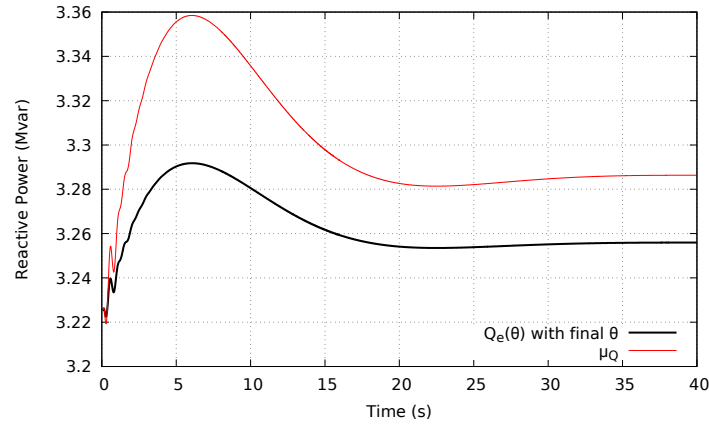
4.11.3 Simulation results for eight SGs in operation

For this configuration, 5 parameters are retained by the procedure of Section 4.6. They are listed in Table. 4.5.

The major difference with respect to the configuration with one SG in operation is that only one parameter, namely the nominal current I_{nom} , is retained for the IBG. It reveals that a stronger penetration of SGs tends to mask the effect of IBGs on the dynamic response of the ADN system.



(a) Active power



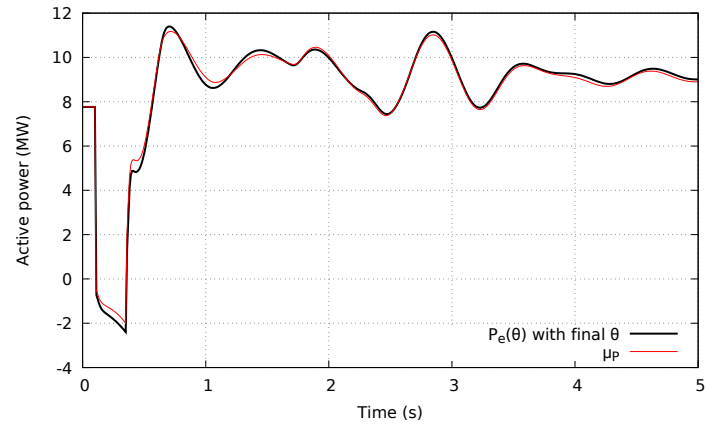
(b) Reactive power

Figure 4.33: Active and reactive powers in response to a frequency transient (ADN No 3 with one SG)

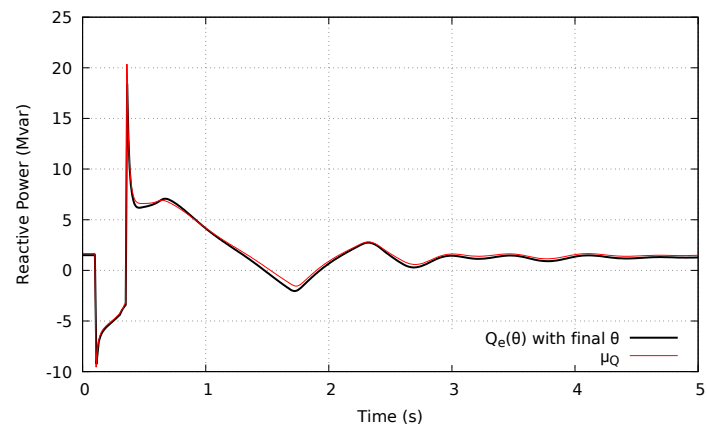
The same conclusion can be drawn for the motor load, as no parameter of the equivalent motor is retained.

Figures 4.34, 4.35 and 4.36 show respectively the active and reactive power responses of the equivalent vs. the reference evolutions μ_P and μ_Q for the disturbances previously considered in the configuration with one SG.

The same conclusions regarding the accuracy of the equivalent can be drawn in spite of the more oscillatory behaviour of the system in the presence of more SGs.

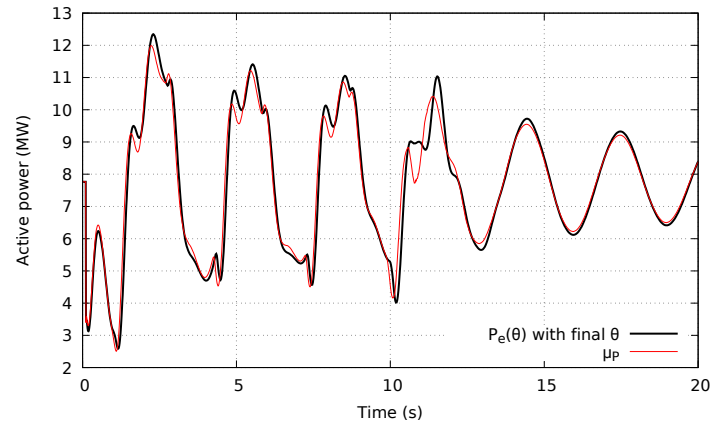


(a) Active power

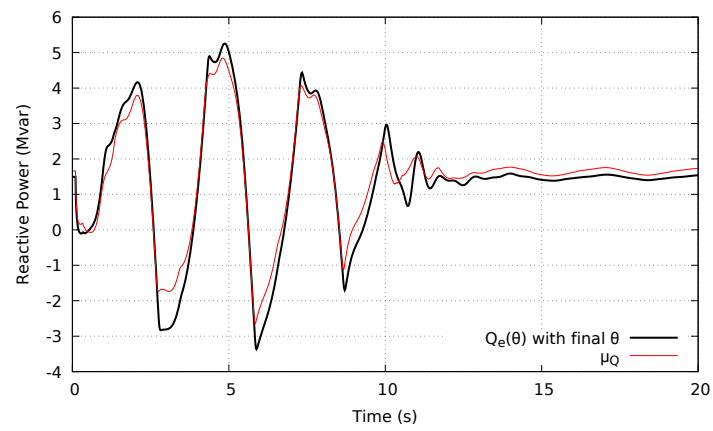


(b) Reactive power

Figure 4.34: Active and reactive powers in response to the non-trained disturbance No 14 (ADN No 3 with eight SGs)

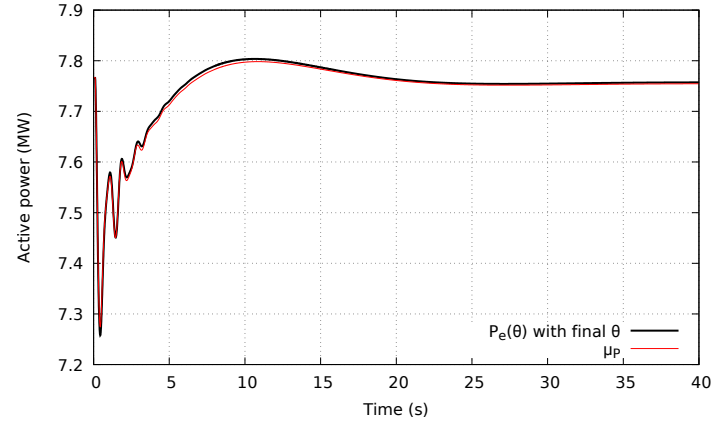


(a) Active power

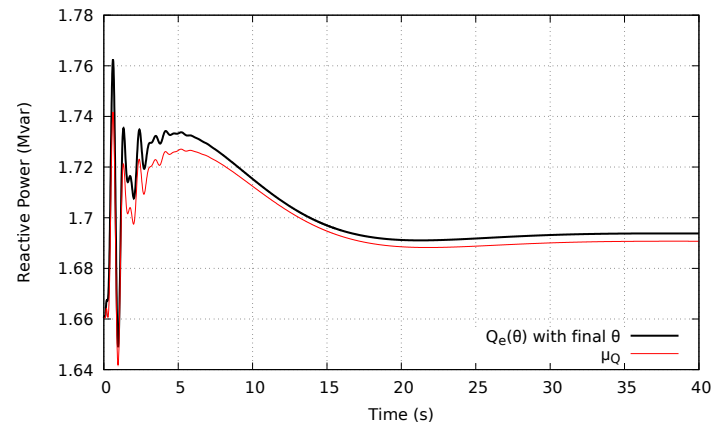


(b) Reactive power

Figure 4.35: Active and reactive power in responses to an electromechanical oscillation (ADN No 3 with eight SGs)



(a) Active power



(b) Reactive power

Figure 4.36: Active and reactive powers in response to a frequency transient (ADN No 3 with eight SGs)

Table 4.6: Reduction of model complexity in terms of differential and algebraic equations

	ADN No 1		ADN No 2		ADN No 3	
	Network	Models	Network	Models	Network	Models
Unreduced	22	997	152	2833	184	5235
Reduced	6	204	6	102	8	122

4.12 Reduction of model complexity

One of the motivation for developing dynamic equivalents is to strongly simplify the ADN models. The simplification brought by using the equivalent ADNs can be assessed in terms of number of differential and algebraic equations in the unreduced vs. the reduced models. The results are given in Table 4.6 for each of the three ADNs. The achieved reduction of model complexity is significant, especially for ADN No 2 and 3, whose unreduced models are much larger than ADN No 1.

4.13 Summary

A complete methodology has been presented to identify ADN equivalents for use in transmission system dynamic simulations.

The proposed procedure is valid for a wide variety of distribution systems. It decomposes into the following steps :

- a weighted least-square problem is solved to make the response of the equivalent approach the average of the randomized responses. The weights reflect the dispersion of the dynamic responses around their average;
- a metaheuristic (Differential Evolution) algorithm is used to deal with this minimization problem;
- for better interpretation of the results, a procedure based on the LASSO method allows removing from the identification the parameters with negligible impact on the response of the equivalent;
- multiple candidate disturbances are considered to avoid over-fitting;
- a recursive procedure is used to involve the smallest possible sub-set of disturbances in the least-square minimization;

- to account for IBG disconnection (in severe scenarios), two sub-sets of parameters are estimated sequentially, using scenarios without and with IBG disconnection, respectively.

Simulation results show that the equivalents can reproduce the nonlinear and discontinuous behaviour of their respective ADN, in particular the disconnection of some IBGs under low voltage conditions. The accuracy has been checked on disturbances not used for training.

Finally, the whole methodology has been applied to a real distribution system, hosting SGs, in addition to IBGs. The results further confirm the efficiency of the method.

Chapter 5

Update of the equivalent with operating conditions

As a follow up of the previous chapter, an approach is presented to update the equivalent in response to varying operating conditions. It starts with testing the accuracy of the equivalent for new operating conditions and proceeds with updating its set of parameters if not accurate enough. This inevitably raises the issue of sharing the work efficiently and fairly between the DSO and the TSO, while taking into account practicalities such as power system knowledge and confidentiality.

The chapter is organized as follows. Section 5.1 introduces the problem. Section 5.2 proposes a general collaborative scheme to update the ADN equivalent with changing operating conditions. The various steps are detailed in Section 5.3 and assigned to either the TSO or the DSO. Moreover, an approach to minimize the number of parameters to adjust is proposed and illustrated through simulation results in Section 5.4. A summary and concluding remarks are offered in Section 5.5.

5.1 Multiple equivalents for multiple operating conditions

While the methodology presented in Chapter 4 considered the derivation of an equivalent at a single operating point, it is important for the TSO to have ADN equivalents accommodating a wide range of operating conditions. This is even more relevant since ADNs host renewable and, hence, highly variable generation in addition to the usual varying loads. All this motivates the development of an approach to update the equivalent when it is found not accurate enough under new operating conditions. Indeed, it seems Utopian to find a single set of parameters enabling the equivalent to cover all possible operating conditions. Instead, multiple sets of parameters, each pertaining to a subset of operating conditions, could advantageously be identified. An alternative would entail updating the equivalent “on the fly” in response to changing operating conditions.

In the former case, the multiple sets of parameters would be stored by the TSO with “labels” referring to the operating conditions they are able to cover. In the latter case, the accuracy of the parameter vector currently used by the TSO would be regularly assessed and updated if the accuracy deteriorates.

The operating conditions considered in this work involve load, irradiation and wind variations. Changes of the distribution network topology, such as the opening of a feeder, are also contemplated.

The simulations of this chapter have been performed on the 75-bus 11-kV distribution grid (i.e. ADN No 2). The topology of its equivalent is shown in Fig. 4.20.

5.2 On the TSO-DSO share of work

The need for understanding and managing TSO-DSO interactions to enforce the security, stability and efficiency of future power systems has gained much attention in recent times [GMR20].

Indeed, Europe’s energy landscape is experiencing a profound change as increasing amounts of renewable energy sources displace conventional forms of generation. This development has gone hand-in-hand with an expanding share of power production taking place at the distribution level. These trends are expected to continue and will often necessitate a revision of the way TSOs and DSOs interact [Gri15]. Indeed, TSOs and DSOs face new challenges that will require greater coordination [CE15].

A greater coordination between TSOs and DSOs implies a larger amount of data exchanged. An overview of such data exchanges to face the challenges posed by distributed energy resources is presented in [LMR⁺18].

Moreover, multiple tools aiming at improving TSOs-DSOs collaboration are proposed, for instance in [FSS⁺16, SMTB], and a model driven methodology to implement an inter-operable communication architecture supporting TSO-DSO information exchange is offered in [SST⁺19].

The derivation of ADN equivalents also requires to increase the TSO-DSO collaboration. The next sections propose a way for TSO and DSO to share the work :

1. for the derivation of an ADN equivalent at a single operating point (this builds on the procedure presented in detail in Chapter 4);
2. for the update of the equivalent, in response to changing operating conditions.

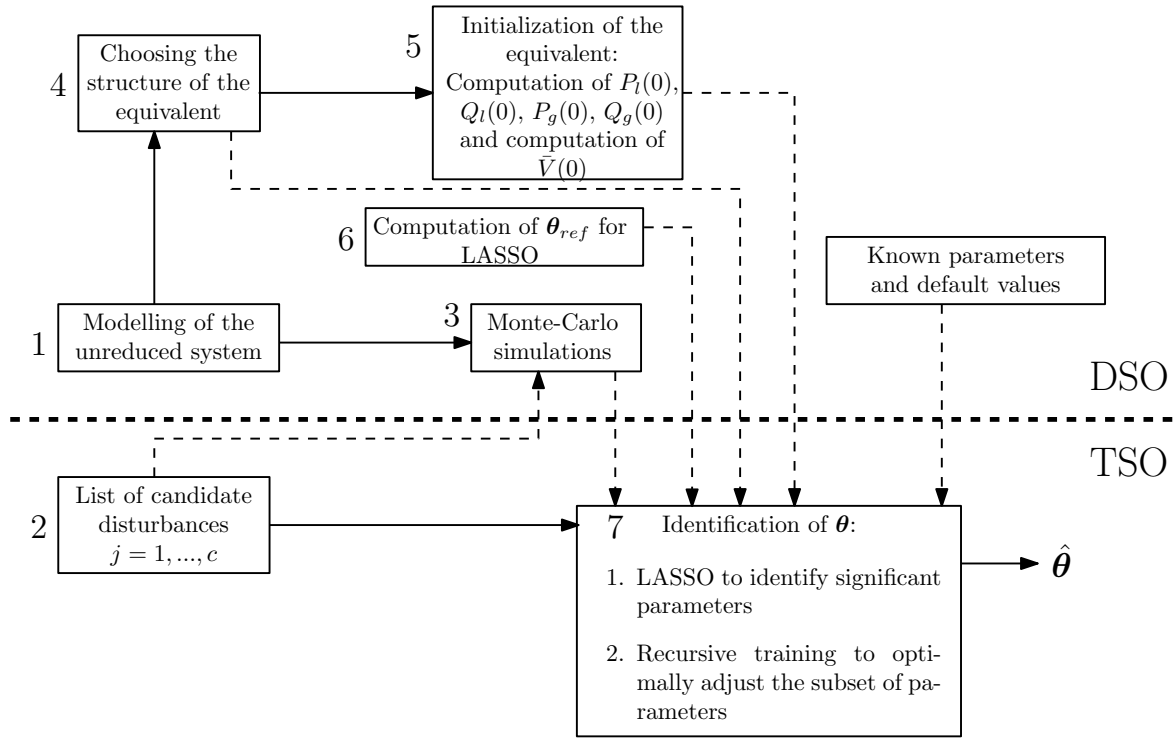


Figure 5.1: The steps towards the derivation of an ADN equivalent considering a single operating point

5.3 Handling of new operating conditions : overview of procedure

5.3.1 Setting up an ADN equivalent for a single operating point

The diagram in Fig. 5.1 shows a decomposition of the steps to derive an ADN equivalent at a given operating point. The upper part of the chart gathers the tasks that should be performed by the DSO while the lower part refers to tasks by the TSO. Dashed arrows represents the flows of data that are exchanged between the two entities. The numbers refer to the sequential steps detailed hereafter :

1. The DSO collects the data of its own system of which a detailed, unreduced model is built;
2. meanwhile the TSO specifies a list of candidate disturbances for the identification of the ADN equivalent;
3. the list of candidate disturbances received by the DSO is used to perform the MC simulations, i.e. to generate the sets of randomized dynamic responses, from which the averages and the variances are extracted and sent to the TSO;
4. based on the knowledge of its system, the DSO selects an appropriate structure (i.e. topology) for the equivalent. The latter is communicated to the TSO;

5. the DSO collects the data to initialize the equivalent, i.e. it computes the pre-disturbance active and reactive powers consumed by the equivalent load $P_l(0)$ and $Q_l(0)$ (see Fig. 4.20). The same is done for the pre-disturbance active and reactive powers produced by the equivalent IBG $P_g(0)$ and $Q_g(0)$ (see Fig. 4.20). Finally, the pre-disturbance voltage $\bar{V}(0)$ at the entry point of the ADN (see Fig. 4.20) is obtained by performing a power flow computation on the unreduced system. Its value is then retained in the equivalent. The pre-disturbance powers ($P_l(0)$, $P_g(0)$, $Q_l(0)$ and $Q_g(0)$) along with $\bar{V}(0)$ are communicated to the TSO, which is now able to run a power flow computation on the equivalent;
6. the DSO determines the θ_{ref} values and transfer them to the TSO (along with default values of known parameters) for use in the LASSO method (see Section 4.6);
7. finally, the TSO carries out the identification of the ADN equivalent, more precisely the computation of $\hat{\theta}$. This is performed in the two steps shown in Fig. 5.1.

5.3.2 Accommodating multiple operating conditions

The steps to accommodate multiple operating conditions are presented in Fig. 5.2 with the same notation as in Fig. 5.1 for the DSO-TSO tasks and the data flows. In this context, the TSO is supposed to have at its disposal a repository of E previously identified equivalents, each characterized by its vector $\hat{\theta}$ of parameters and relative to previously experienced operating conditions.

The successive steps for the handling of a new situation are detailed hereafter with reference to the numbered blocks in Fig. 5.2.

1. To reflect the change of operating conditions or network configuration, the nodal active and reactive powers in the unreduced system are updated by the DSO;
2. the TSO draws the list of c candidate disturbances that will be considered for the training of the equivalent;
3. a new operating point requires new MC simulations. They are performed by the DSO processing the list of disturbances communicated by the TSO. The extracted statistics $\mu_P^{new}(j)$, $\mu_Q^{new}(j)$, $\sigma_P^{new}(j)$ and $\sigma_Q^{new}(j)$ ($j = 1, \dots, c$) are transferred to the TSO;
4. the DSO also computes the new pre-disturbance nodal data of the equivalent, based on the updated nodal active and reactive powers in the unreduced system (see Step 1). Anew, the pre-disturbance voltage $\bar{V}(0)$ at the entry point of the ADN is obtained by performing a power flow computation on the unreduced system and is sent to the TSO along with the updated pre-disturbance powers ($P_l(0)$, $P_g(0)$, $Q_l(0)$ and $Q_g(0)$);

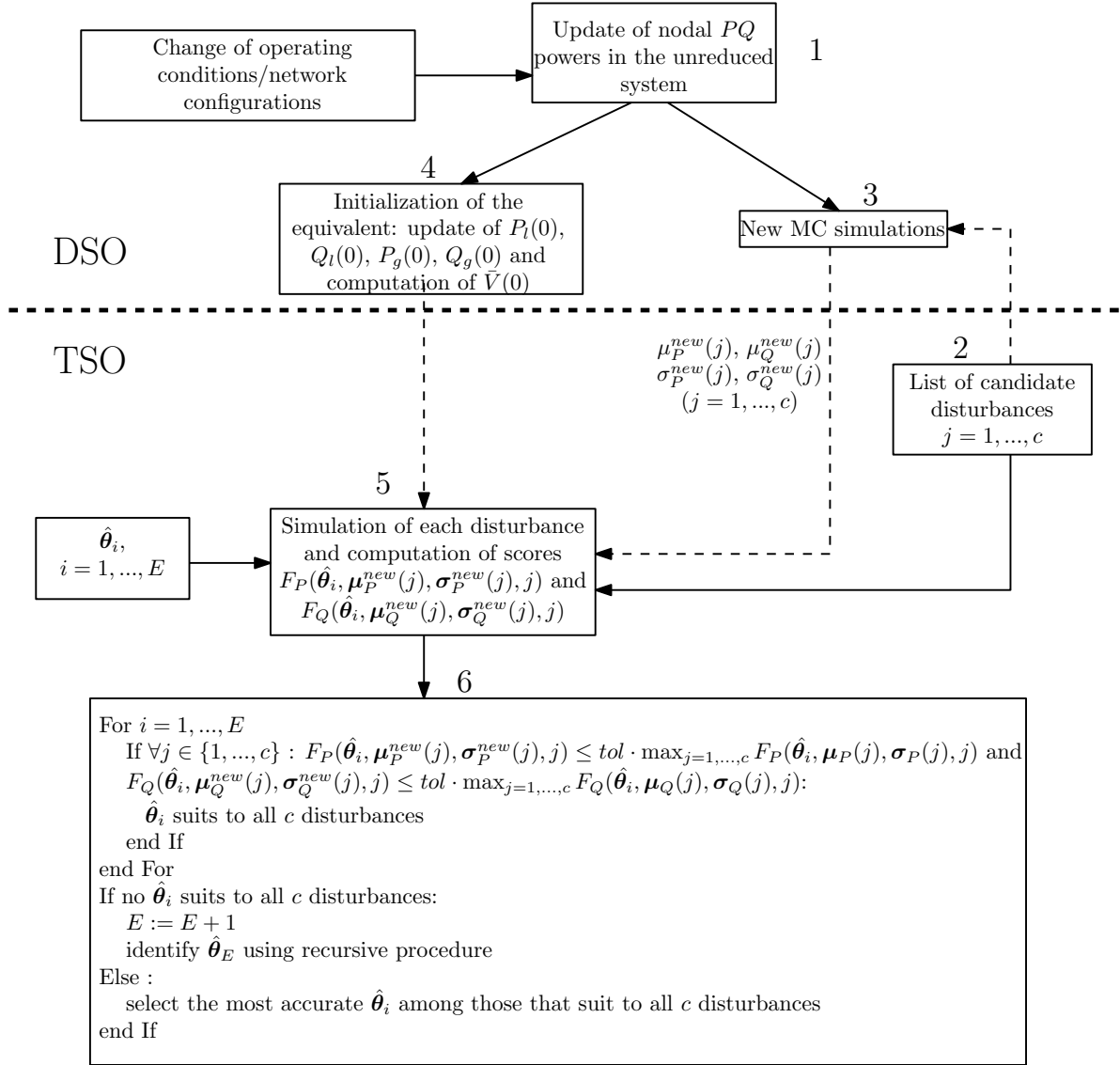


Figure 5.2: The steps towards the update of the equivalent for accomodating multiple operating conditions

5. the TSO simulates the responses (to the c disturbances) of each of the E equivalents available, starting from the initial conditions specified at step 4. From those simulations, the following scores are computed :

$$F_P(\hat{\theta}_i, \mu_P^{new}(j), \sigma_P^{new}(j), j) = \frac{1}{N} \sum_{k=1}^N \left[\frac{P_e(\hat{\theta}_i, j, k) - \mu_P^{new}(j, k)}{\sigma_P^{new}(j, k)} \right]^2 \quad (5.1)$$

$$F_Q(\hat{\theta}_i, \mu_Q^{new}(j), \sigma_Q^{new}(j), j) = \frac{1}{N} \sum_{k=1}^N \left[\frac{Q_e(\hat{\theta}_i, j, k) - \mu_Q^{new}(j, k)}{\sigma_Q^{new}(j, k)} \right]^2 \quad (5.2)$$

where P_e and Q_e are the active and reactive power responses of the equivalent, respectively, and N is the number of discrete times of the simulation;

6. the scores (5.1, 5.2) are used to assess the ability of the available equivalents to deal with the new situation. This consists of comparing, for each candidate disturbance, the score obtained with the parameters $\hat{\theta}_i$ of the i -th equivalent ($i = 1, \dots, E$) with the worst score obtained during the identification of $\hat{\theta}_i$ ¹.

If one or several equivalents pass the accuracy test, there is no need to identify a new one. The equivalent yielding the highest accuracy, evaluated from (4.8, 4.9), is selected.

If no equivalent passes the accuracy test, a new one has to be added to the existing set (i.e. a new $\hat{\theta}_i$ has to be identified). This is considered in further detail in Section 5.4.

It is worth noting that the above procedure does not entail passing the detailed ADN model to the TSO. The latter is simulated by the DSO, thereby avoiding data confidentiality issues, if any.

5.3.3 A possible lighter procedure

An alternative, lighter version of the process, would consist of identifying a representative instance of the ADN model for a given operating point (using the method proposed in Section 3.4). The representative instance would be used to evaluate the accuracy of the available equivalents for varying operating conditions, thereby not requiring new Monte-Carlo simulations (see step 3). This alternative would significantly reduce the computational burden. Yet, this relies on the assumption that the method presented in Section 3.4 would identify the same representative instance of the ADN model, for the different operating conditions.

5.4 Building a new equivalent with minimal update effort

When building an equivalent for new operating conditions, it can be expected that the values of some parameters, inherited from former equivalents, change very little, so that a complete new identification can be avoided.

To identify the parameters of concern, the LASSO technique (see Section 4.6) can be used again, as detailed and illustrated in this section.

¹This latter score should be stored together with $\hat{\theta}_i$. A tolerance (“tol” in Fig. 5.2) can be used to somewhat relax this test.

5.4.1 Proposed approach

Once the accuracy of each $\hat{\theta}_i$ have been assessed, on the c candidate disturbances, for the new operating point, the best among them is used as a reference. We denote :

$$\hat{\theta}^{ref} = \arg \min_{i=1,\dots,E} \frac{1}{c} \sum_{j=1}^c \left[F_P(\hat{\theta}_i, \mu_P^{new}(j), \sigma_P^{new}(j), j) + F_Q(\hat{\theta}_i, \mu_Q^{new}(j), \sigma_Q^{new}(j), j) \right] \quad (5.3)$$

and used this reference in a variant of the LASSO method, as explained next.

The goal being to minimize the number of parameters to adjust, the following objective function is considered :

$$\min_{\theta} F(\theta) + \lambda \sum_{l=1}^n |\hat{\theta}_l^{ref} - \theta_l| \quad (5.4)$$

where

$$F(\theta) = \frac{1}{d} \sum_{j=1}^d [F_P(\theta, j) + F_Q(\theta, j)] \quad (5.5)$$

$$\theta^L \leq \theta \leq \theta^U \quad (5.6)$$

and

$$\theta^L = \hat{\theta}^{ref} - \alpha \hat{\theta}^{ref} \quad (5.7)$$

$$\theta^U = \hat{\theta}^{ref} + \alpha \hat{\theta}^{ref} \quad (5.8)$$

where $0 \leq \alpha \leq 1$.

The d disturbances leading to the maximum (i.e. worst) scores among the c candidate disturbances, defined as :

$$F_P^{max}(\hat{\theta}^{ref}) = \max_{j=1,\dots,c} F_P(\hat{\theta}^{ref}, j) \quad (5.9)$$

$$F_Q^{max}(\hat{\theta}^{ref}) = \max_{j=1,\dots,c} F_Q(\hat{\theta}^{ref}, j) \quad (5.10)$$

are used to solve the above optimization problem.

For an appropriate value of λ , the parameters that vary significantly with respect to $\hat{\theta}^{ref}$ are considered to yield a significant improvement of $F(\theta)$. It is expected that they can be identified in a few iterations of the DE algorithm.

The issue is to determine a good value for λ . Simulation results have shown that $\lambda = F(\hat{\theta}^{ref})$ is a good start.

The process thus starts with $\lambda = F(\hat{\theta}^{ref})$. After a few iterations of the DE algorithm, if no significant improvement of $F(\theta)$ is obtained, λ is decreased and the process continues. It stops

Table 5.1: List of operating conditions and associated $\hat{\theta}_i$

#	Operating conditions	$\hat{\theta}_i$
1	Base load, mild irradiation, strong wind	$\hat{\theta}_1$
2	Base load, mild irradiation, weak wind	$\hat{\theta}_1$
3	Small load, no irradiation, strong wind	$\hat{\theta}_2$
4	Small load, no irradiation, weak wind	$\hat{\theta}_2$
5	Case 1 with one open feeder (see Fig. 5.6)	$\hat{\theta}_3$
6	Small load, strong irradiation, strong wind	$\hat{\theta}_4$
7	Small load, strong irradiation, weak wind	$\hat{\theta}_5$
8	Case 7 with three WTs disconnected	$\hat{\theta}_6$
9	Small load, weak irradiation, strong wind	$\hat{\theta}_5$
10	Small load, weak irradiation, weak wind	$\hat{\theta}_4$
11	Large load, weak irradiation, strong wind	$\hat{\theta}_5$
12	Large load, weak irradiation, weak wind	$\hat{\theta}_1$

when the equivalent is sufficiently accurate with respect to the d disturbances. At this point, if the accuracy test of the equivalent for the remaining $c - d$ disturbances is not passed, the recursive procedure presented in Section 4.5 takes the lead until the accuracy criterion is reached for all c disturbances.

5.4.2 Simulation results

The procedure is illustrated step by step in the remaining of this section.

As previously mentioned, only ADN No 2 is considered.

Multiple realistic operating conditions as well as a change in network topology are contemplated.

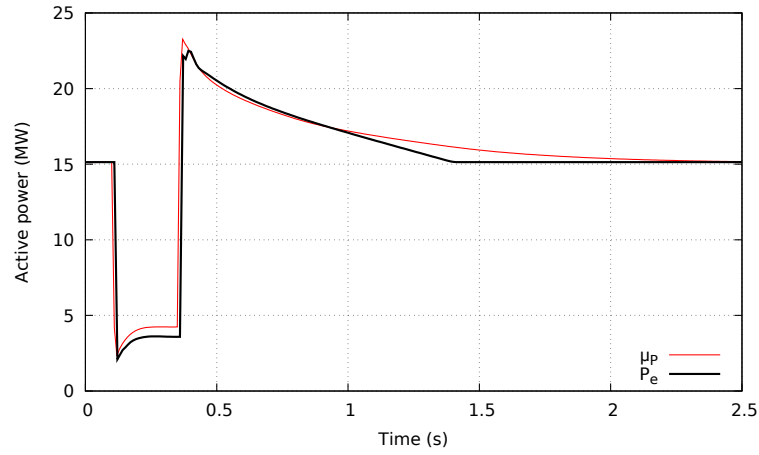
Twelve different operating conditions have been considered by varying the load level as well as the irradiation and wind. They are described in Table 5.1.

The total IBG capacity of the ADN is 14.8 MW, split into 6.8 MW of PV units and 8 MW of WTs. Information about the load, wind and irradiation levels is provided in Table 5.2.

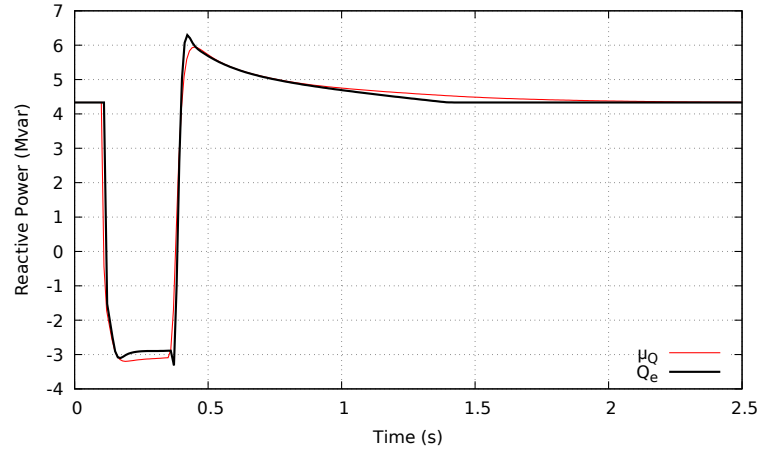
Note that operating conditions 3 and 4 in Table 5.1 account for nights scenarios while the others are days scenarios. For days scenarios it is assumed that the average percentage of motor load in the system is 10% while it is 60% during night, assuming an increased fraction of industrial loads. This information is assumed to be known by the DSO.

Table 5.2: Main characteristics of the operating points. Penetrations in % refer to the installed capacity

Load			Wind		Irradiation		
Small	Base	Large	Weak	Strong	Weak	Mild	Strong
14.9 MW	19.8 MW	30.3 MW	20 %	80 %	10 %	50%	90 %



(a) Active power



(b) Reactive power

Figure 5.3: Operating condition No 2 : active and reactive power responses to disturbance No 12 for $\hat{\theta}_1$

The candidate disturbances are still those in Table 3.2. Only voltage dips are considered, since it has been shown in Chapter 4 that it covers other type of disturbances, while the reverse is not true.

Let us assume that, initially, only a single vector of parameter is available ($E = 1$). The latter

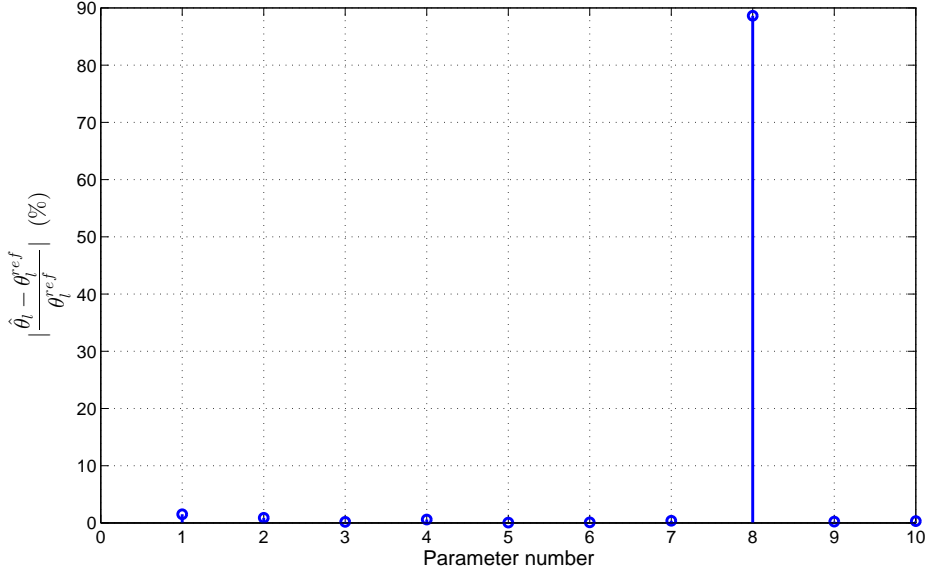


Figure 5.4: Operating condition No 3 : final values of $|\hat{\theta}_l - \theta_l^{ref}| / \theta_l^{ref}$ (in %) with $\theta^{ref} = \hat{\theta}_1$

is denoted by $\hat{\theta}_1$ and has been identified under the operating condition No 1 (see Table 5.1) with 19.8 MW of load and 9.8 MW of IBG production. This is nothing but the vector of parameters identified in Chapter 4 for ADN No 2. Note that 10 parameters were retained in θ for this equivalent.

Let us assume now that operating point No 2 is prevailing, characterized by a lower pre-disturbance WTs production. The total load is 19.8 MW and the total IBG production 5 MW. The accuracy test is performed on $\hat{\theta}_1$ (see Step 6 in Section 5.3.2). It appears that only the disturbance No 12 exhibits scores slightly above 1, which is acceptable accuracy. Therefore, no new identification is required and $\hat{\theta}_1$ can be used for both operating conditions 1 and 2. To illustrate this, the response of the equivalent to disturbance No 12 is compared with the average power response in Fig. 5.3, obtained from MC simulations for the new operating point No 2. It can be seen that the equivalent correctly matches the average response.

Operating condition No 3 is now considered. This is a night scenario. The total load is reduced to 14.9 MW with 60 % of motor load. The total IBG production comes from WTs only and accounts for 6.4 MW.

The accuracy test is performed on $\hat{\theta}_1$ (the only available set of parameters so far) and reveals two disturbances with low accuracy (i.e. scores much larger than 1). These disturbances are used to perform the approach presented in Section 5.4.1. The relative variation of the 10 components of θ with respect to $\theta_{ref} = \hat{\theta}_1$ is shown in Fig. 5.4. It shows very clearly that only parameter No 8, i.e.

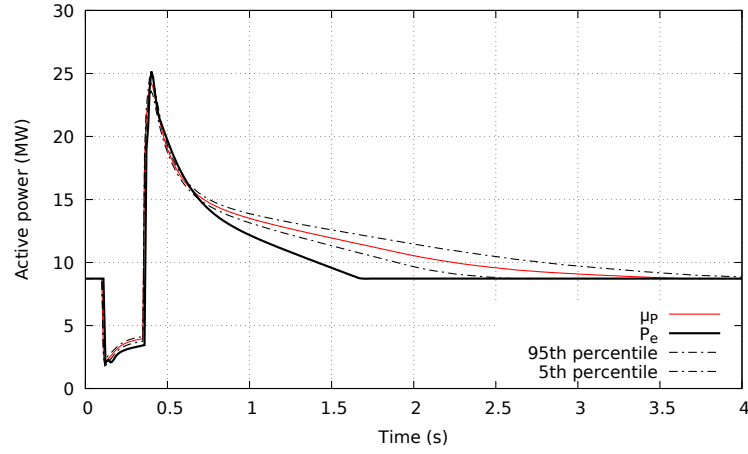
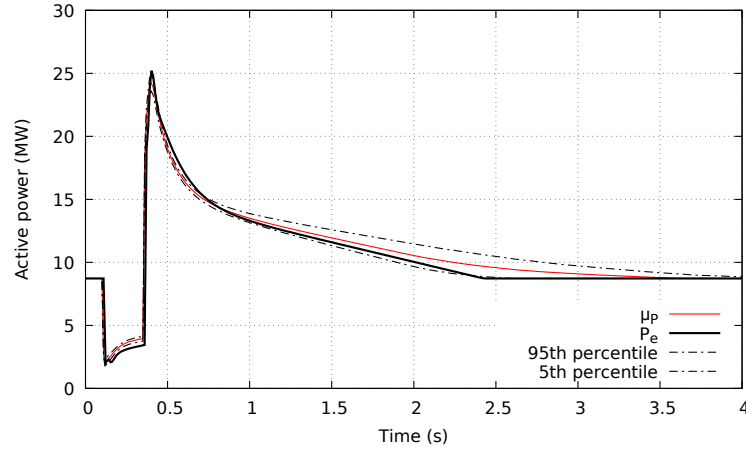
(a) $\hat{\theta}_1$ used in the equivalent(b) $\hat{\theta}_2$ used in the equivalent

Figure 5.5: Operating condition No 3 : active power response to disturbance No 12 for (a) $\hat{\theta}_1$ and (b) $\hat{\theta}_2$

the IBG maximum rate of active current recovery $(\frac{di_p}{dt})_{max}$, needs to be updated. This indicates that mainly the accuracy of the active power responses is affected. Thus $\hat{\theta}_1$ is updated into $\hat{\theta}_2$. With $\hat{\theta}_2$ used in the equivalent, the targeted accuracy is achieved for all c disturbances and the recursive training procedure is not required.

As an illustration, Fig. 5.5 shows the active power responses of the equivalent using $\hat{\theta}_1$ (Fig. 5.5a) and $\hat{\theta}_2$ (Fig. 5.5b), compared with the average active power response obtained from MC simulations. It is seen clearly that the response of the equivalent with $\hat{\theta}_1$ is not accurate because $(\frac{di_p}{dt})_{max}$ is not set to an appropriate value. After adjusting this parameter, Fig. 5.5b confirms that P_e matches μ_P much more accurately.

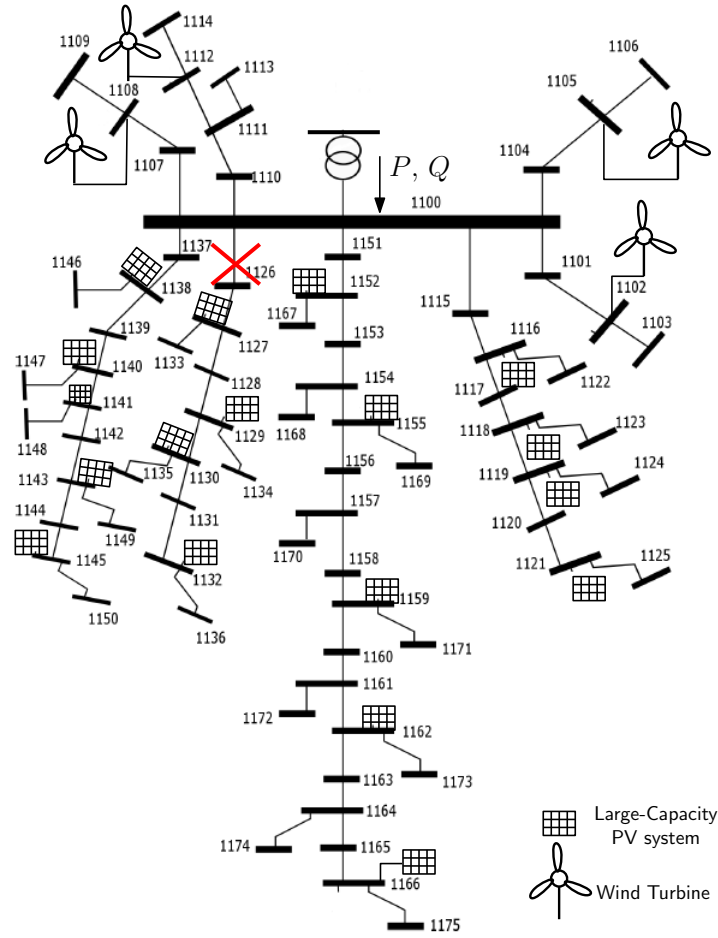


Figure 5.6: ADN No 2 with one open feeder (marked with a red cross)

It makes sense that the rate of active current recovery is affected by this change of operating conditions. Indeed, the PV units do not produce active power, their are not ramping up their active current after the fault (i.e. less active power has been sacrificed), which affects the average rate of recovery of the units distributed in the system. Incidentally, it is very satisfying to find that the results of the “automatic” LASSO-based procedure coincides with expectations coming from “engineering judgment”.

We proceed with operating condition No 4. The accuracy test now performed with the two available parameter sets ($E = 2$) shows that $\hat{\theta}_2$ suits all c disturbances. Therefore, no new identification is required.

Operating condition No 5 corresponds to operating condition No 1 but with one feeder opened (see Fig. 5.6, where the red cross indicates the disconnected feeder). This represents a decrease of

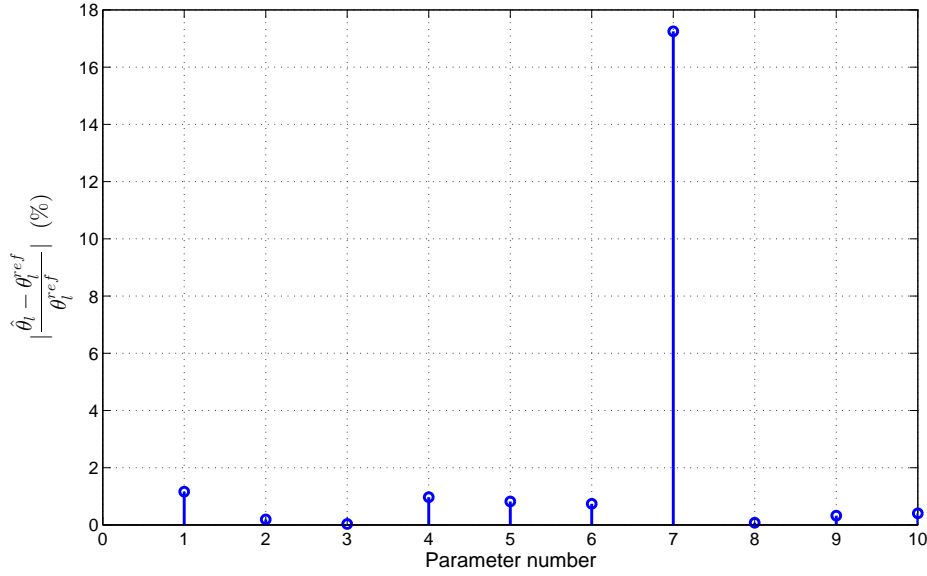


Figure 5.7: Operating condition No 5 : final values of $|\hat{\theta}_l - \theta_l^{ref}|/\theta_l^{ref}$ (in %) with $\theta^{ref} = \hat{\theta}_1$

3 MW of load, 1.4 MW of PV capacity and 0.7 MW of PV production. In total, the load amounts to 16.8 MW and the IBG production to 9.1 MW.

The accuracy test shows that neither $\hat{\theta}_1$ nor $\hat{\theta}_2$ suits all c disturbances. However, $\hat{\theta}_1$ shows better results than $\hat{\theta}_2$. The approach of Section 5.4.1 is thus applied with $\theta_{ref} = \hat{\theta}_1$.

The relative variation of the 10 parameters of θ with respect to $\hat{\theta}_1$ is shown in Fig. 5.7. It reveals that only the parameter No 7, the IBG nominal current I_{nom} , has to be adjusted. Doing so, $\hat{\theta}_1$ is updated into $\hat{\theta}_3$. After adjusting this parameter, the targeted accuracy is achieved for all c disturbances and the recursive training procedure is not called upon.

It is seen in Fig. 5.8 that the value of I_{nom} mainly influences the reactive power response of the equivalent during the voltage dip, when the IBGs are requested to inject reactive current to support their terminal voltage. Before the adjustment of I_{nom} (see Fig. 5.8a), the accuracy is not really acceptable during the voltage dip, while Q_e accurately matches μ_Q when I_{nom} is adjusted (see Fig. 5.8b).

Intuitively, it makes a lot of sense to adjust I_{nom} in the equivalent IBG when a part of the total IBG capacity is lost. This again confirms that the approach can be backed up by rather easy interpretations.

The operating point No 6 is now considered. The latter involves a low load level, a strong irradiation and a strong wind. Hence, the net power entering the system is strongly reduced with

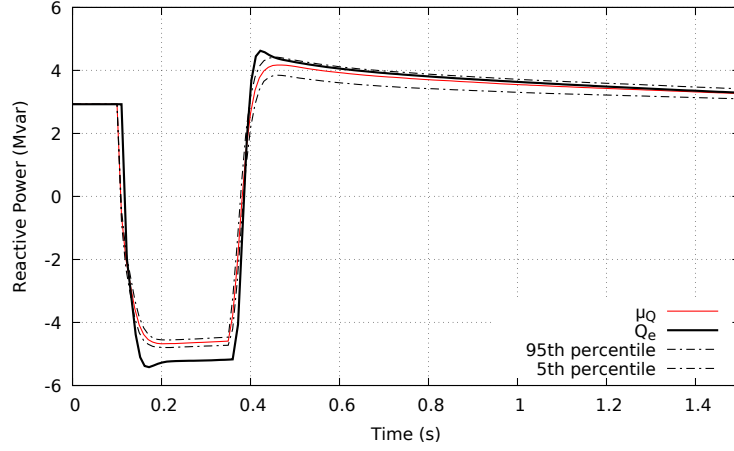
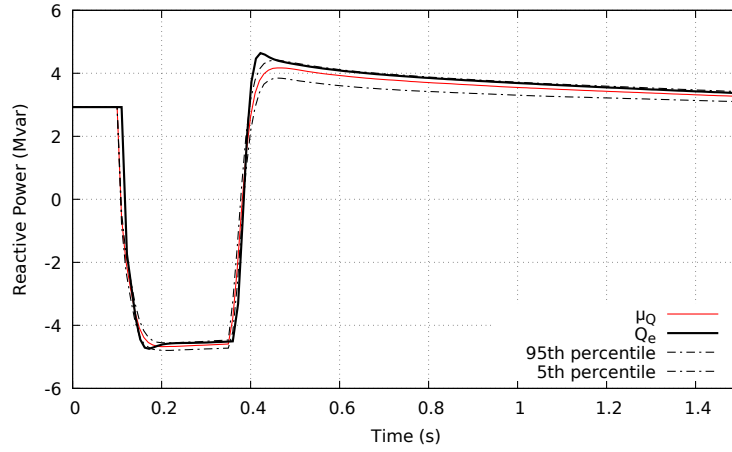
(a) $\hat{\theta}_1$ used in the equivalent(b) $\hat{\theta}_3$ used in the equivalent

Figure 5.8: Operating condition No 5 : reactive power response to disturbance No 12 for (a) $\hat{\theta}_2$ and (b) $\hat{\theta}_3$

respect to previous operating conditions. Indeed, the total load decreases to 14.9 MW and the pre-disturbance IBG production increases to 12.5 MW.

The accuracy test for all available $\hat{\theta}_i$ ($E = 3$) is then performed. Among them, $\hat{\theta}_2$ shows the best performance. However, the accuracy is slightly under what is acceptable. The procedure of Section 5.4.1 with $\theta^{ref} = \hat{\theta}_2$ indicates, in this case, that all parameters but two need to be adjusted, as confirmed by Fig. 5.9. The two parameters that do not require adjustment are the leakage stator inductance of the equivalent motor and the nominal current I_{nom} of the equivalent IBG. It is not straightforward to give an interpretation of this result.

Moreover, after the procedure of Section 5.4.1 is executed, the minimum accuracy of some dis-

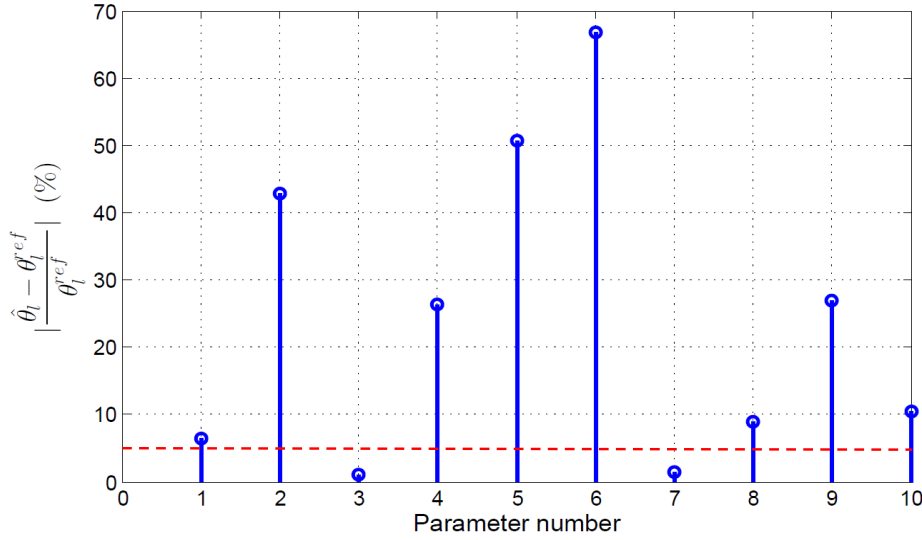


Figure 5.9: Operating condition No 6 : final values of $|\hat{\theta}_l - \theta_l^{ref}| / \theta_l^{ref}$ (in %) with $\theta^{ref} = \hat{\theta}_2$

turbances is not achieved yet. Hence it is required to resort to the recursive training procedure. $\hat{\theta}_4$ is thus obtained. Yet, the active power responses of two training disturbances (No 12 and 7) are still slightly below the accepted tolerance. Figure 5.10 shows the active power responses of the equivalent with $\hat{\theta}_4$ versus the average responses for these two disturbances. The main difference with respect to previous operating conditions is during the voltage dip, when the active powers re-increase rapidly after their initial reduction at the disturbance occurrence (see particularly Fig. 5.10b). This comes from the IBG response. Indeed, since the IBG pre-disturbance production is large, the amount of active power that is sacrificed during the voltage dip (to leave room for reactive current) is important, which increases the net load of the system. Note that, while this part is accurately reproduced by the equivalent model, it encounters more difficulty to reproduce correctly the response of the system after the voltage recovery.

It turns out that, for strong initial IBG production and low load conditions, it is more complex to find a rate of active current recovery that suits to all disturbances with satisfactory accuracy. It appears that in those conditions, the active power recovery of IBGs after a fault, comes from various units of different sizes dispersed in the original system, which is more difficult to reproduce with a single value for the rate of active current recovery, as considered in the equivalent IBG. The value found by least-square minimization is a trade-off that minimizes the error over all considered training disturbances.

This also explains the results of Fig. 5.9, where more parameters move away from their reference value when the sole adjustment of the maximum rate of active current recovery is not sufficient.

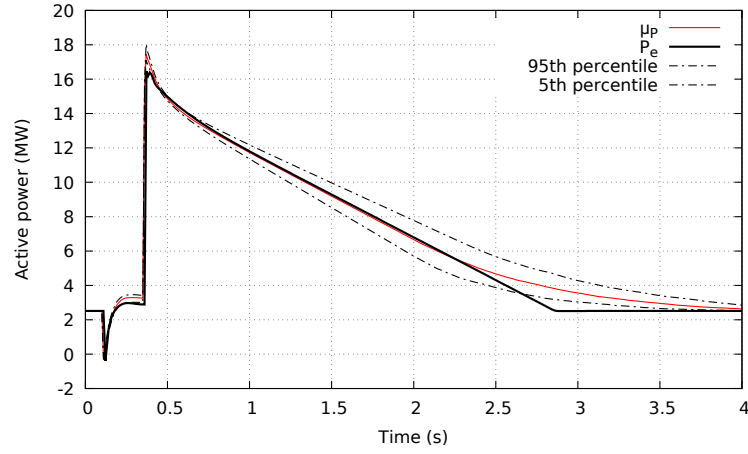
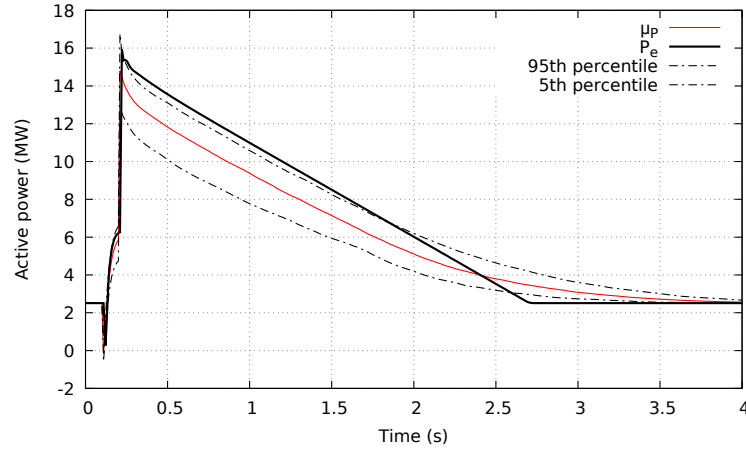
(a) $\hat{\theta}_4$ used in the equivalent : Disturbance No 12(b) $\hat{\theta}_4$ used in the equivalent: Disturbance No 7

Figure 5.10: Operating condition No 6 : active power response to disturbances (a) No 12 and (b) 7 for $\hat{\theta}_4$

Nevertheless, it can be observed from Fig. 5.10 that the response of the equivalent is not so far from the average response.

The operating condition No 7 is now considered. With respect to the previous one, only the wind power is decreased leading to a pre-disturbance IBG production reduced from 12.5 to 7.7 MW.

The accuracy test on all c candidate disturbances does not reveal any $\hat{\theta}_i$ ($E = 4$) with an acceptable accuracy. The parameter set $\hat{\theta}_4$ is the best among them. The procedure of Section 5.4.1 shows that, once again, the maximum rate of active current recovery needs to be adjusted. With the updated parameter vector $\hat{\theta}_5$, the targeted accuracy is achieved for all c disturbances.

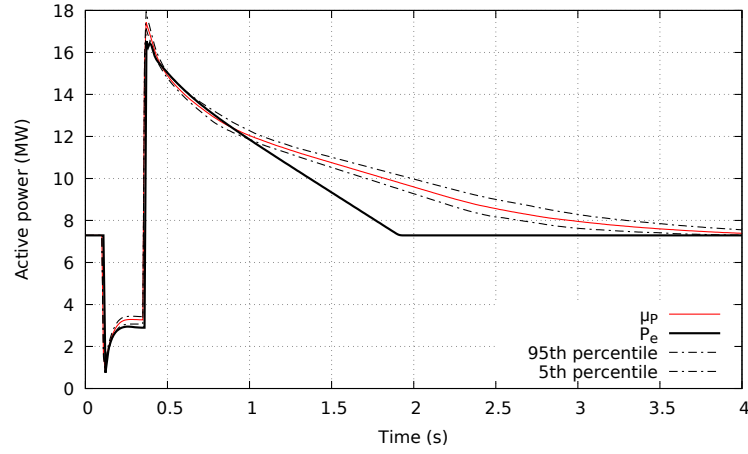
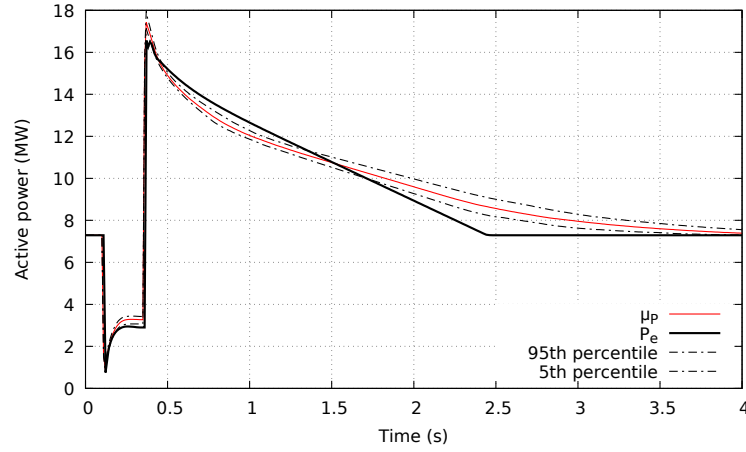
(a) $\hat{\theta}_4$ used in the equivalent(b) $\hat{\theta}_5$ used in the equivalent

Figure 5.11: Operating condition No 7 : active power response to disturbance No 12 for (a) $\hat{\theta}_4$ and (b) $\hat{\theta}_5$

Figure 5.11 shows the active power evolution of the equivalent compared with μ_P in response to disturbance No 12 using $\hat{\theta}_4$ (Fig. 5.11a) and $\hat{\theta}_5$ (Fig. 5.11b), respectively. While the accuracy is significantly improved, one can observe again some difficulties in finding a value for the maximum rate of recovery that suits to all candidate disturbances. Yet, the accuracy is acceptable.

Operating point No 8 is similar to No 7 but with three WTs not in operation. This represents a lack of 6 MW of capacity and 1.2 MW of production.

The accuracy test shows that $\hat{\theta}_2$ is the most accurate among the $E = 5$ parameter sets available ($E = 5$), yet not sufficiently to cover all c candidate disturbances. The procedure of Section 5.4.1 reveals, once again, that I_{nom} is the only parameter to be updated. This makes sense since the

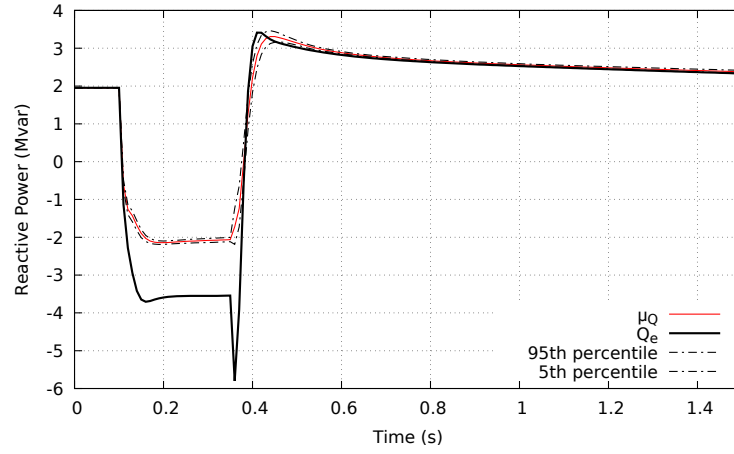
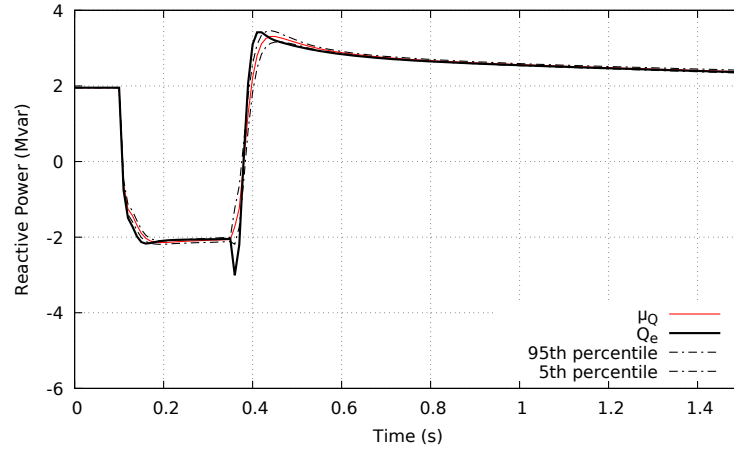
(a) $\hat{\theta}_2$ used in the equivalent(b) $\hat{\theta}_6$ used in the equivalent

Figure 5.12: Operating condition No 8 : reactive power response to disturbance No 12 for (a) $\hat{\theta}_2$ and (b) $\hat{\theta}_6$

operating condition under which $\hat{\theta}_2$ has been identified shows a similar IBG production, but with a strong difference of the total IBG capacity. This leads to adjust $\hat{\theta}_2$ into $\hat{\theta}_6$.

Figure 5.12 compares the reactive power response of the equivalent with μ_Q in the case of disturbance No 12 with $\hat{\theta}_2$ (Fig. 5.12a) and $\hat{\theta}_6$ (Fig. 5.12b), respectively. It can be seen that the response of the equivalent with $\hat{\theta}_2$ is not acceptable. After adjusting I_{nom} (Fig. 5.12b), Q_e matches μ_Q much more accurately, particularly during the voltage dip, where IBGs provide reactive support.

As summarized in the third column of Table 5.1, all remaining operating conditions considered (i.e. Nos 9 to 12) are covered by one of the $E = 6$ available parameter sets. No new parameter adjustment is needed. Time evolutions confirm the adequacy of the equivalent with one of the

parameter sets.

5.5 Summary and conclusions

This chapter has proposed a TSO-DSO share of work for

- deriving an equivalent at a given operating point;
- updating previously available equivalents to accommodate new operating conditions.

The flow of exchanged data is such that the DSO avoids sharing confidential data with the TSO. The flow charts in Figs. 5.1 and 5.2 illustrate these features.

To enrich the set of parameters with minimal effort, an approach that bears the spirit of the LASSO method has been detailed. It allows minimizing the number of parameters of the equivalent to be adjusted when new operating conditions are met. Simulations results reveal the good performances of this method.

From the results presented in this chapter, some general observations can be made :

1. properly reflecting the ADN operating conditions when initializing the (IBG and load) powers in the equivalent makes the subsequent update steps much easier;
2. in particular, only a few dynamic parameters need to be adjusted;
3. it is mainly the parameters of the equivalent IBG that need to be adjusted;
4. among them, the maximum rate of active current recovery $(\frac{di_p}{dt})_{max}$ and the nominal current I_{nom} appear to be the only parameters that need to be updated :
 - it is often required to adjust $(\frac{di_p}{dt})_{max}$ after a significant variation of the pre-disturbance active power produced by IBGs;
 - I_{nom} needs to be updated when the total IBG capacity varies.
5. the accuracy of the equivalent is more impacted for severe disturbances. When testing new operating conditions, scenarios involving IBGs disconnection never exhibit bad scores. The reason is merely that inaccurate IBG parameters have no impact when a significant part of the IBGs are taken out of service;
6. in most cases, a complete new parameter identification can be avoided and the updated set of parameters can be identified with low computational effort in a short amount of time.

This chapter has shown that, depending on the the number E of parameter sets, different levels of work can be encountered :

1. when E is small, new operating conditions require a complete new identification of the parameters (see operating condition No 6 for instance);
2. as E increases, the effort is reduced and only a small sub-set of the parameters have to be updated as there is more chance to find an appropriate $\hat{\theta}_i$ in the available set of equivalents;
3. when E is sufficiently large, updates of the parameter are no longer required as there is more chance to have an accurate $\hat{\theta}_i$ readily available.

Chapter 6

Control of a battery energy storage system to compensate for the equivalent inaccuracies

This chapter proposes a new application for a Battery Energy Storage System (BESS) connected at the distribution level. It consists of controlling the BESS active and reactive powers in such a way that the net power entering the distribution network matches as closely as possible the response of the dynamic equivalent model to large disturbances in the transmission system. This would allow compensating for the inaccuracies of the equivalent and, hence, using the reduced-order model with a higher guarantee of accuracy in dynamic simulations of the transmission system. The battery is supposed to be connected at the main substation of the distribution grid and its active and reactive powers are controlled without using any model of that grid. Simulations results are reported on the CIGRE MV test system (ADN No 1 introduced in Section 1.6.1). Good performances are found in response to disturbances of various severities.

The chapter is organized as follows. Section 6.1 motivates this rather unusual application of a BESS. Section 6.2 presents the overall control configuration while the BESS converter and controller models are detailed in Section 6.3. Section 6.4 deals with the modelling of the voltage phasor measurement process required for real time simulations of the equivalent (in the event of a disturbance in the transmission system). Simulation results, illustrating the performances of the BESS control for various disturbances, are presented in Section 6.5. Finally, the chapter is summarized and concluding remarks are offered in Section 6.6.

6.1 Introduction

Chapters 4 and 5 have proposed a methodology to derive reduced-order models of ADNs matching their average responses. However, Chapter 3 has emphasized that ADN models are affected by uncertainty, which leads to unavoidable discrepancies between the response of the equivalent and that of the real ADN.

This chapter explores a possible solution to the aforementioned problem and, to the author's best knowledge, a new approach. It takes advantage of the growing use of BESS in DNs. Indeed, the BESS technology is constantly evolving and several applications to DNs have become a reality, such as primary frequency control provision [SMN⁺18], flexible power management [KPPBJ18] or participation in voltage regulation [ZGG17]. The recent reference [ZYS⁺20] even proposes a real-time control method for BESSs to provide concurrent primary frequency and local voltage regulation services to power grids.

The idea developed in this thesis can be summarized as follows: in the event of a large disturbance in the transmission system, control the BESS in such a way that the power consumed by the distribution system obeys the equivalent model as closely as possible. The resulting advantage is that the equivalent can be used in dynamic simulations of the transmission system with higher guarantee of accuracy. The BESS being called to respond to infrequent large disturbances and over short periods of time, the energy used is expected to be small. Yet, to minimize the use of the battery (i.e. the energy) for this particular application, it is in the interest of the DSO that the TSO uses in its simulations the best possible equivalent model. In other words, the BESS would be used to increase the reliability of the equivalent model, with an incentive to improve the quality of the latter to minimize the use of the battery.

With this new application, it can be envisaged to update the parameters of the equivalent less frequently, since the BESS would be able to compensate for the inaccuracies of the equivalent with respect to the real system behaviour (which in any case is not known exactly). Yet, because of its limited capacity, there will be some point where the BESS would no longer be able to compensate for the inaccuracies of the equivalent. At that point, an update is essential in order the DSO to provide the service as expected.

6.2 Overview of the proposed BESS control

The overall configuration is sketched in Fig. 6.1. The active and reactive powers (P_t , Q_t) leaving the DN transformer are measured, as well as the voltage phasor $\bar{V} = V e^{j\delta}$ on its Medium Voltage (MV) side. P_t^{fltr} and Q_t^{fltr} are the active and reactive power output of a filter accounting for measurements delay and smoothing. In response to a disturbance in the transmission system

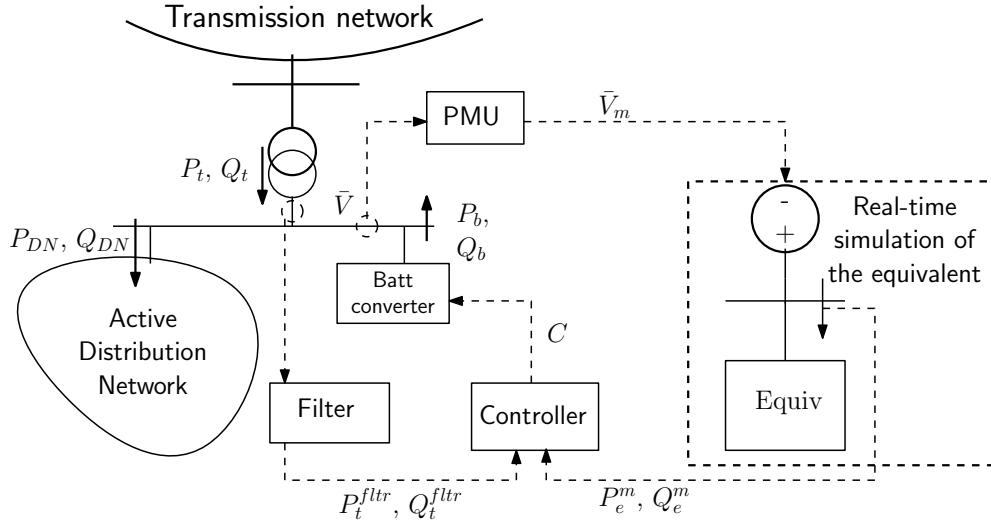


Figure 6.1: Overall configuration

(detected by a significant change in V), the response of the equivalent is simulated in real time using the measured MV voltage phasor \bar{V}_m . A Phasor Measurement Unit (PMU) is needed for that purpose [PT08]. Indeed, it is required to have access to the change in both the voltage magnitude and the phase angle to accurately simulate the response of the equivalent, denoted by P_e^m and Q_e^m . P_e^m and Q_e^m along with the measured powers P_t^{fltr} and Q_t^{fltr} are the inputs of a controller that generates a command C in order the BESS to produce active and reactive powers P_b, Q_b that satisfies $P_t^{fltr} \sim P_e^m$ and $Q_t^{fltr} \sim Q_e^m$. In other words, the battery converter is controlled in such a way that P_t and Q_t evolve with time as closely as possible to the equivalent power responses P_e and Q_e , obtained by simulating the equivalent model directly with \bar{V} , such as the TSO would do in his simulations. Note that $P_t = P_{DN} - P_b$ and $Q_t = Q_{DN} - Q_b$, where P_{DN} and Q_{DN} are respectively the actual active and reactive powers entering the ADN, as shown in Fig. 6.1.

Obviously, the controller must take into account the maximum current of the converter and other limits. It must be emphasized the controller does not use any model of the ADN and the equipment connected to it.

6.3 Modelling the BESS, its converter and its controller

The model of the BESS converter is presented in block-diagram form in Fig. 6.2. This model is based on the generic IBG model presented in Chapter 2. A model of the DC part of the DC/AC converter is not considered since it is not relevant for the range of dynamics considered here [WEC16]. Instead, the DC voltage is assumed to remain constant. This allows the converter to independently control the active and reactive powers [JDM19].

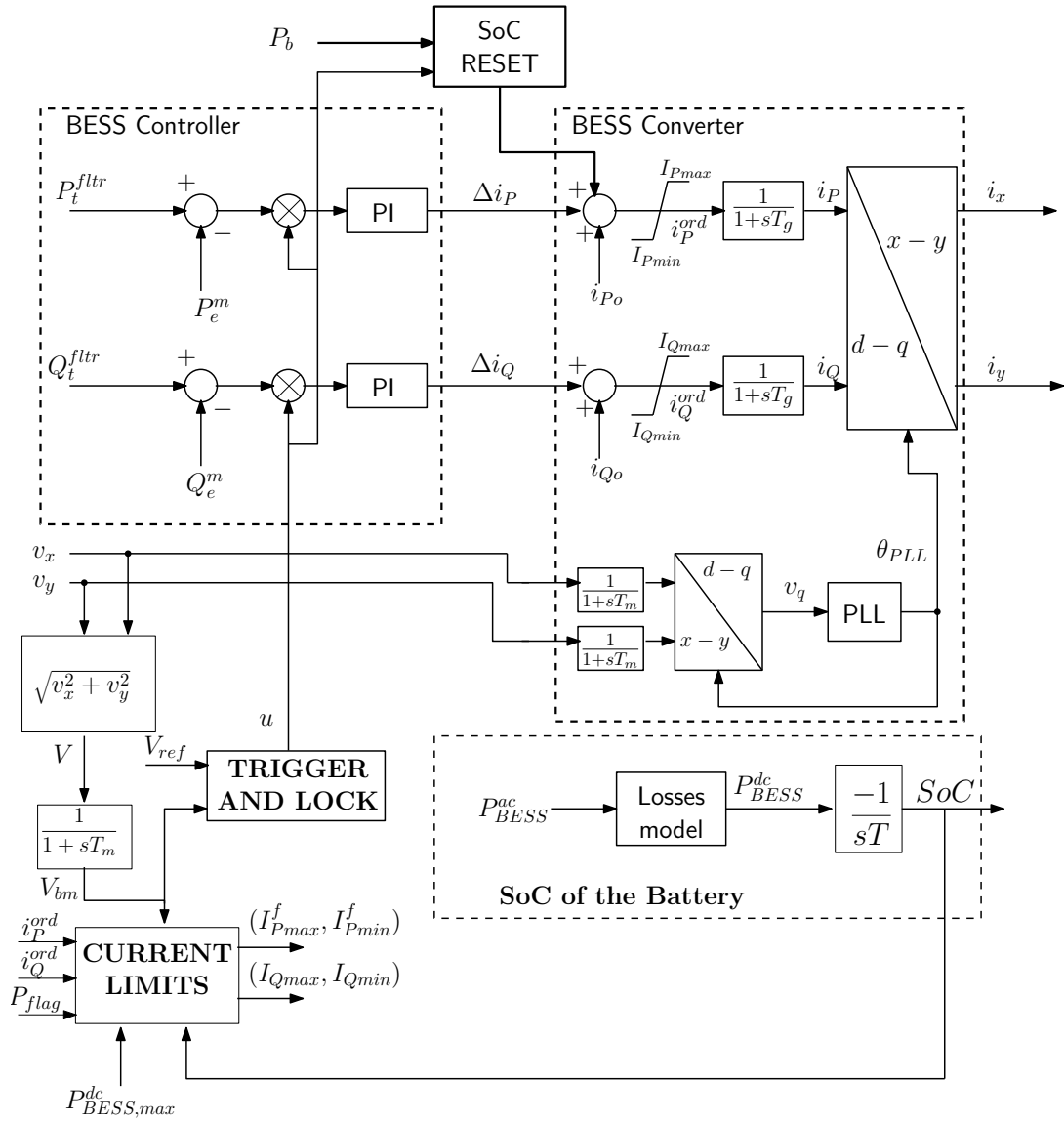


Figure 6.2: Modelling of the controller and the converter of the battery

The inputs v_x and v_y are the projections of the phasor of the terminal voltage on the rotating reference axes (x, y) used in phasor-mode simulation. The outputs i_x and i_y are the corresponding projections of the phasor of the current injected by the BESS.

The time constant T_m accounts for the voltage magnitude measurement delay, while T_g is the time constant of the converter current regulator [MG14b]. i_P^o (resp. i_Q^o) is the initial value of the active (resp. reactive) current, before the disturbance occurrence. The dynamics of the fast electronic components are not considered.

Figure 6.2 also shows the BESS controller. It simply consists of two Proportional-Integral (PI) controllers, one for the active power and the other for the reactive power. The outputs of the latter are corrections of current orders Δi_P and Δi_Q (corresponding to the command C of Fig. 6.1) that are added to i_P^o and i_Q^o yielding to the current orders i_P^{ord} and i_Q^{ord} .

6.3.1 Phase Locked Loop (PLL)

As recalled in Chapter 2, the PLL provides an estimate θ_{PLL} of the terminal voltage phase angle. This is needed to give to the injected current the proper phase angle with respect to that voltage. The PLL model is generic but allows to account for a nonzero response time. It is the same as presented in Chapter 2 (see Fig. 2.7).

6.3.2 Current limits

While controlling the active and reactive powers, the output current must not exceed the converter limit I_{nom} . To this purpose the active and reactive currents are upper limited to :

$$I_{Pmax} = P_{flag} I_{nom} + (1 - P_{flag}) \sqrt{I_{nom}^2 - (i_Q^{ord})^2} \quad (6.1)$$

$$I_{Qmax} = P_{flag} \sqrt{I_{nom}^2 - (i_P^{ord})^2} + (1 - P_{flag}) I_{nom} \quad (6.2)$$

respectively, where P_{flag} is a binary parameter that gives priority to either the active or the reactive current. In the former case, $P_{flag} = 1$, while in the latter case, $P_{flag} = 0$.

Since the BESS powers can flow in both directions, the active and reactive currents are lower limited symmetrically, i.e. :

$$I_{Pmin} = -I_{Pmax} \quad I_{Qmin} = -I_{Qmax}. \quad (6.3)$$

In addition to the converter current, the power P_{BESS}^{dc} delivered by the battery is also limited according to [SMN⁺18] :

$$P_{BESS}^{dc} \leq P_{BESS,max}^{dc} \quad (6.4)$$

where P_{BESS}^{dc} is the sum of the converter active power output and internal losses :

$$\begin{aligned} P_{BESS}^{dc} &= P_{BESS}^{ac} + P^{loss} \\ &= P_{BESS}^{ac} + (1 - \eta) \sqrt{P_{BESS}^{ac2} + Q_{BESS}^{ac2}} \end{aligned} \quad (6.5)$$

with η being the converter efficiency. In a first approximation, an ideal converter ($\eta = 1$) is assumed, which yields :

$$i_P = \frac{P_{BESS}^{ac}}{V_{bm}} \simeq \frac{P_{BESS}^{dc}}{V_{bm}} \quad (6.6)$$

and the limits finally applied to the active current are :

$$I_{Pmax}^f = \min(I_{Pmax}, \frac{P_{BESS,max}^{dc}}{V_{bm}}) \quad (6.7)$$

$$I_{Pmin}^f = \max(I_{Pmin}, -\frac{P_{BESS,max}^{dc}}{V_{bm}}) \quad (6.8)$$

where V_{bm} is the voltage magnitude measured by the BESS (see Fig. 6.2).

6.3.3 Battery state of charge

The State of Charge (SoC) of the battery is explicitly represented as shown in Fig. 6.2. P_{BESS}^{dc} is the power delivered by the battery, the time constant T is the rated maximum charging/discharging time.

This part of the model may also affect the value of I_{Pmin} if $SoC > SoC_{max}$ (resp. the value of I_{Pmax} if $SoC < SoC_{min}$). When the SoC reaches one of its limits, the bound I_{Pmax}^f or I_{Pmin}^f in (6.7, 6.8) is set to zero. This is integrated in the **current limits** block (see Fig. 6.2) which receives SoC as an input. SoC_{min} and SoC_{max} are set to typical values, i.e. 20 % and 80 %, respectively [WEC16].

Note, however, that the battery responding to infrequent large disturbances, it is called to deliver or absorb additional power for very short time durations. The requested amount of energy is thus small. Therefore, the SoC is not expected to vary significantly as shown with a numerical example in [WEC16] (pp.11 and 12).

6.3.4 Resetting the SoC of the BESS

Using the BESS to approach the dynamic response of an equivalent model, should not affect the other services it is expected to provide, such as power balancing, contribution to frequency control, etc. [SMN⁺18, KPPBJ18]. Furthermore, the BESS should be prepared to face the next disturbance.

Therefore, once the system has settled to (quasi-)steady state, it is desirable to restore the SoC of the BESS to the value it would have if no disturbance had occurred. This reset should be smooth to avoid disturbing the ADN and, to some extent, the transmission system. One option is to have the SoC restored before the load tap changer starts acting on the distribution transformer ratio, in order to avoid interactions with that device.

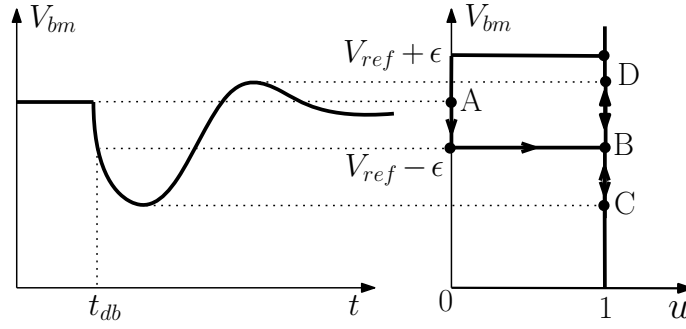


Figure 6.3: Block “trigger and lock” of the BESS

This action is carried out by a separate controller that computes the variation of the energy stored in the BESS due to its dynamic contribution (P_b), i.e. :

$$\Delta E(t) = \int_{t_{dis}}^t (P_b(\tau) - P_b(t_{dis})) d\tau \quad (6.9)$$

where t_{dis} is the time of the disturbance occurrence. That controller adds a second correction to the active current order i_P^{ord} , as shown in Fig. 6.2, in order to slowly steer ΔE back to zero, which resets the SoC of the battery.

6.3.5 Control triggering and locking

To avoid undesired repeated solicitations, the BESS is prevented from reacting to the small voltage variations that accompany load changes, maneuvers, generator voltage adjustments, transformer tap changes, etc. On the contrary, it reacts to more severe disturbances in the transmission grid, such as faults, which are detected through significant variations of V_{bm} .

The purpose of the block “**trigger and lock**” is to : (i) keep the controller idle as long as V_{bm} remains in a deadband $[V_{ref} - \epsilon, V_{ref} + \epsilon]$ where V_{ref} is a reference voltage and ϵ a tolerance; (ii) trigger the control as soon as V_{bm} leaves the deadband and (ii) keep the controller active, whatever the subsequent voltage evolution, until it is reset as previously described.

The output u of the block is a binary variable with value 0 when the controller is idle, and 1 when it is active. Through the multipliers (see Fig. 6.2), $u = 0$ forces the inputs of the PI controllers to zero and hence $\Delta i_P = \Delta i_Q = 0$.

The above features are modelled with an hysteresis block as shown in Fig. 6.3. The right figure shows how u changes for the voltage evolution shown in the left plot. The initial voltage is inside the deadband; the corresponding operating point is A. The voltage leaves the deadband at time t_{db} , causing u to change from 0 to 1 (point B), at which it remains locked. The minimum and maximum voltage deviations correspond to points C and D, respectively. A similar transition takes place if $V_{bm} > V_{ref} + \epsilon$.

6.4 Voltage phasor measurement process

Taking into account the voltage measurement process by a Phasor Measurement Unit (PMU) is somewhat delicate, for at least two reasons :

1. the model is to be used in large-disturbance simulations. While a PMU is a highly accurate power system instrument, its accuracy is considerably impacted by the errors in instrumentation channels (instrument transformers, control cables, attenuators, etc.) and system imbalances [HKM⁺08]. Accuracy is further deteriorated in dynamic conditions (in particular if the dynamics involve power electronics interfaced devices) [HKM⁺08];
2. the simulations in this work are performed under phasor mode approximation. Faithful simulations of a PMU signal processing algorithm must rely on ElectroMagnetic Transient (EMT) simulations of the voltage “wave”. As an alternative, a compromise between efficiency and accuracy would consist of coupling phasor and EMT simulations in a co-simulation approach [PAGVC16], as sketched in Fig. 6.4. The voltage time evolution processed by the PMU algorithm would be reconstructed from the voltage phasors obtained with phasor-mode simulation.

Since the main focus in this part of the thesis was on demonstrating the concept of BESS control, a simple model of the voltage phasor measurement process has been adopted, which tentatively accounts for inaccuracies brought by the PMU as well as by the smoothing of its successive outputs aimed at avoiding outlier phasors in transient conditions.

The choices made to process PMU measurements are presented in some detail in Appendix D and the main steps are as follows:

- the weighted moving average filter is implemented;
- an analytical expression of the weights is derived;
- the time window size is selected in order to reduce the measurement delay without deteriorate the noise filtering;
- the weights are fine tuned to further reduce the delay;
- the performance of the filter is assessed in the presence of measurements noise.

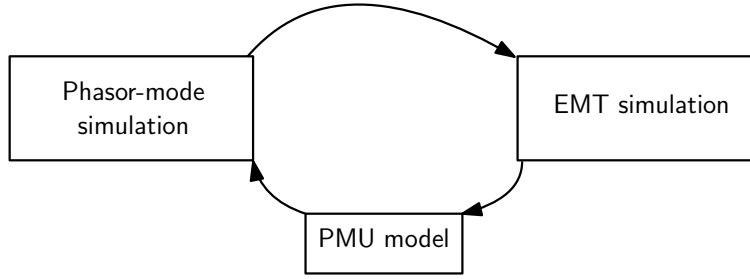


Figure 6.4: Ideal implementation of the PMU in phasor-mode simulation

6.5 Simulation results

6.5.1 Simulation framework

Simulations are reported on the CIGRE MV Distribution Network Benchmark [B⁺14] (ADN No 1, see Section 1.6.1) modified to incorporate a BESS. Its one-line diagram is shown in Fig. 6.5. The BESS, shown in red, is connected to the main substation.

As a reminder, the ADN includes static and motor loads as well as Inverter-Based Generators (IBGs). The large-capacity IBGs have low-voltage ride-through and reactive current injection capabilities, while small residential IBGs have not and disconnect if their terminal voltage falls below 0.8 pu.

The uncertainty affecting the parameters of ADN No 1 has been quantified in Section 3.3.1. From MC simulations, the time-varying averages and variances have been extracted.

The equivalent ADN model has been tuned to approach the average response of the ADN, obtained from the MC simulations. Note that this model accounts for the disconnection of residential IBGs in low voltage conditions.

Yet, due to the uncertainty affecting the unreduced model, the responses to voltage disturbances of the real system might be different from those average responses.

To better illustrate the new proposed BESS application, an instance of the (randomized) unreduced ADN model whose power response is “far” from the average (see Chapter 3), has been considered. Indeed, this will require a larger contribution from the BESS.

The filter that processes the power flows P_t and Q_t through the transformer is modelled by a first-order transfer function, whose time constant T_{fltr} is set to 10 ms. The outputs of the filter are P_t^{fltr} and Q_t^{fltr} .

All disturbances are applied on the High Voltage (HV) side of the transformer in the detailed ADN. The time constant T_g of the BESS converter (see Fig. 6.2) is set to 20 ms. Before any disturbances,

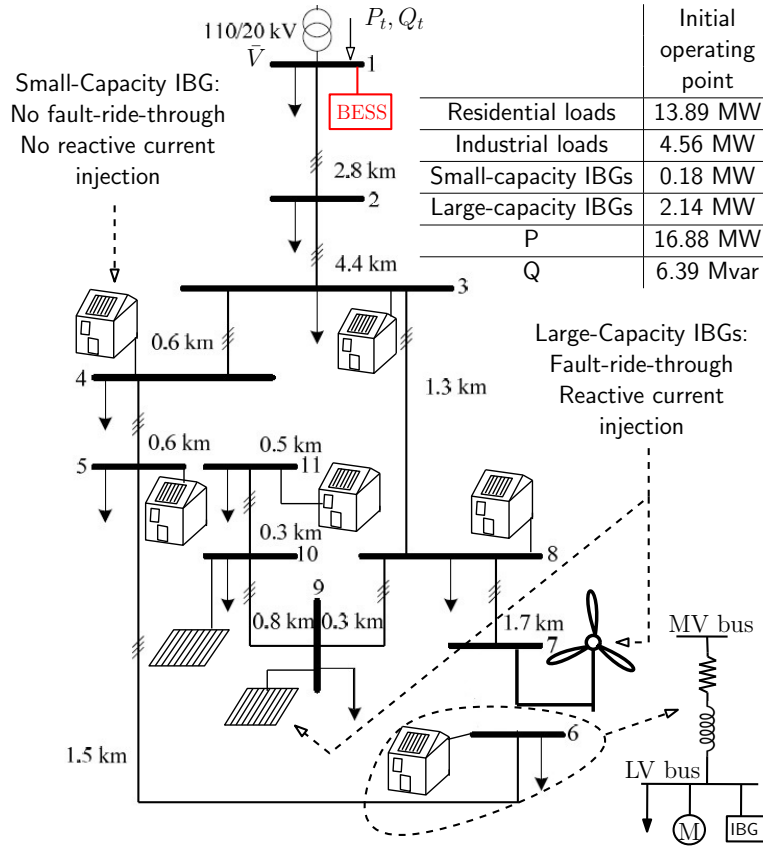


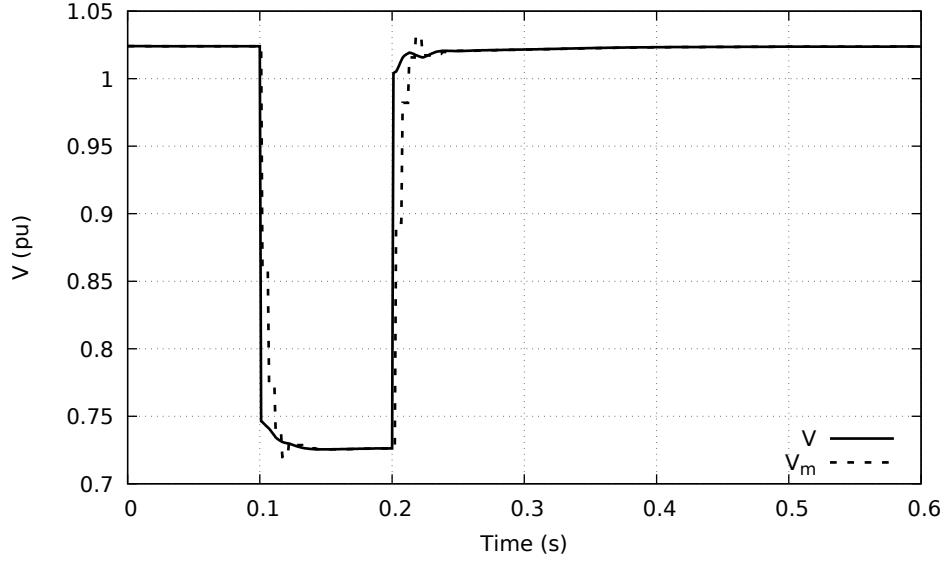
Figure 6.5: One-line diagram of the modified version of the CIGRE MV Distribution Network Benchmark; the BESS is shown in red

the BESS produces $P_b(0) = 2$ MW and $Q_b(0) = 1$ Mvar. In order the equivalent to match the pre-disturbance power entering the unreduced ADN, the pre-disturbance BESS power is incorporated in the slack load of the equivalent (see Fig. 6.6). The parameters of the BESS PI controllers (see Fig. 6.2) have been heuristically optimized to achieve good performances considering multiple disturbances.

In our simulations, $\epsilon = 0.05$ pu and $V_{ref} = 1$ pu (see Fig. 6.3). The deadband is thus $[0.95 \ 1.05]$ pu.

It is important to emphasize the difference between P_e and P_e^m . P_e is the active power consumed by the ADN equivalent subject to the disturbance affecting the transmission system as shown in Fig. 6.6a. In other words, this is the response of the equivalent when used by the TSO in its dynamic simulations. As explained above, in this section, P_e is affected by some inaccuracy which the BESS should compensate.

P_e^m refers to the same power flow but determined by the real-time simulation of the ADN equiv-

Figure 6.7: Time evolution of V and V_m for a mild voltage dip

1 ms. A separate “discrete controller” implements the weighted moving average filter processing the output of the PMU (see Section 6.4). In RAMSES the term discrete controller refers to a piece of code that is “visited” at the end of each (above mentioned) time step. It issues an updated value of the voltage phasor \bar{V}_m every 5 ms. This phasor is used in the simulation that mimics a real-time simulator of the equivalent and generates the P_e^m and Q_e^m values. As regards this real-time simulator, note that it is assumed to have a negligible computing time, so that no corresponding delay is assumed. This is acceptable considering the small size of the equivalent model.

The BESS controller is also simulated through a discrete controller that generates the Δi_P and Δi_Q commands every 5 ms. To that purpose, the PI controller equations are implemented in discrete time form.

6.5.3 Scenario 1 : voltage dips

First, the performance of the BESS is assessed in the event of voltage dips at transmission level. Figure 6.7 shows the time evolution of the voltages V and V_m (see Fig. 6.1), respectively, for a voltage dip of 0.3 pu lasting 100 ms. This voltage dip is considered to be “mild”. It triggers and locks the BESS controller, as detailed in Section 6.3.5. The active power evolutions with and without the BESS controller as well as the active power delivered by the BESS are shown in Fig. 6.8. Figure 6.8a compares the evolution of P_e and P_t in the absence of the BESS controller. It clearly shows that the evolution of P_t does not match very well the evolution of P_e . On the other hand, when the BESS controller is active, P_t is much closer to P_e , as can be seen in Fig. 6.8b. The evolution of P_t^{fltr} and P_e^m (see Fig. 6.1) shown in Fig. 6.8c confirms that the BESS controller

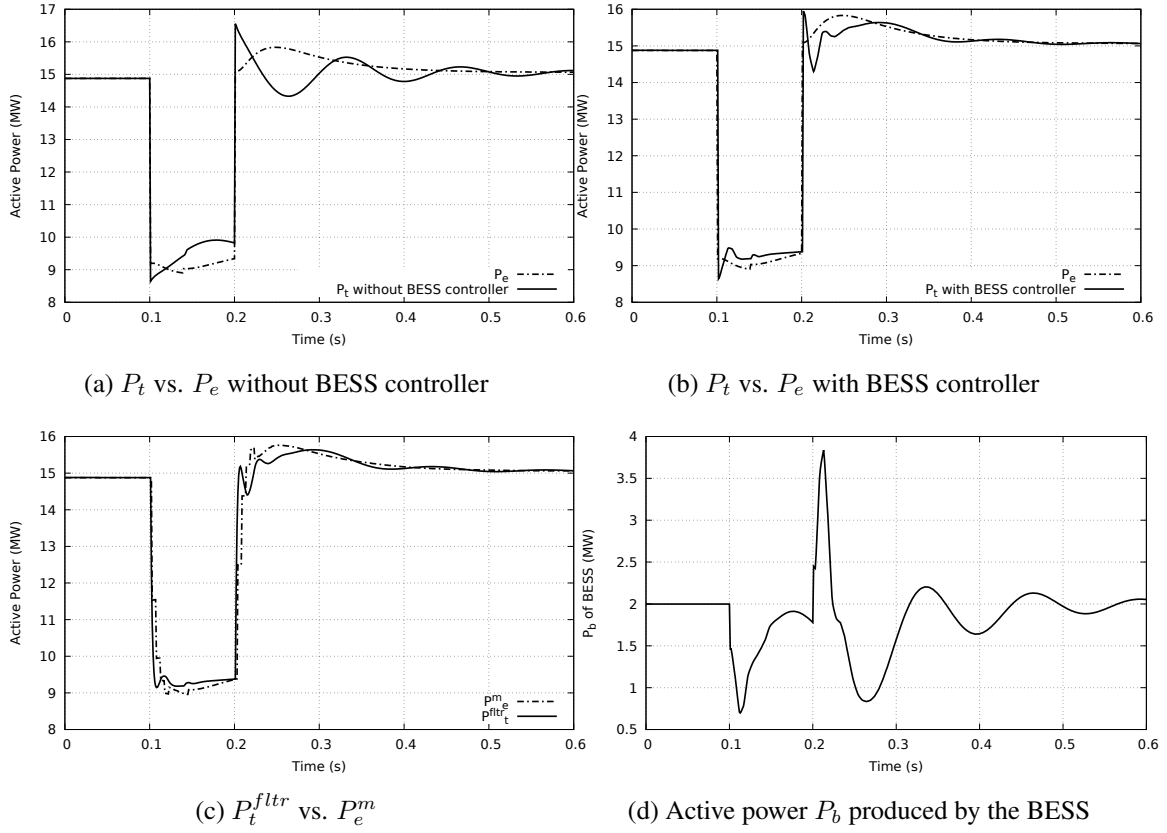


Figure 6.8: Performance of BESS regarding the active power in response to a mild voltage dip

performs its tasks quite well. Finally, the active power P_b produced by the BESS in Fig. 6.8d shows that the BESS generates active power oscillations to compensate for the oscillatory discrepancies between P_e and P_t .

The reactive power evolutions in response to the same voltage dip, again with and without the BESS control, are shown in Fig. 6.9, together with the reactive power Q_b produced by the BESS. The same observations as for the active power can be made.

Next, a “severe” voltage dip is considered. The latter has a depth of 0.7 pu and lasts 250 ms. Figure 6.10 shows the time evolution of the voltage V and V_m . The active and the reactive power evolutions are shown in Fig. 6.11 and Fig. 6.12, respectively. As for the mild voltage dip, the BESS achieves good performance since the power evolutions P_t and Q_t closely match their P_e and Q_e counterparts. As expected, both the active and reactive powers deviation of the BESS with respect to $P_b(0)$ and $Q_b(0)$ are larger for the severe voltage dip, as the inaccuracies to compensate are more important.

While all the figures of this scenario show that the BESS performs generally well, there are some

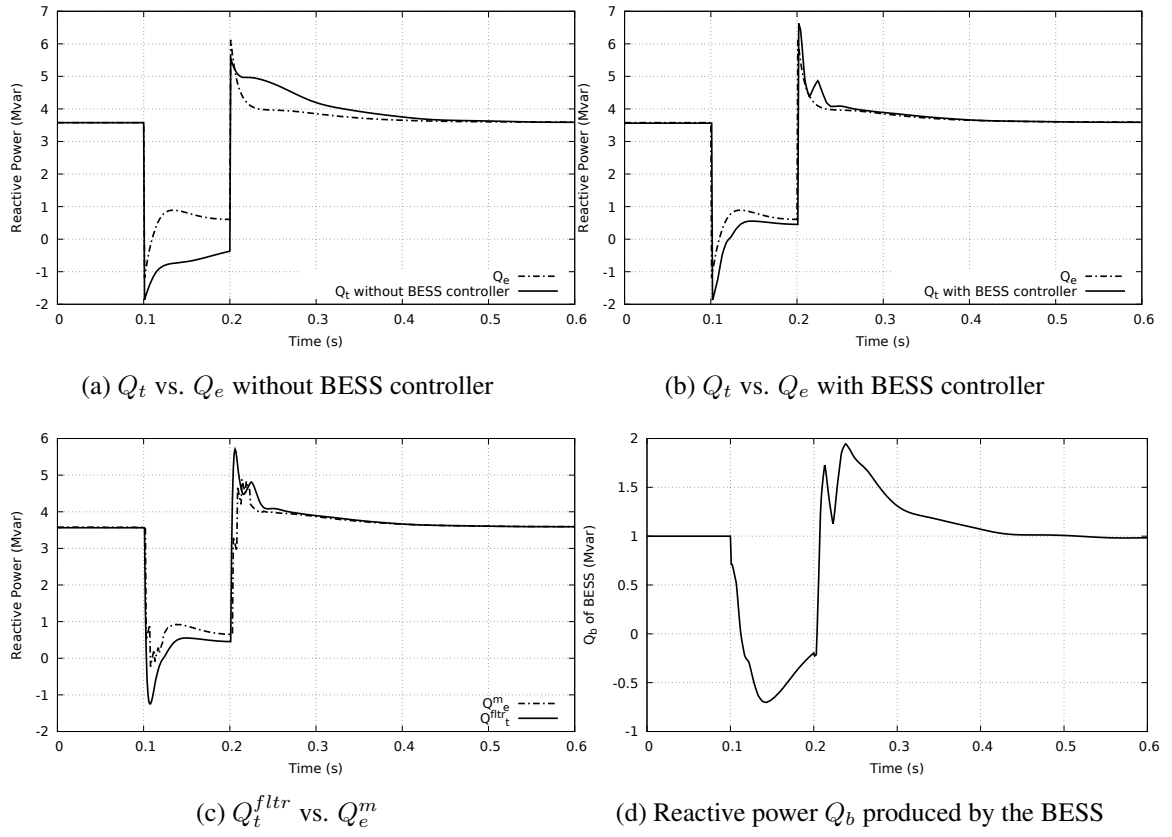


Figure 6.9: Performance of BESS regarding the reactive power in response to a mild voltage dip

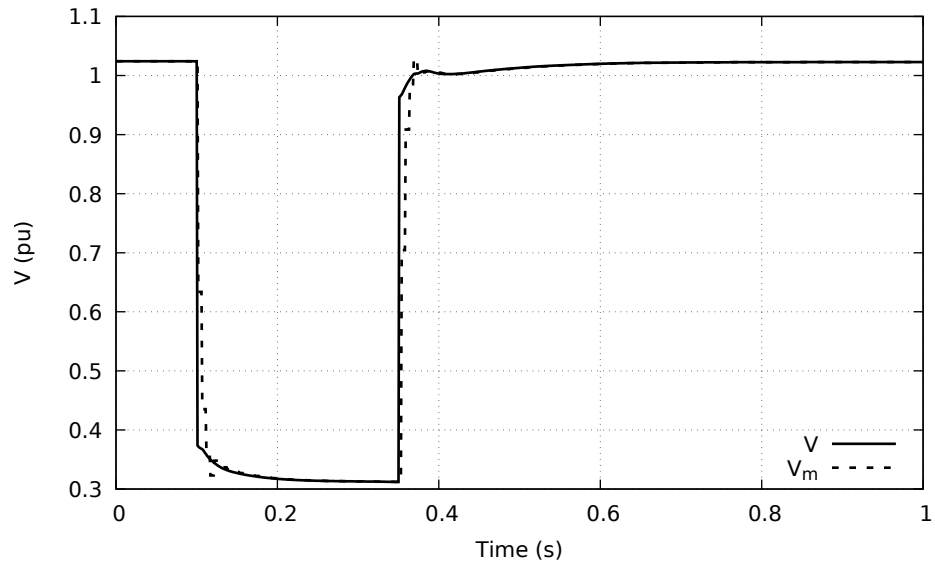


Figure 6.10: Time evolution of V and V_m for a severe voltage dip

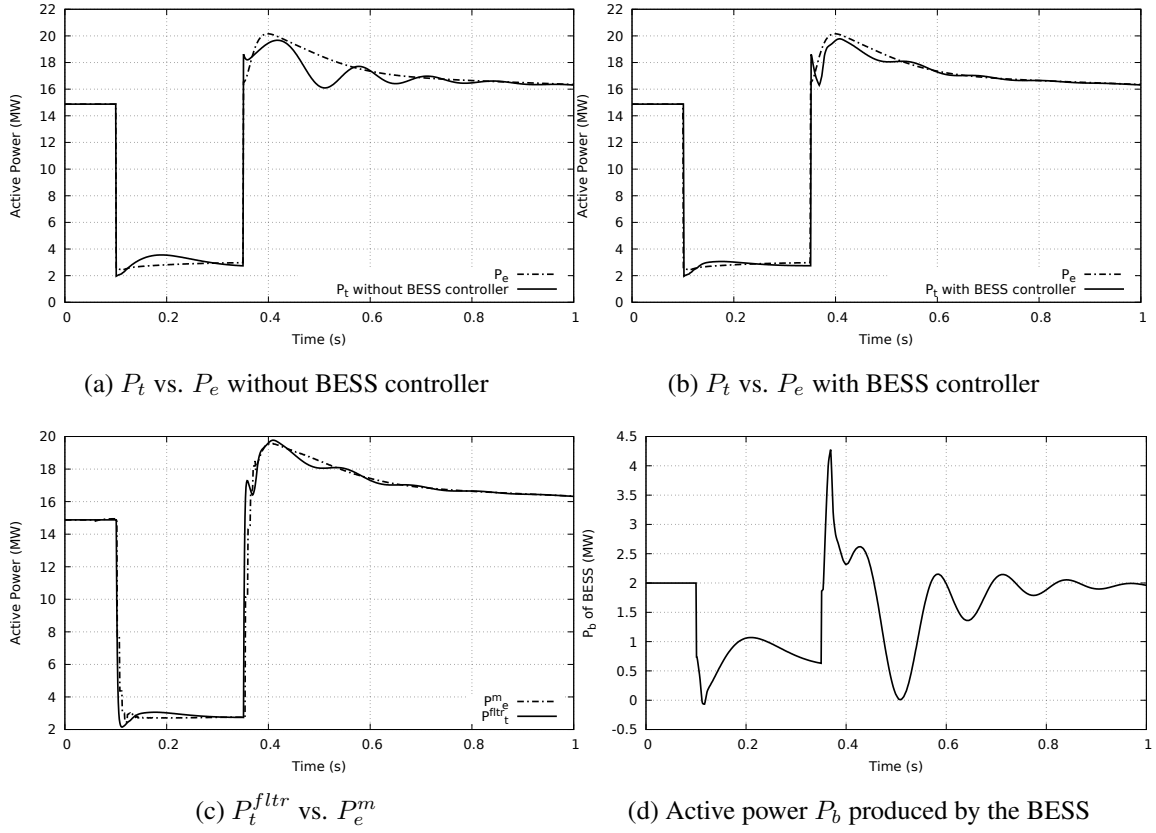


Figure 6.11: Performance of BESS regarding the active power in response to a severe voltage dip

unavoidable differences between P_t and P_e that the BESS controller is not able to compensate, due to the delay induced by the voltage phasor measurement process. This is mostly visible right after the voltage recovery.

6.5.4 Scenario 2 : electromechanical oscillation

The performance of the BESS is now assessed in case of an electromechanical oscillation. This involves an oscillation of voltage magnitude and phase angle of \bar{V}_{tr} as considered in Section 4.9.6. Because the voltage variation is much slower than for voltage dips, the measured voltage \bar{V}_m is very close to \bar{V} . Figure 6.13 (resp. Fig. 6.14) shows the resulting active (resp. reactive) power evolutions. While the effect of the BESS controller is less visible for the active power, since P_t and P_e are close to each other without the BESS contribution, it is not the case for the reactive power. Indeed, compared to Fig. 6.14a where the BESS controller is not active, Fig. 6.14b shows that the BESS is requested to strongly reduce the discrepancies between Q_t and Q_e . This is confirmed by Figs. 6.13c and 6.14c showing respectively the active and reactive powers produced by the BESS.

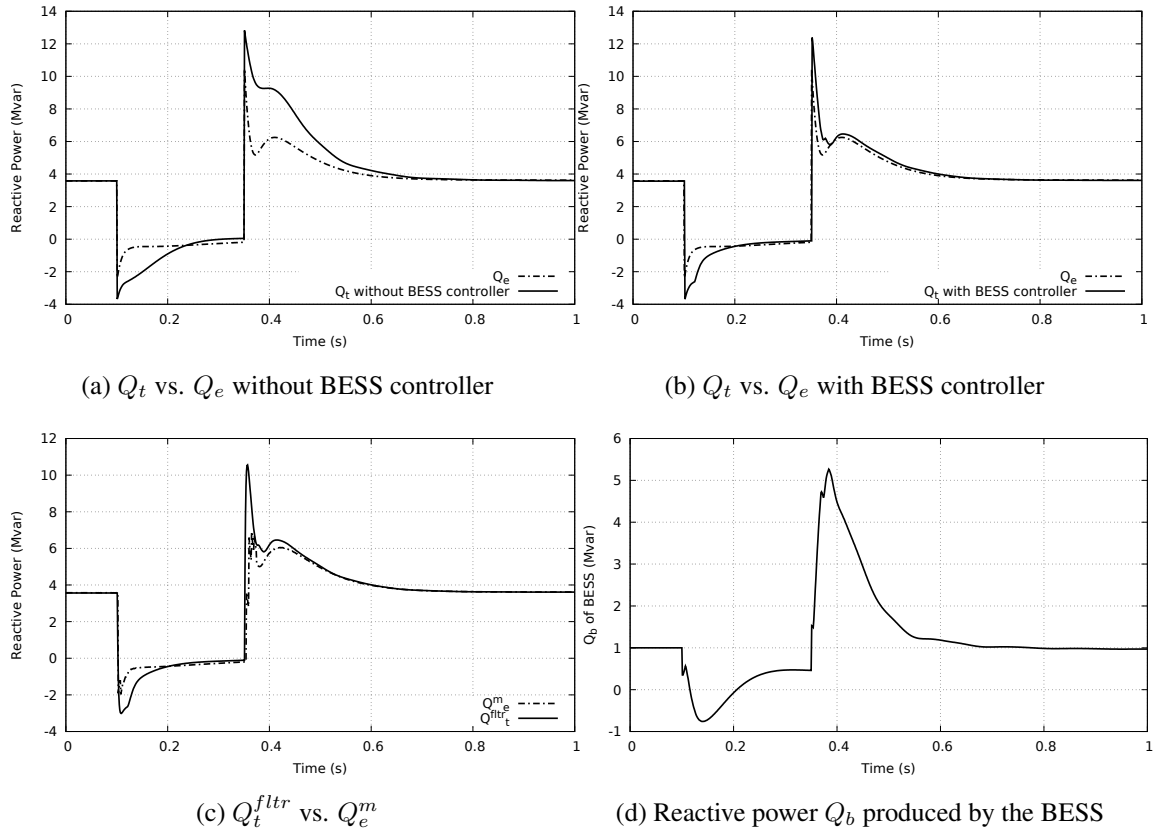


Figure 6.12: Performance of BESS regarding the reactive power in response to a severe voltage dip

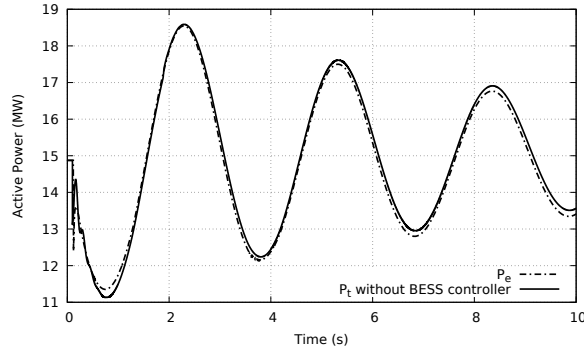
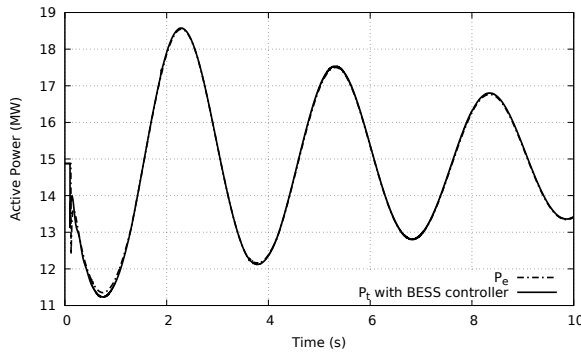
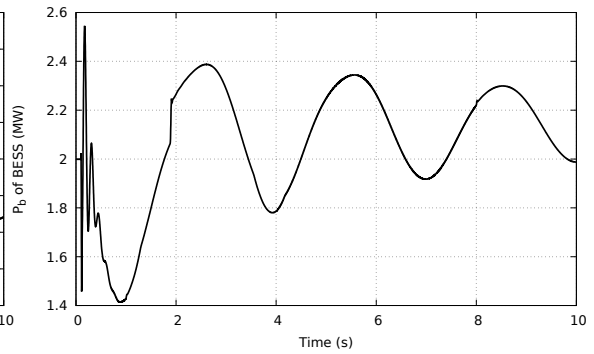
(a) P_t vs. P_e without BESS controller(b) P_t vs. P_e with BESS controller(c) Active power P_b produced by the BESS

Figure 6.13: Performance of BESS regarding the active power in response to an electromechanical oscillation

6.5.5 Scenario 3 : voltage dip followed by a phase jump

The performance of the BESS controller is further checked in response to a voltage dip followed by a phase jump. A voltage dip of 0.8 pu lasting for 100 ms followed by a phase jump of -10 degrees is applied on the transmission side of the transformer in Fig. 6.5. Furthermore, in this scenario, the post-disturbance voltage magnitude is slightly lower than its pre-disturbance value.

The evolutions of the voltage magnitudes V and V_m as well as phase angle δ and δ_m are shown in Fig. 6.15. It can be seen that the model of the voltage phasor measurement process (see Section 6.4) provides a slightly delayed but overall correct information about the voltage phase angle. At $t = 0.1$ s, when the voltage dip takes place, δ is reduced. At $t = 0.2$ s, when the voltage recovers, the reverse evolution of δ is combined with the imposed phase jump of -10 degrees, resulting in a net decrease of approximately 4 degrees.

Figure 6.16 refers to the active power evolutions. Again, the BESS control effectively compensates the difference between P_t and P_e . This indicates the good performance of the BESS in response to

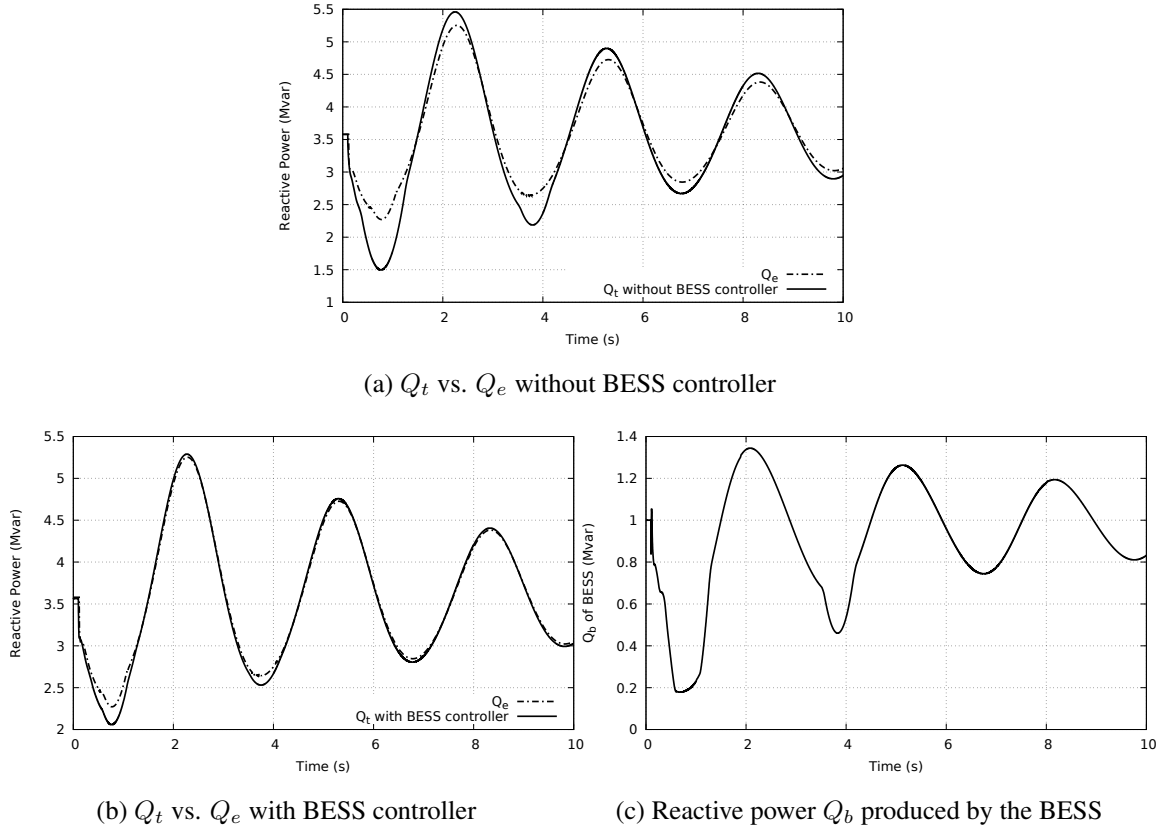


Figure 6.14: Performance of BESS regarding the reactive power in response to an electromechanical oscillation

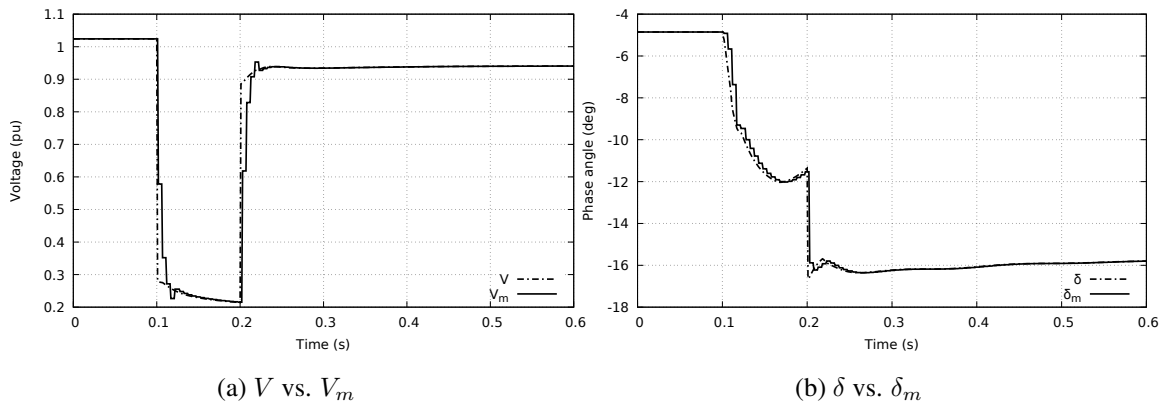


Figure 6.15: Voltage dip followed by phase jump: time evolution of (a) V , V_m and (b) δ , δ_m

what can be considered as a large phase jump. The same observations can be made for the reactive power, shown in Fig. 6.17.

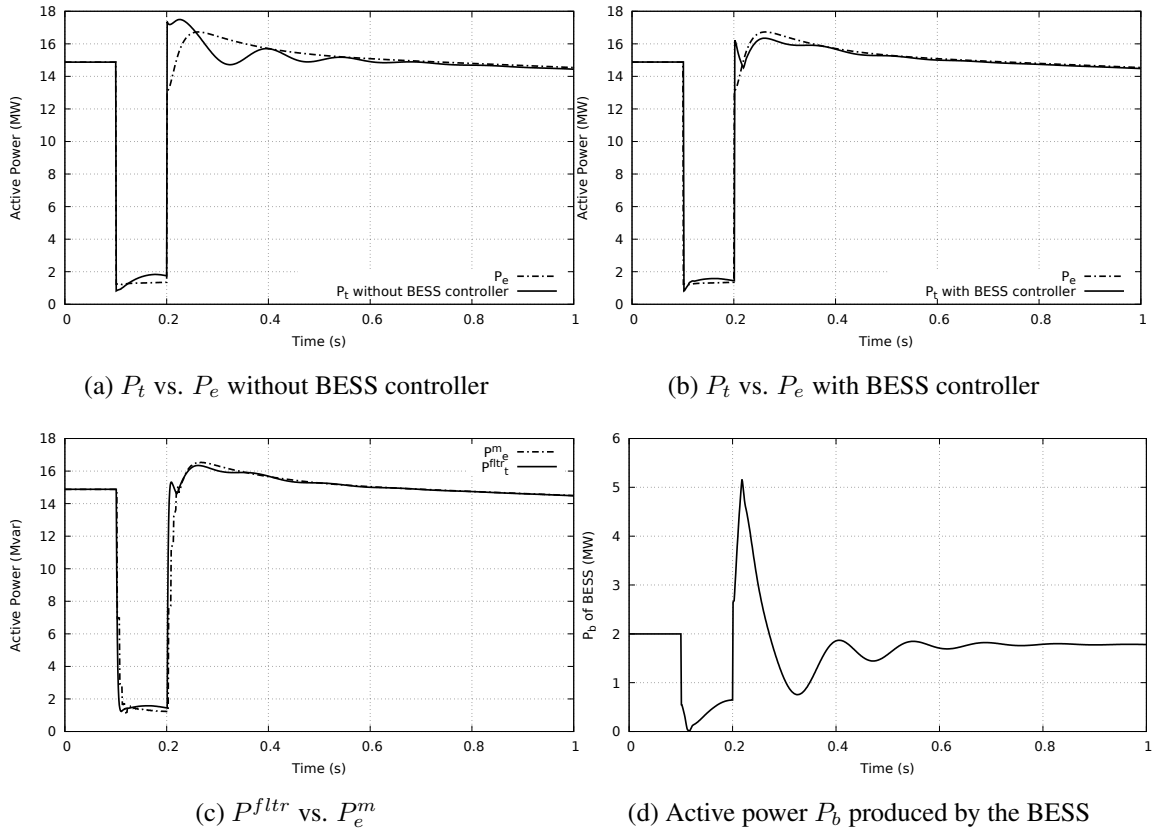


Figure 6.16: Performance of BESS regarding the active power in response to a voltage dip followed by a phase jump

6.5.6 Scenario 4 : connection of a capacitor bank in the MV grid

The first three scenarios involved disturbances occurring in the transmission system. It is also of interest to validate the BESS control in response to an event taking place in the MV grid itself. To this purpose, starting from the post-disturbance operating point of Scenario 3 (see previous section) with a reduced voltage magnitude, a capacitor bank with a nominal reactive power of 5 Mvar is connected at $t = 1$ s, to correct the voltage. The capacitor is connected at the main substation (bus 1 in Fig. 6.5). The BESS control, previously triggered by the incident of Scenario 3, is assumed to remain active.

The behaviour of the BESS controller is first investigated in case the real time simulation of the equivalent is not informed of the capacitor bank connection, which is thus not taken into account when calculating P_e^m and Q_e^m .

Figure 6.18 illustrates the effect of the BESS on the reactive power evolution. Without the BESS intervention, Fig. 6.18a shows that, as expected, the connection of the capacitor bank decreases

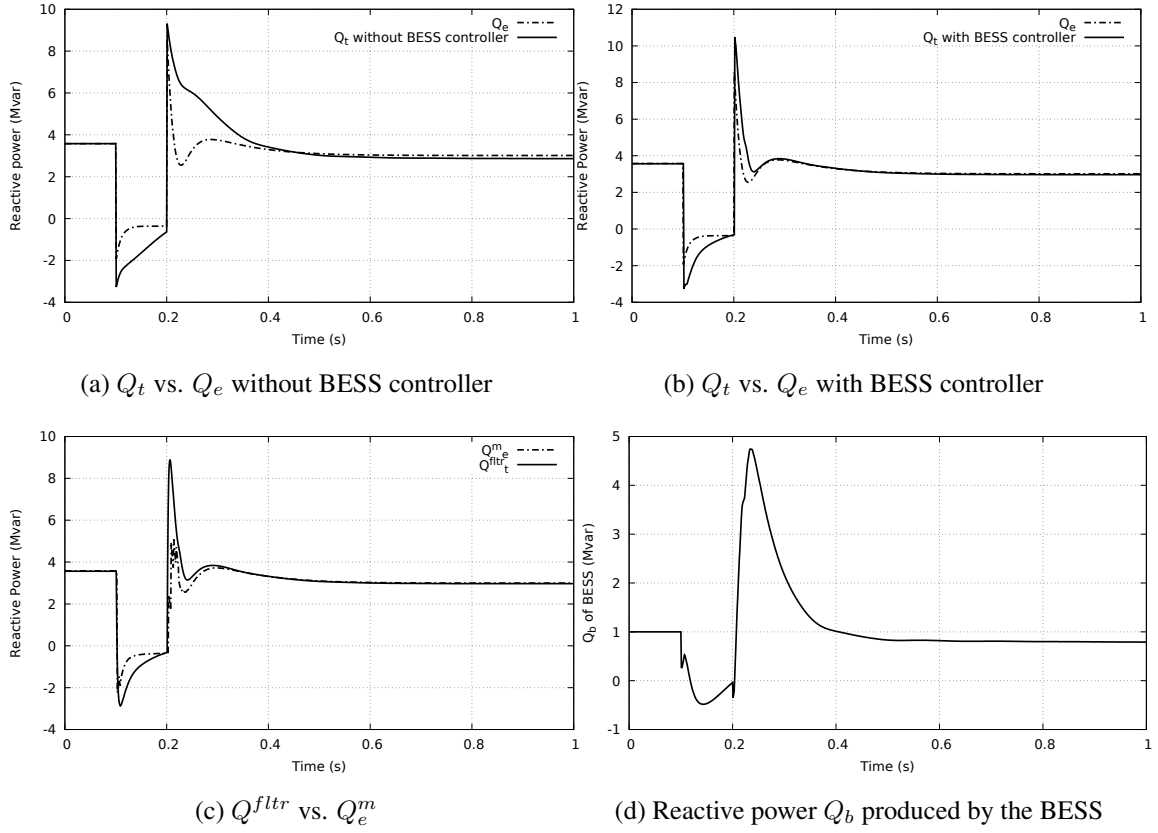


Figure 6.17: Performance of BESS regarding the reactive power in response to a voltage dip followed by a phase jump

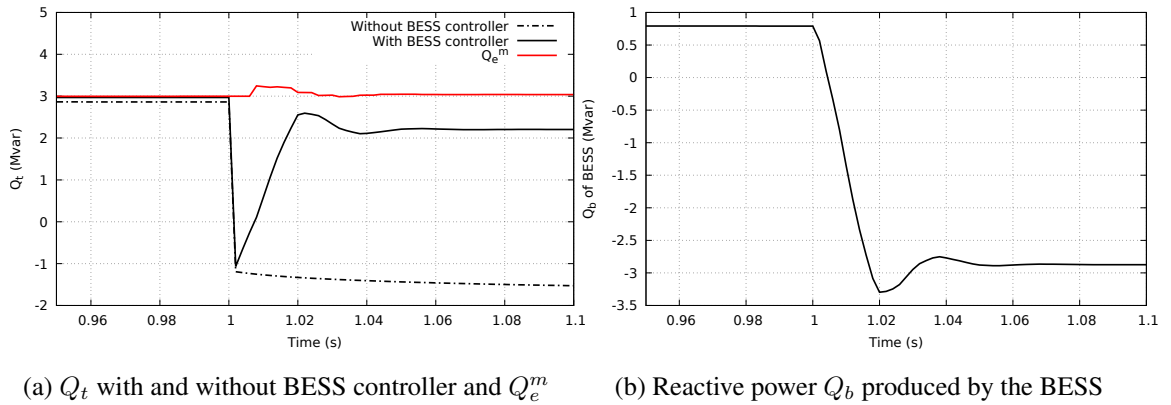


Figure 6.18: Effect of the BESS controller on the reactive power in the event of the connection of a capacitor bank at $t = 1$ s, this event being unknown in the real-time simulation of the equivalent

the amount of reactive power Q_t flowing through the transformer. On the other hand, under the effect of the BESS controller, Q_t is unduly corrected. Its input Q_e^m is almost not modified (see the

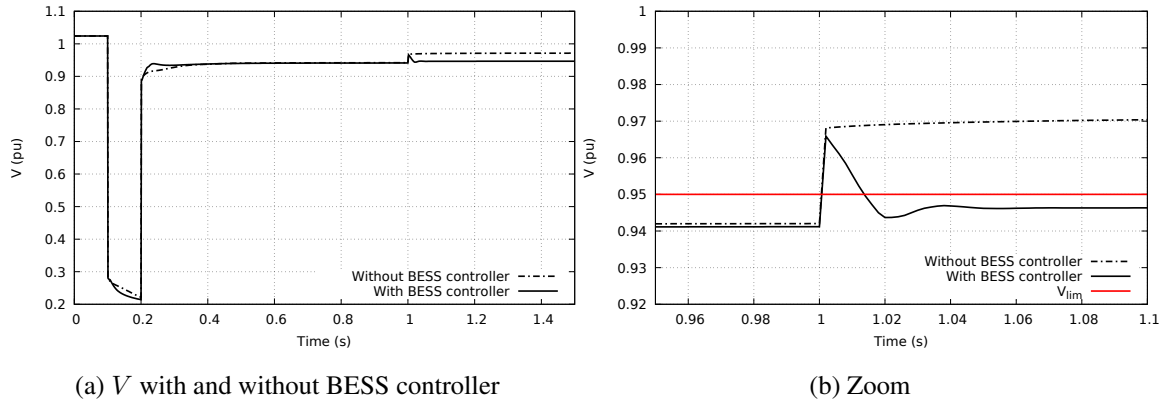


Figure 6.19: Effect of the BESS controller on the voltage V in the event of the connection of a capacitor bank at $t = 1$ s, this event being unknown in the real-time simulation of the equivalent

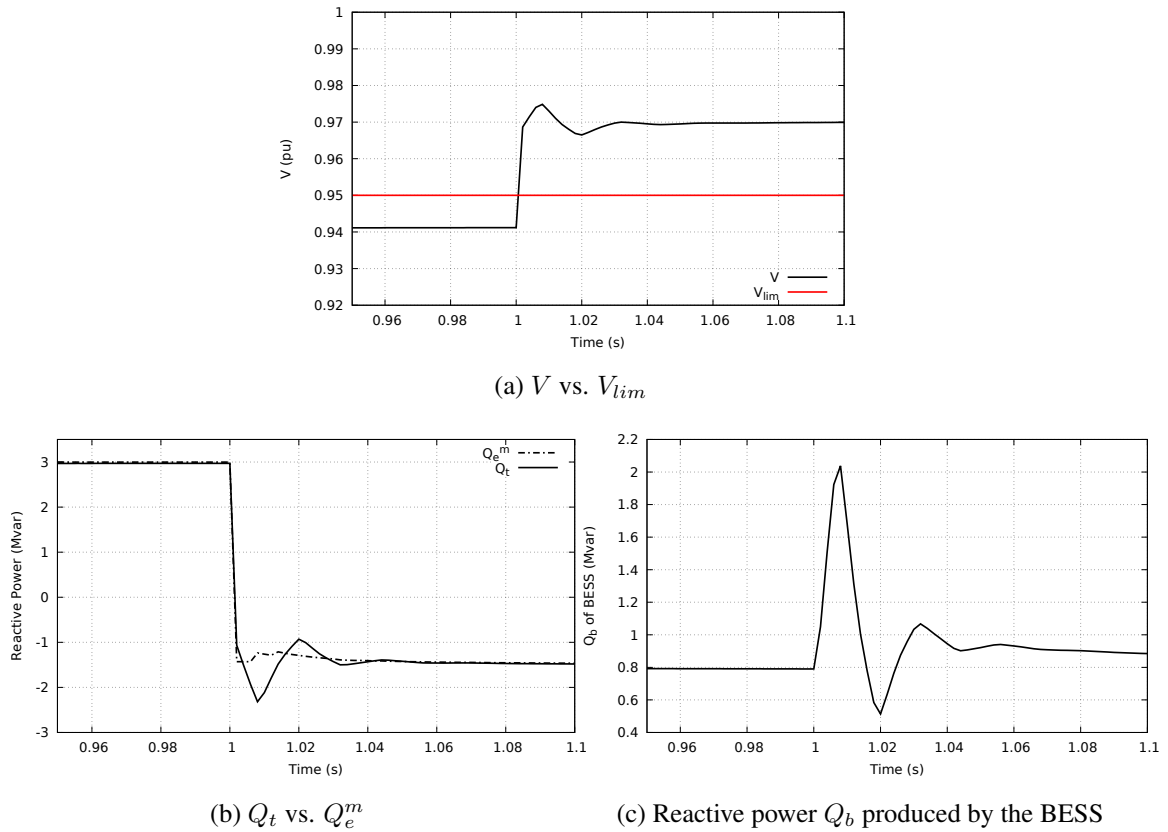


Figure 6.20: Effect of the BESS controller in the event of the connection of a capacitor bank at $t = 1$ s, this event being known in the real-time simulation of the equivalent

curve in red in Fig. 6.18a). The reactive power Q_b produced by the BESS is shown in Fig. 6.18b. It can be seen that the BESS decreases its reactive power production Q_b soon after the capacitor

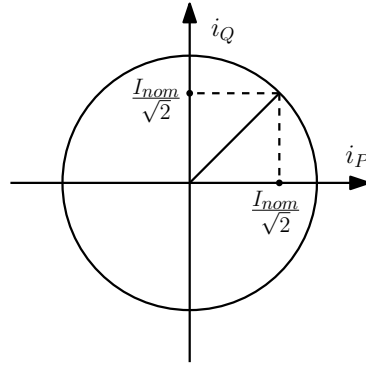


Figure 6.21: Computation of current limits; combined P and Q priority

bank is connected, thereby partially cancelling the effect of the latter.

The effect on the voltage V is seen in Fig. 6.19. Without the BESS controller, the connection of the capacitor bank brings the voltage back above 0.95 pu while, with the BESS controller, the voltage fails reaching this value. This is more visible in Fig. 6.19b, where a zoom on the voltage evolution is offered.

When the connection of the capacitor bank is not taken into account in the real-time simulation of the equivalent, the BESS consumes a large part of the capacitor bank production, to counteract its effect. In that case, the connection of the capacitor bank is thus ineffective.

The connection of the capacitor bank is now taken into account in the real-time simulation of the equivalent. In this case, the voltage is successfully brought back above 0.95 pu as shown in Fig. 6.20a. Figure 6.20b shows the consumed reactive power Q_e^m determined by the real-time simulator of the equivalent. It is reduced under the effect of the capacitor bank connection. The reactive power Q_b produced by the BESS is shown in Fig. 6.20c. After some transient, due to the response time of the controller, Q_b returns to its pre-connection value, in fact slightly above due to the voltage rise induced by the bank connection.

It can be concluded that the connection of the capacitor bank should be accounted in the real-time simulation of the equivalent, to avoid being counteracted by the BESS.

6.5.7 Current limiters taken into account

This section discusses the effect of the power priority implemented in the BESS controller, when the converter current limiters are taken into account (see Section 6.3.2) and become active in response to the severe voltage dip considered in Section 6.5.3. To reach the current limits, the nominal apparent power of the BESS converter has been reduced to 5 MVA.

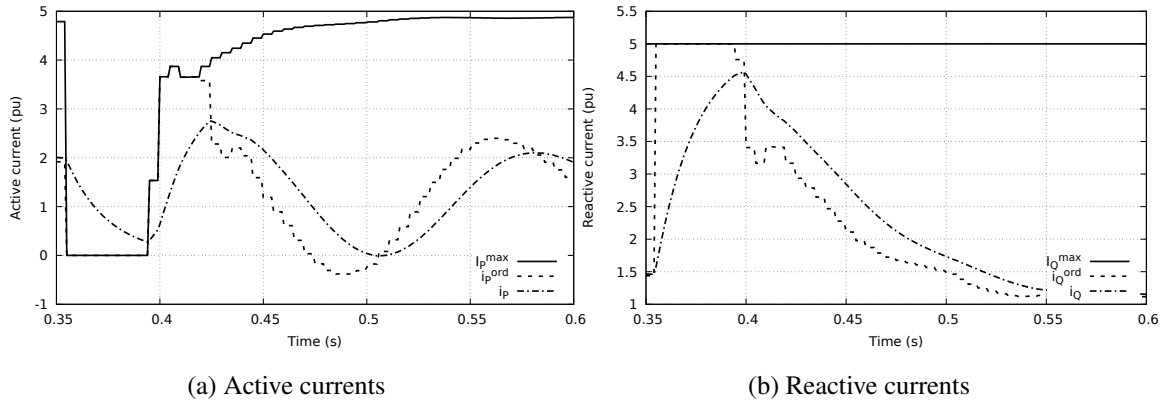


Figure 6.22: Active and reactive currents of BESS controlled according to Q-priority

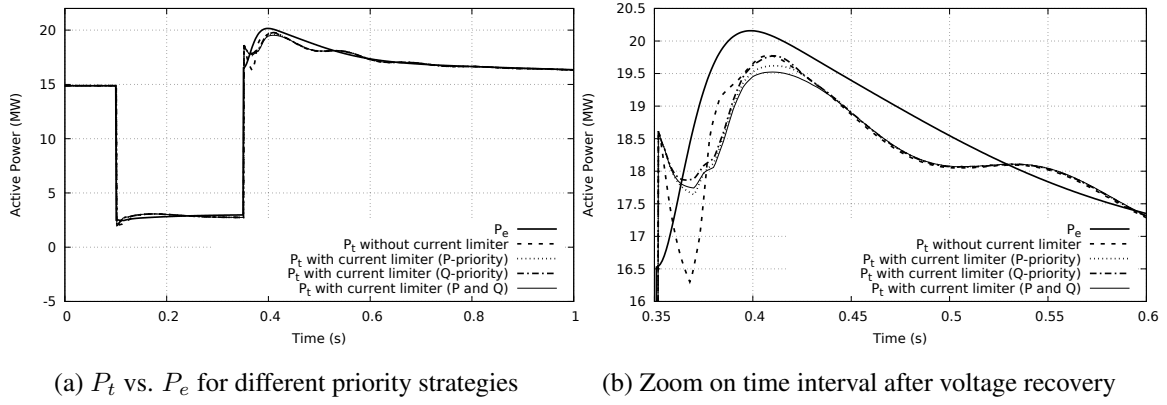


Figure 6.23: Severe voltage dip: impact of current priority on active power response

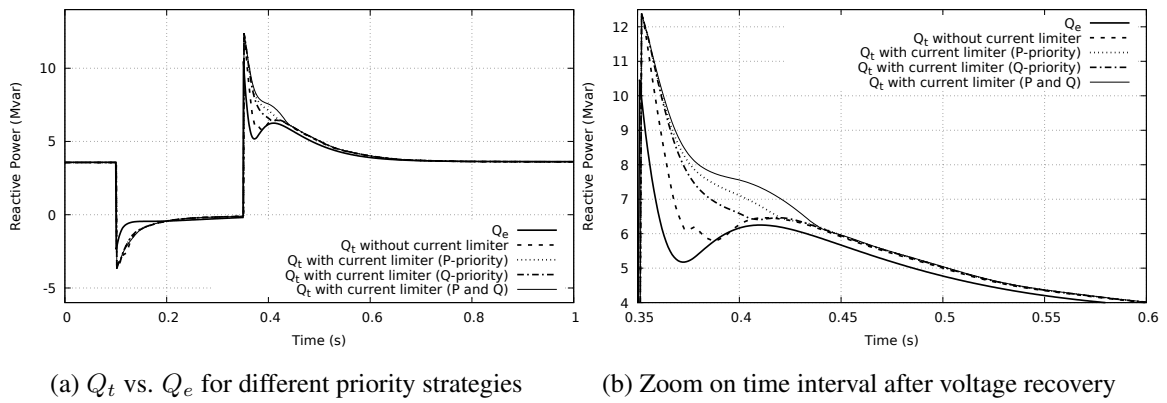


Figure 6.24: Severe voltage dip: impact of current priority on reactive power response

Three settings are investigated :

1. active power priority (P priority), corresponding to $P_{flag} = 1$ in (6.1, 6.2);
2. reactive power priority (Q priority), corresponding to $P_{flag} = 0$ in (6.1, 6.2);
3. combined active and reactive priority (P and Q priority). This assumes that the reactive current limits are computed as [LBP⁺17, KOYT16] :

$$I_{Qmax} = -I_{Qmin} = \frac{I_{nom}}{\sqrt{2}} \quad (6.10)$$

which attributes the same maximum value to the active and reactive currents, as shown in Fig. 6.21.

Coming back to Fig. 6.11a, it can be seen that after voltage recovery and for $t \leq 0.45$ s, the difference between P_t and P_e is small. Hence, the active current correction Δi_P is also small. On the other hand, at the same time, the discrepancy between Q_t and Q_e is large, and so is Δi_Q .

Assuming that the Q-priority has been selected, Fig. 6.22a (resp. 6.22b) shows the active (resp. reactive) current command i_P^{ord} (resp. i_Q^{ord}), the active (resp. reactive) current injected by the BESS i_P (resp. i_Q) and the maximum active (resp. reactive) current limit I_{Pmax} (resp. I_{Qmax}) (see Fig. 6.2). As expected, the BESS injects a large reactive current (mainly for $t \leq 0.4$ s) and I_{Pmax} decreases to zero, to leave room for that reactive current injection. I_{Qmax} remains at the maximum possible value as expected.

The corresponding powers P_t , Q_t , P_e and Q_e are shown in Figs. 6.23 and 6.24 for each of the three aforementioned settings (P, Q, P and Q priority).

Figure 6.23b zooms over the immediate time interval after voltage recovery. It can be seen that the active power response is little impacted by the priority setting. This is due to the fact that Δi_P is small when its upper bound I_{Pmax} drops. On the other hand, the choice of the priority impacts more noticeably the reactive power, as can be seen in Fig. 6.24b. The Q priority exhibits the best performance, as Q_t gets closer to Q_e .

The P priority appears to show better performance than the combined P and Q priority. Indeed, as mentioned above, when Δi_Q is large, Δi_P is small and thus the limit given by (6.10) is actually more constraining than the one given by (6.2).

Figure 6.23b calls for a final comment. It shows that the discrepancy between P_t and P_e is larger without than with current limiters. This is due to the delay between P_t^{fltr} and P_e^m at voltage recovery (see Fig. 6.11c), leading to an undesirable large correction Δi_P , which is avoided when current limits are taken into account.

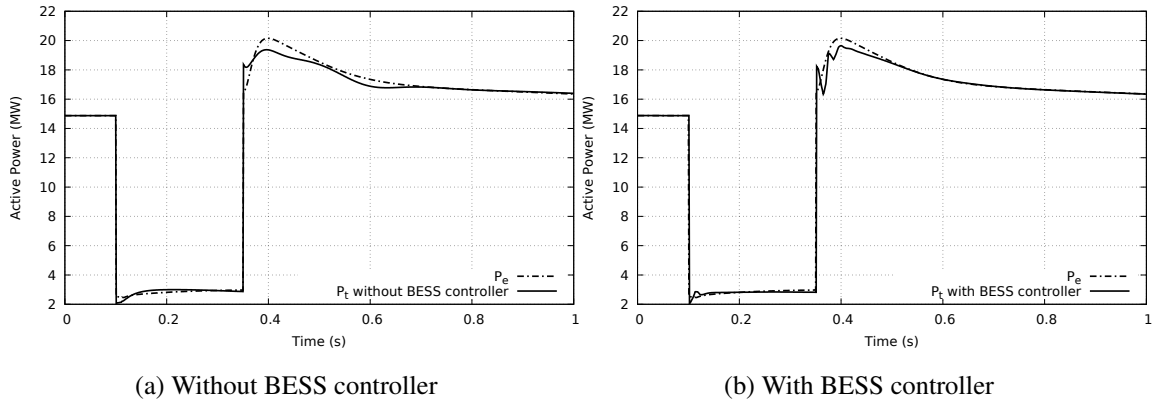


Figure 6.25: ADN A: P_t vs. P_e (a) without and (b) with BESS controller

These results suggest that the choice of the priority should be based on the reactive power response and that it is advisable to select the Q priority. Yet, other tests are needed to confirm this trend.

The Q priority appears as the “lower cost” option since active power is “sacrificed” when the current limit is hit, i.e. the amount of energy requested from the BESS is decreased.

It is clear that the reactive power reserve has a significant importance for the BESS to perform properly in response to a fault. Indeed, a larger initial reactive power production brings the initial injected current closer to the converter limit I_{nom} . In the event of a fault, it is then more probable that this limit is reached, forcing the active power produced by the BESS to be reduced, if the Q priority is selected. However, the pre-disturbance reactive power of the BESS depends on other services it is expected to provide, such as voltage regulation or power factor. In case of a very limited reactive power reserve, it would be advisable to switch on a nearby capacitor bank in order to release some reactive power reserve.

6.5.8 Performance of the BESS when the equivalent is more accurate

This section illustrates the BESS controller performance for the severe voltage dip considered in Section 6.5.3, when the equivalent is more accurate.

To that purpose, two instances of the ADN model are considered. The first one, denoted ADN A, is an instance whose power response is close to the equivalent, i.e. the equivalent is accurate. The second one, denoted ADN B, is the one considered so far, i.e. whose power response is farther from that of the equivalent, i.e. the equivalent is less accurate.

The performance of the BESS facing ADN A is shown in Fig. 6.25 (resp. 6.26). As expected, the BESS controller succeeds reducing the difference between P_t and P_e (resp. Q_t and Q_e), but it is

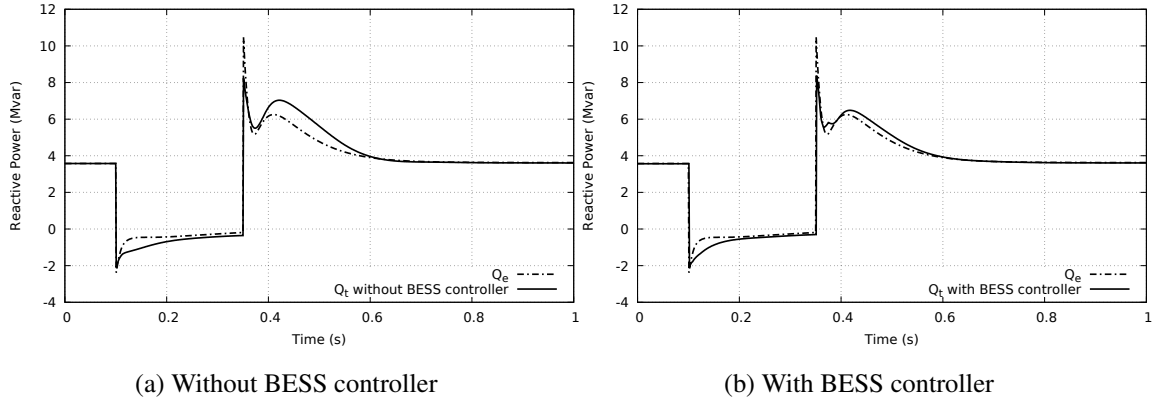


Figure 6.26: ADN A: Q_t vs. Q_e (a) without and (b) with BESS controller

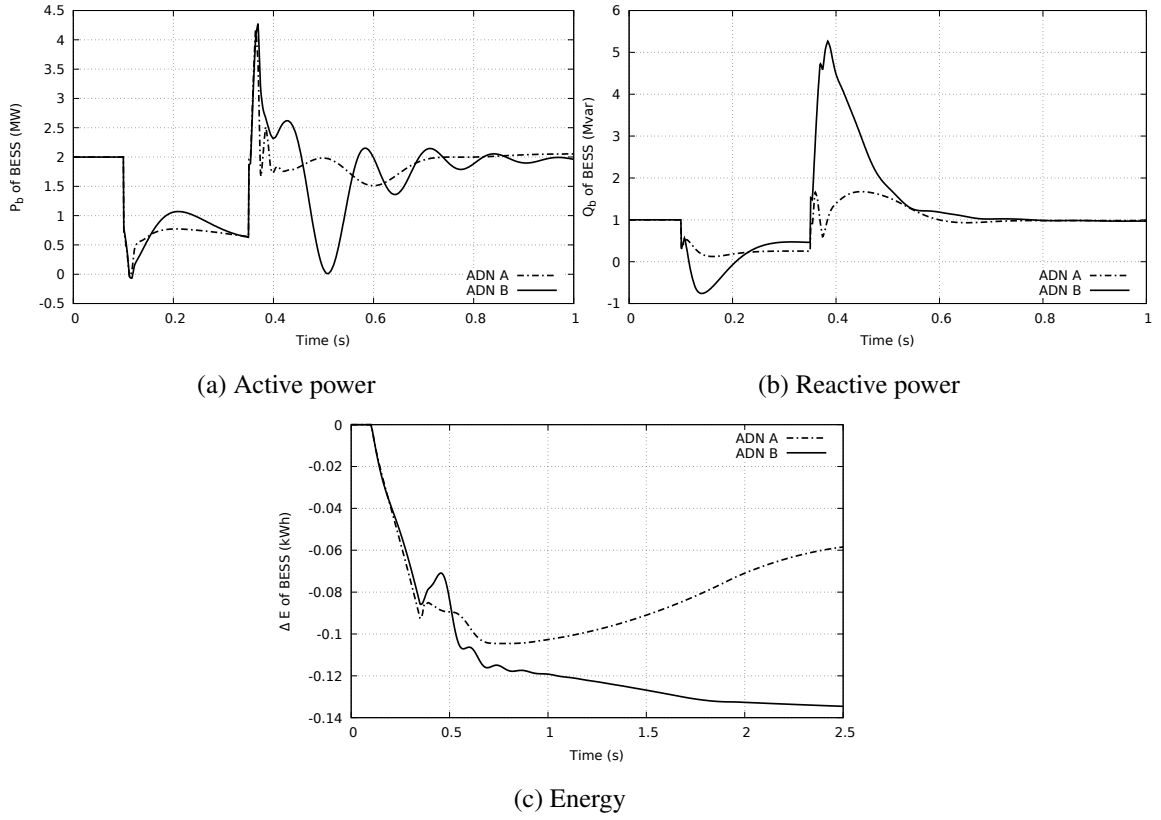


Figure 6.27: Comparison of BESS powers and energy dealing with ADN A and ADN B

also seen that, without the BESS controller, the mismatch between P_t and P_e (resp. Q_t and Q_e) is significantly smaller with ADN A than with ADN B (see Fig. 6.11).

Figure 6.27 further compares the responses of the BESS dealing with ADN A and ADN B, re-

spectively. The variation of energy ΔE (see (6.9)) is shown in Fig. 6.27c. All these plots confirm that the variations of active and reactive powers (with respect to $P_b(0)$ and $Q_b(0)$) are larger for ADN *B*. Needless to say, the energy variation ΔE of the BESS is larger as well. Yet it remains small.

That energy variation can be used as a measure of accuracy of the equivalent with respect to the real, unreduced system. Furthermore, if for a given disturbance, ΔE exceeds some threshold, it is an indication that the equivalent should be updated. From a market viewpoint, it is also an economical incentive to perform that update².

However, the ΔE metric only takes into account the accuracy of the equivalent with respect to active power. To encompass the reactive power counterpart, it is suggested to consider :

$$\Delta F(t) = \int_{t_{dis}}^t (Q_b(\tau) - Q_b(t_{dis})) d\tau \quad (6.11)$$

as an additional quality index for the equivalent, where t_{dis} is the time when the disturbance occurs. Note that ΔF has no physical meaning. It merely allows to quantify the reactive power variation of the BESS with respect to $Q_b(t_{dis})$.

Finally, the measure of accuracy of the equivalent could combined ΔE and ΔF into a single composite index, for instance :

$$\Delta S = \sqrt{\Delta E^2 + \Delta F^2} \quad (6.12)$$

in order to have a single quantity that simultaneously takes into account the accuracy of the equivalent with respect to both the active and the reactive power.

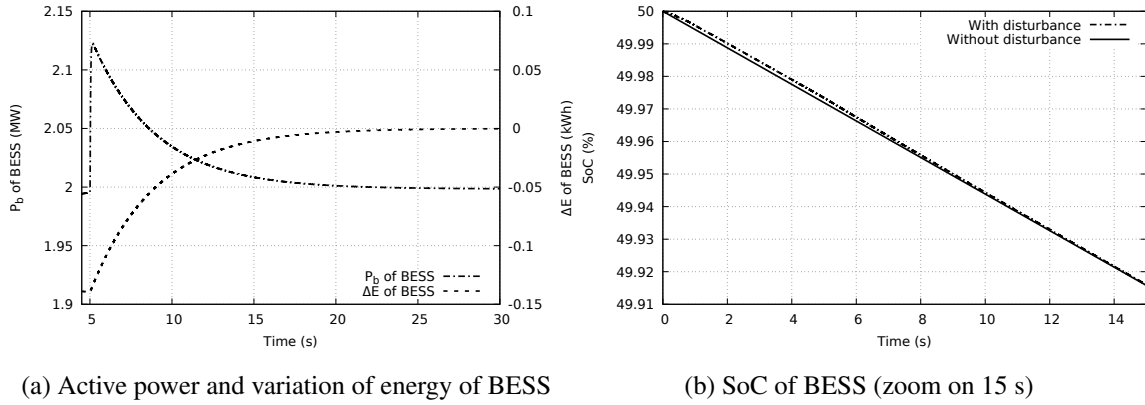
For instance, at $t = 2.5$ s and for $t_{dis} = 0.1$ s, we have, for ADN *A*, $\Delta S = 0.263$ and for ADN *B*, $\Delta S = 0.523$.

6.5.9 Resetting the BESS to compensate for its dynamic contribution

The goal of this reset is to steer ΔE back to zero when the transients have completely died out. This is easily achieved with an integral controller using ΔE as input and adding its output to i_P^{ord} (see Fig. 6.2). At the same time, u is reset to zero to disable the BESS control based on power flows.

The corresponding simulation results are shown in Fig. 6.28. After the severe voltage dip previously considered for ADN *B*, at $t = 5$ s, when power flows P_t and Q_t have come back to steady state, the reset process starts. ΔE increases progressively and reaches zero after 20 s. Figure 6.28a

²It is in the interest of both the TSO and the DSO to perform that update. It is a matter of model accuracy for the former and energy saving for the latter.

Figure 6.28: Resetting of BESS after a severe voltage dip; ADN *B*

also shows the evolution of P_b . In the specific scenario, P_b must be increased to compensate for the energy accumulation.

Finally, Fig. 6.28b shows the evolution of the SoC and compares it to the case without disturbance. It is seen that the reset brings the SoC back to the value it would have if no disturbance had occurred.

6.6 Summary and conclusions

This chapter has proposed a new application for a BESS connected to a distribution grid. It consists of controlling its active and reactive powers so that the net power entering the distribution grid evolves with the distribution voltage as closely as possible to the response provided by an equivalent model.

The objective is to increase the reliability of dynamic simulations of disturbances in the transmission system, in which the equivalent model can be used to represent the distribution system, with a higher guarantee of accuracy. The proposed controls aim at compensating for the inaccuracies of that equivalent model, linked to ADN model uncertainty.

In the event of a disturbance, the idea is to measure the voltage at the entry point of the distribution grid with a PMU, whose voltage phasor measurement is processed as detailed in Section 6.4. The measured voltage is used in a real-time simulation of the equivalent. The so computed response of the equivalent is used as a reference to control with a BESS the net power entering the grid.

The BESS does not react to voltage deviations below some threshold. When activated, its active and reactive powers are adjusted by PI controllers.

The results show good performance with the BESS able to bring the power flows close to the reference after a voltage change, for various type of disturbances. Yet it has been shown that, just after voltage recovery, delay induced by the voltage phasor measurement process leads unavoidably to discrepancies that cannot be compensated by the controller. The response to an event taking place in the distribution grid, the impact of the current limiters and the choice of the power priority has also been investigated.

If the dynamic behaviour of the equivalent model is closer to that of the real system, the BESS is less solicited and its control is easier. Moreover, the delivered energy is reduced.

Finally, it is worth noting an additional advantage of this application: it allows less frequent updates of the equivalent, since the BESS partly compensates for its possible inaccuracies.

Chapter 7

General conclusion

7.1 Summary of work and main contributions

Undoubtedly, the replacement of conventional generators by more and more IBGs connected at distribution level increases the need to have accurate ADN models to account for their effects in dynamic simulations and grid stability studies. The simulation of combined Transmission and Distribution systems raises the issue of model maintenance and in some cases, confidentiality. Therefore, the derivation of reduced-order, equivalent models of ADNs appears to be a relevant solution. Those equivalents are intended to be attached to the transmission system model for use by the TSO in its dynamic studies, and more particularly for the simulation of large disturbances taking place in the transmission system.

This thesis has proposed a comprehensive simulation-based methodology for the derivation of such equivalents. The latter are of the grey-box type and their parameters are adjusted to match as closely as possible the response of the unreduced, detailed ADN models.

First, generic load and IBG models have been detailed. The load model is divided into a static and a dynamic part while the IBG model renders typical controls of the converter in response to voltage and frequency deviations, in adequacy with current grid code requirements. These models have been developed under the phasor-mode approximation, typical of large-scale dynamic studies. Rotor angle, frequency and voltage stability studies are targeted. They could also pertain to instability modes stemming from power electronics converters. The transmission system is modeled by a voltage source able to vary its magnitude and phase angle. The latter is used to generate various voltage signals to account for typical events taking place in the transmission system. The proposed models are deemed representative of what could be used in practice, considering the available information and grid codes. Moreover, the methodology exposed in this thesis is not

bound to particular models but, instead, could be extended to other components. More importantly, it has been ensured that the model accounts for representative nonlinearities encountered in practice.

An approach to take into account the uncertainty affecting dynamic behaviours of ADN components has been proposed. The latter involves Monte-Carlo simulations. A simple procedure has been adopted to select the number of these Monte-Carlo simulations. From randomized time evolutions, the time-varying averages and standard deviations are extracted. The parameters of the equivalent are adjusted to match as closely as possible the average of the randomized responses, while their dispersion (reflected by the standard deviations) is accounted for through the weights embedded in the least-square minimization. A metaheuristic (Differential Evolution) algorithm has been used to deal with the minimization problem.

For a better interpretation of the results, a LASSO-based approach allows removing from the identification the parameters with a negligible impact on the accuracy of the equivalent. Furthermore, to avoid over-fitting, multiple candidate disturbances are considered. Yet, a recursive procedure is used to involve the smallest possible sub-set of disturbances in the weighted least-square minimization, guarantying the accuracy of the equivalent with respect to the other candidate disturbances. The methodology accounts for IBGs disconnection (in severe scenarios) by estimating sequentially two sub-sets of parameters, using scenarios without and with IBGs disconnection, respectively.

Simulation results reported on three different ADNs have shown that the equivalents can reproduce the nonlinear and discontinuous behaviour of their respective ADN, in particular the disconnection of some IBGs under low voltage conditions. The accuracy has been checked on disturbances not used for training. The methodology has also been tested on the model of a real distribution grid hosting PV units and synchronous generators.

Furthermore, a procedure to update the equivalent with changing operating conditions has been detailed. It consists of testing the accuracy of available equivalents, and, if none is accurate enough, it proceeds with updating the parameters of the “less inaccurate” one. For efficiency reasons, a LASSO-based procedure minimizes the number of parameters to update. Simulation results have shown, in most cases, that this procedure yields results in agreement with “engineering judgment”, and leads to updating a (very) small subset of parameters.

Finally, a new application for a BESS connected to a distribution grid has been proposed. It consists of controlling its active and reactive powers so that the net power entering the distribution system evolves as closely as possible to the response provided by an equivalent model. The objective is to use the equivalent model with a higher guarantee of accuracy. The BESS actually compensates for the inaccuracies of that model, partly inherited from ADN model uncertainty. In

the event of a disturbance (and only in this case), the idea is to measure the voltage at the entry point of the distribution grid with a PMU. The measured voltage is used in a real-time simulation of the equivalent. The so computed response of the equivalent is used as a reference to control with a BESS the net power entering the grid. The results show good performance with the BESS able to bring the power flows close to that desired reference after a voltage change, for various type of disturbances, but within the limits imposed by the voltage phasor measurements process. An additional advantage of this application is the less frequent updates of the equivalent, since the BESS partly compensates for its possible inaccuracies.

7.2 Directions for future work

While this thesis has proposed a complete, detailed methodology for the derivation of ADN equivalents, several challenges have yet to be addressed. The following extensions could be investigated.

Modelling and applications

- Although the methodology is not bound to a particular model, it would be of interest to test its performance for ADNs hosting loads with a growing use such as heat pumps, electric vehicles [GPP19], motor drives, etc.
- This work has focused on three-phase balanced systems (a simplifying assumption acceptable in European grids relying on three-phase distribution). Moreover, the simulated voltage dips account for three-phase balanced faults. The simulation of unbalanced faults and the modelling of unbalanced grids could increase the scope of applications. This would of course require to represent each phase separately ...
- ... but it would also allow incorporating further components such as single-phase inverters for PV units connected to low-voltage grids, or single-phase induction motors, for instance.
- Essentially fast controls of IBGs, such as reactive current injection, have been considered in this work. However there has been a significant research dealing with slower but coordinated IBG control schemes. One example is the improvement of the distribution grid voltage profile [GEC17, SB17]. It would be of interest to enlarge the field of application of the ADN equivalent by encompassing those controls. One example of application is long-term voltage stability, for which it has been shown that distribution grid voltage restoration by dispersed IBGs (in addition to the classical distribution transformer LTC control) may accelerate the load power restoration and, hence, precipitate the fall of voltages [AVVC15] consecutive to a severe outage in the transmission grid. Incidentally, it turns out that of equivalent network

shown in Fig. 4.20, with its aggregate load and IBG connected to distinct buses, is probably not appropriate to reproduce the above mentioned effect of IBGs on loads. The structure shown in Fig. 4.5 should be preferred.

- Conversely, IBGs may contribute to enhancing long-term voltage stability in emergency situations, if properly controlled together with the distribution transformer LTC, as illustrated in [POVC20]. Incorporating such controls schemes would be a welcome extension of the equivalent considered in this thesis.
- The dynamic studies could also be extended to situations where the distribution system itself becomes unstable, for instance due to stalling of induction motors.

Handling of model uncertainty

- The analysis of the uncertainty affecting the ADN models has shown that the randomized power evolutions are generally grouped around their (time-varying) averages. Indeed, for a given discrete time of the simulation, the distribution of power values is close to a Gaussian one. Yet, this could not always be the case.

First, if “outlier” trajectories were present, the median would provide a more robust estimate than the average.

Next, if the randomized power evolutions showed up in multiple, clearly separated groups, one option would be to resort to a partitioning algorithm to identify clusters of trajectories. For instance, the k-means or k-medoids algorithm [Kau87] could be used. This would yield multiple time-varying reference evolutions, leading to identify either multiple equivalents (one per cluster) or a single equivalent whose response would jointly minimize (in the least-square sense) the differences with respect to the multiple reference evolutions.

Large-scale studies

- This thesis has focused on validating the ADN equivalent on a single instance of that ADN subject to changes of a voltage source replacing the transmission grid. The performance of the proposed approach could be further validated by performing large-scale studies involving a detailed transmission system model with a large number of attached equivalents, as considered in [AVVC15, POVC20]. Those studies would be closer to the final use of the equivalent by the TSO.

Updating the equivalent

- While the removal of a feeder has been considered in Chapter 5, future work could include more impacting network topology changes, such as the reconfiguration of a distribution grid that can be fed from two substations.
- The approach of Chapter 5 to deal with changing operating conditions consists of progressively building a collection of equivalents to accommodate newly encountered operating conditions. A complementary analysis would consist of classifying those equivalents with respect to attributes typical of operating conditions, such as the time of the day or week, the load level, the solar irradiance of PV panels, the wind speed in WTs, etc. A machine learning method could be used to that purpose. The so obtained classification would allow to retrieve more directly the most appropriate equivalent among the existing set, based on the current value of the attributes.

Control of battery energy storage system

- A more accurate modeling of the PMU could be used for further validation of the proposed concept. Besides the filtering of the PMU outputs, the model could go deeper in the signal processing used in the PMU itself.
- Instead of the simple PI controllers considered for controlling the active and reactive powers produced by the battery energy storage system, more advanced control schemes could be contemplated such as Model Predictive Control (MPC), which could potentially better anticipate of the near future impacts of the control actions taken.

Appendix A

Comparison of ULiège IBG and WECC type 4 models

The Western Electricity Coordinating Council (WECC) “promotes Bulk Electric System reliability in the Western Interconnection of North America. It is responsible for compliance monitoring and enforcement. It also provides an environment for the development of Reliability Standards and the coordination of the operating and planning activities of its members” [[wecrg](#)].

A.1 Overview of the WECC type 4 model

The WECC type 4 model is the most developed model of converter-based generator used by North American industry for dynamic simulations and grid stability studies. This model is able to accommodate various combinations of inverter-level control modes.

A schematic overview of the Type 4 Wind Turbine (WT) as well as a block-diagram of the main parts of the model are provided in Fig. [A.1](#). The model is composed of :

- the plant level control module (repc.a);
- the electric control module (reec.a);
- the converter module (regc.a).

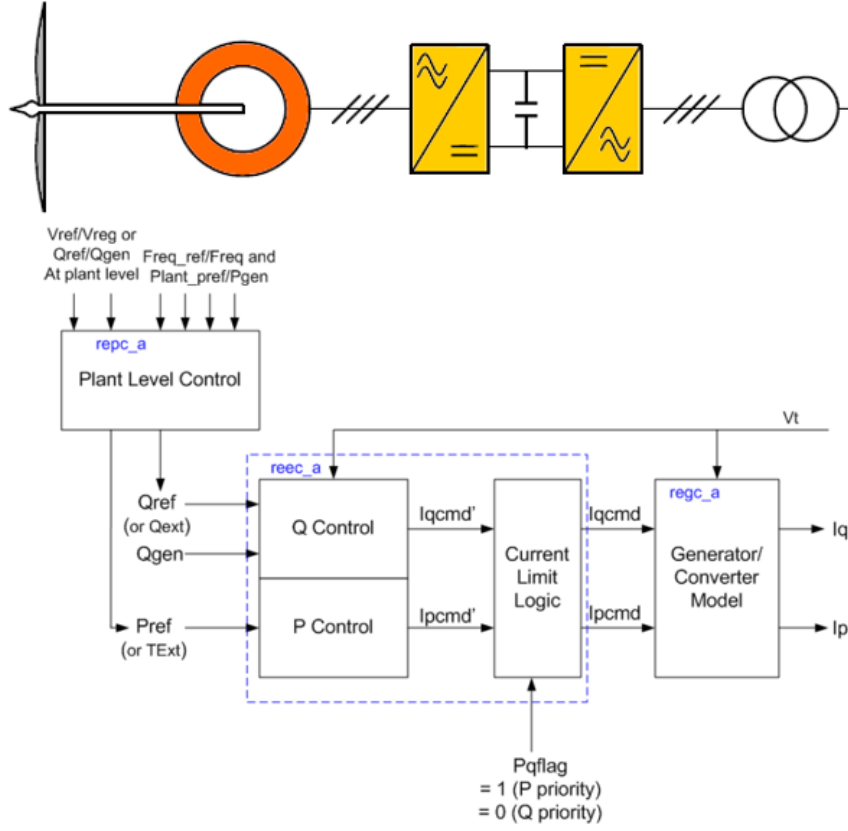


Figure A.1: Schematic overview and block-diagram representation of the WECC Type 4 WT model [MG14a]

A.2 Assumptions and selected configuration

The *repc_a* module is not considered as it is assumed that the reference active power P_{ref} and reactive power Q_{ref} are constant for the duration of our simulations.

The electric control module (*reec_a*) is shown in block-diagram form in Fig. A.2. It is able to accommodate different control strategies. For a relevant comparison with the model used in this thesis, the local coordinated Q/V control mode has been selected as it involves reactive current injection during voltage dips, based on voltage measurements. For this particular configuration, the binary parameter Q_{ext} is set to zero, while $VFlag$ and $QFlag$ are set to one (see Fig. A.2). The values of these binary parameters lead to focus on the subsystem shown with the blue arrow in the figure. Moreover, the drive train model is not considered, since torsional oscillations are out of the scope of this thesis. Therefore, the parameter $PFlag$ is set to zero, which corresponds to the blue arrow in the lower part of the figure.

The converter module (*regc_a*) is shown in block-diagram form in Fig. A.3. The latter involves a

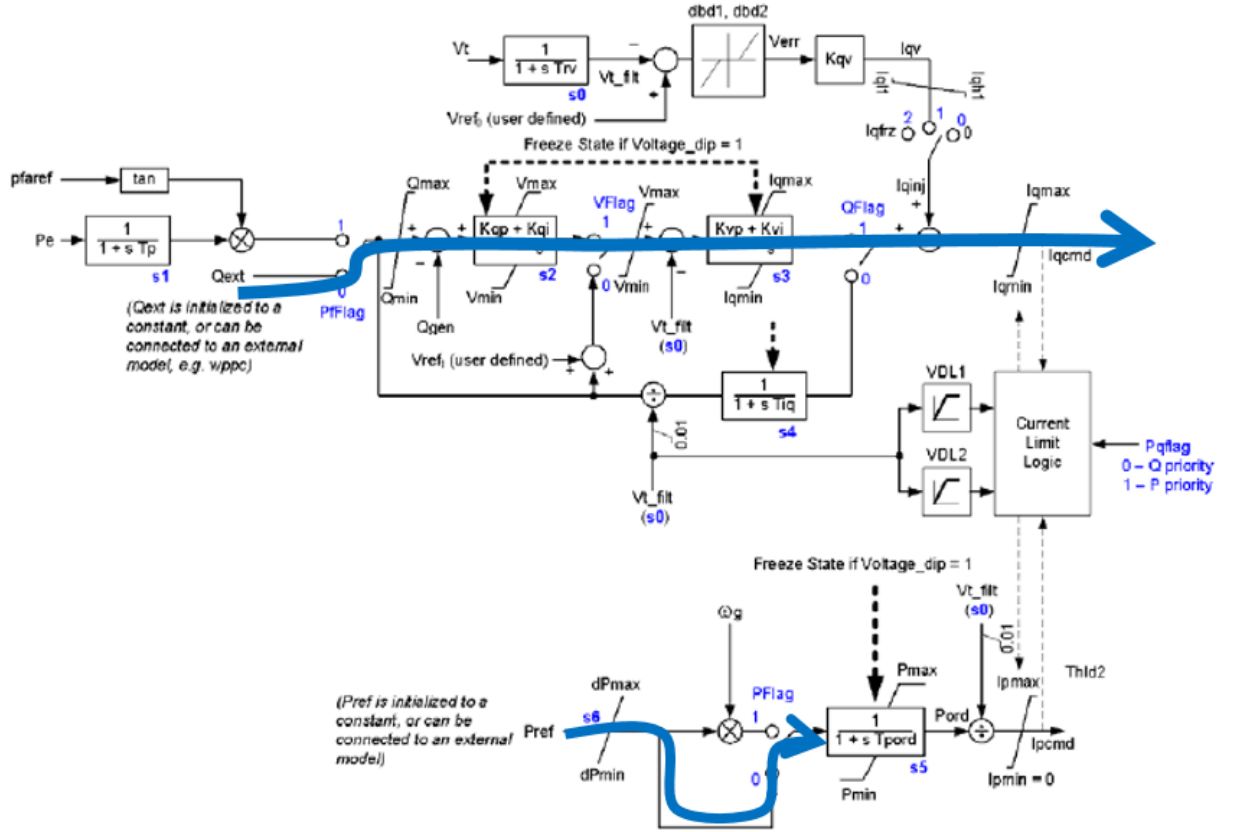


Figure A.2: Block-diagram of the electric control module (reec_a). The blue arrows indicate the value of the binary parameters for the local coordinated Q/V control mode without the drive train model [MG14a]

converter lag-time constant T_g as for the ULiège IBG model.

On the other hand, as no typical value is provided in WECC reports for the Low Voltage Power Logic (LVPL), it has been decided to ignore this block. Hence, the parameter L_{vplsw} is set to zero.

One of the major differences between the WECC and the ULiège models is the presence of a “low voltage active current management” block and the absence of a PLL in the former model (see Fig. A.3). This appears to be a limitation of the WECC model. In fact, it is said in [PSGS⁺15] that the converter PLL has been neglected for the most part and the low voltage active current management logic attempts in a rather rudimentary way to approximate the response of the PLL during severe voltage dips. This would unavoidably lead to a mismatch in terms of active current and power between the WECC and ULiège models. Furthermore it appears that PLLs (particularly for IBGs connected to distribution grids [LRC⁺15]) may have a non negligible response time, which motivates to represent them, at least with a generic model. Therefore, it has been preferred

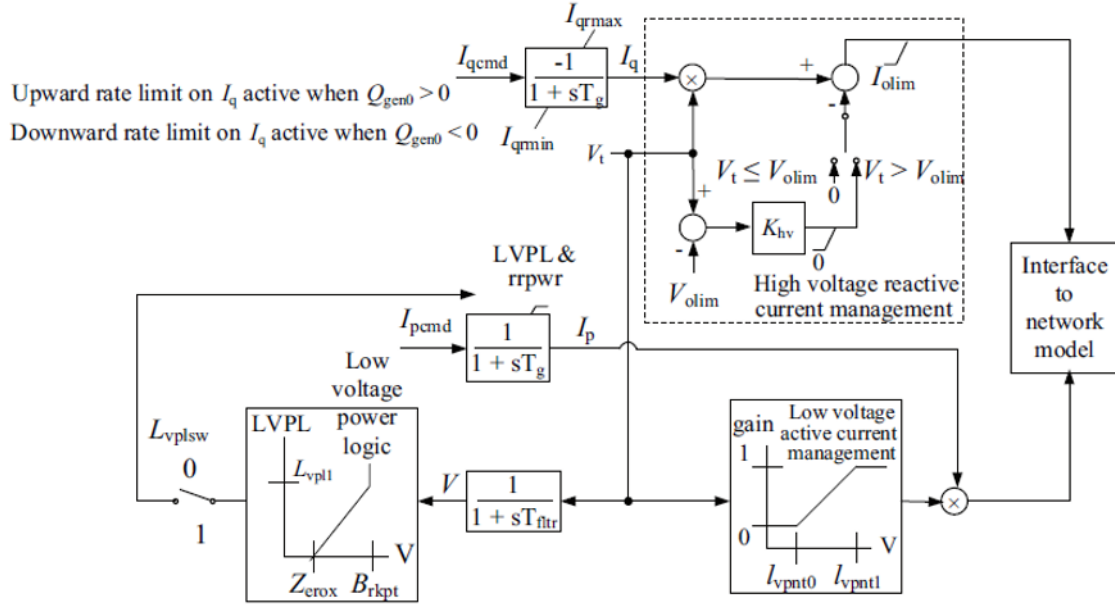


Figure A.3: Block-diagram of the converter module (regc_a) [MG14a]

Table A.1: WECC model, values of the PI controllers parameters

Parameter	Value
K_{qp}	0.2
K_{qi}	0.1
K_{vp}	0
K_{vi}	40

to bypass the low voltage active current management block and consider the same PLL in both models. This leads to an “hybrid” WECC model. The PLL was shown in Fig. 2.7.

Finally the parameters of the PI controllers of the reec.a module have no specified range of values in [MG14a]. Therefore they have been adjusted in order to match the typical behaviour of IBG units dictated by grid codes (e.g. NC RfG (ENTSO-e), VDE AR N 4105/ BDEW MV (Germany), IEEE 1547 (United States)). The values of the PI controllers parameters are shown in Table A.1. The other parameters of the WECC model are set to the typical values recommended in [MG14a].

A.3 Optimal adjustment of the ULiège IBG model parameters

This section aims at showing that the ULiège IBG model is able to match a particular configuration of the WECC model in response to voltage dips of various severities. It has been chosen to adjust six parameters of the ULiège IBG model. Let them be grouped in a vector \mathbf{U} .

First the equations (2.35, 2.36) of the inverter current limits are rewritten as :

$$I_{Pmax} = P_{flag} I_{nom} + (1 - P_{flag}) \sqrt{I_{max1}^2 - i_{Qcmd}^2} \quad (\text{A.1})$$

$$I_{Qmax} = P_{flag} \sqrt{I_{nom}^2 - i_{Pcmd}^2} + (1 - P_{flag}) I_{max2} \quad (\text{A.2})$$

where I_{max1} and I_{max2} , included in \mathbf{U} , can be greater than the nominal current I_{nom} ¹ of the inverter. The following parameters are also included in \mathbf{U} :

- the time constants T_m and T_g (see Fig. 2.5);
- the slope k_{RCI} and voltage threshold V_{S1} (see Fig. 2.9).

\mathbf{U} is optimally adjusted as the solution of :

$$\min_{\mathbf{U}} J(\mathbf{U}) = \frac{1}{dN} \sqrt{\sum_{j=1}^d \sum_{k=1}^N J_P(k, j, \mathbf{U}) + J_Q(k, j, \mathbf{U})} \quad (\text{A.3})$$

$$\text{where } J_P(k, j, \mathbf{U}) = [P_{IBG}(k, j, \mathbf{U}) - P_{WT4}(k, j, \mathbf{U})]^2 \quad (\text{A.4})$$

$$\text{and } J_Q(k, j, \mathbf{U}) = [Q_{IBG}(k, j, \mathbf{U}) - Q_{WT4}(k, j, \mathbf{U})]^2 \quad (\text{A.5})$$

$$\text{with } \mathbf{U}^{min} \leq \mathbf{U} \leq \mathbf{U}^{max} \quad (\text{A.6})$$

where :

- P_{WT4} (resp. Q_{WT4}) is the active (resp. reactive) power response of the WECC type 4 WT model;
- P_{IBG} (resp. Q_{IBG}) is the active (resp. reactive) power response of the ULiège IBG model;
- \mathbf{U}^{min} and \mathbf{U}^{max} keep \mathbf{U} in realistic range of values;
- d is the number of voltage dips considered in the minimization problem;
- N is the number of time steps in the simulation.

The metaheuristic DE algorithm has been used to solve the above minimization problem.

¹This allows to inject a reactive current greater than I_{nom} during severe voltage dips. The duration of such event being short, there are no risk to damage the electronic components of the converter, due to thermal inertia.

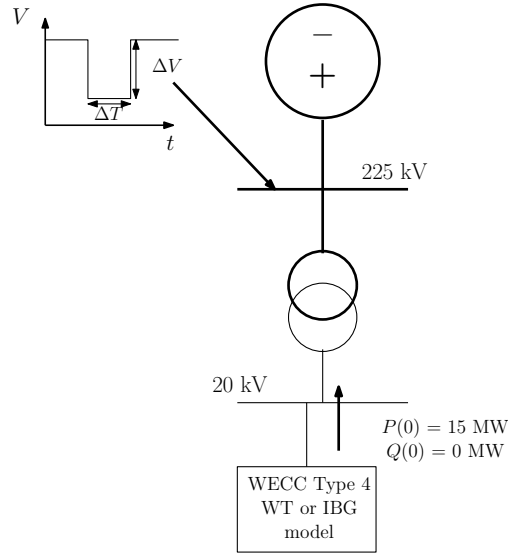


Figure A.4: Test system for the comparison of ULiège IBG with WECC WT type 4 models

A.4 Simulation results

This section compares the active (resp. reactive) current and power responses of both models to voltage dips, not used for the adjustment of the IBG parameters. Simulation results are reported on the small test system shown in Fig. A.4. The voltage dips, characterized by a depth ΔV and a duration ΔT , are applied on the high voltage (225 kV) side of the transformer. The pre-disturbance production is $P(0) = 15 \text{ MW}$ and $Q(0) = 0 \text{ Mvar}$.

Figures A.5, A.6 and A.7 show the active and reactive currents and powers of both models in response to the voltage dips ($\Delta V = 0.3 \text{ pu}$, $\Delta T = 100 \text{ ms}$), ($\Delta V = 0.5 \text{ pu}$, $\Delta T = 100 \text{ ms}$) and ($\Delta V = 0.7 \text{ pu}$, $\Delta T = 250 \text{ ms}$), respectively. It is seen that, with the previously described IBG parameter adjustment, a real good match can be achieved between both models.

It can also be concluded that, although it is of higher order, the WECC WT type 4 model (involving PI controllers and the time constant T_g) shows a very well damped response oscillating around that of the (only) 1st-order IBG model used in this thesis. As a reminder, the latter computes the reference current values and only considers the time constant T_g .

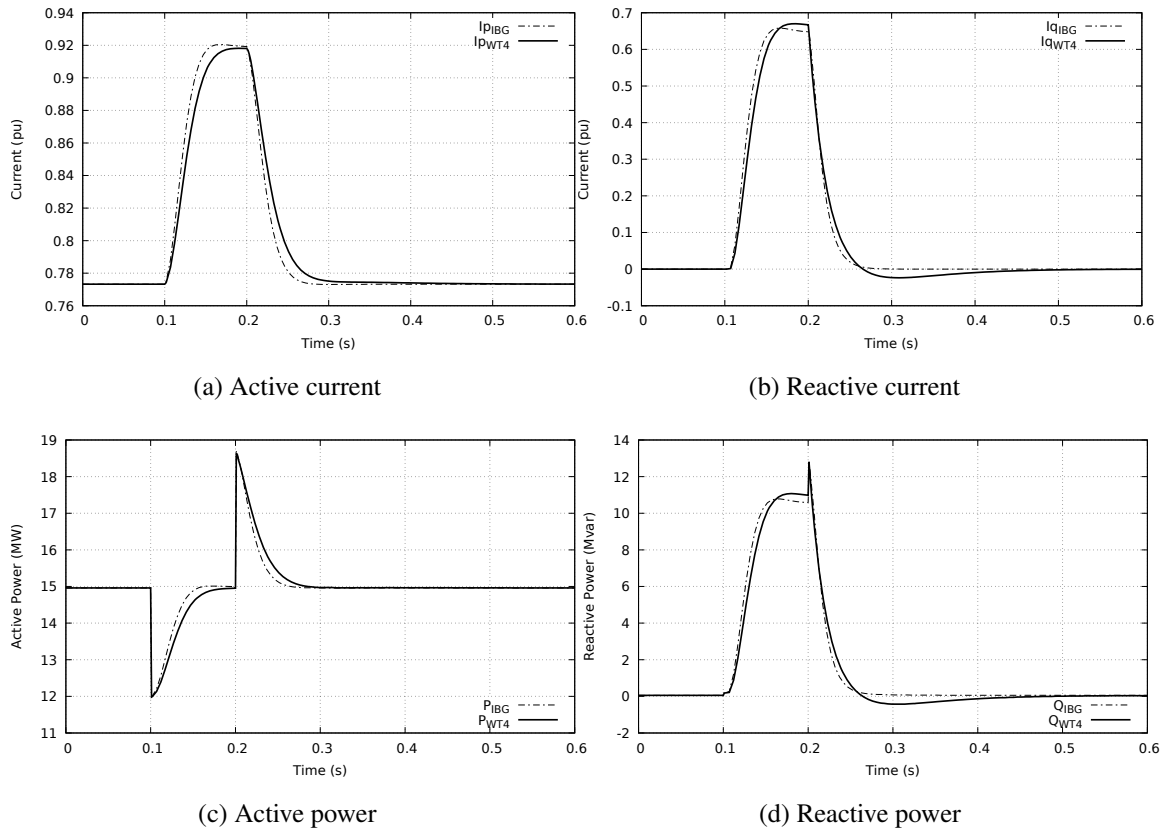


Figure A.5: Comparison of ULiège IBG with WECC WT type 4 models for a voltage dip with $\Delta V = 0.3$ pu and $\Delta T = 100$ ms

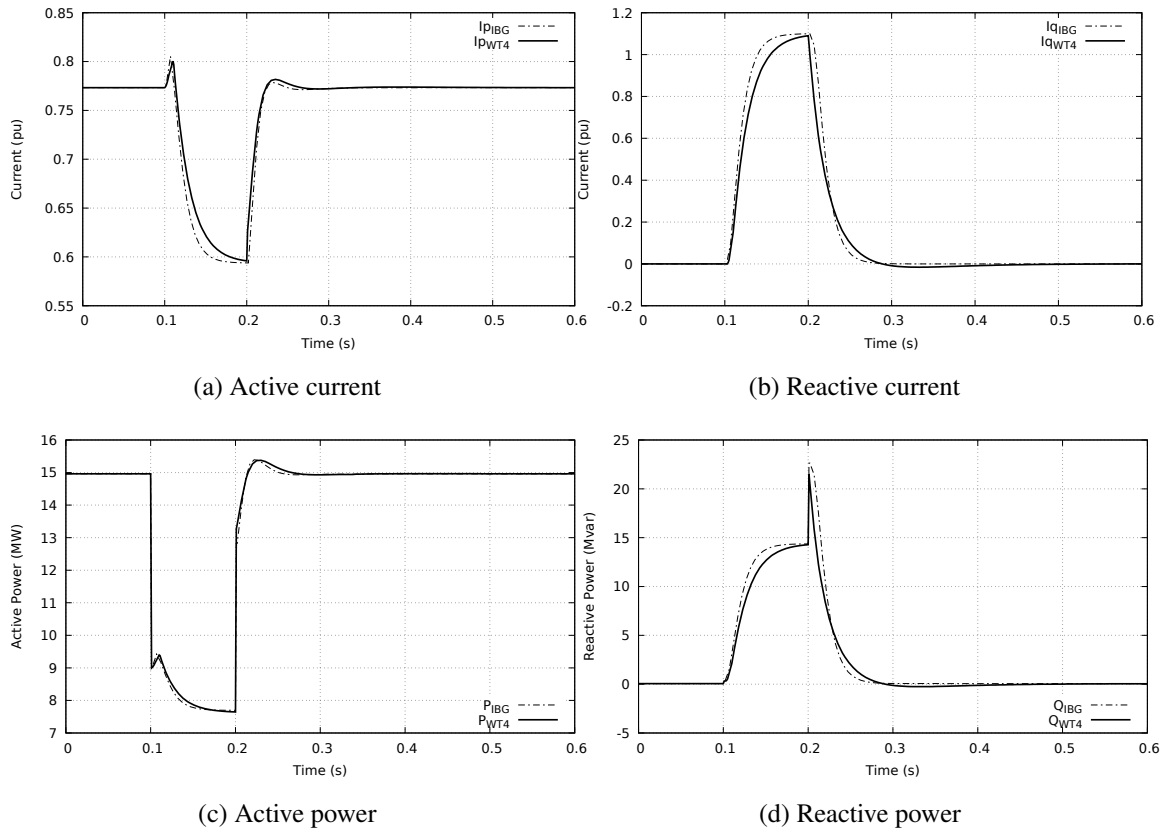


Figure A.6: Comparison of ULiège IBG and WECC WT type 4 models for a voltage dip with $\Delta V = 0.5$ pu and $\Delta T = 100$ ms

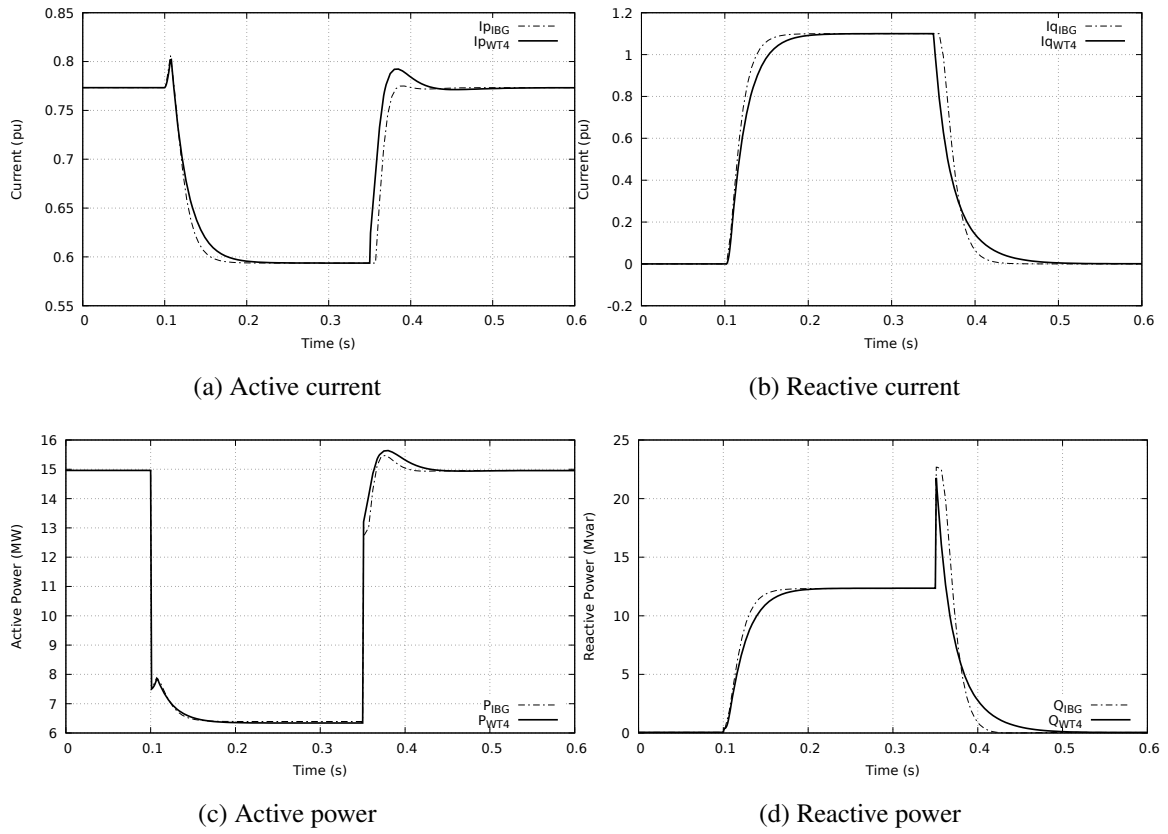


Figure A.7: Comparison of ULiège IBG and WECC WT type 4 models for a voltage with of $\Delta V = 0.7$ pu and $\Delta T = 250$ ms

Appendix B

Alternative objective functions for the identification of the equivalent

B.1 Non-weighted least-square objective

The non-weighted least-square minimization takes on the form:

$$\min_{\boldsymbol{\theta}} F(\boldsymbol{\theta}) = \frac{1}{d} \sum_{j=1}^d [F_P(\boldsymbol{\theta}, j) + F_Q(\boldsymbol{\theta}, j)] \quad (\text{B.1})$$

$$\text{where } F_P(\boldsymbol{\theta}, j) = \frac{1}{N} \sum_{k=1}^N [P_e(\boldsymbol{\theta}, j, k) - \mu_P(j, k)]^2 \quad (\text{B.2})$$

$$F_Q(\boldsymbol{\theta}, j) = \frac{1}{N} \sum_{k=1}^N [Q_e(\boldsymbol{\theta}, j, k) - \mu_Q(j, k)]^2 \quad (\text{B.3})$$

$$\text{and with } \boldsymbol{\theta}^L \leq \boldsymbol{\theta} \leq \boldsymbol{\theta}^U \quad (\text{B.4})$$

where μ_P and μ_Q are the average power evolutions extracted from the MC simulations. Weights reflecting the dispersion of power values are no longer considered here.

This objective function can be used with ADN models showing, for each j and k value, a small dispersion of their response in spite of the parameter randomization.

B.2 Alternative weighted least-square objective

Another variant of the objective function consists of further penalizing the deviation from $\mu_P(j, k)$ (resp. $\mu_Q(j, k)$) when the response exhibits large deviations from its pre-disturbance value $\mu_P(0)$ (resp. $\mu_Q(0)$). This can be formulated as:

$$\min_{\boldsymbol{\theta}} F(\boldsymbol{\theta}) = \frac{1}{d} \sum_{j=1}^d [F_P(\boldsymbol{\theta}, j) + F_Q(\boldsymbol{\theta}, j)] \quad (\text{B.5})$$

$$\text{where } F_P(\boldsymbol{\theta}, j) = \frac{1}{N} \sum_{k=1}^N \alpha_P(j, k) [P_e(\boldsymbol{\theta}, j, k) - \mu_P(j, k)]^2 \quad (\text{B.6})$$

$$F_Q(\boldsymbol{\theta}, j) = \frac{1}{N} \sum_{k=1}^N \alpha_Q(j, k) [Q_e(\boldsymbol{\theta}, j, k) - \mu_Q(j, k)]^2 \quad (\text{B.7})$$

$$\text{with } \alpha_P(j, k) = |\mu_P(0) - \mu_P(j, k)| \quad (\text{B.8})$$

$$\text{with } \alpha_Q(j, k) = |\mu_Q(0) - \mu_Q(j, k)| \quad (\text{B.9})$$

$$\text{and with } \boldsymbol{\theta}^L \leq \boldsymbol{\theta} \leq \boldsymbol{\theta}^U. \quad (\text{B.10})$$

This assigns higher weights to points in time when the power excursions are large, i.e. when the system is more disturbed.

B.3 Barrier functions

In this case, a reference power evolution is no longer considered. Instead, time-varying confidence intervals are used. They are retrieved from the distribution of dynamic responses in the MC simulations. The confidence intervals can be obtained from the 5-th and 95-th percentiles, for instance. Furthermore, all points falling in the confidence interval are indiscriminately deemed accurate.

This can be formulated as :

$$\min_{\boldsymbol{\theta}} F(\boldsymbol{\theta}) = \frac{1}{d} \sum_{j=1}^d [F_P(\boldsymbol{\theta}, j) + F_Q(\boldsymbol{\theta}, j)] \quad (\text{B.11})$$

$$\text{with } F_P(\boldsymbol{\theta}, j) = \frac{1}{N} \sum_{k=1}^N F_P(\boldsymbol{\theta}, j, k) \quad (\text{B.12})$$

$$F_Q(\boldsymbol{\theta}, j) = \frac{1}{N} \sum_{k=1}^N F_Q(\boldsymbol{\theta}, j, k) \quad (\text{B.13})$$

where the errors at time k are given by the quadratic barrier functions :

$$F_P(\boldsymbol{\theta}, j, k) = \begin{cases} [P_l(j, k) - P_e(\boldsymbol{\theta}, j, k)]^2 & \text{if } P_e(\boldsymbol{\theta}, j, k) < P_l(j, k) \\ [P_u(j, k) - P_e(\boldsymbol{\theta}, j, k)]^2 & \text{if } P_e(\boldsymbol{\theta}, j, k) > P_u(j, k) \\ 0 & \text{otherwise,} \end{cases}$$

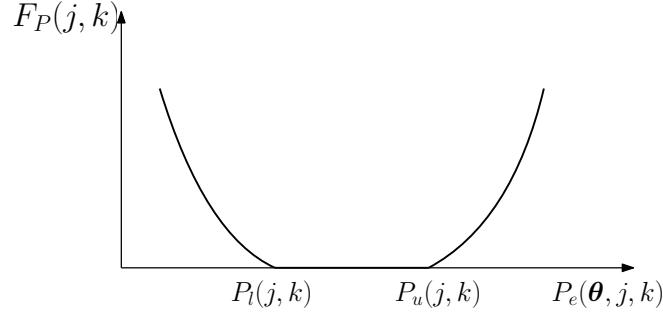


Figure B.1: Barrier function that can be used in the identification of the equivalent

$$F_Q(\theta, j, k) = \begin{cases} [Q_l(j, k) - Q_e(\theta, j, k)]^2 & \text{if } Q_e(\theta, j, k) < Q_l(j, k) \\ [Q_u(j, k) - Q_e(\theta, j, k)]^2 & \text{if } Q_e(\theta, j, k) > Q_u(j, k) \\ 0 & \text{otherwise,} \end{cases}$$

under the constraints :

$$\theta^L \leq \theta \leq \theta^U \quad (\text{B.14})$$

where :

$P_l(j, k)$ is the time-varying lower bound of the confidence interval of active power

$Q_l(j, k)$ is the corresponding bound for reactive power;

$P_u(j, k)$ is the time-varying upper bound of the confidence interval of active power;

$Q_u(j, k)$ is the corresponding bound for reactive power;

The barrier function is illustrated for the active power in Fig B.1. The idea is to ideally force the dynamic responses of the equivalent to fall inside the confidence interval $[P_l(j, k) \ P_u(j, k)]$ for all d disturbances. If this was achieved, the objective function in (B.11) would reach a zero value. The same applies for the reactive power.

Appendix C

Measurement-based identification of aggregate PV models¹

The goal of the study reported in the Appendix was to build aggregate models of :

1. distributed PV units (connected to the distribution system);
2. PV farms (connected to the transmission system)

based on measurements collected during the August 2018 separation event in Australia. This event led to large frequency deviations in the Australian National Electricity Market (NEM) [[Aus19a](#)].

These aggregate models are intended to be embedded into transmission system models and, to start with, the Australian 14-generator test system [[M. 14](#)], a simplified model of the Australian NEM grid, used by researchers of the University of Melbourne.

C.1 Overview of the event

On Saturday 25 August 2018, an event saw the loss of the AC interconnector between the Queensland (QLD) and New South Wales (NSW) regions, followed by loss of the AC interconnector between South Australia (SA) and Victoria (VIC). There was a single lightning strike on a transmission tower structure supporting the two circuits of the 330 kV Queensland New South Wales interconnector (QNI) lines. The lightning strike triggered a series of reactions creating faults on

¹This appendix presents results obtained during an internship in the team of Prof. P. Mancarella at the University of Melbourne, Australia.

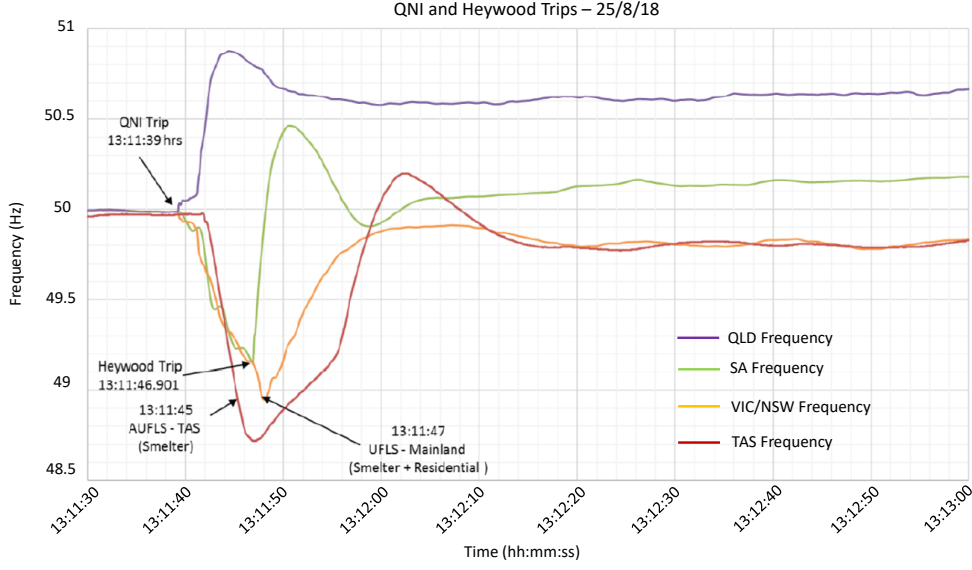


Figure C.1: Measured frequency signals during the separation event. Adapted from [Aus19a]

each of the two circuits of QNI at 13:11:39. The QLD and NSW power systems then lost synchronism, islanding the QLD region two seconds later, at 13:11:41. At the time, 870 MW of power was flowing from QLD to NSW. QLD experienced an immediate supply surplus, resulting in a rise in frequency to 50.8 Hz. The remainder of the National Electricity Market (NEM) experienced a supply deficit, resulting in a reduction in frequency.

This appendix focuses on the QLD state, which faced the most critical frequency rise. As an illustration, the frequency signals measured during the event in different states, including QLD, are shown in Fig. C.1.

At the time of the event, the total capacity of distributed PV units was 2177 MW. Their pre-disturbance active power production was 1043 MW. Nine PV farms were also in operation for a total capacity of 586 MW. Their pre-event generation was 286 MW [Aus19a].

Note that, the large connected PV capacity at the time of the event had a non-negligible impact on the QLD frequency.

C.2 Measurement-based identification

Because of the dispersed nature of PV units in the grid, their different control settings and commissioning dates, the frequency response is different from one unit to another. This raises the issue of properly identifying an aggregate model. Its parameters, grouped in a vector θ , are adjusted in the least-square sense to have the frequency response of the aggregate models of distributed PV

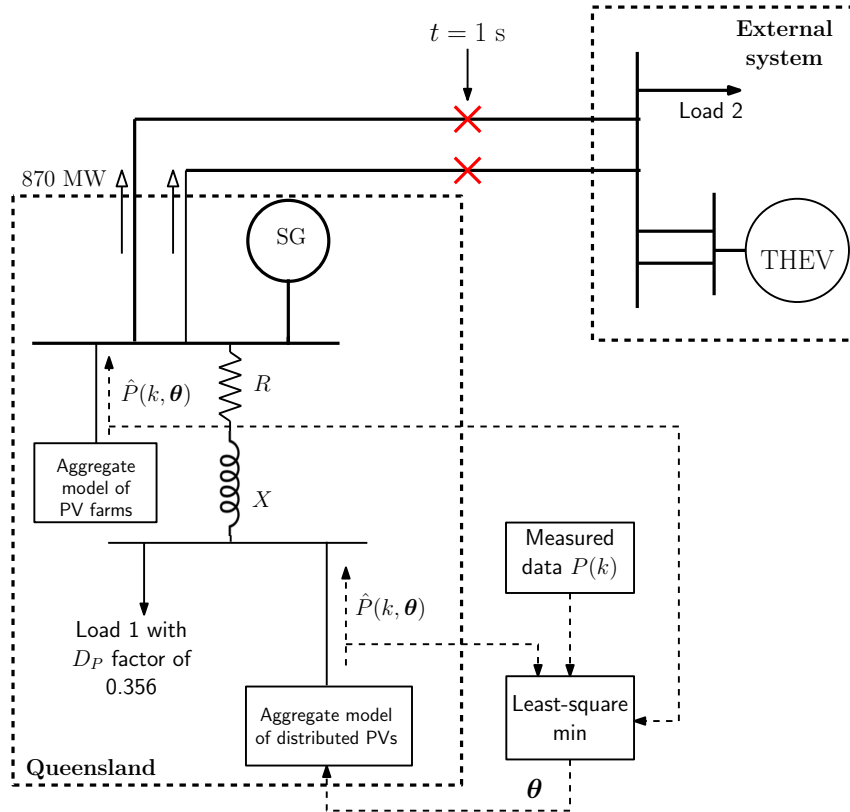


Figure C.2: Test system and closed-loop measurement based identification

units (resp. PV farms) as close as possible to the combined measured response of the distributed PV units (resp. PV farms) during the event under study.

C.2.1 Closed-loop identification process

Contrary to an “open-loop” identification process, in which a pre-defined, invariant frequency disturbance is applied, a “closed-loop” identification process has been carried out. The latter allows, during the identification process, to take into account the continuous impact on frequency of the active power response given by the aggregate PV model. Indeed, in a closed-loop identification, the change in model parameters during the identification, modifying its active power response, can have a substantial impact on the frequency, influencing in turn the active power response of the model, and eventually the value of the identified parameters. There is also the added value of using real measurements (although the limitation of this approach has been discussed in Section 1.4).

The process is illustrated in Fig. C.2 where the frequency deviation is reflected by the rotor speed of an equivalent Synchronous Generator (SG). The frequency is also computed inside the aggregate models of PV units (more precisely in the model of their PLLs) which change their active power

output accordingly. The latter is compared with the measured data and θ is updated until the stopping criterion of the least-square minimization is satisfied.

C.2.2 Available measurements

The measurements collected during the event fall in two categories :

1. active power coming from distributed PV responses;
2. active power produced by transmission-connected PV farms.

In fact, there was no direct measurement of the combined output of the distributed PV units during the event under study. Instead, a record of the total regional load was available. Now, reduction of the output of distributed behind the meter PV units appears as an increase of the demand. Further post-event PV analysis reported in [Aus19a] confirmed that indeed the available regional demand response was giving an accurate estimation of the distributed PV units active power reduction. The report [Aus19a] suggests that it decreased by approximately 165 MW as the result of the event. The same analysis confirmed that it was also giving a good estimate of the time when that PV production reached its lowest value. Based on this information, an estimate of the decrease in time of the PV units active power has been derived. The active power reduction comes from :

- PV units disconnection, for “old” units compliant with with AS/NZ4777.3-2005 requirement [Aus16, Aus19b];
- PV units droop response, for “new” units compliant with AS/NZ4777.2-2015 requirement [Aus16, Aus19b].

Since we only know the active power reduction ΔP and the time it took to reach this reduction Δt , the active power evolution of distributed PV units evolves with a constant slope $\Delta P/\Delta t$. For seek of simplicity, this is referred to as the “measured response” in the sequel.

The power outputs of the transmission-connected PV farms, on the other hand, were directly available. PV farms are expected to provide a droop response in response to over-frequency [Aus19a]. Therefore, the combined response of PV farms appears to follow a piece-wise linear evolution with time because the MW reductions from individual units varied in size and timing [Aus19a] and because the QLD frequency increases almost linearly with time (see Fig. C.1). Moreover, it has been shown that the response was delivered ineffectively due to a coordination delay issue. Indeed, much of the response to over-frequency was delivered to the system after frequency has reached its maximum. The combined response of PV farms has been smoothened. Again, for simplicity, the smoothened measurement is also referred as to the “measured response” in the sequel.

These measured responses are used as reference in the least-square minimization presented in the next section.

C.2.3 Formulation of least-square minimization problem

The parameter vector θ of the aggregate model is adjusted in order to minimize the least-square error :

$$\varepsilon_1(\theta) = \frac{1}{N} \sum_{k=0}^N [P(k) - \hat{P}(k, \theta)]^2 \quad (\text{C.1})$$

under the constraint :

$$\theta^L \leq \theta \leq \theta^U. \quad (\text{C.2})$$

where k refers to the discrete time of the time-domain simulation solver, N is the total number of discrete times, $P(k)$ is the measured power response of PV units and $\hat{P}(k, \theta)$ is the corresponding evolution given by the aggregate models (see Fig. C.2).

As mentioned in the previous section, only the active power recordings were available and have been used. The frequency evolution, on the other hand, has not been considered. By fitting the active power responses with the aggregate models, there is no control on the frequency deviation, in particular on the maximum reached frequency in the post-disturbance period, which is a concern for the system operator.

A compromise solution has been adopted by adding a penalty term to the objective (C.1). The error to minimize becomes :

$$\varepsilon_2(\theta) = \varepsilon_1(\theta) + \gamma |f_{max} - \hat{f}_{max}(\theta)| \quad (\text{C.3})$$

where f_{max} is the maximum frequency observed in QLD during the event and $\hat{f}_{max}(\theta)$ is the maximum frequency reached in the simulation of the event for the current value of θ . γ is a scaling factor that must be selected large enough in order to have $|f_{max} - \hat{f}_{max}(\theta)| \approx 0$ but not too large to avoid deteriorating $\varepsilon_1(\theta)$.

The DE algorithm has been used to minimize the error (C.3). The optimization process has been stopped when the decrease between two successive values of $\varepsilon_1(\theta)$ is less than 0.1 MW during 10 DE iterations.

C.3 Modelling of network components

C.3.1 PV model

Regarding the modelling of PV units, only controls responding to frequency variations are considered (see Section 2.3.4), which strongly simplifies the IBG model of Fig. 2.5. However, to account

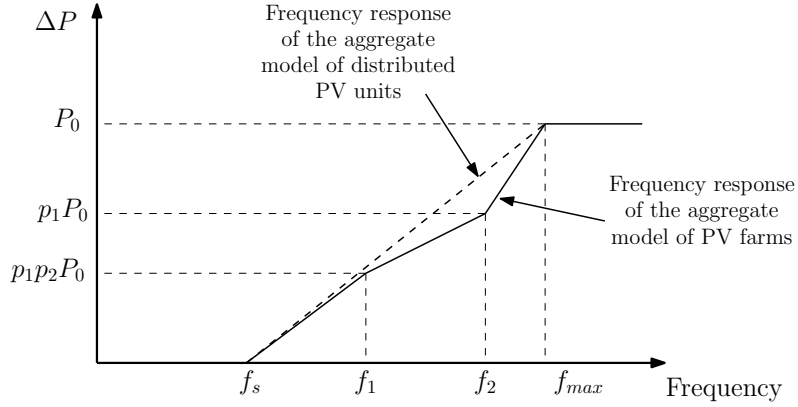


Figure C.3: Frequency-power characteristics used in the aggregate PV models

for the piece-wise droop response of transmission-connected PV farms, a modified frequency response characteristic has been considered. It is shown in Fig. C.3 where ΔP is the active power reduction, P_0 is the pre-event active power production, $p_1, p_2 \in [0, 1]$ and $f_1, f_2 \in [f_s, f_{max}]$. Moreover, the coordination delay is taken into account by applying a first-order transfer function with a time constant T_c to the estimated frequency signal provided by the PLL (with a response time of τ_{PLL}). The output of this transfer function is the signal used to control the active power output.

As a reminder, PV units sustain their minimum level of active power output until the frequency gets back to an acceptable value (see Section 2.3.4). A direct consequence is that only frequency rises have an impact on PV power responses.

All in all, we have :

- $\theta = [f_s, f_{max}, \tau_{PLL}]$ for the aggregate model of distributed PV units;
- $\theta = [f_s, f_{max}, f_1, f_2, p_1, p_2, T_c, \tau_{PLL}]$ for the aggregate model of PV farms.

C.3.2 Load model

The effect of load on frequency variations is an important matter that might have a non-negligible influence on the results of the identification. The load sensitivity to frequency variation is accounted by [Kun94] :

$$P_l = P_{lo} \left(1 + D_P \frac{\Delta f}{f_N} \right) \quad (C.4)$$

where P_{lo} is the pre-contingency active power consumption, Δf is the frequency deviation with respect to its nominal value f_N and D_P is the “damping” factor reflecting the above mentioned sensitivity.

C.3.3 Synchronous generator model

A sixth-order model of SG is used [Kun94]. A simple model of thermal unit and speed governor together with a generic model of excitation system with power system stabilizer have been considered.

C.4 Test system for the parameter identification

As the number of time-domain simulations called by the DE algorithm is large, it is attractive to have a simple, yet representative, test system. The latter is detailed in Fig. C.2. It involves an equivalent SG accounting for the total synchronous generation of QLD at the time of the event. The aggregate model of PV farms is connected to the same bus as the SG since PV farms are connected to the transmission system. Load 1 is an equivalent accounting for the demand of QLD at the time of the event. The aggregate model of distributed PV units is connected to the same bus as Load 1. The resistance R and reactance X account for distribution transformers and feeders. The external system is modeled by a Thevenin equivalent and the equivalent Load 2. QLD and the external system are connected through a double 330-kV line accounting for the QNI (see Section C.1). The load of the external system is adjusted until the power transfer from QLD to the external system reaches 870 MW, the value observed at the moment of the event.

C.4.1 Estimation of the D_P factor

By rearranging the terms of (C.4), D_P is given by

$$D_P = \frac{\Delta P_l / P_{lo}}{\Delta f / f_N} \quad (\text{C.5})$$

where $\Delta P_l = P_l - P_{lo}$.

All terms can be estimated based on data available in [Aus19a]. The results are provided in Table C.1. The load increase ΔP_l following the QNI disconnection has been estimated by removing the effect of PV units in the net demand.

Table C.1: Data for the estimation of D_P

Parameter	Value
P_{lo}	6143 MW
ΔP_l	35 MW
f_N	50 Hz
Δf	0.8 Hz
D_P	0.356

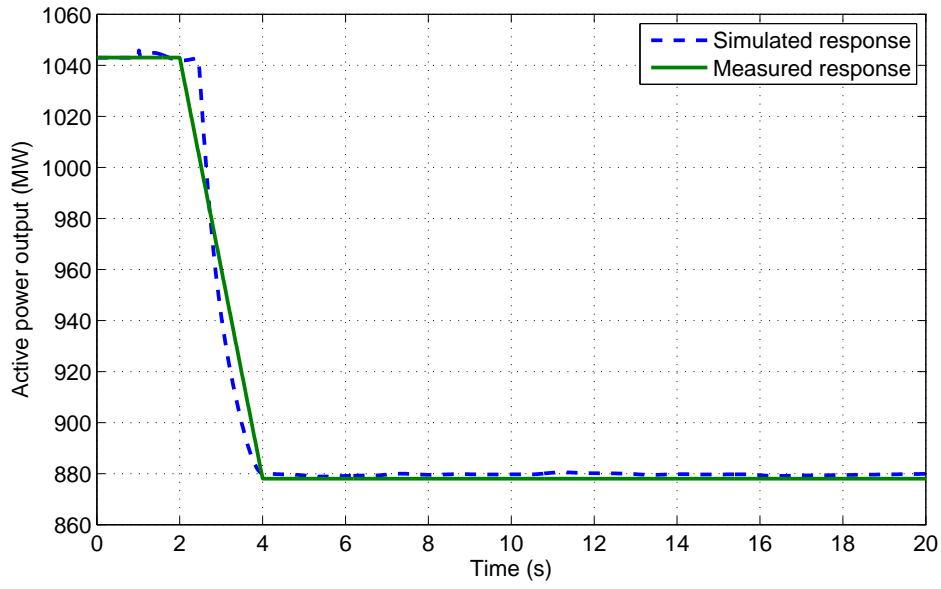


Figure C.4: Measured response of distributed PV units and simulated response after the parameter identification

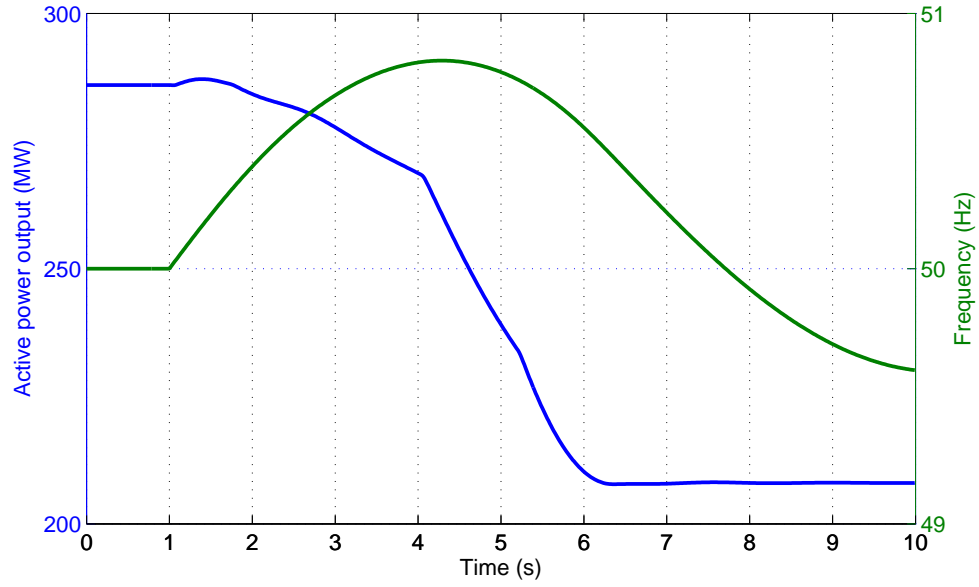
C.5 Simulation results

At $t = 1$ s, the double 330-kV line is opened, to mimic the separation of QLD from the rest of the system (see Fig. C.2).

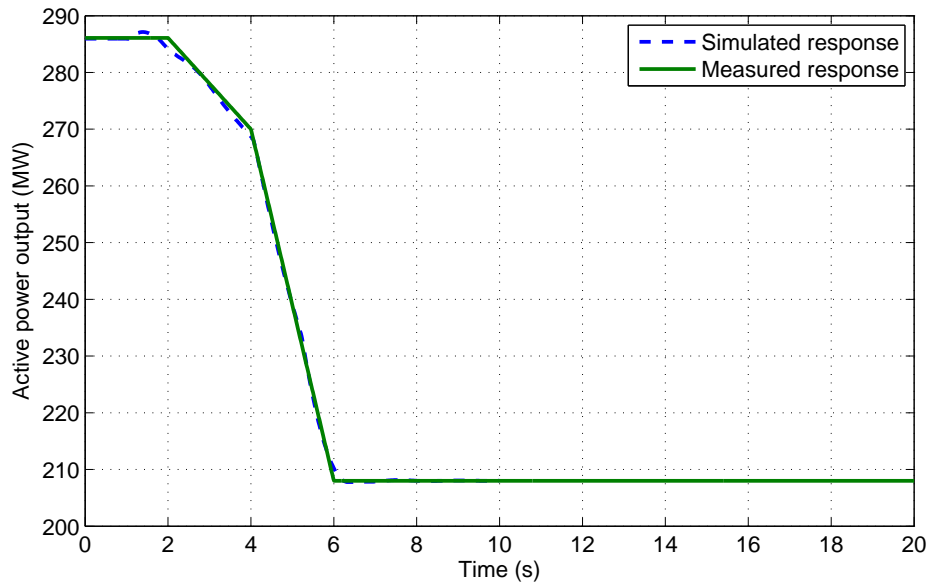
After a few trials, the parameter γ of (C.3) has been set to 200. The maximum simulated frequency $\hat{f}_{max}(\theta)$ is 50.788 Hz, very close to the measured maximum frequency of 50.8 Hz.

C.5.1 Distributed PV units

Figure C.4 compares the measure and simulated responses of the distributed PV units. They are very close to each other, which shows that the parameters lead to a good fit.



(a) Simulated active power response and frequency



(b) Measured vs. Simulated response

Figure C.5: Results of parameter identification of aggregate PV farms

C.5.2 PV farms

Figure C.5a shows the simulated active power output of the aggregate model of PV farms as well as the simulated frequency. Note that the inertia constant of the equivalent SG has been carefully

adjusted such that the simulated rate of change of frequency is similar to the actual one following the event.

Finally, a comparison of the measured and simulated responses is provided in Fig. C.5b. It can be seen that the modified frequency-power characteristic is able to fit the combined measured response of the PV farms.

C.6 Scalability of the method

It is worth repeating that the identification being performed from a single set of measurement, there is in principle no guarantee that the results would be accurate for another scenario, i.e. the results may overfit this particular frequency disturbance. On the other hand, the response of PV units to over-frequency is not expected to qualitatively change in other over-frequency scenarios since the units are only responsive to the maximum frequency. In fact, it is not clear whether another over-frequency event would bring useful additional information and would allow identifying a better value of the parameters. For a researcher it is desirable to check the validity of the results against another, future disturbance but this viewpoint is not likely to be shared by the Australian consumers !

Appendix D

PMU measurements processing

This appendix explains how voltage phasor measurement from a PMU are processed in the BESS application of Chapter 6.

D.1 Overview of the model

The Weighted Moving Average (WMA) filter has been applied on the MV voltage phasor \bar{V} (see Fig. 6.1). Certainly, more elaborate filtering techniques exist. However, the goal is to use a simple filter able to handle measurement errors while the delay introduced by the filter is kept acceptable. In this regards, WMA appeared to be a suitable choice. Indeed, in [Smi13] the MA is said to be the most common filter in digital signal processing, mainly because it is the easiest digital filter to understand and use. Moreover it appears to be optimal in reducing random noise while retaining a sharp step response. As a comparison, [BBB⁺16] uses a sliding window median filter for noise rejection of PMUs data.

To assess the effect of PMU measurement errors, random noise is going to be added to the voltage phasor \bar{V} provided by phasor-mode simulation.

Gaussian noise with zero mean and standard deviation of 0.003 pu appears to be a reasonable choice [BBB⁺16]. The noise is thus randomly generated in the range $[-0.009; 0.009]$. For simplicity, it is added to the v_x and v_y components of \bar{V} .

The time step of the phasor-mode simulation has been decreased to 1 ms. The PMU is assumed to sample the MV voltage \bar{V} at a rate of 200 samples per second, i.e. every $\Delta t = 5$ ms and applies

the WMA filter to the samples. This can be expressed analytically as :

$$v_x^f(t) = \sum_{i=0}^{N-1} W_i(N) v_x^n(t - i\Delta t) \quad (\text{D.1})$$

$$v_y^f(t) = \sum_{i=0}^{N-1} W_i(N) v_y^n(t - i\Delta t) \quad (\text{D.2})$$

where v_x^n (resp. v_y^n) is the noisy x (resp. y) voltage component, N is the time window length and $W_i(N)$ are the weights attributed to each sample in the time window.

The measured voltage magnitude and phase angle are obtained as :

$$V_m = \sqrt{(v_x^f)^2 + (v_y^f)^2} \quad (\text{D.3})$$

$$\delta_m = \tan^{-1}\left(\frac{v_y^f}{v_x^f}\right). \quad (\text{D.4})$$

Two issues in using the WMA filter lie in the choice of (i) the time window size N and (ii) the values of the weights $W_i(N)$.

The choice of the time window size is actually a compromise between the measurement delay and the noise filtering. The measured voltage will evolve more smoothly for a longer time window, but the delay will increase as well.

For the application proposed in Chapter 6, the delay is very important and must be reduced as far as possible to allow a prompt reaction of the BESS.

The choice of the weights $W_i(N)$ can be the result of an heuristic tuning. Yet, it is more convenient to have an analytical expression for the $W_i(N)$ for easier comparison of different time windows, and to avoid re-tuning the weights for each time window size. Therefore, it has been chosen to :

1. derive an analytical expression of the weights $W_i(N)$;
2. chose an appropriate time window size N ;
3. fine tune the weights $W_i(N)$ to further improve the performance of the filter.

D.2 Analytical expression of the weights

In this section, the classical Moving Average (MA) technique, i.e. $W_i(N) = 1/N \ \forall i$, is compared with a WMA whose weights are given in [Shm02] :

$$W_i(N) = \frac{2N(2N-3) + 9 - 6i(N-1)}{N(N^2+6)} \quad (\text{D.5})$$

as a result of the minimization of the global filtering error [Shm02].

These two methods have been compared on a given noisy voltage dip signal. Based on multiple simulation results (not reported here), the following conclusions can be drawn:

1. with the MA filter, the voltage measurement is affected by a large delay;
2. the delay appears strongly reduced with the weights given by (D.5);
3. yet, the weights given by (D.5) induce overshoots for sudden changes of the voltage magnitude. This is hardly acceptable as it is going to distort the equivalent power response P_e^m and Q_e^m (see Fig. 6.1).

In order to reduce the delay that affects the MA filter, while reducing the overshoot, a trade-off consists of averaging the weights of the MA filter with the weights given by (D.5). The resulting weights are given by :

$$W_i(N) = \frac{2N(2N - 3) + 15 - 6i(N - 1) + N^2}{2N(N^2 + 6)}. \quad (\text{D.6})$$

As an illustration, a comparison of respectively (i) the classical MA filter, (ii) the WMA filter with weights given by (D.5) and (iii) the same with weights given by (D.6) is offered in Fig. D.1 for $N = 5$.

It is seen, indeed, that the MA filter induces an important delay. Moreover, it confirms that the weights given by (D.5) produce overshoots at the voltage drop and voltage recovery instants while the weights given by (D.6) provide a trade-off between both cases.

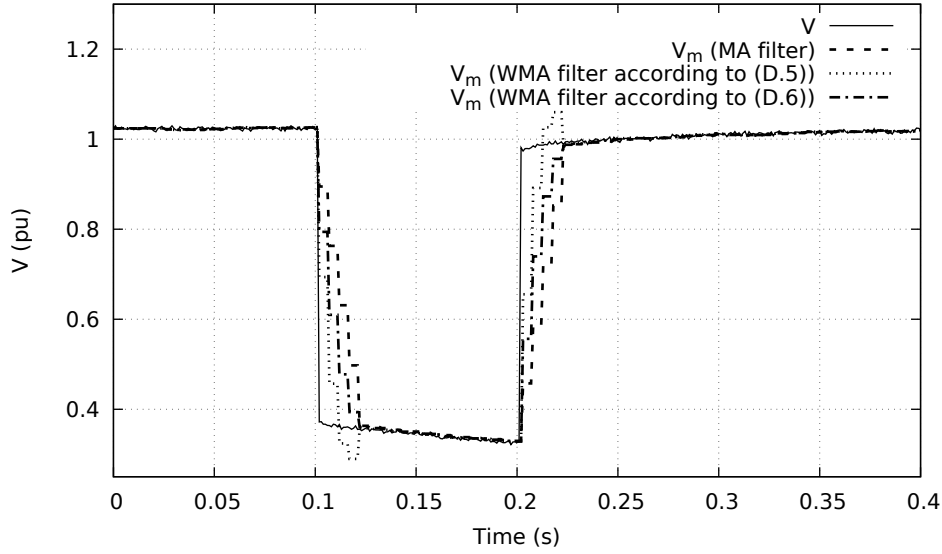


Figure D.1: Comparison of noisy voltage magnitude V with V_m using 1. MA filter, 2. WMA filter with weights given by (D.5) and 3. WMA filter with weights given by (D.6)

D.3 On the size of the time window

The impact of the window size on the voltage measurements delay has been also investigated for the same noisy voltage dip signal. Fig. D.2 compares the measured voltage magnitude for a time window size of 3, 5 and 10, respectively. The use of (D.6) allows to easily adjust the weights with N . Figure D.2 shows that, as expected, the minimum delay is achieved for the smallest N . When comparing the filtering of noise in the zoom displayed in the figure, it can be observed that the latter is not that much impacted by the window size of this example. This would lead to choose the smallest possible N . Yet, a time window size of $N = 5$ has been chosen in our simulations of the PMU reported in Chapter 6, as it appears to be a more realistic choice [Smi13].

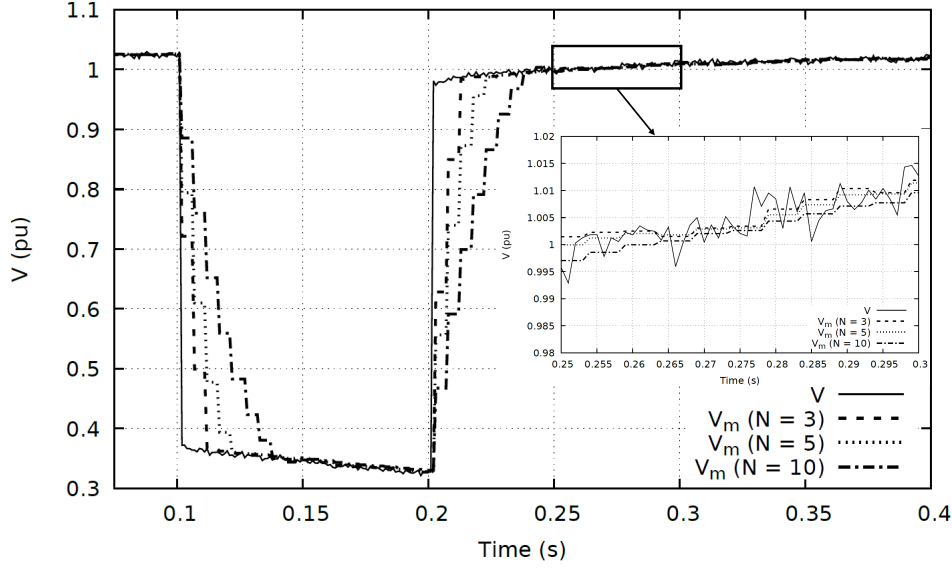


Figure D.2: Comparison of noisy voltage magnitude V with V_m for $N = 3$, $N = 5$ and $N = 10$ using WMA filter with weights given by (D.6)

D.4 Fine tuning of the weights

Once the window size is selected, some fine tuning of the WMA weights is still possible. A heuristic process is applied in order to minimize the delay ΔT and the overshoot ΔV of the voltage measurement, as defined in Fig. D.3.

Finally, Fig. D.4 compares the measured voltage magnitudes with the weights heuristically adjusted and with the weights of (D.6) for the same noisy voltage signal V . It can be seen that a much smaller delay can be achieved while avoiding unacceptable overshoots. The tuned weights have been chosen in our simulations reported in Chapter 6.

While the measurement noise has been considered for the tuning of the WMA filter, it is absent in the simulation results reported in Chapter 6.

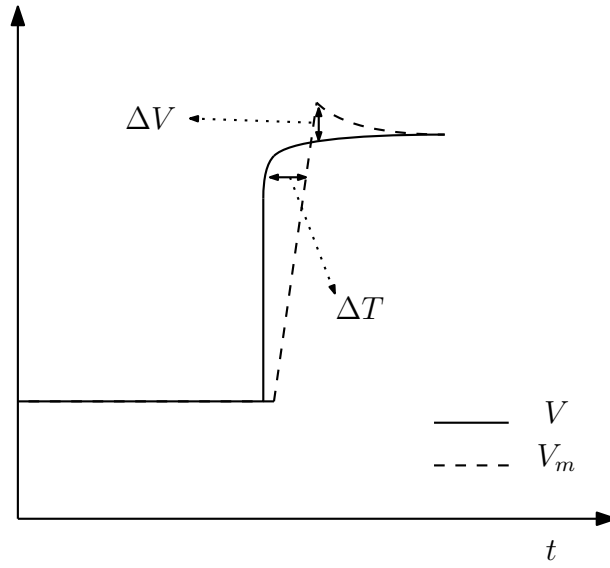


Figure D.3: Representation of the delay ΔT and the overshoot ΔV of the measured voltage V_m with respect to the voltage V

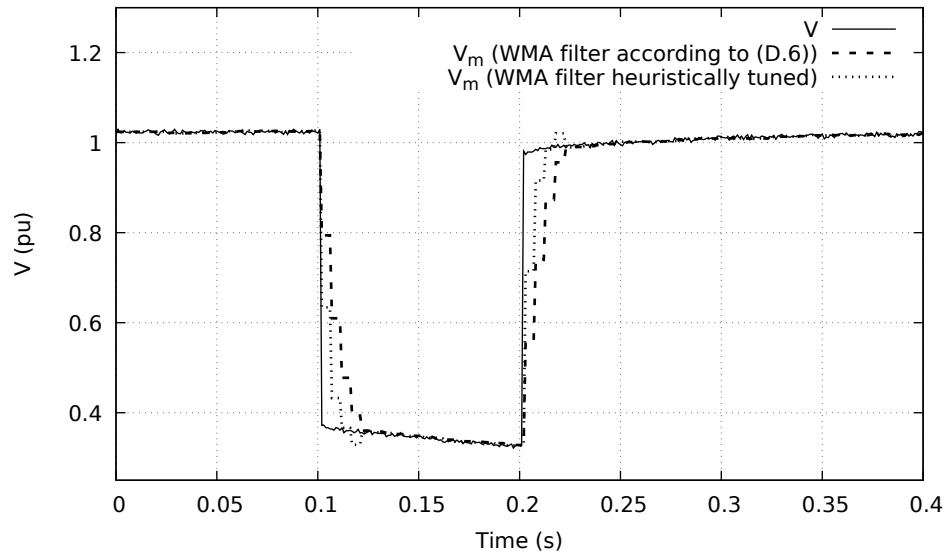


Figure D.4: Comparison of measured voltage V_m with the noisy voltage V using two WMA filters : with weights given by (D.6) and with weights heuristically tuned

Bibliography

- [A. 07] A. Ishchenko, J. M. A. Myrzik and W. L. Kling. Dynamic equivalencing of distribution networks with dispersed generation using hankel norm approximation. *IET Generation, Transmission & Distribution*, 1(5):818–825, 2007.
- [A. 15] A. V. Jayawardena, L. G. Leegahapola, D. A. Robinson and S. Perera. Representation of a grid-tied microgrid as a reduced order entity for distribution system dynamics and stability studies. *International Journal of Electrical Power and Energy Systems*, 73:591–600, 2015.
- [AMM19] A. Adrees, J. V. Milanović, and P. Mancarella. Effect of inertia heterogeneity on frequency dynamics of low-inertia power systems. *IET Generation, Transmission & Distribution*, 13(14):2951–2958, 2019.
- [ANL⁺12] U. D. Annakkage, N. K. C. Nair, Y. Liang, A. M. Gole, V. Dinavahi, B. Gustavsen, T. Noda, H. Ghasemi, A. Monti, M. Matar, R. Iravani, and J. A. Martinez. Dynamic system equivalents: A survey of available techniques. *IEEE Trans. on Power Delivery*, 27(1):411–420, 2012.
- [AP12] M. A. M. Ariff and B. C. Pal. Coherency identification in interconnected power systeman independent component analysis approach. *IEEE Transactions on Power Systems*, 28(2):1747–1755, 2012.
- [Ari15] P. Aristidou. *Time-domain simulation of large electric power systems using domain-decomposition and parallel processing methods*. PhD thesis, Université de Liège, Belgium, 2015.
- [Aus16] Australian Energy Market Operator (AEMO). Response of existing pv inverters to frequency disturbances. April 2016.
- [Aus19a] Australian Energy Market Operator (AEMO). Final report-queensland and south australia system separation on 25 august 2018. 2019.

- [Aus19b] Australian Energy Market Operator (AEMO). Technical integration of distributed energy sources. 2019.
- [AVVC15] P. Aristidou, G. Valverde, and T. Van Cutsem. Contribution of distribution network control to voltage stability: A case study. *IEEE Transactions on Smart Grid*, 8(1):106–116, 2015.
- [AWW⁺17] A. Arif, Z. Wang, J. Wang, B. Mather, H. Bashualdo, and D. Zhao. Load modeling. A review. *IEEE Transactions on Smart Grid*, 9(6):5986–5999, 2017.
- [B. df] B. Weise. Angle Instability of Generating Units with Fully Rated Converters in Cases of Low Voltages. *Chinese Wind and Solar Grid Integration Conference*, August 7-8, 2014. Available: http://www.cwpc.cn/cwpp/files/7414/1050/5492/5-1.Presentation_WiSoGIC2014_Bernd_Weise_Rev2_slides_hidden.pdf.
- [B⁺14] S. Barsali et al. *Benchmark systems for network integration of renewable and distributed energy resources*. CIGRE Task Force, 2014.
- [BA19] A. K. Bharati and V. Ajjarapu. Investigation of relevant distribution system representation with dg for voltage stability margin assessment. *IEEE Transactions on Power Systems*, 35(3):2072–2081, 2019.
- [BBB⁺16] M. Brown, M. Biswal, S. Brahma, S. J. Ranade, and H. Cao. Characterizing and quantifying noise in pmu data. In *2016 IEEE Power and Energy Society General Meeting (PESGM)*, pages 1–5. IEEE, 2016.
- [BCR⁺18] Z. Boussaada, O. Curea, A. Remaci, H. Camblong, and N. Mrabet Bellaaj. A non-linear autoregressive exogenous (narx) neural network model for the prediction of the daily direct solar radiation. *Energies*, 11(3):620, 2018.
- [BHP94] P. N. Brown, A. C. Hindmarsh, and L. R. Petzold. Using krylov methods in the solution of large-scale differential-algebraic systems. *SIAM Journal on Scientific Computing*, 15(6):1467–1488, 1994.
- [Boe16] J. C. Boemer. *On Stability of Sustainable Power Systems: Network Fault Response of Transmission System with Very High Penetration of Distributed Generation*. PhD thesis, Delft University of Technology, The Netherlands, 2016.
- [Boh06] T. P. Bohlin. *Practical grey-box process identification: theory and applications*. Springer Science & Business Media, 2006.

- [BVK13] Y. Bae, Trung-K. Vu, and Rae-Y. Kim. Implemental control strategy for grid stabilization of grid-connected pv system based on german grid code in symmetrical low-to-medium voltage network. *IEEE Transactions on Energy Conversion*, 28(3):619–631, 2013.
- [C. 94] C. W. Taylor. *Power System Voltage Stability*. Mc Graw Hill, EPRI Power Engineering Series, 1994.
- [C. 19] C. Zheng, S. Wang, Y. Liu, C. Liu, W. Xi, C. Fang and S. Liu. A novel equivalent model of active distribution networks based on lstm. *IEEE Trans. on Neural Networks and Learning Systems*, 30(9):2611–2624, Sept. 2019.
- [CE15] EDSO Cedec and Eurelectric ENTSOe. Geode, General guidelines for reinforcing the cooperation between TSOs and DSOs. 2015.
- [Cor17a] North American Electric Reliability Corporation. Distributed Energy Resources Connection Modeling and Reliability Considerations. February 2017.
- [Cor17b] North American Electric Reliability Corporation. 1200 MW Fault Induced Solar Photovoltaic Resource Interruption Disturbance Report. *Southern California 8/16/2016 Event*, June 2017.
- [CPVC] G. Chaspierre, P. Panciatici, and T. Van Cutsem. Dynamic Equivalent of a Distribution Grid Hosting Dispersed Photovoltaic Units. *Proc. IREP’ 17 Symposium*, pages 1–12.
- [CPVCss] G. Chaspierre, P. Panciatici, and T. Van Cutsem. Modelling Active Distribution Networks under Uncertainty: Extracting Parameter Sets from Randomized Dynamic Responses. *Proc. 20th PSCC conference*, Dublin (Ireland), 2018, in press.
- [DAB⁺09] T. Degner, G. Arnold, M. Braun, D. Geibel, W. Heckmann, and R. Bründlinger. Utility-scale pv systems: grid connection requirements, test procedures and european harmonisation. *Photovoltaics International*, pages 132–136, 2009.
- [DDTR96] M. K. Donnelly, J. E. Dagle, D. J. Trudnowski, and G. J. Rogers. Impacts of the distributed utility on transmission system stability. *IEEE Transactions on Power Systems*, 11(2):741–746, 1996.
- [DMSY18] M. G. Dozein, P. Mancarella, T. K. Saha, and R. Yan. System strength and weak grids: fundamentals, challenges, and mitigation strategies. pages 1–7, 2018.

- [E. 19] E. O. Kontis, T. A. Papadopoulos, M. H. Syed, E. Guillo-Sansano, G. M. Burt and G. K. Papagiannis. Artificial-intelligence method for the derivation of generic aggregated dynamic equivalent models. *IEEE Trans. on Power Systems*, 34(4):2947–2956, Jul. 2019.
- [EUg19] Commission regulation (eu) 2016/631 of 14 april 2016 establishing a network code on requirements for grid connection of generators. pages 1–68, 27 April 2016. Available: https://www.entsoe.eu/network_codes/rfg/. [Accessed October 2019].
- [F. 13] F. O. Resende, J. Matevosyan and J. V. Milanovic. Application of dynamic equivalence techniques to derive aggregated models of active distribution network cells and microgrids. *Proc. 2013 IEEE PES Grenoble PowerTech conf.*, pages 1–6, 2013.
- [F. 17] F. Conte, F. D’Agostino, S. Massucco, G. Palombo, F. Silvestro, C. Bossi and M. Cabiati. Dynamic equivalent modelling of active distribution networks for tso-dso interactions. In *Innovative Smart Grid Technologies Conference Europe (ISGT-Europe), 2017 IEEE PES*, pages 1–6. IEEE, 2017.
- [F. 19] F. Conte, F. D’Agostino and F. Silvestro. Operational constrained nonlinear modeling and identification of active distribution networks. *Electric Power Systems Research*, 168:92–104, 2019.
- [Fen12] X. S. Feng. *Dynamic Equivalencing of Distribution Network with Embedded Generation*. PhD thesis, The University of Edinburgh, UK, 2012.
- [FSS⁺16] N. Fonseca, J. Silva, A. Silva, J. Sumaili, L. Seca, R. Bessa, J. Pereira, M. Matos, P. Matos, A. C. Morais, et al. evolvdso grid management tools to support tso-dso cooperation. 2016.
- [G. 16] G. Zhang, Z. Du, C. Li, Y. Ni and C. Wang. A methodology for equivalent modeling of distribution system based on nonlinear model reduction. *International Journal of Electrical Power and Energy Systems*, 83:203–212, 2016.
- [G. 18] G. Chaspierre, P. Panciatici and T. Van Cutsem. Aggregated Dynamic Equivalent of a Distribution System hosting Inverter-based Generators. *Proc. 20th PSCC conference*, Dublin (Ireland), 2018.
- [GEC17] Q. Gemine, D. Ernst, and B. Cornélusse. Active network management for electrical distribution systems: problem formulation, benchmark, and approximate solution. *Optimization and Engineering*, 18(3):587–629, 2017.
- [Glo89] K. Glover. *A tutorial on Hankel-norm approximation*. Springer, 1989.

- [GMR20] D. M. Gonzalez, J. Myrzik, and C. Rehtanz. The smart power cell concept: mastering tso–dso interactions for the secure and efficient operation of future power systems. *IET Generation, Transmission & Distribution*, 14(13):2407–2418, 2020.
- [GPP19] F. Gonzalez, M. Petit, and Y. Perez. Impact of non-systematic electric vehicle charging behaviour on a distribution substation. *IEEE PES Innovative Smart Grid Technologies Europe (ISGT-Europe)*, 2019.
- [GR71] G. H. Golub and C. Reinsch. *Singular value decomposition and least squares solutions*. Springer, 1971.
- [GRBP16] D. Gusain, J. L. Rueda, J. C. Boemer, and P. Palensky. Identification of dynamic equivalents of active distribution networks through mvmo. *IFAC-PapersOnLine*, 49(27):262–267, 2016.
- [Gri15] Towards Smarter Grids. Developing tso and dso roles and interactions for the benefit of consumers. *ENTSO-E: Brussels, Belgium*, 2015.
- [Gut02] R. T. Guttromson. Modeling distributed energy resource dynamics on the transmission system. *IEEE Trans. on Power Systems*, 17:1148–1153, Nov. 2002.
- [H. 15] H. Golpira, H. Seifi and M. R. Hegifham. Dynamic equivalencing of an active distribution network for large-scale power system frequency stability studies. *IET Generation, Transmission & Distribution*, 9(15):2245–2254, Nov. 2015.
- [HKM⁺08] Z. Huang, B. Kasztenny, V. Madani, K. Martin, S. Meliopoulos, D. Novosel, and J. Stenbakken. Performance evaluation of phasor measurement systems. In *2008 IEEE Power and Energy Society General Meeting-Conversion and Delivery of Electrical Energy in the 21st Century*, pages 1–7. IEEE, 2008.
- [HMR⁺20] N. Hatziaegyriou, J. V. Milanović, C. Rahmann, V. Ajjarapu, C. Cañizares, I. Erlich, D. Hill, I. Hiskens, I. Kamwa, B. Pal, P. Pourbeik, J. Sanchez-Gasca, A. Stankovic, T. Van Cutsem, V. Vittal, and C. Vournas. Stability definitions and characterization of dynamic behavior in systems with high penetration of power electronic interfaced technologies. *IEEE PES Technical Report PES-TR77*, 2020.
- [HPN00] I. A. Hiskens, M. A. Pai, and T. B. Nguyen. Bounding uncertainty in power system dynamic simulations. In *Power Engineering Society Winter Meeting, 2000. IEEE*, volume 2, pages 1533–1537. IEEE, 2000.
- [IEE95] IEEE Task Force on Load Representation for Dynamic Performance. Standard Load Models for Power Flow and Dynamic Performance Simulation. *IEEE Trans. on Power Systems*, 10(3):1302–1313, Aug. 1995.

- [IEE05] IEEE Power Engineering Society. IEEE Recommended Practice for Excitation System Models for Power System Stability Studies. *Technical report*, 2005.
- [IEE19] IEEE Standards Coordinating Committee 21. IEEE Standard for Interconnection and Interoperability of Distributed Energy Resources with Associated Electric Power Systems Interfaces. Approved 15 February 2019.
- [IRL⁺12] P. Irminger, D. T. Rizy, H. Li, T. Smith, K. Rice, F. Li, and S. Adhikari. Air conditioning stall phenomenon-testing, model development, and simulation. In *PES T&D 2012*, pages 1–8. IEEE, 2012.
- [Ish08] A. Ishchenko. Dynamics and Stability of Distribution Networks with Dispersed Generation. PhD Thesis, Technische Universiteit Eindhoven, The Netherlands, 2008.
- [J. 13] J. V. Milanovic and S. M. Zali. Validation of Equivalent Dynamic Model of Active Distribution Network Cell. *IEEE Trans. on Power Systems*, 28(3):2101–2110, 2013.
- [J. 14] J. V. Milanovic (convener). Modelling and aggregation of loads in flexible power networks. *Report of CIGRE WG C4.605*, 2014.
- [Jay15] A. V. Jayawardena. *Contributions to the development of microgrids: Aggregated modelling and operational aspects*. PhD thesis, University of Wollongong, Australia, 2015.
- [JDM19] A. Jalali, M. G. Dozein, and P. Mancarella. Frequency Stability Provision From Battery Energy Storage System Considering Cascading Failures with Applications to Separation Events in Australia. *Proc. 13th IEEE PES PowerTech conference*, Milan(Italy), 2019.
- [JPK⁺18] K. W. Jones, P. Pourbeik, G. Kobet, et al. Impact of inverter based generation on bulk power system dynamics and short-circuit performance. *Task Force on Short-Circuit and System Performance Impact of Inverter Based Generation*, Tech. Rep. PESTR68, 2018.
- [K. 18] K. Yamashita (Convenor CIGRE) and H. Renner (Convenor CIRED). Modelling of inverter-based generation for power system dynamic studies. *C4/C6/CIRED, Technical Brochure*, May 2018.
- [Kau87] L. Kaufmann. Clustering by means of medoids. In *Proc. Statistical Data Analysis Based on the L1 Norm Conference, Neuchatel, 1987*, pages 405–416, 1987.
- [KHBL13] P. Kotsampopoulos, N. Hatziargyriou, B. Bletterie, and G. Lauss. Review, analysis and recommendations on recent guidelines for the provision of ancillary services

- by Distributed Generation. *Proc. IEEE Intern. Workshop on Intelligent Energy Systems*, pages 185–190, 2013.
- [KOYT16] K. Kawabe, Y. Ota, A. Yokoyama, and K. Tanaka. Novel dynamic voltage support capability of photovoltaic systems for improvement of short-term voltage stability in power systems. *IEEE Transactions on Power Systems*, 32(3):1796–1804, 2016.
- [KPPBJ18] N. Karthikeyan, B. R. Pokhrel, J. R. Pillai, and B. Bak-Jensen. Utilization of battery storage for flexible power management in active distribution networks. *2018 IEEE Power & Energy Society General Meeting (PESGM)*, pages 1–5, 2018.
- [Kun94] P. Kundur. *Power system stability and control*. McGraw-hill New York, 1994.
- [KV11] G. Kaestle and T. K. Vrana. Improved requirements for the connection to the Low Voltage grid. *21st International Conference on Electricity Distribution*, Frankfurt, 2011.
- [L. 99] L. Ljung. *System identification: theory for the user*. PTR Prentice Hall, Upper Saddle River, NJ, 1999.
- [LBP⁺17] G. Lammert, J. C. Boemer, D. Premm, O. Glitza, L. D. Pabon Ospina, D. Fetzer, and M. Braun. Impact of fault ride-through and dynamic reactive power support of photovoltaic systems on short-term voltage stability. pages 1–6, 2017.
- [Lju01] L. Ljung. Black-box models from input-output measurements. *Proceedings of the 18th IEEE instrumentation and measurement technology conference*, 1:138–146, 2001.
- [LMR⁺18] E. Lambert, H. Morais, F. Reis, R. Alves, G. Taylor, A. Souvent, and N. Suljanovic. Practices and architectures for TSO-DSO data exchange: European landscape. pages 1–6, 2018.
- [LPPO⁺18] G. Lammert, D. Premm, L. D. Pabon Ospina, J. C. Boemer, M. Braun, and T. Van Cutsem. Control of photovoltaic systems for enhanced short-term voltage stability and recovery. *IEEE Transactions on Energy Conversion*, 34(1):243–254, 2018.
- [LRC⁺15] A. Luna, J. Rocabert, J. I. Candela, J. R. Hermoso, R. Teodorescu, F. Blaabjerg, and P. Rodriguez. Grid voltage synchronization for distributed generation systems under grid fault conditions. *IEEE Transactions on Industry Applications*, 51(4):3414–3425, 2015.

- [M. 96] M. K. Donnelly, J. E. Dagle, D. J. Trudnowski and G. J. Rogers. Impacts of the Distributed Utility on Transmission System Stability. *IEEE Trans. on Power Systems*, 11(2):741–746, 1996.
- [M. 14] M. Gibbard and D. Vowles. Simplified 14-generator model of the South East Australian power system. *The University of Adelaide, Australia*, 2014.
- [MA13] V. Miranda and R. Alves. Differential evolutionary particle swarm optimization (DEEPSO): a successful hybrid. *2013 BRICS Congress on Computational Intelligence and 11th Brazilian Congress on Computational Intelligence*, pages 368–374, 2013.
- [MDH⁺18] F. Milano, F. Dörfler, G. Hug, D. J. Hill, and G. Verbič. Foundations and challenges of low-inertia systems. In *2018 Power Systems Computation Conference (PSCC)*, pages 1–25. IEEE, 2018.
- [MF02] V. Miranda and N. Fonseca. EPSO-best-of-two-worlds meta-heuristic applied to power system problems. *Proceedings of the 2002 Congress on Evolutionary Computation*, 2:1080–1085, 2002.
- [MG14a] Western Electricity Coordinating Council Modeling and Validation Work Group. WECC Wind Power Plant Dynamic Modeling Guide. *WECC Renewable Energy Modeling Task Force*, April 2014.
- [MG14b] Western Electricity Coordinating Council Modeling and Validation Work Group. WECC Solar Plant Dynamic Modeling Guidelines. *WECC Renewable Energy Modeling Task Force*, May 2014.
- [Moo97] C. Z. Mooney. *Monte Carlo Simulation*, volume 116. Sage Publications, 1997.
- [N. 17] N. Hatziargyriou (convenor). Contribution to bulk system control and stability by distributed energy resources connected at distribution network. *IEEE PES Tech. Report PES-TR22*, 2017.
- [N. 19] N. Fulgêncioa, C. Moreira, L. Carvalho and J. P. Lopes. Aggregated dynamic model of active distribution networks for large voltage disturbances. *Electric Power Systems Research*, 178:1–13, 2019.
- [ODD03] M. L. Ourari, L. A. Dessaint, and V. Q. Do. Coherency approach for dynamic equivalents of large power systems. In *International conference on power systems transients–IPST*, pages 1–6, 2003.

- [P. 14] P. Aristidou, D. Fabozzi and T. Van Cutsem. Dynamic simulation of large-scale power systems using a parallel Schur-complement-based decomposition method. *IEEE Trans. on Parallel and Distributed Systems*, 25(10):2561–2570, 2014.
- [P. 15] P. Aristidou and T. Van Cutsem. A Parallel Processing Approach to Dynamic Simulations of Combined Transmission and Distribution Systems. *International Journal of Electrical Power & Energy Systems*, 72:58–65, 2015.
- [P. 18] P. R. Mier. A tutorial on differential evolution with python. Toulouse (France), September 5, 2017. url: <https://pablormier.github.io/2017/09/05/a-tutorial-on-differential-evolution-with-python/> [Accessed September 2018].
- [PAGVC16] F. Plumier, P. Aristidou, C. Geuzaine, and T. Van Cutsem. Co-simulation of electromagnetic transients and phasor models: A relaxation approach. *IEEE Transactions on Power Delivery*, 31(5):2360–2369, 2016.
- [PGG⁺20] M. Paolone, T. Gaunt, X. Guillaud, M. Liserre, S. Meliopoulos, A. Monti, T. Van Cutsem, V. Vittal, and C. Vournas. Fundamentals of power systems modelling in the presence of converter-interfaced generation. *Electric Power Systems Research*, 189, 2020.
- [POVC20] L. D. Pabon Ospina and T. Van Cutsem. Emergency support of transmission voltages by active distribution networks: a non-intrusive scheme. *IEEE Transactions on Power Systems (in press)*, 2020.
- [Pre16] Traian-N. Preda. *Modelling of Active Distribution Grids for Stability Analysis*. PhD thesis, Norwegian University of Science and Technology Norway, 2016.
- [PSGS⁺15] P. Pourbeik, J. J. Sánchez-Gasca, J. Senthil, J. Weber, A. Ellis, S. Williams, S. Serman, K. Bolton, N. Miller, R. J. Nelson, et al. Value and limitations of the positive sequence generic models of renewable energy systems. *This is a brief white-paper prepared by an Ad hoc group within the WECC Renewable Energy Modeling Task Force*, 2015.
- [PSL05] K. Price, R. M. Storn, and J. A. Lampinen. *Differential Evolution - A Practical Approach to Global Optimization*. Springer, 2005.
- [PT08] A. G. Phadke and J. S. Thorp. *Synchronized phasor measurements and their applications*, volume 1. Springer, 2008.
- [PV14] L. Papangelis and C. Vournas. Design principles of wind turbine inertia emulators for autonomous systems. *IFAC Proceedings Volumes*, 47(3):5844–5851, 2014.

- [PWR⁺] P. Pourbeik, J. Weber, D. Ramasubramanian, J. Sanchez-Gasca, J. Senthil, P. Zakhast, J. C. Boemer, A. Gaikwad, I. Green, and S. Tacke. An aggregate dynamic model or distributed energy resources or power system stability studies. *Cigre Science & Engineering*, (14):38–48.
- [R. 96] R. Lind and D. Karlsson. Distribution System Modelling for Voltage Stability Studies. *IEEE Trans. on Power Systems*, 11(4):1677–1682, Nov. 1996.
- [RC13] C. Robert and G. Casella. *Monte Carlo statistical methods*. Springer Science & Business Media, 2013.
- [Ren20] Ren 21. Renewables 2019 Global Status Report. 2019. Available: https://www.ren21.net/wp-content/uploads/2019/05/gsr_2019_full_report_en.pdf [Accessed May 2020].
- [RL17] M. Rasouli and C. Lagoa. A nonlinear term selection method for improving synchronous machine parameters estimation. *International Journal of Electrical Power & Energy Systems*, 85:77–86, 2017.
- [RTS07] M. H. F. Rahiman, M. N. Taib, and Y. M. Salleh. Black box modeling of steam distillation essential oil extraction system using armax structure. In *2007 International Conference on Intelligent and Advanced Systems*, pages 1059–1062. IEEE, 2007.
- [rV15] VDE-AR-N 4120. Technical requirements for the connection and operation of customer installations to the high-voltage network (TCC High-Voltage). pages 1–123, January 2015.
- [RWR12] M. Rasouli, D. T. Westwick, and W. D. Rosehart. Reducing induction motor identified parameters using a nonlinear lasso method. *Electric power systems research*, 88:1–8, 2012.
- [S. 13] S. M. Zali and J. V. Milanovic. Generic Model of Active Distribution Network for Large Power System Stability Studies. *IEEE Trans. on Power Systems*, 28(3):3126–3133, 2013.
- [SB17] H. Soleimani Bidgoli. *Real-time Corrective Control in Active Distribution Networks*. PhD thesis, Université de Liège, Liège, Belgique, 2017.
- [SBGVC16] H. Soleimani Bidgoli, M. Glavic, and T. Van Cutsem. Receding-Horizon Control of Distributed Generation to Correct Voltage or Thermal Violations and Track Desired Schedules. *Proc. 19th PSCC conf.*, 2016.

- [Shm02] Y. S. Shmaliy. A simple optimally unbiased MA filter for timekeeping. *IEEE transactions on ultrasonics, ferroelectrics, and frequency control*, 49(6):789–797, 2002.
- [Smi13] S. Smith. *Digital Signal Processing: A practical guide for engineers and scientists*. Newnes, Chapter 15, 2013.
- [SMN⁺18] G. P. Schiapparelli, S. Massucco, E. Namor, F. Sossan, R. Cherkaoui, and M. Paolone. Quantification of primary frequency control provision from battery energy storage systems connected to active distribution networks. *2018 Power Systems Computation Conference (PSCC)*, pages 1–7, 2018.
- [SMTB] A. Z. M. Shahriar Muttalib, G. A. Taylor, and M. E. Bradley. Developing and enhancing business processes to enable higher levels of TSO-DSO interaction. *CIREN Workshop*.
- [SS04] A. M. Stankovic and A. T. Saric. Transient power system analysis with measurement-based gray box and hybrid dynamic equivalents. *IEEE Transactions on Power Systems*, 19(1):455–462, 2004.
- [SST⁺19] N. Suljanović, A. Souvent, G. Taylor, M. Radi, J. Cantenot, E. Lambert, and H. Morais. Design of interoperable communication architecture for tso-dso data exchange. pages 1–6, 2019.
- [T. 06] T. Van Cutsem, Q. Renoy, and D. Lefebvre. Modelling the short-term and long-term aggregate response of multiple loads fed through a sub-transmission network. in *Proc. IEEE Power System Conference and Exposition*, 2006.
- [Tib96] R. Tibshirani. Regression shrinkage and selection via the lasso. *Journal of the Royal Statistical Society: Series B (Methodological)*, 58(1):267–288, 1996.
- [Tro09] E. Troester. New german grid codes for connecting pv systems to the medium voltage power grid. In *2nd International workshop on concentrating photovoltaic power plants: optical design, production, grid connection*, pages 9–10, 2009.
- [VCct] T. Van Cutsem. Power system dynamics, control and stability. *Lecture notes, Univ. of Liège*, 2020, available at <https://people.montefiore.uliege.be/vct/>.
- [VCGR⁺15] T. Van Cutsem, M. Glavic, W. Rosehart, J. Andrade dos Santos, C. Cañizares, M. Kanatas, L. Lima, F. Milano, L. Papangelis, R. Andrade Ramos, et al. Test systems for voltage stability analysis and security assessment. Technical report, IEEE, 2015.

- [VCV98] T. Van Cutsem and C. Vournas. *Voltage stability of electric power systems*. Springer, 1998.
- [VFGL⁺18] T. K. Vrana, D. Flynn, E. Gomez-Lazaro, J. Kiviluoma, D. Marcel, N. Cutululis, and J. C. Smith. Wind power within european grid codes: Evolution, status and outlook. *Wiley Interdisciplinary Reviews: Energy and Environment*, 7(3):e285, 2018.
- [VKA18] R. Venkatraman, S. K. Khaitan, and V. Ajjarapu. Dynamic co-simulation methods for combined transmission-distribution system with integration time step impact on convergence. *IEEE Transactions on Power Systems*, 34(2):1171–1181, 2018.
- [VT04] J. Vesterstrom and R. Thomsen. A Comparative Study of Differential Evolution, Particle Swarm Optimization, and Evolutionary Algorithms on Numerical Benchmark Problems. *Congress on Evolutionary Computation, 2004 CEC2004*, pages 1980–1987, 2004.
- [WEC16] WECC Battery Storage Dynamic Modeling Guideline. November, 2016.
- [wecrg] WECC website : <http://www.wecc.org>.
- [Wei15] B. Weise. Impact of k-factor and active current reduction during fault-ride-through of generating units connected via voltage-sourced converters on power system stability. *IET Renewable Power Generation*, 9(1):25–36, 2015.
- [WFGVC17] T. Weckesser, V. Franz, E. Grebe, and T. Van Cutsem. A model reduction approach for simulation of long-term voltage and frequency dynamics. *2017 IEEE PowerTech Conference*, pages 1–6, Manchester (UK), 2017.
- [X. 18] X. Wu, X. Lei, Y. Lan, A. Monti and F. Gao. A new dynamic equivalent of active distribution network for transient analysis. *2018 International Conference on Power System Technology (POWERCON)*, pages 529–536, Guangzhou (China), 2018.
- [X. 19] X. Shang, Z. Li, J. Zheng and Q.H. Wu. Equivalent modeling of active distribution network considering the spatial uncertainty of renewable energy resources. *International Journal of Electrical Power and Energy Systems*, 112:83–91, 2019.
- [YZP07] J. Yang, J. Zhang, and W. Pan. Dynamic equivalents of power system based on extended two particle swarm optimization. 5:609–613, 2007.
- [Zal12] S. M. Zali. *Equivalent Dynamic Model of Distribution Network with Distributed Generation*. PhD thesis, The University of Manchester, UK, 2012.

- [ZGG17] M. Zeraati, M. E. H. Golshan, and J. M. Guerrero. A consensus-based cooperative control of pev battery and pv active power curtailment for voltage regulation in distribution networks. *IEEE Transactions on Smart Grid*, 10(1):670–680, 2017.
- [ZM17] Y. Zhu and J. V. Milanović. Automatic identification of power system load models based on field measurements. *IEEE Transactions on Power Systems*, 33(3):3162–3171, 2017.
- [ZWM11] S. M. Zali, N. C. Woolley, and J. V. Milanović. Development of equivalent dynamic model of distribution network using clustering procedure. *17th Power Systems Computation Conference*, 2011.
- [ZYS⁺20] A. Zecchino, Z. Yuan, F. Sossan, R. Cherkaoui, and M. Paolone. Optimal provision of concurrent primary frequency and local voltage control from a bess considering variable capability curves: Modelling and experimental assessment. *Proc. 21th PSCC conf.*, Porto (Portugal), 2020.